

Proceeding of JSPS-CAS Core University Program Seminar
on Production and Control of High Performance Plasmas
with Advanced Plasma Heating and Diagnostic Systems

4-7 November 2008, Lijiang, China

Edited by
Xiang GAO and Shigeru MORITA

Abstract

The JSPS-CAS Core University Program (CUP) seminar on "Production and control of high performance plasmas with advanced plasma heating and diagnostic systems" took place in Shiner hotel, Lijiang, China, 4-7 November 2008. This seminar was organized in the framework of CUP in the field of plasma and nuclear fusion. One special talk and 34 oral talks were presented in the seminar including 16 Japanese attendees.

Production and control of high performance plasmas is a crucial issue for realizing an advanced nuclear fusion reactor in addition to developments of advanced plasma heating and diagnostics. This seminar was motivated along the issues. Results obtained from CUP activities during recent four years were summarized. Several crucial issues to be resolved near future were also extracted in this seminar.

Key words: high performance plasmas, advanced fusion reactor, magnetically confined devices, improved confinement, steady state operation, MHD stability, high beta plasmas, plasma collapse, edge plasma control, advanced plasma heating, advanced plasma diagnostics.

Organization Committee

Xiang GAO (Chairperson, Institute of Plasma Physics, Chinese Academy of Sciences, China)

Shigeru MORITA (Chairperson, National Institute for Fusion Science)

Program Committee

Kongjia WANG (Institute of Plasma Physics, Chinese Academy of Sciences, China)

Xiang GAO (Institute of Plasma Physics, Chinese Academy of Sciences, China)

Longwen YAN (Southwestern Institute of Physics, China)

Xuantong DING (Southwestern Institute of Physics, China)

Jin LIU (Yunnan University, China)

Kazuo TOI (National Institute for Fusion Science, Japan)

Shigeru MORITA (National Institute for Fusion Science, Japan)

Shunsuke IDE (Japan Atomic Energy Agency, Japan)

Takashi MAEKAWA (Kyoto University, Japan)

Kazuaki HANADA (Kyushu University, Japan)

Conference Secretariat

Shaohua DONG (Secretary, Institute of Plasma Physics, Chinese Academy of Sciences, China)

Liqun HU (Scientific secretary, Institute of Plasma Physics, Chinese Academy of Sciences, China)

Yinxian JIE (Scientific Secretary, Institute of Plasma Physics, Chinese Academy of Sciences, China)

Mayumi KATO (Secretary, National Institute for Fusion Science, Japan)

Preface

The JSPS-CAS Core University Program (CUP) seminar on "Production and control of high performance plasmas with advanced plasma heating and diagnostic systems" took place in Shiner hotel, Lijiang, China, 4-7 November 2008. This seminar was organized in the framework of CUP in the field of plasma and nuclear fusion.

Production and control of high performance plasmas is a crucial issue for realizing an advanced nuclear fusion reactor. For the purpose developments of advanced plasma heating and diagnostics become also extremely important. A lot of CUP collaboration programs have been carried out along the aim in the category of "improvement of core plasma properties". Results obtained from CUP activities during recent four years were summarized in this seminar. Several crucial issues to be resolved near future were also extracted. One special talk and 34 oral talks were presented in the seminar including 16 Japanese attendees. The presentations were mainly focused on the following topics.

1. Production and transport of high-performance plasmas
2. Discharge trial toward steady state operation
3. MHD stability and plasma collapse of high-beta plasmas
4. Particle and energy control of edge and divertor plasmas
5. Advanced heating scenarios
6. Advanced plasma diagnostics

These topics are very important, regardless of the difference in magnetic configurations such as tokamaks and helical devices. Each of them was intensively discussed from both sides of experimental and theoretical studies. In addition, engineering aspects were also stressed on several topics.

This seminar was closed with great success, clarifying remarkable progress in researches related to these important topics obtained through CUP. The organizing and program committees are grateful to all participants for their supports and corporation to this seminar.

Xiang GAO and Shigeru MORITA
Chairpersons of the Organizing Committee

Contents

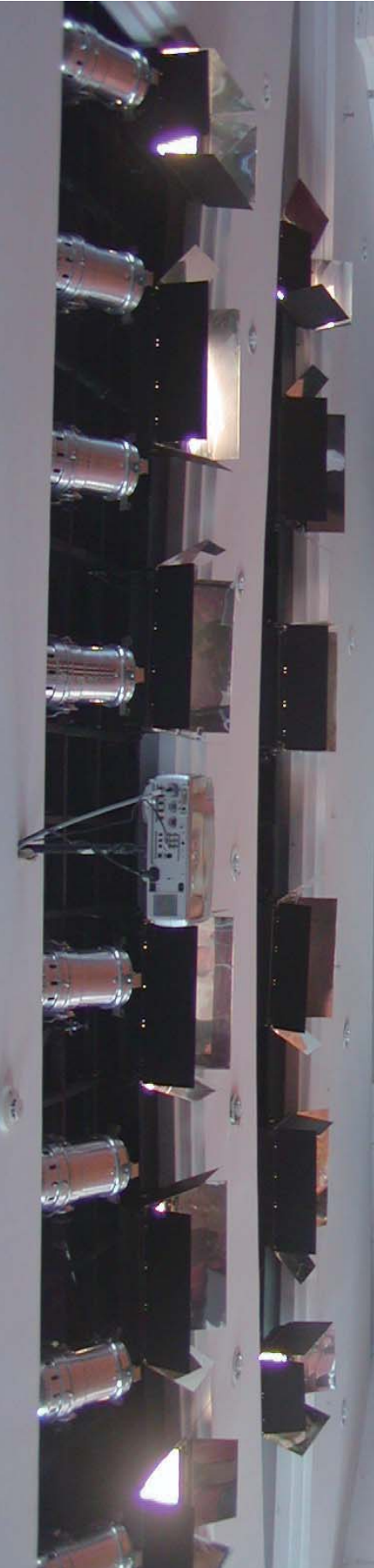
Preface

Contents

Photo of Participants

1. Basic elements in drift wave turbulence.....	1
T. WATARI (NIFS)	
2. Plasma shape control on EAST.....	45
B. XIAO (ASIPP)	
3. Recent Results of JT-60 Experiments.....	48
Y. KOIDE (JAEA)	
4. Recent Progress of the HL-2A tokamak.....	49
X. DUAN (SWIP)	
5. Current Ramp-up by Microwave Power in the LATE Device	53
T. MAEKAWA (Kyoto University)	
6. Research Activities and Plan of Electron Cyclotron Wave Startup and Alfvén Wave Current Drive at SUNIST	58
Y. TAN (Tsinghua University)	
7. Reconstruction of the TEXT-U tokamak in China	68
Zhuang Ge and Y. DING (HUST)	
8. Contribution of the Large Helical Device Plasmas to Alfvén Eigenmode Physics in Toroidal Plasmas.....	75
K. TOI (NIFS)	
9. Progress on edge and core impurity transport study with development of spectroscopic instruments in LHD.....	81
S. MORITA (NIFS)	
10. Plasma sheath resistance measurement by reference probe in PECVD coating machine	102
Q. WANG (Northeastern University)	
11. Progress of Long Pulse and LHCD Discharges on HT-7 Tokamak	110
X. GAO (ASIPP)	
12. Present Progress of Plasma Transport Study on HL-2A	122
X. DING (SWIP)	
13. Particles Behavior in Quasi-steady-state AC Plasmas on HT-7 Tokamak	128
Y. JIE (ASIPP)	
14. Investigation of experimental configuration for electron Bernstein wave heating on LHD.....	137
H. IGAMI (NIFS)	
15. Study of high power ICRF antenna design in LHD.....	151
H. KASAHARA (NIFS)	
16. Energetics of resistive wall modes in flowing plasmas.....	166
M. HIROTA (JAEA)	

17. Recent Progress of Neutral Beam Injector and Beam Emission Diagnosis in LHD	174
K. IKED (NIFS)	
18. Density limits with different fuelling methods in the HL-2A tokamak	185
L. W. YAN (SWIP)	
19. Modelling of EAST with LHRF and NBI	201
D. ZHOU (ASIPP)	
20. Soft x-ray tomography on HT-7 tokamak	209
K. CHEN (ASIPP)	
21. Evaluation of the Optical Design of Laser Thomson Scattering Diagnostics for High-Temperature EAST Tokamak and Low-Temperature MAP-II Divertor Simulator	221
S. KADO (The University of Tokyo)	
22. Dynamics of dust particle in SOL/Divertor plasma of HL-2A	226
Y. TOMITA (NIFS)	
23. Analysis on EAST LHCD operation space by using simple Core-SOL-Divertor model	230
R. HIWATARI (CRIEPI)	
24. Two dimensional density fluctuation measurements during the non-inductive current ramp-up phase in the compact plasma wall interaction experimental device CPD	242
H. ZUSHI (Kyushu University)	
25. Recent Progress of the HL-2A Laser Interferometer	247
Y. ZHOU (SWIP)	
26. Plasma boundary position measurements using frequency sweep microwave reflectometer in LHD	251
T. TOKUZAWA (NIFS)	
27. Experimental progress on the EAST superconductor tokamak	265
L. HU (ASIPP)	
28. Data Processing of Divertor Probes on EAST	268
J. WANG (ASIPP)	
29. Soft x-ray PHA diagnostic for the electron temperature measurement on EAST	273
P. Xu (ASIPP)	
30. Development of a heavy ion beam probe for measuring electrostatic potential profile and its fluctuation in LHD	279
T. IDO (NIFS)	
31. Recent Progress in Heliotron J Experiments for Exploration of the Helical-Axis Heliotron Concept	294
T. MIZUUCHI (Kyoto University)	
32. Ion Cyclotron Resonance Heating System on EAST	298
L. WANG (ASIPP)	
Agenda	303
List of Participants	305



Basic elements in drift wave turbulence

T. Watari (National Institute for Fusion Science)

This is a lecture note used at "JSPS-CAS Core University Program Seminar on "Production and Control of High Performance Plasmas with Advanced Plasma Heating and Diagnostic systems" (4 - 7, November, 2008 Leijiang, China)

Thanks to the long efforts of researchers toward nuclear fusion, plasma physics is gradually reaching the level of maturity. It is now recognized that anomalous transport is caused by drift wave turbulence and, therefore, experimental investigations in this field are becoming more and more important.

In this lecture, we try to introduce the following important notions governing drift wave turbulence:

Contents:

- I. Linear theory of drift waves
- II. Hasegawa-Mima and Hasegawa-Wakatani Equations
(Conservation of energy and enstrophy)
- III. Power spectrum observed in experiments and simulations
- IV. Energy transfer in k-space
- V Linear Response function for zonal flows
- VI. Excitation of zonal flows by drift wave turbulence
- VII. Experimental determination of transfer function
- VIII Streamers and blobs

Section-I. Linear theory of drift waves

The dispersion relation of drift waves and stability/instability condition are obtained in linear theory in which nonlinear terms are ignored. Yet, it is important to study the linear theory for only the linearly unstable modes grow. A brief review of the linear theory here will be useful also as an introduction to various terms used in the following sections discussing advanced physics in nonlinear stage.

(I-1) Geometry considering drift waves:

Drift wave is caused due to the density and temperature gradients. According to the success of tokamaks and helical systems in the nuclear fusion research, many theoretical explorations were made based on torus. However, due to the relative complexity of the drift waves, experimental geometry is in theories reduced to idealized simpler ones. For example, a part of torus plasma is approximated by a cylindrical plasma as shown in Fig.1 (a). Further simplification is made by regarding an annuli of the cylinder as a slab as shown in Fig.1 (b).

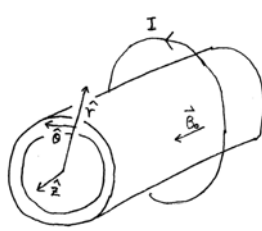


Fig.1(a)

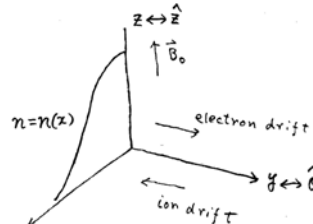


Fig.1(b)

(I-2) The simplest dispersion relation of drift wave

Now let us derive the simplest dispersion relation of drift wave on this slab geometry. Electrons and ions are subject to diamagnetic drift which are, when gradient of ion temperatures are ignored, given by

$$v_{d,y,e} = -\frac{cT_i}{eB} \frac{1}{n_0} \frac{dn_0}{dx}, \quad v_{d,y,i} = \frac{cT_i}{eB} \frac{1}{n_0} \frac{dn_0}{dx} \quad . \quad (1)$$

The momentum continuity equation is given by

$$mn(\frac{\partial \vec{v}_\perp}{\partial t} + \vec{v} \cdot \vec{\nabla} \vec{v} \mid_\perp) = ne[\vec{E} + \frac{1}{c} \vec{v}_\perp \times \vec{B}] - \vec{\nabla} p \quad (2)$$

Here, $\vec{v} \cdot \vec{\nabla} \vec{v}$ contains one of the nonlinearity term but it is ignored in this section (linear theory). In many of the cases, the electrostatic approximation is valid to drift waves:

$$\vec{E} = -\vec{\nabla} \tilde{\phi}, \quad \tilde{\phi} = \sum_{\vec{k}} \tilde{\phi}_{\vec{k}}(t) e^{i\vec{k} \cdot \vec{x} - i\omega t} \quad (3)$$

Equation (2) is solved for each order of $(1/\omega_{c,i})$; the lowest order solution is so-called $\vec{E} \times \vec{B}$ drift.

$$\vec{v}_{\perp} = \frac{c}{B^2} [\vec{E} \times \vec{B}] = \frac{c}{B^2} [\vec{E} \times \vec{B}] = -ik_y \tilde{\phi} \frac{c}{B} [\hat{y} \times \hat{z}] = -ik_y \tilde{\phi} \frac{c}{B} \hat{x} \quad (4)$$

Note that it does not depend on the sign of charge of particles and, therefore, does not cause charge separation. Density continuity equation is used in determining ion density perturbation:

$$\frac{\partial n}{\partial t} + \operatorname{div}(n\vec{v}) = 0 \quad (5)$$

where $\operatorname{div}(n\vec{v})$ contains another source of nonlinearity which is disregarded in this section. By substituting Eq. (4) in Eq.(5), we obtain:

$$n_i = \frac{1}{i\omega} (-ik_y \frac{c}{B} \cdot \frac{\partial n_0}{\partial x}) \tilde{\phi} = -\frac{1}{\omega} (k_y \frac{c}{B} \cdot \frac{\partial n_0}{\partial x}) \tilde{\phi} = -\frac{1}{\omega} (k_y \frac{c}{B} \cdot \frac{\partial n_0}{\partial x}) \tilde{\phi} = -\frac{\omega_{*,i}}{\omega} \left(\frac{e_i \tilde{\phi}}{T_i} \right) \quad (6)$$

Where we have defined drift frequency of ion

$$\omega_{*,i}(k_y) = k_y \left(\frac{cT_i}{e_i B} \right) \frac{1}{n_{i0}} \frac{\partial n_{i0}}{\partial x} \quad . \quad (7)$$

On the other hand, the perturbation of electron density is given by so-called adiabatic response.

$$n_e = \frac{e\varphi}{T_e} n_{e,0} \quad (8)$$

Finally, charge neutrality condition $e_i n_i - e n_e = 0$ is used in order to obtain the dispersion relation.

Using Eqs.(6) and (8), we obtain the simplest dispersion relation:

$$\omega = -\frac{e_i^2}{e^2} \frac{T_e}{T_i} \omega_{*,i} = -\frac{e_i}{e} k_y \left(\frac{cT_e}{eB} \right) \frac{1}{n_{i0}} \frac{\partial n_{i0}}{\partial x} = -k_y \left(\frac{ZcT_e}{eB} \right) \frac{1}{n_0} \frac{\partial n_0}{\partial x} = \omega_* \quad (9)$$

where

$$\omega_* = -k_y \left(\frac{ZcT_e}{eB} \right) \frac{1}{n_0} \frac{\partial n_0}{\partial x} \quad (10)$$

is one important value which is simply referred to as "drift wave frequency".

(I-2) The role of magnetic shear

In the experimental research, it is reported that the magnetic shear of the confining magnetic configuration affects the energy transport of plasmas. Correspondingly, there are many theoretical works that analyzed the effects of magnetic shear on the drift waves. In Fig.2 (a), magnetic lines on

two magnetic flux surfaces are illustrated in red- and black- lines. A perspective view of them from outside of the torus is shown in Fig.2 (b). The most naive consideration invoked by this figure is that mode number k -parallel increases boundlessly as the wave propagate out from the resonance surface if poloidal mode number k_θ is kept constant.

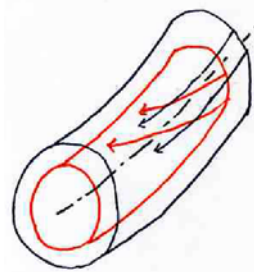


Fig.2(a)

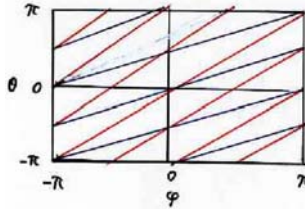


Fig.2(b)

This is the simplest explanation of the stabilizing effect of the drift wave. However, it was found in the later works that effect of mode coupling alters the effectiveness of the magnetic shear on stabilization.

(I-3) Torus effect (effects of good/bad curvature and mode coupling)

Passing particle Instabilities:

In order to avoid bulky explanations, we start with viewing the following equation determining drift waves [1-2]. This equation is suitable to describe so called ITG mode (ion temperature gradient mode); this equation is still simple, for it still stands on the electrostatic approximation and assumes adiabatic electron response.

$$\left\{ \rho_i^2 \frac{\partial^2}{\partial x^2} - \left(\frac{\varepsilon_n}{b^{1/2} \tau q \Omega} \right)^2 \left(\frac{\partial}{\partial \theta} + i k_\theta s x \right)^2 - \frac{2 \varepsilon_n}{\tau \Omega} \left(\cos \theta - \frac{i \sin \theta}{k_\theta} \frac{\partial}{\partial x} \right) - \left(\frac{\Omega - 1}{\tau \Omega + (1 + \eta_i)} + b \right) \right\} \phi(\theta, x) = 0 \quad (11)$$

, where

$$\begin{aligned} \Omega &= -\frac{\omega}{\tau_e \omega_{*,i}(k_y)}, \quad \varepsilon_n \equiv \frac{L_n}{R}, \quad b = b_\theta = (k_\theta \rho_i)^2, \\ \tau &= \frac{T_e}{T_i}, \quad \eta_i = \frac{d \ln(T_i)}{d \ln(n)} \end{aligned} \quad (12)$$

Note that ε_n is proportional to $1/R$ i.e., this term vanishes in the limit of $R \rightarrow \infty$.

This term is originated from

$$\vec{k} \cdot \vec{v}_{D,i} = \vec{k} \cdot \frac{c}{eB} \left\langle \frac{v_{\perp}^2}{m} \vec{\kappa} \times \vec{b} + \mu \frac{\vec{\nabla}B}{B} \times \vec{b} \right\rangle \approx \vec{k} \cdot \frac{2cT}{eB} \left\langle \vec{\kappa} \times \vec{b} \right\rangle \quad (13)$$

Indeed a magnetic flux surface is a 2D-torus imbedded in 3-D space; magnetic lines of force have normal- and geodesic- curvatures $(\vec{\kappa}_n, \vec{\kappa}_g)$ with the following definitions.

$$\begin{aligned} \vec{\kappa} &= (\vec{\nabla}B) / B = \vec{\kappa}_n + \vec{\kappa}_g \\ \vec{\kappa}_n &= \hat{r}(\hat{r} \cdot \vec{\nabla}B) / B = -\hat{r}(1/R) \cos \theta \quad (14) \\ \vec{\kappa}_g &= (\vec{\theta} \cdot \vec{\nabla}B) / B = \vec{\theta}(1/R) \sin \theta \end{aligned}$$

And gives the third term of Eq. (11)

$$\begin{aligned} \vec{k} \cdot \vec{v}_{D,i} &\approx \vec{k} \cdot \frac{cT_i}{eB} \left\langle \vec{b} \times \vec{\kappa} \right\rangle = \vec{k} \cdot \frac{cT_i}{eB} \frac{1}{R} \left\langle \vec{b} \times (\hat{\theta} \sin \theta - \hat{r} \cos \theta) \right\rangle \\ &= -\frac{cT_i}{eB} \frac{1}{R} \left\langle k_r \sin \theta + k_{\theta} \cos \theta \right\rangle = -\frac{1}{\tau} \omega^* \frac{L_n}{R} \left\langle \cos \theta - i \sin \theta \frac{1}{k_{\theta}} \frac{\partial}{\partial r} \right\rangle. \end{aligned} \quad (15)$$

This term, which did not appear in the cylindrical geometry (being the case in the limit of $R \rightarrow \infty$), takes essential roles in 3-D torus geometry.

In order to know the distance/closeness of the ITG mode from/to the Hasegawa- Mima and Hasegawa-Wakatani equations, It is instructive to trially ignore the terms with proportionality factor ε_n ; then we find a simplified equation

$$\left\{ \rho_i^2 \frac{\partial^2}{\partial x^2} - \left(\frac{\Omega - 1}{\pi \Omega + (1 + \eta_i)} + b \right) \right\} \phi = 0 \quad (16)$$

Equation (11) were successfully used in many theoretical researches on passing particles drift waves, where, as named, passing particles play a dominant role.

Simply put, it is known that 1) the magnetic shear has stabilizing effect, the non uniformity of the magnetic field induces mode coupling which is destabilizing. We distinguish this Linear Mode Coupling from Nonlinear Mode coupling, which we will study in the following chapters. It is noted, however, they have the same structure in physics, rooted on inappropriateness of Fourier analyses in nonuniform plasmas: In Linear Mode Coupling, the non-uniformity is due to that of equilibrium parameter (toroidicity) which is static, while in Nonlinear mode coupling the non-uniformity is due to drift wave itself which is time dependent. Note also that the radial variation of plasma parameters (such as electron/ion density and temperatures, space potential, and rotational transform) is another source of non-uniformity; However, they have different appearances, for they are not periodic in the direction of minor radius.

The notion of "magnetic well/hill" is the other important viewing point of toroidal effects. "Magnetic well/hill" refers to $1/B$ averaged over poloidal angle. This mean value is assumed to be zero in Eq.(11), as it is the case in simple tokamaks. However, Eq.(11) allows a wave field $\phi(\theta, x)$ localized in the larger major radius side of a tokamak. Bad curvature effect is thereby amplified and

this "ballooning effect" tends to destabilize the plasma.

We skip explanations of ETG (Electron Temperature Gradient Mode), which is regarded as another kind of important passing particle instability. Electron temperature mode is subject to an equation of the same structure reversing the role of electrons and ions. Therefore, it is easy to deduce theoretical predictions in analogy to ITG mode.

I-4) Trapped Particle Instability.

Trapped electron mode is one of the important mode, for it is easily destabilized and can account for the anomalous energy and particle transport [3-7].

$$1 + \tau - (\tau + \frac{\omega_e^*}{\omega})\Gamma_0 - \eta_i \frac{\omega_e^*}{\omega} b(\Gamma_1 - \Gamma_0) - (2\varepsilon)^{1/2} < \frac{\omega - \omega_e^*[1 + \eta_e(E/T_e - 3/2)]}{\omega - \omega_{D,e}(E/T_e) + i\nu_{eff}(E/T_e)^{-1.5}} > = 0 \quad (17)$$

where

$$\eta_e = \frac{d \ln(T_e)}{d \ln(n)}, \quad \nu_{eff}(E/T_e) = v_e / \varepsilon, \quad \varepsilon = r/R \quad (18)$$

$$\omega_{D,e} = \varepsilon_n \omega_e^*, \quad \Gamma_0 = e^{-b} I_0(b), \quad \Gamma_1 = e^{-b} I_1(b)$$

The first 4 terms are attributed to passing ions. The last term is attributed to trapped electrons, the proportionality factor $(2\varepsilon)^{1/2}$ being population of trapped electrons. It is noted that trapped electrons undergoes precessional motion and they experience bad curvature in the larger major radius board.

Though a linear theory is a handy simplified tool to study drift wave turbulence, it sometimes gives important information on transport: For instance, the stability threshold of ITG can determine the experimental gradient of ion temperature. As it is combined with quasi-linear theory, it predicts positive energy transport (out flux) and negative particle transport (in flux).

It is predicted that the instability which rely on adiabatic response would not give useful account for anomalous electron heat- and particle-transports. Thus ETG and TEM are considered to be important player in determining electron transports.

It is noted that in present day large tokamaks the density profiles are very flat. Theories have to give a consistent explanation of realized profiles of electron and ion temperature as well as density profile.

In moving to H-M and H-W equations in next section, it is noted that in the ion terms of Eq.(17) are the same as those of Eq. (11); in the limit of $\varepsilon \rightarrow 0$ we obtain

$$\frac{(\Omega - 1)}{\Omega \tau + (\eta_i + 1)} + b = 0 \quad (19)$$

which is a reproduction of Eq.(16). When $\eta_i = 0$, Eq. (19) gives even simpler form

$$\omega = \frac{\omega_e^*}{1 + b\tau} = \frac{\omega_e^*}{1 + k_\perp^2 \rho_s^2} \quad . \quad (18)$$

We take this as another standard form of dispersion relation, constituting the base of the Hasegawa-Mima and Hasegawa-Wakatani Equations. Though H-M and H-W are simplifications, the way of handling nonlinearity in these equations may be valid to trapped electron modes.

References to Section-I

- [1] J.Wesson, "tokamaks", Oxford Science Publication, 1996; second edition
- [2] R.J. Hastie, K.W.Hesketh, J.B.Taylor, Nuclear Fusion, 9(1979)1223,
"Shear Damping of two dimensional drift waves in a large-aspect-ratio tokamak"
- [3] W.M.Tang, P.H.Rutherford, H.P.Furth, and J.C.Adam
Physical Review letters
8(1975)660
- [4] W.M.Tang, Nuclear Fusion, 188 (1978)1089
"Microinstability theory in tokamaks"
- [5] A.Fujisawa, A.Ouroua, J.W.Heard, T.P.Crowley, P.M.Schoch, K.A.Connor, R.L. Hickok,
Nuclear Fusion, 36(1996)375, "Ballooning characteristics in density fluctuations observed with the
2Mev Heavy ion beam probe on the Text-U tokamak"
- [6] Tilman Dannert and Frank Jenko, Physics of Plasmas, 12(2005)072309
"Gyro-kinetic simulation of collisionless trapped- electron mode turbulence"
- [7] F.Jenko, T.Dannert, C. Angioni, Plasma Phys. Control. Fusion, 47(2005) B195-B206
"Heat and particle transport in a tokamak: advances in nonlinear gyrokinetics"

Section-II Hasegawa-Mima and Hasegawa-Wakatani equations

II-1 Equations:

The Hasegawa-Mima equation

The following equation is referred to as Hasegawa-Mima equation [1]; adiabatic

response is assumed for electron motion with the electrostatic wave form $\vec{E} = -\vec{\nabla}\phi$.

$$\phi = \sum_{\vec{k}} \phi_{\vec{k}}(t) e^{i\vec{k} \cdot \vec{x} - i\omega t}.$$

$$(1 - \rho_s^2 \nabla_{\perp}^2) \frac{\partial \phi}{\partial t} + v_d \frac{\partial \phi}{\partial y} - \frac{c}{B} [\phi, \nabla^2 \phi] = 0 \quad (1)$$

where

$$v_{d,y} = -\frac{cT_e}{eB} \frac{1}{n_0} \frac{dn_0}{dx} \quad (2)$$

It is found that the first two terms in Eq.(1) gives the standard drift wave frequency

$$\omega = \omega_* = \frac{k_y v_d}{(1 + \rho_s^2 k_{\perp}^2)} \quad (3)$$

with a finite Larmor radius modification over Eq.(I-10). The third term is the nonlinear coupling term expressed in terms of the bracket [] defined by $[\phi_1, \phi_2] = \hat{z} \cdot (\nabla \phi_1 \times \nabla \phi_2)$.

The nonlinear term thus reads

$$[\phi, \nabla^2 \phi] = \hat{z} \cdot (\vec{\nabla} \phi \times \vec{\nabla} (\nabla^2 \phi)) \quad (4)$$

and is referred to as "polarization nonlinearity" distinguished from $\vec{E} \times \vec{B}$ nonlinearity.

Eq.(1) takes the following form in Fourier space:

$$\frac{\partial \phi(k, t)}{\partial t} = \Lambda_l \phi(k, t) + \frac{1}{2} \sum_{\vec{k} = \vec{k}_1 + \vec{k}_2} \Lambda_{k_1, k_2}^k \phi(k_1, t) \phi(k_2, t) \quad (5)$$

, where the nonlinear term appears as:

$$\Lambda_{k_1, k_2}^k = \sum_{\vec{k} = \vec{k}_1 + \vec{k}_2} \hat{z} \cdot (\vec{k}_1 \times \vec{k}_2) (k_2^2 - k_1^2) \phi_{k_1} \phi_{k_2} \quad (6)$$

The Hasegawa-Wakatani equation

Hasegawa-Wakatani equation is a two field equation including variables ϕ and n and takes the following form:

$$(\frac{\partial}{\partial t} - \vec{\nabla} \phi \times \hat{z} \cdot \vec{\nabla}) \nabla^2 \phi = \bar{C}_1 (\phi - n) + C_2 \nabla^4 \phi + C_3 \phi \quad (7)$$

$$(\frac{\partial}{\partial t} - \vec{\nabla} \phi \times \hat{z} \cdot \vec{\nabla}) (n + \ln n_0) = \bar{C}_1 (\phi - n) \quad (8)$$

Here, the normalizations adopted are $e\phi/T_e \equiv \phi$ $n/n_0 \equiv n$ $\omega_{ci}t \equiv t$ and $x/\rho \equiv x$.

This equation has three dissipation terms $\bar{C}_1 = \frac{T_e}{e^2 n_0 \eta \omega_{ci}} \frac{\partial^2}{\partial z^2}$, $\bar{C}_2 = \frac{\mu}{\rho_s^2 \omega_{ci}}$, and

$\bar{C}_3 = \frac{\omega_* T_i}{\omega_{ci} T_e} (\omega_* \approx \frac{\nu_{ti}}{qR})$, which respectively represent resistive destabilizing term, viscosity

stabilizing term, and ion Landau damping term. Since the adiabatic approximation $n_e = e\phi / T_e$ is not used, H-W equation covers a broader physics in drift wave than H-M equation does.

The adiabatic approximation $n = e\phi / T_e$, corresponds to an approximation $\phi - n = 0$ in this set of equations. Indeed the linked Eqs.(7) and (8) are then decoupled and reduces to Eq. (1) except for the presence of two dissipation terms.

In Fourier space, H-W equation is expressed by the following form

$$\frac{\partial}{\partial t} (k^2 \phi_k) + \frac{1}{2} \sum_{\vec{k}=\vec{k}_1+\vec{k}_2} \Lambda_{k_1, k_2}^k \phi(k_1, t) \phi(k_2, t) = -\bar{C}_1(\phi - n) - C_2 \nabla^4 \phi - C_3 \phi \quad (9)$$

$$\frac{\partial}{\partial t} n_k + i\omega_e^* \phi_k + \sum_{k=k_1+k_2} (\vec{k}_1 \times \hat{z}) \cdot k_2 \phi_{k_1} n_{k_2} = \bar{C}_1(\phi - n) \quad (10)$$

II-2 Conserved quantities in H-M and H-W equations

Conserved quantities in H-M equations

The H-M Equation is a loss-less system and it is known that, total energy W and enstrophy U are conserved. It may be easy to show that these quantities are conserved by using the partial integration. It is noted that "conservation" means that the nonlinearity has such conservation properties.

Energy conservation is stated in real space representation as follows:

$$\frac{1}{2} \frac{\partial}{\partial t} \int \frac{1}{2} [\phi^2 + (\nabla \phi)^2] dV \equiv \frac{\partial W}{\partial t} = - \int \vec{J}_1 \cdot d\vec{S} \quad (11)$$

Here,

$$W = \int \frac{1}{2} [\phi^2 + (\nabla \phi)^2] dV \quad (12)$$

is the sum of kinetic energy and potential energy and

$$\vec{J}_1 = -\phi \frac{\partial}{\partial t} \nabla \phi + \phi \nabla^2 \vec{\nabla} \phi \times \hat{z} \quad (13)$$

is the energy flux density vector in real space.

Enstrophy conservation is stated in real space representation as follows:

$$\frac{1}{2} \frac{\partial}{\partial t} \int \frac{1}{2} [(\nabla \phi)^2 + (\nabla^2 \phi)^2] dV \equiv \frac{\partial U}{\partial t} = - \int \vec{J}_2 \cdot d\vec{S} \quad . \quad (14)$$

Here,

$$U = \int \frac{1}{2} [(\nabla \phi)^2 + (\nabla^2 \phi)^2] dV \quad (15)$$

is the sum of kinetic energy and squared vorticity and

$$\vec{J}_2 = -\nabla \phi \frac{\partial}{\partial t} \phi - \frac{1}{2} \phi (\nabla^2 \phi)^2 \vec{\nabla} \phi \times \hat{z} \quad . \quad (16)$$

is the enstrophy flux density vector in real space.

Conserved quantities in Fourier space

Such conservation properties are expressed in Fourier space as follows:

Energy conservation is translated as

$$\frac{d}{dt} W = \frac{d}{dt} \sum_{k_x, k_y} W_k = 0 \quad (17)$$

with

$$W_k = \sum_{k_x, k_y} \frac{1}{2} (1 + k^2) |\phi_k|^2 \quad . \quad (18)$$

Enstrophy conservation is transformed as

$$\frac{d}{dt} U = \frac{d}{dt} \sum_{k_x, k_y} U_k = 0 \quad (19)$$

with

$$U_k = \frac{1}{2} (1 + k^2)^2 |\phi_k|^2 \quad . \quad (20)$$

In the Fourier space representation, $|\phi_k|^2$, W_k , and U_k are mutually related by

Eqs.(18)-(19) and therefore only one of these variables has to be known. In the following discussions, we will be working in Fourier space rather than working in real space.

II-3: Power spectrum- $|\phi_k|^2$, energy spectrum- W_k , and enstrophy spectrum, U_k of a fully relaxed state.

Fully relaxed state in H-M equations

Since the mother equation Eq. (5) is cast into Hamiltonian formulation, we can regard $\text{Re}[\phi_k]$ and $\text{Im}[\phi_k]$ as canonical quantities and setup micro-canonical distribution assuming equal partition over points in the phase space. The canonical distribution function is determined by the standard procedure of variational method:

The entropy function S is defined by

$$S = -k_B \int f(\text{Re}[\phi_k], \text{Im}[\phi_k]) \ln(f(\text{Re}[\phi_k], \text{Im}[\phi_k])) d\text{Re}[\phi_k] d\text{Im}[\phi_k] \quad (21)$$

The auxiliary conditions are $E = \text{const}$ and $U = \text{const}$, which are defined by

$$E = \int (1+k^2)(\text{Re}[\phi_k])^2 + (\text{Im}[\phi_k])^2 d\text{Re}[\phi_k] d\text{Im}[\phi_k] \quad (22)$$

and

$$U = \int (1+k^2)^2 (\text{Re}[\phi_k])^2 + (\text{Im}[\phi_k])^2 d\text{Re}[\phi_k] d\text{Im}[\phi_k] \quad . \quad (23)$$

The Gaussian distribution function

$$f = C \times \exp[-(\alpha(1+k^2) + \beta(1+k^2)^2)|\phi_k|^2] \quad (24)$$

is obtained as the solution to the Euler equation of $H = S + \alpha E + \beta U$. This procedure is similar to that deriving Taylor relaxed state by minimizing total energy under helicity conservation.

With the distribution function $f(\phi_k)$ thus obtained, $\langle |\phi_k|^2 \rangle$ is calculated in integration with a moment $[(\text{Re}[\phi_k])^2 + (\text{Im}[\phi_k])^2]$.

$$\langle |\phi_k|^2 \rangle = \int [(\text{Re}[\phi_k])^2 + (\text{Im}[\phi_k])^2] f d\text{Re}[\phi_k] d\text{Im}[\phi_k] = \frac{1}{(\alpha(1+k^2) + \beta(1+k^2)^2)} \quad (25)$$

Similarly, $\langle E_k \rangle$ is calculated with the moment $[(1+k^2)(\text{Re}[\phi_k])^2 + (\text{Im}[\phi_k])^2]$

$$\langle E_k \rangle = \int [(1+k^2)(\text{Re}[\phi_k])^2 + (\text{Im}[\phi_k])^2] f d\text{Re}[\phi_k] d\text{Im}[\phi_k] \quad . \quad (25)$$

$$= \frac{(1+k^2)}{(\alpha(1+k^2) + \beta(1+k^2)^2)} = \frac{1}{(\alpha + \beta(1+k^2))}$$

Similarly, by multiplying the moment $[(1+k^2)^2(\text{Re}[\phi_k])^2 + (\text{Im}[\phi_k])^2]$, we obtain

$$\begin{aligned}
\langle U_k \rangle &= \int [(1+k^2)^2 (\operatorname{Re}[\phi_k])^2 + (\operatorname{Im}[\phi_k])^2] f d \operatorname{Re}[\phi_k] d \operatorname{Im}[\phi_k] \\
&= \frac{(1+k^2)}{(\alpha + \beta(1+k^2))} \quad . \quad (26)
\end{aligned}$$

Under this relaxed state, $\langle |\phi_k|^2 \rangle, \langle E_k \rangle$, and $\langle U_k \rangle$ has the following asymptotic

dependences on k : $\langle |\phi_k|^2 \rangle \sim k^{-4}, \langle E_k \rangle \sim k^{-2}$, and $\langle U_k \rangle \sim k^0$. Therefore, it is an appearance of a general tendency that "energy condensates at low- k and enstrophy condensates at high- k ".

With the assumption of isotropic turbulence, Eq. (3) admits the following approximated equality:

$$\omega \approx \frac{k_y v_d}{1+k^2 \rho^2} \approx k_y v_d \propto k_y \approx k \quad . \quad (27)$$

Therefore this tendency is restated as follows: "energy condensates in low frequency and enstrophy condensates in high frequency".

Fully relaxed state in H-W system

It is shown that the H-W system has the following conserving quantities

$$E_\phi = \int (\vec{\nabla} \tilde{\phi})^2 dr^3 \quad (28) \quad E_n = \int (\tilde{n})^2 dr^3 \quad (29)$$

$$\Omega_\phi = \int (\vec{\nabla}^2 \tilde{\phi})^2 dr^3 \quad (30) \quad \Gamma = - \int (\tilde{n} \vec{\nabla}^2 \tilde{\phi}) dr^3 \quad (31)$$

The quantities are referred to as fluid kinetic energy (E_ϕ), fluid internal energy (E_n), fluid enstrophy (Ω_ϕ), and cross-correlation (Γ). Applying the variational method to H-W system gives the following spectra:

$$\langle n_k^2 \rangle = \frac{4(\beta + \gamma k^2)}{(4\alpha(\beta + \gamma k^2) - \eta^2 k^2} \quad (32)$$

$$\langle \phi_k^2 \rangle = \frac{4\alpha}{k^2(4\alpha(\beta + \gamma k^2) - \eta^2 k^2} \quad (33)$$

$$\langle n_k \phi_{-k} \rangle = - \frac{-2\eta}{k^2(4\alpha(\beta + \gamma k^2) - \eta^2 k^2} \quad (34)$$

Thus the spectrum of the fully relaxed state expected from H-W system is separated in more number of regimes.

Since H-W and H-M equations are not very different in nonlinear coupling, dominated by the polarization nonlinearity, we continue discussion with the latter type of equation.

References for Section-II

- [1] A.Hasegawa and K.Mima, Phys. Fluids, 21(1978)87,
"Psudo-three-dimensional turbulence in magnetized non-uniform plasma"
- [2] A.Hasegawa and M.Wakatani, PRL, 59(1987)1581,
"Self -Organization of Electrostatic Turbulence in a Cylindrical Plasma"
- [3] Masahiro Wakatani and Akira Hasegawa, Phys. Fluids, 27(1984)611
"A collisional drift wave description of edge turbulence"
- [4] F.Y.Gang, B.D.Scott, P.H.Diamond, Phys. Fluids B, 1 (6) 1989,
"Statistical mechanics of a two-field model of drift wave turbulence"

Section-III Power spectrum observed in experiments

Potential fluctuation in H-1 result

Let us compare the theoretical prediction of the power spectrum for the relaxed state with available experimental data and simulation results.

Shown in Fig.3 is the power spectrum realized in experiments on the H-1 stellarator device [1]

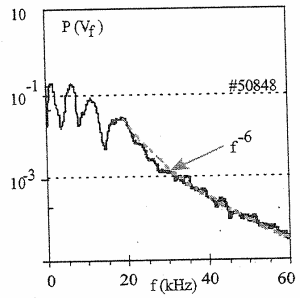


FIG. 4. Power spectrum of the floating potential fluctuations.

Fig.3

In this figure, $P(V_f) = \langle V_f^* V_f \rangle$ is plotted versus frequency, where V_f is the floating potential obtained with a probe, which represents potential ϕ . Therefore, the result in Fig.3 is translated as

$P_k = \langle \phi_k^* \phi_k \rangle \propto f^{-6}$. Considering that $2\pi f = \omega = k_y v_d / (1 + k^2) \propto k_y$ this result is translated to be

k -spectrum: $P_k = \langle \phi_k^* \phi_k \rangle \propto k^{-6}$. The obtained k dependence is thus steeper than the one expected theoretically for fully relaxed state $P_k \propto k^{-4}$.

Knowing that $W(k_x, k_y) = (1 + k^2) \langle \phi_k^* \phi_k \rangle$, this result corresponds to $W(k_x, k_y) \propto k^{-4}$.

Vortexes in Fluid (A table top experiment)

Another interesting result was obtained by the same group using a table-top experimental device as shown in Fig.4 (a). Vortexes are excited in the fluid in a vat by means of combined effect of magnetic field (multi-pole magnets are installed on the bottom) and electric current flowing in the electrolyte fluid. Figure 4(b) shows the time sequence showing how the vortex size is shifted towards larger scale; this tendency agrees with the previous statement that "energy condensates at low- k ".

Figure 4(c) suggests that $E_k \propto k^{-3.5}$ in early phase and $E_k \propto k^{-3.3}$ after the relaxation proceeded further. Here u_k is the velocity of the fluid measured by means of a camera. $E_k = k u_k^2 / 2$ is the kinetic energy of the fluid; later we learn that this corresponds to $kW(k_x, k_y)$ in drift wave turbulence. This result is therefore aligned to the previous experimental data that disagreed with the theoretical prediction given for a relaxed state.

According to the Kraichnan, Navier Stokes equation describing 2-D fluid vortex has the same structure as that of H-M equation specifically in nonlinear energy transfer. It is known that $E_k = k u_k^2 / 2$ and squared vorticity $U_k = k^2 E_k$ is conserved; the latter corresponds to conservation of enstrophy in drift wave theory.

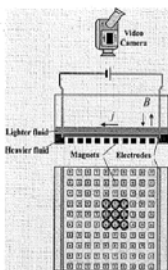


FIG. 1. (Color online) Experimental setup for studying evolution of the energy turbulence. A matrix of 10×10 magnetic dipoles (permanent magnets $4 \times 5 \times 10$ mm 3 , $B=0.33$ T on the surface of the magnet) is placed under the cell. As electric current flowing between the electrodes ($0.1-4$ A) interacts with the spatially varying magnetic field to generate $(J \times B)$ -driven vortices (diameter ~ 12 mm) above each of the magnetic dipoles.

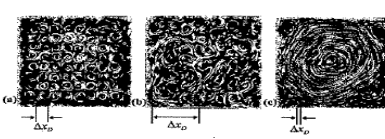


FIG. 2. Evolution of turbulence in a thin layer of electrolyte in a cell during spectral condensation. Trajectories of the tracer particles averaged over 12 frames of recorded video are shown. (a) The initial (linear) stage, $t=3$ s. (b) The inverse cascade stage, $t=25$ s. (c) The condensate stage, $t=60$ s. Δx_D represents the spatial scale of the trace particle transport during three stages of the flow evolution.

Fig.4(a)

Fig.4(b)

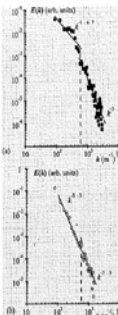


FIG. 4. (Color online) Energy spectra of the fluid velocities (a) during the inverse cascade stage of the flow development and (b) after the condensate has formed. The injection scale k_i is shown by the vertical dashed line.

Fig.4(c)

Power spectrum realized in simulations

A) Hasegawa (1979) paper (Ref.[3])

H-M and H-W are simplified systems of equations and they were solved numerically. Let us review the results of such simulations found in several papers.

The power spectrum reported in Ref. [3] (Hasegawa, et al., 1979) is shown in Fig.5.

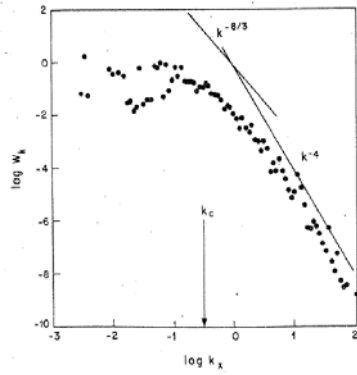


FIG. 3. W_x vs k_x for $k_z=0.28$, Indicating a higher level of turbulence than in Figs. 1 and 2. The hydrodynamic turbulence region is extended to a smaller value of k .

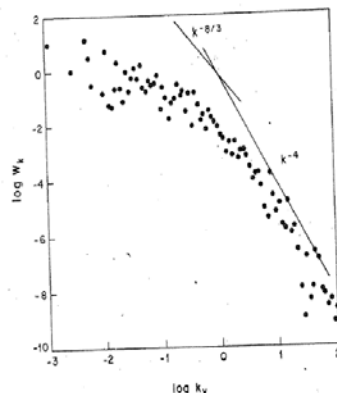


FIG. 4. W_x vs k_y for $k_z=0.28$.

Fig.5

Though it was assumed (in deriving fully relaxed state) that turbulence is isotropic, this assumption is unnecessary in simulations. This paper gives a power spectrum $W(k_x, k_y)$ in terms of separate k_x and k_y dependences: It is recognized that

$$W_k = W(k_x, k_y) \propto k_x^{-4} \propto k_y^{-4} \quad (1)$$

in the high- k range and

$$W_k = W(k_x, k_y) \propto k_x^{-8/3} \propto k_y^{-8/3} \quad (2)$$

in the low- k range.

B) Simulation results by D. Fyfe et al., (Ref. [4])

The power spectrum reported in Ref. [4] (D. Fyfe, et al., 1979) is shown in Fig.6.

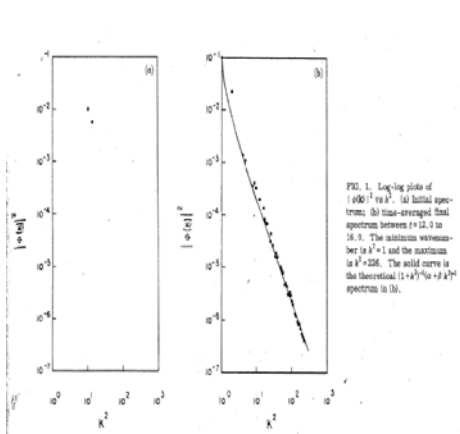


FIG. 1. Log-log plots of $|\phi_k|^2$ versus k^2 . (a) Initial spectrum; (b) time-averaged final spectrum between $t=12.0$ to 16.0 . The minimum wavenumber is $k^2=1$ and the maximum is $k^2=226$. The solid curve is the theoretical $(1+k^2)^{-6}$ spectrum in (b).

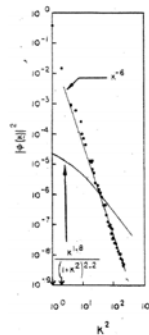


FIG. 2. A forced, dissipative spectrum resulting from $k_x^2 = 1, 2$ only. The least-squares straight line fit gives $|\phi_k|^2 \propto k^{-6.4}$. Here, as in the other plots, $|\phi_k|^2$ is averaged over all wavenumbers in the same k^2 bin. Only every point is plotted for $0 < k^2 < 30$, only every other point is plotted for $30 < k^2 < 196$, and every fourth point for $196 < k^2 < 226$. The points are time-averaged over 1024 time steps between $t=48$ and $t=56$. $\nu=10^6$.

Fig.6

In Fig.6, $|\phi_k|^2$ is plotted versus k revealing $|\phi_k|^2 \propto k^{-6}$. This result has the same dependence as Eq. (1), for

$$W(k_x, k_y) = (1 + k^2) \langle \phi_k^* \phi_k \rangle.$$

To summarize, the power spectrum obtained in experiments and simulations are clearly different from that obtained theoretically for fully relaxed state.

This disagreement is attributed to that what undergoing in experiments and simulations are not the complete relaxations but driven-damp processes. Indeed, in experimental situations, drift wave is excited in the k -range where growth rate is positive and absorbed in the k -range where it is negative. In simulations, instead, certain source and sink of drift waves have to be assigned for the problems to be solvable. From this point of view, H-W equation is a little more realistic than H-M system, for it anyway has assumed terms of sources and sinks. They are not much different however in learning properties of nonlinear interaction, specifically in studying so-called inertial range.

C) Simulation results by Horton et al (Ref.[5])

In obtaining these results, it was assumed that turbulences were isotropic. However, considering that

$$\omega = k_y v_d / (1 + k_x^2 + k_y^2),$$

it is also possible to seek for similarity ranges without assuming isotropic . The paper by Horton (Ref.[5], 1994) derived the following non isotropic dependences as an extension of Kraichnan's method (see Ref.[1] in section-IV).

$$W(k_x, k_y) = \begin{cases} W_0 \left(\frac{k_0}{k_x}\right)^2 \left(\frac{k_0}{k_y}\right)^{3/2} & k_x \rho_s \gg 1 \\ W_0 \left(\frac{k_0}{k_x}\right)^3 \left(\frac{k_0}{k_y}\right)^{3/2} & k \rho_s \ll 1 \end{cases} \quad (3)$$

A simulation was performed in the same paper giving the results in Fig.7, where the kinetic energy

$W(k_x, k_y) = (1 + k^2) \langle \phi_k^* \phi_k \rangle$ is plotted versus k_x and k_y .

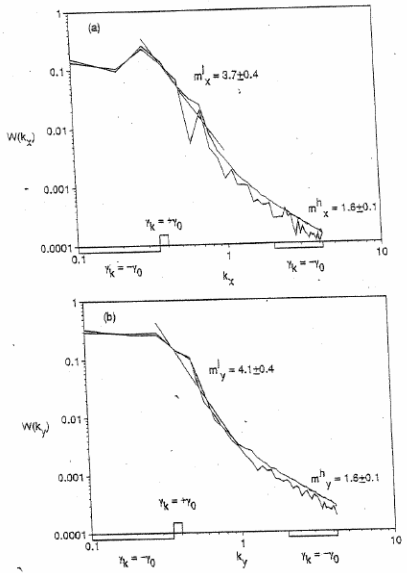


Fig.7

This result suggests some deviation of $W(k_x, k_y) = (1 + k^2) \langle \phi_k^* \phi_k \rangle$ from $W(k_x, k_y) \propto k^{-4}$ law at extremely large k -range where the approximation $\omega = k_y v_d / (1 + k^2) \propto k_y$ does not hold.

References for section-III

- [1] M.G.Shats, H.Xia, and H.Punzman, Physical Review Letters, 71(2005)046409
"Spectral condensation of turbulence in plasmas and fluids and its role in low-to high phase transition"
- [2] H.Xia, M.G.Shats, Physics of Plasma, 11(2004)561
"Spectral energy transfer and generation of turbulence structures in toroidal plasmas"
- [3] Akira Hasegawa, Carol G. MacLennan, Yuji Kodama, Physics Fluids 22(1979)2122
"Nonlinear behavior and turbulence spectra of drift waves and Rossby wave"

- [4] David Fyfe, David Montgomery, Phys. Fluids 22(1979)246
 "Possible inverse cascade behavior for drift wave"
 [5] Wendell Horton and Akira Hasegawa, Chaos vol. 14, No.2, 1994,
 "Quasi-two dimensional dynamics of plasmas and fluids"

Section-IV Energy transfer in k-space

We studied in the previous section that so-called fully relaxed state is not likely to be realized and underlying physics are driven damp processes. In this section, we study the nonlinear processes from this point of view. As we have learned in section-III, the Navier Stokes equation as applied to 2-D fluid vortexes has the same structure as H-M equation which governs drift wave turbulence. Therefore, the mathematical methods developed in studying the former can be applied to the latter. We first introduce the consideration presented in the old paper, Ref. [1] by R.H. Kraichnan, 1967.

Fluid motion is subject to Navier Stokes equation

$$\frac{\partial \vec{v}}{\partial t} + \vec{v} \cdot \vec{\nabla} \vec{v} = -\nabla p + \nu \nabla^2 \vec{v} . \quad (1)$$

In this paper, the energy transfer equation of 2-D turbulence is introduced in the following form:

$$\left(\frac{\partial}{\partial t} + 2\nu k^2 \right) E(k) = T(k) \quad (2)$$

, where

$$E(k) = \pi k W(k_x, k_y), \quad W(k_x, k_y) = \left(\frac{D}{2\pi} \right)^2 \langle |u(k)|^2 \rangle \quad (3)$$

and

$$T(k) = \frac{1}{2} \int_0^\infty \int_0^\infty T(k, p, q) dp dq$$

$$T(k, p, q) = T(k, q, p) T(k, p, q) = 2\pi k \operatorname{Im}(2\pi / |\sin(p, q)|) \left(\frac{D}{2\pi} \right)^4 \quad (4)$$

$$\cdot (k_m \delta_{i,j} + k_j \delta_{i,m}) \langle u_i(k) u_j(p) u_m(q) \rangle$$

The summation is made for triads satisfying

$$\vec{k} = \vec{p} + \vec{q}, \quad k = |\vec{k}|, \quad p = |\vec{p}|, \quad q = |\vec{q}| . \quad (5)$$

Kraichnan found the following conservation equation holds indicating conservation of fluid kinetic energy

$$T(k, p, q) + T(p, q, k) + T(q, p, k) = \text{const} \quad (6)$$

also the following equality holds indicating conservation of squared vorticity

$$k^2 T(k, p, q) + p^2 T(p, q, k) + q^2 T(q, p, k) = \text{const} \quad (7)$$

He also defined energy transfer function $\Pi(k)$ and enstrophy transfer function $Z(k)$ in order to study the properties of nonlinear energy transfer.

$$\Pi(k) = \frac{1}{2} \int_k^\infty dk' \int_0^k \int_0^k T(k', p, q) dp dq - \frac{1}{2} \int_0^k dk' \int_k^\infty \int_k^\infty T(k', p, q) dp dq \quad (8)$$

$$Z(k) = \frac{1}{2} \int_k^\infty k'^2 dk' \int_0^k \int_0^k T(k', p, q) dp dq - \frac{1}{2} \int_0^k k'^2 dk' \int_k^\infty \int_k^\infty T(k', p, q) dp dq \quad (9)$$

These quantities have the properties shown in Table-I for similarity ranges defined by n in the following equation.

$$\frac{E(ak)}{E(k)} = a^{-n} \quad (10)$$

$n=5/3$ similarity range $n=3$ similarity range

$\Pi(k)$	$\Pi(k) < 0$	$\Pi(k) = 0$
$Z(k)$	$Z(k) = 0$	$Z(k) > 0$
$E(k)$	$\propto k^{-5/3}$	$\propto k^{-3}$

Table-I

In $n=5/3$ similarity range, energy down cascades with k -independent flow rate and enstrophy flow vanishes. In $n=3$ similarity range, enstrophy normally cascades with k -independent flow rate and energy flow vanishes.

For $E(k) = \pi k W(k_x, k_y)$, $n=3$ regime here is translated as $W(k_x, k_y) \propto k^{-4}$ and $|\phi(k)|^2 \propto k^{-6}$

regime. Thus experimental observations and simulation results that we saw in the previous section were given appropriate accounts.

Looking back at the simulation result in Fig.5, the data deviate from $W(k_x, k_y) \propto k^{-4}$ in the low- k regime suggesting the presence of $n=5/3$ similarity range.

Direction of energy transfer

So far, we applied Fourier analyses in configuration space but did not for time. For a weak turbulence, Fourier analyses can be applied both to configuration space and time; the quantities are then expressed in the following form with frequency as functions of wave number [2].

$$\phi(r, t) = \sum_k \phi_k e^{-i\omega_k t + i\vec{k} \cdot \vec{r}}$$

Then the freedom of nonlinear interaction is reduced by the additionally imposed frequency

matching condition $\omega_{\vec{k}} = \omega_{\vec{p}} + \omega_{\vec{q}}$ added to $\vec{k} = \vec{p} + \vec{q}$:

Frequency matching condition is expressed by the following equation.

$$\frac{p_y v_d}{1 + p_x^2 + p_y^2} + \frac{(k_y - p_y)v_d}{1 + (k_x - p_x)^2 + (k_y - p_y)^2} - \frac{k_y v_d}{1 + (k_x)^2 + (k_y)^2} = 0 \quad (11)$$

With given value of wave number, k , the nonlinear interaction occurs along the line in the $p_x - p_y$ plane as shown in Fig.8(a).

If $|\vec{p}| \ll |\vec{k}|$, Eq.(11) is transformed as

$$\vec{p} \cdot \vec{\nabla}_{\vec{k}} [k_y v_d - \omega_{\vec{k}}] = 0 \quad (12)$$

suggesting that nonlinear interaction should occur along constant $[k_y v_d - \omega_{\vec{k}}]$. Shown in Fig.8(b) is the contour plot of $[k_y v_d - \omega_{\vec{k}}]$, where we find the waves born with large k_y have to decrease in k_y and increase in k_x . It is shown, through such considerations, that isotropization and inverse energy cascade is the general feature of H-M system.

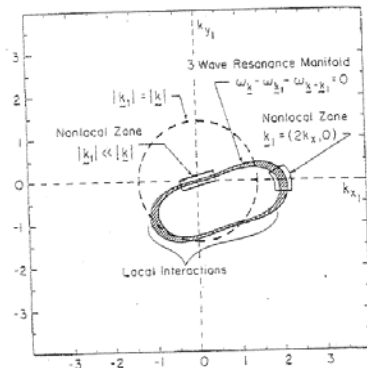


Fig.8(a)

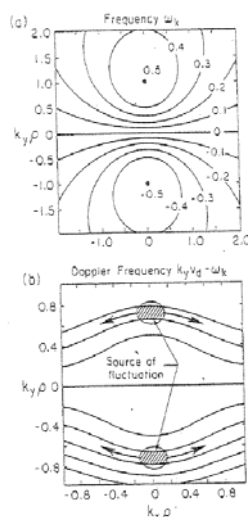


Fig.8(b)

Kolmogorov Law:

It is good to recall the knowledge related to Navier Stokes turbulence in fluid dynamics.

$$\rho \frac{\partial \vec{v}}{\partial t} + \rho \vec{v} \cdot \vec{\nabla} \vec{v} = \mu \nabla^2 \vec{v} . \quad (13)$$

The ratio of the second term on LHS to the viscosity term on the RHS is called Reynolds number.

$$R = O(\vec{v} \cdot \vec{\nabla} \vec{v} / (\mu / \rho) \nabla^2 \vec{v}) = [\rho l v / \nu] \quad (14)$$

It is known that turbulent flow occurs as Reynolds number is large. Indeed, in two dimensional flow of drift wave, this term is identified as nonlinear term and sometimes referred to as Reynolds stress. In hydrodynamic turbulences, the viscosity term is neglected for long scaled vortexes exceeding some typical value l_0 . Thus, there occurs only the flow of energy in k -space. Let the local (uniform in real space) energy dissipation as

$$\varepsilon = [(\mu) v^2] \quad (15)$$

Then, the a dimensional analysis gives

$$[(k \rho I_k) \sqrt{I_k k^3}] = \varepsilon; \quad I_k dk \Leftrightarrow k u_k^2 dk . \quad (16)$$

i.e., the well known Kolmogorov law is obtained.

$$I_k = k u_k^2 = (\varepsilon / \rho)^{2/3} k^{-5/3} . \quad (17)$$

This dimensional analysis suggests that the wave energy flows in k -space. Similar analysis in 3-D hydrodynamic turbulence (replacing Eq.(16)by $I_k dk \Leftrightarrow k^2 u_k^2 dk$) gives the same equation as Eq.(16) which predicts the same power dependence.

$$[(k \rho I_k) \sqrt{I_k k^3}] = \varepsilon; \quad I_k dk \Leftrightarrow k^2 u_k^2 dk$$

Returning to 2D problem, we consider an enstrophy sink ε_ω which is in the dimension of local dissipation rate of squared vorticity, $[L^3 (m L^2 T^{-2}) L^{-2} T^{-1}]$. Then a similar analysis gives

$$k^2 (k \rho I_k) \sqrt{I_k k^3} = \varepsilon_\omega \quad (18)$$

i.e., the other inertial range is obtained.

$$I_k = (\varepsilon_\omega / \rho)^{2/3} k^{-3} \quad (19)$$

These considerations are summarized in Fig.9, showing the presence of two regimes:

The $n = 5/3$ regime appears in the low- k range showing the dependence

$I_k = (\varepsilon / \rho)^{2/3} k^{-5/3}$. The $n = 3$ regime appears in the high- k range showing the

dependence $I_k = (\varepsilon_\omega / \rho)^{2/3} k^{-3}$. The transitional point denoted by k_c in the figure is

determined formally by the ratio of $\varepsilon_\omega / \varepsilon$. In the actual situation however such point will be determined by the spectrum of the energy source.

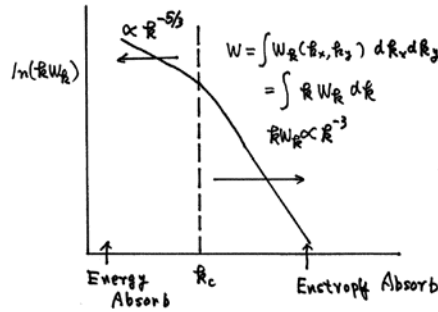


Fig. (9)

For more details, readers are guided to Refs.[3-5].

References for Section-IV

- [1] Robert H., Kraichnan, Physics Fluids, 10(1967)1417
"Inertial Ranges in two-dimensional turbulence"
- [2] Wendel Horton, Akira Hasegawa, Chaos 4(1994)227,
"Quasi-two-dimensional dynamics of plasmas and fluids"
- [3] B.B. Kadomtsev, Plasma Turbulence, Academic Press, 1965
- [4] A.N. Kolmogorov, Dokl. Acad. Nauk SSSR, 30(1941)301-305
- [5] A.N. Kolmogorov, J. Fluid Mech., 13(1962)82

Section-V. Linear Response Function for zonal flows

I am very happy in writing this section, with that the many contributions[1-4] have been done by Chinese researchers under the collaboration under CUP. In Japan also there are many contributions in this research field, though I can list only limited number of them [5-8] due to space.

A. mechanism of Geodesic acoustic mode

The zonal flow is interpreted as plasma flow with zero- or low- toroidal and poloidal mode numbers with large radial mode number. Since plasma rotation is related to the radial electric field by $\vec{V} = \vec{E} \times \vec{B} / B^2$, the zonal flow is also viewed as radial electric field with large radial mode number. It is known that there are two branches of zonal flow: the Stationary Zonal Flow and the oscillating Geodesic Acoustic Mode.

Rotation of the plasma creates radial current with the presence of the geodesic curvature of the magnetic lines of force. The $\vec{j} \times \vec{B}$ force due to this current gives the plasma rotation restoring force and therefore the plasma rotation becomes oscillatory. This mode is referred to as geodesic acoustic mode (GAM).

The mechanism of plasma rotation and radial electric field is itself a very interesting research subject and has been investigated by many researchers as a part of neoclassical theory. Particularly, in tokamaks with toroidal symmetry only poloidal viscosity appears. This rather static plasma rotation is referred to stationary zonal flow and is believed to have very low damping rate.

Recent investigations gave experimental evidences of existing stationary zonal flow and GAM oscillations. These two modes are energized in torus plasmas with certain mechanisms of excitation. In recent investigations plasma turbulence caused by the micro-instabilities are called for as the mechanisms of excitation. The zonal flow is in turn supposed to regulate the turbulence and, therefore, it is gathering more and more attentions.

Figure 10 illustrates the mechanism of the GAM oscillation: Under the presence of the radial electric field \vec{E}_r , there exists plasma rotation ($\vec{v}_\theta = \vec{E}_r \times \vec{B} / B^2$). With the existence of the toroidal effect, there occurs the divergence of the flow inside the flux surface causing up-down asymmetry:

$$\tilde{n}_i = n_{i,0} \int dt \frac{2}{R_0} \sin \theta \frac{\tilde{E}_r}{B_0} \quad (1)$$

If the plasma motion is adiabatic, this density perturbation causes the up-down asymmetry of the ion pressure

$$\tilde{p} = \gamma \tilde{n}_i T_{i,0} \propto \sin \theta. \quad (2)$$

The poloidal pressure gradient causes $\vec{\nabla}p \times \vec{B}$ current across the flux surface,

$$\tilde{j}_r = \frac{1}{B} \frac{1}{r} \frac{\partial \tilde{p}}{\partial \theta} \square \gamma(n_{i,0} T_{i,0}) \frac{2}{BB_0 R_0} \cos \theta \int dt \tilde{E}_r, \quad (3)$$

which is integrated to give

$$\int j_r dS = \gamma(\tilde{n}_i T_{i,0}) n_{i,0} (2\pi)^2 \frac{2r}{B_0^2 R_0} \int dt E_r. \quad (4)$$

On the other hand, the time varying electric field is accompanied by so-called polarization current:

$$\tilde{j}_\perp \square \frac{\omega_{p,i}^2}{\omega_{c,i}^2} \frac{1}{4\pi} \frac{dE_r}{dt} \quad (5)$$

which is integrated over the flux surface to give

$$\int j_r dS \square \frac{\omega_{p,i}^2}{\omega_{c,i}^2} \frac{1}{4\pi} (2\pi)^2 R_0 r \frac{dE_r}{dt} . \quad (6)$$

By equating the two currents Eq.(4) and Eq.(6), we obtain an equation of motion including oscillatory motion:

$$\frac{d^2 E_r}{dt^2} + \omega_{G,A}^2 E_r = 0 \quad (7)$$

with

$$\omega_{G,A}^2 = \frac{2\gamma}{R_0^2} \frac{T_{i,0}}{m_i} \quad . \quad (8)$$

Thus the GAM oscillation is characterized by $\omega \approx \sqrt{2\gamma T_i / m_i} / R_0$. In the discussion above, response of the particles only to the uniform potential filed has been taken into consideration.

Inclusion of response to non-uniform potential filed yields additional term to the GAM frequency giving the general form:

$$\omega_{G,A}^2 = \frac{1}{R_0^2} \frac{\gamma_1 T_{i,0} + \gamma_2 T_{e,0}}{m_i} \quad (9)$$

where γ_1 and γ_2 are constants of order unity.

More detailed explanation of GAM including the excitation mechanism is found in Ref.[3] for Section-VI.

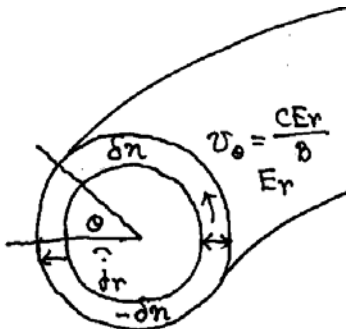


Fig. 10

B. Extension to the helical systems and the response function in the low frequency range

So far is the interpretation of the mechanism of GAM oscillation obtained by Winsor et al. . The kinetic extension including stellarator is presented in the following using the scheme developed by Watari et al [9-12]; the currents across the flux surface is balanced.

The polarization current j_{pol} and the current due to the geodesic curvature $j_{geo}(\psi)$ are expressed in the following forms using the conductivities σ_{pol} and σ_{geo} (more exactly admittances between two adjacent flux surfaces).

$$j_{geo}(\psi) = -\sigma_{geo}(\psi) \frac{d\phi}{d\psi} \quad (10)$$

$$j_{pol}(\psi) = -\sigma_{pol}(\psi) \frac{d\phi}{d\psi} \quad (11)$$

Here, $j_{pol} \propto \sigma_{pol}$ is the classical polarization current, which is known to be proportional to ω .

Using the generalized expressions (9) and (10), we obtain the expression of the dispersion relation of GAM oscillations valid to tokamaks and helical systems [12],

$$j_{total} = \tilde{\sigma}_{pol} \left(\frac{\omega}{i} - \tilde{\omega}_G^2 \sum_{m,n} \eta_{m,n}^2 F_{m,n} \right) \frac{\partial \phi}{\partial \psi} = 0 \quad (12)$$

Here, $\tilde{\sigma}_{pol}$ is the proportionality coefficient of the classical polarization current and $\tilde{\omega}_G^2 = \frac{T_i}{m_i R^2}$

represent typical tokamak GAM frequency. In obtaining Eq.(12), the magnetic field is Fourier decomposed in order to facilitate the calculation of geodesic curvature.

$$B^2 = B_0^2 (1 + \sum_{m,n} \delta_{m,n}(\psi) \cos(m\theta - n\zeta)) \quad (13)$$

Here, $\eta_{m,n}^2$ and l_ψ^2 are geometric factors, which characterizes the confining magnetic field:

$$\eta_{m,n}^2 \equiv \frac{(mB_\zeta + nB_\theta)^2 \delta_{m,n}^2(\psi)}{4B_t^2 l_\psi^2} \quad (14), \quad \text{and} \quad l_\psi^2 \equiv q^2 \int \frac{1}{B^2} |\nabla \psi|^2 d\theta d\zeta \quad (15).$$

Equation (14) contains $\delta_{m,n}$, which represents the geodesic curvature of (m,n) ripple component. It is easy to show that Eq.(12) reduces to the tokamak formula for $n=0$; $\delta_{m=1,n=0}$ then turns out to be $1/R_0$ as it appears in Eq.(1) and represents the geodesic curvature of a tokamak of circular cross section. Since the direction of the ion current depends on the sign and the amplitude of the geodesic curvature, it is predicted that the density perturbation in a helical system takes the maximum and minimum values along the lines of $(m\theta - n\zeta) = \pm\pi/2$, respectively. The magnetic lines of force short circuit these incremental and decremental charges and, therefore, GAM oscillation is expected to occur under limited conditions in helical devices.

The $F_{m,n}$ in Eq.(12) is expressed as follows:

$$F_{m,n} = F_U(\zeta_{m,n}) + F_{NU}(\zeta_{m,n}) = -2 \frac{1}{ik_{\square,m,n} v_T} (Z_{geo,1}(\zeta_{m,n}) - \chi_{m,n} \zeta_{m,n} Z_{geo,2}(\zeta_{m,n})) \quad (16)$$

where the argument $\zeta_{m,n} = \omega/k_{\square,m,n} v_T$ is calculated by using the wave number

$$k_{\square,m,n} = (mB^\theta - nB^\zeta) / B.$$

Here, $\chi_{m,n}$ represents the response to the induced nonuniform potential field which is proportional to $Z_{geo,2}(\zeta)$:

$$\chi_{m,n} = (k_{D,e}^2 / k_{D,i}^2) + (1 + \zeta_{m,n} Z_p(\zeta_{m,n}))^{-1} \cdot Z_2(\zeta_{m,n}) \quad (17)$$

The involved two dispersion functions $Z_{geo,1}(\zeta)$ and $Z_{geo,2}(\zeta)$ are defined as follows:

$$Z_{geo,1} = \frac{1}{\sqrt{\pi}} \int \frac{1}{x-\zeta} (x^4 + x^2 + \frac{1}{2}) \exp(-x^2) dx \quad (18)$$

$$Z_{geo,2} = \frac{1}{\sqrt{\pi}} \int \frac{1}{x-\zeta} (x^2 + \frac{1}{2}) \exp(-x^2) dx , \quad (19)$$

which differ from the well known plasma dispersion function

$$Z_p = \frac{1}{\sqrt{\pi}} \int \frac{1}{x-\zeta} \exp(-x^2) dx \quad (20)$$

by the weights in the integrand, $(x^4 + x^2 + \frac{1}{2})$ and $(x^2 + \frac{1}{2})$.

The way of determining the GAM frequency according to Eq.(12), which means balance of radial, is illustrated in Fig.11: The straight line represents classical polarization current and the curve represents geodesic (neoclassical) current. The frequency is determined as the frequency where they cross.

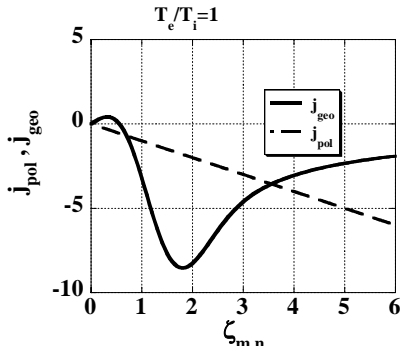


Fig.11

C. Unified Response function for stationary zonal flow and GAM.

Stationary zonal flow and GAM are the well known zonal flows. It is known that trapped particles take a dominant role in the former while passing particles take the dominant role in GAM dynamics. In Ref.[12], a scheme of integration along particle orbit is employed and a unified expression of the two mechanisms was given.

This scheme is briefly introduced with the idea of response function in order to bridge this section to the next.

The linear response function is the ratio of the induced charge of low-mode-number to the external charge $\rho_{ext}(\omega, k_r)$.

$$\phi_{l=0}(\omega, k_r) = \sum_{l'} R(\omega, k_r) \rho_{ext}(\omega, k_r) = \sum_{l'} \frac{1}{D(\omega, k_r)} \rho_{ext}(\omega, k_r) \quad (21)$$

Here, $R(\omega, k_r) \equiv 1/D(\omega, k_r)$ and therefore solving for $R(\omega, k_r)$ is identical to solving for $D(\omega, k_r)$. It is expected that the dispersion function $D(\omega, k_r)$ in the denominator approaches a constant value at the low frequency limit giving the so-called neoclassical shielding effect and that $D(\omega, k_r) = 0$ is satisfied at a certain frequency ω in the higher frequency range; the former corresponds to stationary zonal flow and the latter corresponds to GAM. Thus the present task is to reformulate $R(\omega, k_r)$ (or $D(\omega, k_r)$) with full inclusion of finite orbit effects. In most of the works in the past, parabolic dispersion functions were solved, which is 2nd order in radial wave number k_r .

$$D(\omega, k_r) \propto (a - b(\omega)) k_r^2 \quad (22)$$

Though Eq. (22), gives the local oscillation frequency of GAM, it is not appropriate for discussion of the radial structure of the GAM. Therefore, we will derive a quadratic dispersion function, adding to it the 4-th order term in k_r :

$$D(\omega, k_r) \propto (a - b(\omega)) k_r^2 + c(\omega) k_r^4 \quad (23)$$

Thanks to the inclusion of the Finite orbit effects and to the quadratic dispersion relation obtained, the GAM solution is now dependent on the radial wave number.

Fig.12 show a typical result:

In the figure, GAM is characterized by the cutoff and resonance pair and the presence of two bands of GAM. The frequency that had been referred to as "GAM frequency" is identified as the cut off frequency. Fig.12 suggests that the wave propagates radially, claiming reconsideration of the naïve paradigm that the GAM can regulate drift wave turbulence and improve transport.

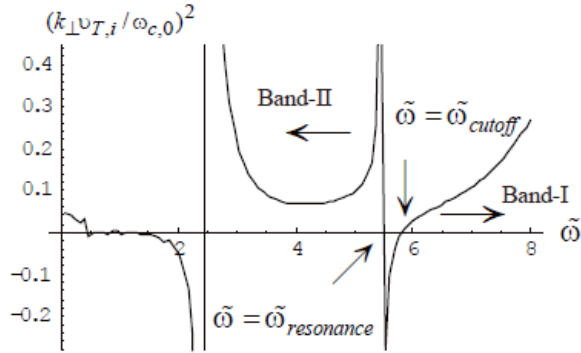


Fig.12

This approach is considered as generalization of the neoclassical polarization current. The appropriateness of this extension is confirmed by looking into the low frequency range shown in Fig.13 ; the numerical result is summarized as

$$\tilde{\rho}_{l=0,ind}^{0 \rightarrow 2} = \tilde{\rho}_{l=0,clas}^{0 \rightarrow 2} (1 + 1.6(q^2 / \sqrt{\epsilon})) \quad (24)$$

and the analytically it corresponds to the well known expression

$$\tilde{\rho}_{l=0}^{(n=2)} = -\frac{1}{2\pi\bar{g}} \oint \frac{dl}{B} \int d^3v \left[\left(\frac{\tilde{v}_\parallel(\theta)}{\tilde{\omega}_c(\theta)} \right)^2 - \left(\frac{\tilde{v}_\perp(\theta)}{\tilde{\omega}_c(\theta)} \right)^2 + \frac{1}{2} \left(\frac{\tilde{v}_\perp(\theta)}{\tilde{\omega}_c(\theta)} \right)^2 \right] \tilde{\phi}_{l=0} \quad (25)$$

which appears in Ref[3] of section-VI.

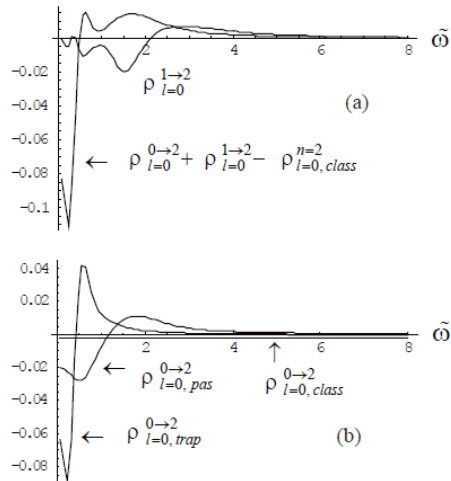


Fig.13

So far, we have shown the response function driven by the ambient turbulence. The external charge is assumed incoherent to the mode under consideration, and therefore, the driving force is regarded as noise. More interesting is the opposite case where functional derivative is non-zero, i.e.,

$$R(\omega, k) = R_0(\omega, k) + \frac{\delta R}{\delta \phi} \phi \quad . \quad (26)$$

In this case, the second term has to be included in the equation describing zonal flows and suggests possible existence of unstable or reduced damping of zonal flows.

References for Section V:

Experimental

- [1] G.S.Xu, et al., Physical Review Letters, 91(2003)125001
"Direct Measurement of Poloidal Long Wave length Flows in the HT-7 Tokamak"
- [2] K.J.Zhao, et al., Physical Review Letters, 96(2006)255004
"Toroidal Symmetry of the Geodesic Acoustic Mode Zonal flow in a Tokamak Plasma"

Theoretical

- [3] Zhe Gao, et al., Physics of Plasmas, 15(2008) 072511,
Eigen-mode Analysis of geodesic acoustic modes
- [4] Zhe Gao, et al., Physics of Plasmas, 13 (2006)100702
Multiple eigenmodes of geodesic acoustic mode in collision less plasmas
Many contributions were also made in Japan.
e.g., A.Fujisawa, Y.Hamada, T.Ido, K.Itoh, H. Sanuki, H. Sugama
- [5] Hamada, et al., Nuclear Fusion,45(2005)81,
"Zonal flow in the geodesic acoustic mode frequency range in the JIPP T-IIU tokamak plasmas"
- [6] A.Fujisawa, et al., Phys. Rev. Letters, 93(2004)165002,
"Identification of Zonal Flows in a Toroidal Plasma"
- [7] Ido, Nuclear Fusion, 46(2006)512,
"Observation of the interaction between the geodesic acoustic mode and ambient fluctuation in the JFT-2M tokamak"
- [8] H.Sugama, and T.H.Watanabe, Phys. Rev. Letts. 94(2005)115001
"Dynamics of Zonal Flow in helical systems"
- [9] T.Watari, et al, Phys. Plasmas, 12(2005)062304-1~8
"Extension of geodesic acoustic mode theory to helical plasmas"
- [10] T.Watari, et al. , Phys. Plasmas, 13(2006)062504-1~13

“Geodesic acoustic mode oscillation in the low frequency range”

[11] T.Watari, et al., Plasma Science and Technology, 8(2006)105

"Zonal flows and geodesic acoustic mode oscillations in tokamaks and helical systems"

[12] T.Watari, et al., , Phys. Plasmas, vol.14(2007) 112512,

“Unified response function for zonal flows with full finite orbit effects”

Section-VI Excitation of zonal flow by drift wave turbulence

Stringer spin-up, Winsor-Hallatschek, and Random shearing

In the long history of research in drift wave turbulence, the paradigm that the zonal flows is excited by the turbulent drift waves and regulate the turbulence has widely accepted. Here, we briefly discuss possible mechanisms exciting zonal flows and introduce technical terms such as "Stringer spin-up", Winsor-Hallatschek mechanism", and "Random shearing". We treat this problem with the following simplified set of equations, which is found in the paper by Itoh et al., [1].

$$\frac{\partial}{\partial t} n + \vec{\nabla} \cdot n \vec{V}_{\perp} + \vec{\nabla} \cdot n \vec{V}_{\parallel} = S \quad (1)$$

$$nm_i \left(\frac{\partial}{\partial t} \vec{V} + \vec{V} \cdot \vec{\nabla} \vec{V} \right) + \vec{\nabla} p - \vec{J} \times \vec{B} = Sm_i \vec{V} \quad (2)$$

$$\nabla \cdot \vec{J} = 0 \quad (3)$$

$$\vec{E} + \vec{V} \times \vec{B} = 0 \quad (4)$$

The second term $f^{\theta} = n_i m_i \vec{V} \cdot \vec{\nabla} \vec{V}$ in Eq. (2) is referred to as Reynolds stress, for which we will give some interpretations in the following context.

Wave kinetic equation with nonlinear term

It would be convenient to introduce "Wave Kinetic Equation" before we step into the mechanisms of zonal flow excitation. The wave kinetic equation is obtained in the following way [2] including the nonlinear term on the RHS.

$$\frac{d}{dt} n_{\vec{k}} = \frac{\partial n_{\vec{k}}}{\partial t} + \vec{v}_g \cdot \vec{\nabla} n_{\vec{k}} - \frac{d\omega_{\vec{k}}}{d\vec{r}} \cdot \vec{\nabla} n_{\vec{k}} = 2\gamma_k n_{\vec{k}} + NLT(k) \quad (5)$$

where

$$n_{\vec{k}} = \frac{1}{|\omega_k|} (1+k^2) |\phi_{\vec{k}}|^2 \quad \vec{v}_g = \frac{\partial \omega_{\vec{k}}}{\partial \vec{k}} \quad (6)$$

and

$$NLT(k) = \pi \int dk_1 dk_2 \left| v_{1,2}^1 \right|^2 [n_{\vec{k},1} n_{\vec{k},2} - sg(\omega_k \omega_1) n_{\vec{k}} n_{\vec{k},2} - sg(\omega_k \omega_2) n_{\vec{k}} n_{\vec{k},1}] \times \delta(\vec{k} - \vec{k}_1 - \vec{k}_2) \delta(\omega_k - \omega_{k_1} - \omega_{k_2}) \quad . \quad (7)$$

This equation is valid for weakly turbulent plasma, for in the derivation an assumption

$\sum_k \langle |\phi(t)|_{\vec{k}}^2 \rangle = \sum_k \langle |\phi_{\vec{k}}|^2 \rangle \delta(\omega - \omega_{\vec{k}})$ is made and an additional frequency matching

condition, $\omega_k - \omega_{k_1} - \omega_{k_2} = 0$ is imposed. WKE is however applied to plasmas of stronger turbulence sometimes it gives better insights.

The density fluctuation $n_{\vec{k}}$, which is defined as $\frac{1}{|\omega_k|} (1+k^2) |\phi_{\vec{k}}|^2$, is referred to as action in

literatures, is regarded as the number density of wave packets. The conservation properties of the nonlinear term $NLT(k)$ have been already discussed in section 4.

Nonlocal interaction

Since WKE is based on WKB approximation, it is not always appropriate to apply it to zonal flows. Therefore, we separate the drift wave fluctuation from that of zonal flows and apply WKE only to the former [3].

$$\frac{\partial \tilde{N}}{\partial t} + (\vec{v}_g) \cdot \vec{\nabla} \tilde{N} - \frac{\partial}{\partial x} (\omega_k + k_\theta V_{E,q}) \cdot \frac{\partial N}{\partial \vec{k}} = \gamma_k \tilde{N} \quad (8)$$

Here, it is noted that the γ_k on the RHS contains both linear growth rate and the part of $NLT(k)$ that is proportional to N . The non-localized nonlinear interaction of present interest is included on the LHS in terms of

$$V_{Eq} = -c \nabla \phi / B = -(ciq/B) e^{iqr} \quad (9)$$

Here, zonal flow is assumed to have wave numbers $k_\theta = 0$ and $k_r = q$. Equation (8) has the following solution:

$$\tilde{N} = \frac{1}{B} \gamma_k \frac{q^2 k_\theta}{(\Omega_q - (\vec{v}_g) \cdot \vec{q})^2 + \gamma_k^2} \frac{\partial N}{\partial k_r} \phi = \frac{\delta N}{\delta \phi} \phi \quad (10)$$

where

$$\frac{\delta N}{\delta \phi} = \frac{1}{B} \gamma_k \frac{q^2 k_\theta}{(\Omega_q - (\vec{v}_g) \cdot \vec{q})^2 + \gamma_k^2} \frac{\partial N}{\partial k_r} \phi \quad (11)$$

Reynolds stress and Random shearing

Remembering that the nonlinear term (Reynolds stress) on the LHS of Eq. (2) is originated from momentum transfer tensor in the fluid equation, we give the following interpretation to this term:

$$f^\theta = n_0 m \frac{\partial}{\partial r} \langle V_r V_\theta \rangle = \langle \frac{\partial}{\partial r} \left(\sum_k k_\theta v_{gr} \frac{\delta N}{\delta \phi} \phi_q \right) \rangle \quad (12)$$

Then, Eq.(12) may be rewritten as

$$\frac{\partial}{\partial r} \langle V_r V_\theta \rangle = -\frac{1}{n_0 m_i} \langle \frac{c}{B} \sum_k 2k_\theta^2 \rho_s^2 q^2 \frac{1}{(1+k_\perp^2 \rho_s^2)^2} R(k, q) k_r \frac{\partial \eta}{\partial k_r} \phi_q \rangle \quad (13)$$

in terms of

$$R(k, q) \equiv \frac{\gamma_k}{(\Omega_q - (\vec{v}_g) \cdot \vec{q})^2 + \gamma_k^2} \quad . \quad (14)$$

Equation (13) reads that gradient of enstrophy $\eta = (1 + k_\perp^2 \rho_s^2) \omega_k N_k$ of drift wave causes a force driving zonal flows. As it is clear in this derivation, the Reynolds stress is originated from the shearing of drift wave structure by the zonal flows. For this reason, this mechanism is referred to as "random shearing" mechanism.

Stringer spin-up and Winsor-Hallatschek mechanisms

Returning to Eq. (1), the second term is interpreted as the particle source associated with anomalous loss flux. This term is taken as the driving term of the system and for convenience it is divided into time-independent part $F_1(r, \theta)$ and time-dependent part $F_2(r, \theta, t)$:

$$-\vec{\nabla} \cdot n \vec{V}_\perp \Big|_{ext} = F_0 + F_1(r, \theta) + F_2(r, \theta, t) \approx F_1(r, \theta) + F_2(r, \theta, t) \quad (15)$$

The following two terms of parallel flow are induced by these two terms of perpendicular particle flows:

$$\frac{1}{qR} \frac{\partial}{\partial \theta} n \vec{V}_{\perp,1} = (-\vec{\nabla} \cdot n \vec{V}_\perp) = F_1(r, \theta) \quad (16)$$

and

$$\frac{1}{qR} \frac{\partial}{\partial \theta} n \vec{V}_{\perp,1,s} = (-\vec{\nabla} \cdot n \vec{V}_\perp) = F_{1,c}(r, \theta) \cos \theta \quad . \quad (17)$$

Using these expressions, Eqs. (1-4) are solved to yielding the following dispersion equation.

$$[-i\omega + (\frac{\delta}{\delta\phi} \tilde{V}_r \tilde{V}_\theta) \frac{B}{c} + \frac{2}{R} c_s^2 \frac{i(\frac{1}{R} + \frac{1}{2} \tilde{F}_{2,s})(\omega + i\nu) + \frac{1}{r} \frac{1}{qR} \cos\theta \frac{\partial V_\square}{\partial\theta}}{(\omega(i\nu + \omega) - c_s^2 (\frac{1}{qR})^2)}] \tilde{V}_{E \times B} = 0 \quad (18)$$

The solution to Eq.(18) has Geodesic Acoustic Mode, which has well known real frequency

$$\omega^2 = \frac{2c_s^2}{R^2} (1 + \frac{1}{2} (\frac{1}{q})^2) \quad (19)$$

and growth rate consisted of 4 terms:

$$\gamma = \frac{q^2}{(2q^2 + 1)} ((1/2q^2 \mu_\square k_\perp^2 - \gamma_{asym} + \gamma_{WH} + \gamma_{Reynolds}) \quad (20)$$

The second term, involving $\tilde{F}_{1,c}$, is originated from poloidal asymmetry of the loss particles flux.

$$\gamma_{asym} = \frac{R}{r} \overline{\cos\theta F_1(\theta)} = \frac{R}{r} \overline{\cos^2\theta} \tilde{F}_{1,c} \quad (21)$$

This term is referred to as Stringer spin-up term [4].

The third term, involving $\tilde{F}_{2,s}$, is originated from time-dependent up-down asymmetry of the loss particles flux. This mechanism of exciting zonal flow is referred to as Winsor-Hallatschek mechanisms [5]. The fourth term is caused by the Reynolds stress and is referred to as "Random Shearing mechanism [3] previously discussed. Finally, the first term originated from viscosity of the plasma and is always stabilizing. GAM oscillation will be destabilized if the sum of these dissipative terms becomes positive.

References for section-VI

[1] K.Itoh, K. Hallatschek, and S-I. Itoh, Plasma Phys. Control. Fusion, 47(2005) 451-458,
"Extension of geodesic acoustic mode in toroidal plasmas"

[2] Wendell Horton and Akira Hasegawa, Chaos, Vol4, No.2, 1994,
"Quasi-two dimensional dynamics of plasmas and fluids"

[3] Diamond, M.N.Rosenbluth, PRL, 22(2000)4842
"In search of the Elusive Zonal flow using Cross-Bi-coherence Analyses"

[4] A.B. Hassam and J.F. Drake, Physics Fluids, B5(1993)4022
"Spontaneous poloidal spin-up of tokamak plasmas: Reduced equations, physical mechanism, and sonic regimes" (Extension of Stringer Spin-up problem)

[5] K.Hallatschek and D.Biskamp, Phys. Rev. Letts., 86(2001)1223

"Transport Control by Coherent zonal flows in the core edge transition regime"

Section-VII Experimental determination of transfer functions

In the previous sections, we have learned how the drift wave transfers wave energy in k -space. Now let us investigate how these nonlinear processes are fulfilled in the real plasmas.

Ritz-Kim method

Ritz et al explored a method of determining transfer function from observed fluctuation data [1], which was followed by a work proposing an improvement [2]. We identify these two works and introduce in the following.

Let us denote say the experimentally obtained potential signal at time t and $t + \tau$ by $X_k = \phi(k, t)$ and $Y_k = \phi(k, t + \tau)$. (1)

which can be separated in amplitude and phase

$$X(k, t) = |X(k, t)| e^{i\Theta(k, t)}. \quad (2)$$

Then, the drift wave evolution equation

$$\frac{\partial \phi_k(k, t)}{\partial t} = (\gamma_k + i\bar{\omega}_k)\phi_k(k, t) + \frac{1}{2} \sum_{k_1+k_2=k} \Lambda_k^0(k_1, k_2)\phi(k_1, t)\phi(k_2, t) \quad (3)$$

is transformed in the following difference equation form:

$$Y(k, t) = L_k X(k, t) + \frac{1}{2} \sum_{k_1, k_2} Q_k^{k_1, k_2} X_{k_1} X_{k_2} \quad (4)$$

Here,

$$L_k = \frac{\Lambda_k^L \tau + 1 - i[\Theta(k, t + \tau) - \Theta(k, t)]}{e^{-i[\Theta(k, t + \tau) - \Theta(k, t)]}} \quad (5)$$

is referred to as linear transfer function and

$$Q_k^{k_1, k_2} = \frac{\Lambda_k^0(k_1, k_2)\tau}{e^{-i[\Theta(k, t + \tau) - \Theta(k, t)]}} \quad (6)$$

is referred to as non-linear transfer function.

Multiplication of various moments to the mother equation Eq.(3) gives infinite set of

cumulant equations:

$$\langle Y_k X_k^* \rangle = L_k \langle X_k X_k^* \rangle - \sum_{\substack{k_1 \geq k_2 \\ k=k_1+k_2}} Q_k^{k_1, k_2} \langle X_k^* X_{k_1} X_{k_2} \rangle \quad (7)$$

$$\langle Y(k, t) Y^*(k, t) \rangle = L_k \langle Y_k X^*(k, t) \rangle + \sum_{k_1, k_2} Q_k^{k_1, k_2} \langle Y_k X_{k_1}^* X_{k_2}^* \rangle \quad (8)$$

$$\langle Y_k X_{k_1}^* X_{k_2}^* \rangle = L_k \langle X_k X_{k_1}^* X_{k_2}^* \rangle - \sum_{\substack{k_1 \geq k_2 \\ k=k_1+k_2}} Q_k^{k_1, k_2} \langle X_{k_1} X_{k_2} X_{k_1}^* X_{k_2}^* \rangle \quad (9)$$

This set of equations is solved by truncating, for instance, at fourth moment and limiting wave number space by $-n \leq k \leq n$ with an appropriate number n .

Noting that k_1 and $k_2 (= k - k_1)$ are subject to each other, we regard $Q_k^{k_1, k_2}$,

$\vec{B}_k = \langle Y_k^* X_{k_1} X_{k_2} \rangle$, and $\vec{A}_k = \langle X_k^* X_{k_1} X_{k_2} \rangle$ as n number of vectors of element n .

Similarly, $\vec{F}_k^{-1} = \langle X_{k_1} X_{k_2} X_{k_1}^* X_{k_2}^* \rangle$ is regarded as n number of $n \times n$ matrix.

Then, we obtain

$$\langle Y_k X_k^* \rangle = L_k \langle X_k X_k^* \rangle - \vec{Q}_k \cdot \vec{A}_k \quad (10)$$

$$\langle Y(k, t) Y^*(k, t) \rangle = L_k \langle Y_k X(k, t) \rangle + \vec{Q}_k^* \cdot \vec{B}_k^* \quad (11)$$

$$(\vec{B}_k^*)^T = L_k (\vec{A}_k^*)^T - \vec{Q}_k \cdot \vec{F}_k \quad (12)$$

Equation (12) is formally solved for \vec{Q}_k by multiplying inverse matrix \vec{F}_k^{-1} .

$$\vec{Q}_k = (\vec{B}_k^*)^T \cdot \vec{F}_k^{-1} - L_k (\vec{A}_k^*)^T \cdot \vec{F}_k^{-1} \quad (13)$$

Two expressions of L_k is obtained from Eq. (10) and (11)

$$L_k = \frac{\langle Y_k X_k^* \rangle - (\vec{B}_k^*)^T \cdot \vec{F}_k^{-1} \cdot \vec{A}_k}{\langle X_k X_k^* \rangle - (\vec{A}_k^*)^T \cdot \vec{F}_k^{-1} \cdot \vec{A}_k} \quad (14)$$

and

$$L_k = \frac{\langle Y Y^* \rangle - (\vec{B}_k^*)^T \cdot \vec{F}_k^{-1} \cdot \vec{B}_k}{\langle Y_k X_k^* \rangle - (\vec{A}_k^*)^T \cdot \vec{F}_k^{-1} \cdot \vec{B}_k} \quad . \quad (15)$$

L_k is obtained by solving the linked equation Eqs.(14) and (15) and \vec{Q}_k is obtained by using the result in Eq.(13). Growth rate is deduced in a simpler short-cut procedure:

$$\begin{aligned} L_k L_k^* &= \frac{\langle Y_k X_k^* \rangle - (B^*)^T \cdot F^{-1} \cdot A \langle Y_k Y_k^* \rangle - \langle B \rangle^T \cdot (F^{-1})^* \cdot B^*}{\langle X_k X_k^* \rangle - (A^*)^T \cdot F^{-1} \cdot A \langle X_k^* Y_k \rangle - \langle A \rangle^T \cdot (F^{-1})^* \cdot B^*} \\ &= \frac{\langle Y_k Y_k^* \rangle - \langle B \rangle^T \cdot (F^{-1})^* \cdot B^*}{\langle X_k X_k^* \rangle - (A^*)^T \cdot F^{-1} \cdot A} = 1 + \frac{(A^*)^T \cdot F^{-1} \cdot A - \langle B \rangle^T \cdot (F^{-1})^* \cdot B^*}{\langle X_k X_k^* \rangle - (A^*)^T \cdot F^{-1} \cdot A} \end{aligned} \quad (16)$$

, where we have used the properties $(B^*)^T \cdot F^{-1} \cdot A = \langle A \rangle^T \cdot (F^{-1})^* \cdot B^*$ and imposed the steady state condition $\langle Y_k Y_k^* \rangle = \langle X_k X_k^* \rangle$. Thus the growth rate of the drift wave with mode number k is given by

$$\gamma_k = \frac{L_k L_k^* - 1}{\tau} = \frac{1}{\tau} \frac{(A^*)^T \cdot F^{-1} \cdot A - \langle B^* \rangle^T \cdot (\tilde{F}^{-1}) \cdot B}{\langle X_k X_k^* \rangle - \langle (A^*)^T \cdot F^{-1} \cdot A \rangle} \quad (17)$$

If random phase approximation is applied as it was done in Ref. [1], the Matrix \tilde{F} becomes diagonal and the formulation is simplified. The unknown quantities L_k and $Q_k^{k_1, k_2}$ are given in the following forms.

$$L_k = \frac{\langle X_k^* Y_k \rangle - \sum_{\substack{k_1 \geq k_2 \\ k=k_1+k_2}} \frac{\langle X_k^* X_{k_1} X_{k_2} \rangle \langle X_k X_{k_1}^* X_{k_2}^* \rangle}{\langle |X_{k_1} X_{k_2}|^2 \rangle}}{\langle X_k X_k^* \rangle - \sum_{\substack{k_1 \geq k_2 \\ k=k_1+k_2}} \frac{|\langle X_k^* X_{k_1} X_{k_2} \rangle|^2}{\langle |X_{k_1} X_{k_2}|^2 \rangle}} \quad (18)$$

$$Q_k^{k_1, k_2} = \langle |X_{k_1}|^2 |X_{k_2}|^2 \rangle^{-1} (L_k \langle X_k X_{k_1}^* X_{k_2}^* \rangle - \langle Y_k X_{k_1}^* X_{k_2}^* \rangle) \quad (19)$$

P.Mantz et al [3], tried application of this method to H-W system, where more complicated nonlinear term play a role.

Crossley 's method

A new method which is referred to as "amplitude correlation method" was introduced by Crossley [4].

The amplitude correlation $K(\tau)$ is defined as a correlation of squared density fluctuation between two different bands in k -space, $k_a \Delta k$ and $k_b \Delta k$.

$$K(\tau) = \langle [n_{ka}^2(t)][n_{kb}^2(t+\tau)] \rangle \quad (20)$$

In Fig.10, $K(\tau)$ is calculated with the experimental data for two different pairs of wave number bands.

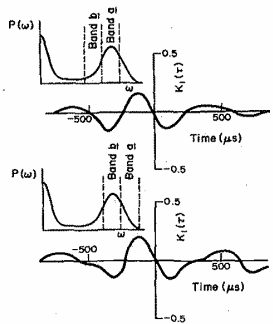


FIG. 6.—The amplitude correlation between sub-bands of the drift-wave spectral peak, as shown in the insets. Top: centre and lower bands; bottom: upper and central bands.

Fig.15

So defined, if $K(\tau) > 0$ for $\tau < 0$, it means the wave energy is transferred from high wave number to low wave number as anticipated in the previous sections. The instance in Fig.10 seems to be support theoretical predictions(inverse cascade). Validity of this method is discussed for instance in Ref. [5] and needs further consideration.

References for Section-VII

- [1] Ch.P.Ritz, E.J.Powers, and D.Bengston, Phys. Fluids, B1(1989)153,
"Experimental measurement of three-wave coupling and energy transfer"
- [2] J.S.Kim, R.D.Durst, and R.J.Fonck, E.Fernandez, A.Ware, and Terry
"Technique for the experimental estimation of nonlinear energy transfer in fully developed turbulence."
- [3] P.Mantz, M.Ramish, U.Stroth, V.Naulin, and B.D.Scott
Plasma Physics and Controlled Fusion, 50(2008)035008(12pp)
"Bispectral experimental estimation of the non-linear energy transfer in two dimensional plasma turbulence"
- [4] F.J. Crossley, P.Uddholm, P.Duncan, M.Khalid, M.G.Rusbridge,
Plasma Phys. Control. Fusion, 34(1992)235
"Experimental study of drift-wave saturation in quadrupole geometry"
- [5] Plasma Phys. Control. Fusion, 35(1993)1701, H.L. Pcseli and J. Trulsen,
"On the interpretation of experimental methods investigating nonlinear wave phenomena"

Section-VIII Streamers and blobs

One of the interesting theoretical topics related to drift wave turbulence is the streamer. Streamers appear as a potential and density perturbations with radially long and poloidally short wave length. In experiments, it may appear as a avalanche like loss of particle- and energy- losses. Figure-1 shows an example of such phenomena observed in JIPP T-IIU tokamak [1].

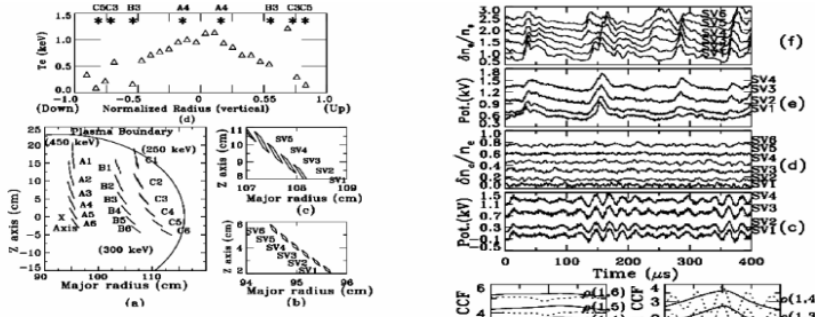


FIG. 1. (a) Location and direction of alignment of 6 SVs of the HIBP at 18 steps discussed in this Letter. Label A stands for the beam energy of 450 keV, label B for 300 keV, and label C for 250 keV. (b) Shape and positions for SVs at step A4 and (c) is for C2. (d) The vertical profile of electron temperature across the axis obtained by YAG Thomson scattering measurement. The positions of SVs at various steps are shown for reference.

Fig.16

Below, a model of streamer related to drift wave turbulence is introduced based on Ref.[2] This paper starts from the following H-M type two field equation.

$$\partial_t(\tilde{n} - \rho_x^2 \Delta_\perp \frac{e}{T_e} \tilde{\phi}) + \nu^* \partial_y \frac{e}{T_e} \tilde{\phi} + \bar{v}_E \cdot \nabla(\tilde{n} - \rho_s^2 \Delta_\perp \frac{e}{T_e} \tilde{\phi}) + \tilde{v}_E \cdot \nabla(\bar{n} - \rho_s^2 \Delta_\perp \frac{e}{T_e} \bar{\phi}) = 0 \quad (1)$$

$$\partial_t \Delta_\perp \bar{\phi} + \bar{v}_E \cdot \nabla \Delta_\perp \tilde{\phi} = 0 \quad (2)$$

$$\partial_t \bar{n} + \nu^* \partial_y \frac{e}{T_e} \bar{\phi} + \bar{v}_E \cdot \nabla \bar{n} = 0 \quad (3)$$

In Eqs.(1)-(3), waved quantities represent short wave length disturbances due to drift wave turbulence. The barred quantities denote long wavelength disturbances including zonal flow and streamers; thus these two mechanisms are discussed on the same footing based on Eqs.(1)-(3). Slowly varying time T and space $\vec{X} = X(X, T)$ are introduced representing the scales of the barred quantities and they are also associated with the envelope modulation of drift wave turbulence.

$$\tilde{\phi} = \Phi(X, T) e^{i(\vec{k} \cdot \vec{x} - \omega t)} + cc, \quad \tilde{n}(X, T) = N e^{i(\vec{k} \cdot \vec{x} - \omega t)} + cc, \quad N = e\Phi / T_e \quad (4)$$

Using the technique of reductive perturbation the following set of equations is obtained.

$$i\epsilon\hat{\partial}_\tau N + \left(\frac{\partial^2 D}{\partial k_x^2} \partial_{xx} + \frac{\partial^2 D}{\partial k_y^2} \partial_{yy} + \frac{\partial^2 D}{\partial k_x \partial k_y} \partial_{xy} \right) \cdot N + \rho_s^2 \Omega_i (\vec{k} \times \nabla \bar{\phi} \frac{e}{T_e}) \cdot \hat{z} N - \frac{1}{(1 + \rho_s^2 k^2)} \rho_s^2 \Omega_i (\vec{k} \times \nabla \bar{n}) \cdot \hat{z} N = 0 \quad (5)$$

$$(\varepsilon\partial_\tau - \vec{v}_g \cdot \vec{\nabla}) \left(\frac{\partial^2}{\partial X^2} + \frac{\partial^2}{\partial Y^2} \right) (e/T_e) \bar{\phi} + \frac{1}{2} \rho_s^2 \Omega_i [k_x k_y (\partial_{YY} - \partial_{XX}) + (k_x^2 - k_y^2) \partial_{XY}] |N|^2 = 0 \quad (6)$$

$$(\epsilon \partial_\tau - \vec{v}_g \cdot \vec{\nabla}) \bar{n} + \nu^* \frac{\partial}{\partial Y} \frac{e\bar{\phi}}{T_e} = 0 \quad (6)$$

Here, the first and second terms are originated from the following WKB considerations:

$$\begin{aligned}
\vec{I} &= \int D(\vec{r}, \vec{r}', t - t') \cdot \phi(\vec{r}', t') d\vec{r}' dt' = \int_{-\infty}^t dr' dt' D\left(\frac{\vec{r} + \vec{r}'}{2}, \vec{r} - \vec{r}', \frac{t + t'}{2}, t - t'\right) \cdot \phi(\vec{r}', t') d\vec{r}' dt' \\
&= \int_{-\infty}^t dr' dt' \{ D(\vec{r}, \vec{r} - \vec{r}', t - t') + D_{AH}(\vec{r}, \vec{r} - \vec{r}', t - t') \\
&\quad + \left(\frac{\vec{r}' - \vec{r}}{2}\right) \cdot \frac{\partial}{\partial \vec{r}} D(\vec{r}, \vec{r} - \vec{r}', t - t') + \left(\frac{t' - t}{2}\right) \frac{\partial}{\partial t} \tilde{D}(\vec{r}, \vec{r} - \vec{r}', t - t')\} \\
&\quad \times \{(\phi(r, t) + (\vec{r}' - \vec{r}) \cdot \frac{\partial \phi(r, t)}{\partial \vec{r}} + \frac{1}{2}[(\vec{r}' - \vec{r}) \cdot \frac{\partial}{\partial \vec{r}}]^2 \phi(r, t) + (t' - t) \cdot \frac{\partial \phi(r, t)}{\partial t})
\end{aligned} \tag{7}$$

The lowest order term is vanished as $D(\vec{r}, \vec{k}, \omega) \cdot \phi(r, t) = 0$ is employed

$$\begin{aligned}
I = & -i \int d\omega dk \left\{ \frac{1}{2} \frac{\partial}{\partial \vec{k}_i} \cdot \frac{\partial D(\vec{r}, \vec{k}, \omega)}{\partial \vec{r}_i} + \frac{\partial D(\vec{r}, \vec{k}, \omega)}{\partial \vec{k}_i} \cdot \frac{\partial}{\partial \vec{r}_i} \right\} \cdot \phi(r, t) \\
& + i \int d\omega dk \left\{ \frac{1}{2} \frac{\partial}{\partial \omega} \cdot \frac{\partial D(\vec{r}, \vec{k}, \omega)}{\partial t} \cdot \phi(r, t) + \frac{\partial D(\vec{r}, \vec{k}, \omega)}{\partial \omega} \cdot \frac{\partial \phi}{\partial t} \right\} - D_a(\vec{r}, \vec{k}, \omega) \cdot \phi \\
& + \frac{1}{2} \int d\omega dk \left(\frac{\partial^2 D(\vec{r}, \vec{k}, \omega)}{\partial k_x^2} \partial_{XX} + \frac{\partial^2 D(\vec{r}, \vec{k}, \omega)}{\partial k_y^2} \partial_{YY} + \frac{\partial^2 D(\vec{r}, \vec{k}, \omega)}{\partial k_x \partial k_y} \partial_{XY} \right) \cdot \phi = 0
\end{aligned} \tag{8}$$

Streamers

Streamers are described by taking the limit of $\partial_x \rightarrow 0$:

$$\bar{n} = v^* / (\partial \omega / \partial k_y) \frac{e\bar{\phi}}{T_e} \quad (9)$$

$$\frac{\partial}{\partial Y} \frac{e\phi}{T_e} = 2\rho_s^2 \Omega_i k_y k_x / (\partial \omega / \partial k_y) |N|^2 \quad (10)$$

$$i\partial_\tau N + \frac{1}{2} \left(\frac{\partial^2 \omega}{\partial k_y^2} \partial_{YY} \right) N + \frac{2\rho_s^4 k_x^2 k_y \Omega_i^2}{(\partial \omega / \partial k_y)} \left(1 - \frac{\nu^*}{1 + \rho_s^2 k^2} \right) N |N|^2 = 0 \quad (11)$$

This is a kind of Nonlinear Shroedinger Equation, which can be solved with an assumed wave form,

$$N = N_0 e^{iQ_y Y} e^{-i(\Omega + i\gamma)\tau} :$$

$$\gamma^2 = -\alpha_1^2 Q_y^4 + 2\alpha_1 \alpha_2 Q_y^2 \quad (12)$$

$$\Omega = -\alpha_2 |N_0|^2 \quad . \quad (13)$$

where

$$\alpha_2 = \frac{2\rho_s^4 k_x^2 k_y \Omega_i^2}{(\partial \omega / \partial k_y)} \left(1 - \frac{\nu^*}{1 + \rho_s^2 k^2} \right) \quad \text{and} \quad \alpha_1 = \frac{1}{2} \left(\frac{\partial^2 \omega}{\partial k_y^2} \partial_{YY} \right). \quad (14)$$

The necessary condition of instability is

$$3[1 + \rho_s^2 k_x^2] > \rho_s^2 k_y^2 \quad (15)$$

and the maximum growth rate

$$\gamma_{\max} = |\alpha_2| |N_0|^2$$

occurs at modulational wave number

$$Q_y = \frac{\alpha_1}{\alpha_2} |N_0|^2 = \frac{2\Omega_i \rho_s^2 k_x k_y}{\nu^* \left| 1 + \rho_s^2 k_x^2 - \rho_s^2 k_y^2 \right|} \frac{(1 + \rho_s^2 k^2)^{5/2}}{3^{1/2} [(1 + \rho_s^2 k_x^2) - \rho_s^2 k_y^2 / 3]^{1/2}} |N_0|^2 . \quad (16)$$

Zonal flow

Zonal flows are obtained in the other limit, $\partial_Y \rightarrow 0$. We obtain

$$i\partial_\tau N + \frac{1}{2} \left(\frac{\partial^2 \omega}{\partial k_x^2} \partial_{XX} \right) N + \frac{2\Omega_i^2 \rho_s^4 k_x^2 k_y}{(\partial \omega / \partial k_x)} |N|^2 N = 0 \quad (17)$$

This NLS equation gives the instability condition

$$1 + \rho_s^2 k_y^2 - \rho_s^2 k_x^2 > 0 \quad (18)$$

and the maximum growth rate occurs at modulational wave number

$$Q_x = |N_0| \left(\frac{2\Omega_i^2 (1 + \rho_s^2 k^2)^5}{(\nu^*)^2 |1 + \rho_s^2 k_y^2 - \rho_s^2 k_x^2|} \right)^{1/2} \quad (19)$$

The thresholds of streamer and zonal flows are shown in Fig.17.

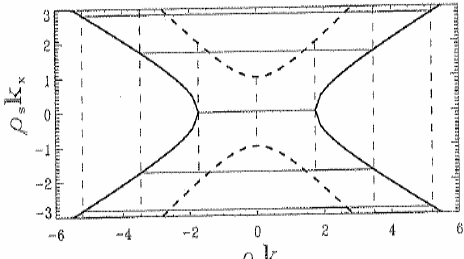


Fig.17

Shown above is one possible mechanism causing a streamer, in which radially long perturbation of density and potential associated with envelope modulation of drift wave is suggested to be observed. The model introduced here is not the only one and there may be other mechanisms which accounts for intermittent events. Such phenomena are interesting as candidates of mechanisms accounting for SOC (self organized criticality [3]). The following references are available for further study in this field, [4-7].

Blobs:

Though it is not major scope of this lecture, "bubble formation" is reported to occur in the scrape off layers of tokamaks and theoretical models are presented [8-11]. These phenomena are locally referred to as IOP (intermittent plasma object). Such intermittent events are sometimes studied in terms of probability distribution function PDF. In order to take out events from general form of fluctuations, Conditional averaging is applied to experimental data. The PDF are sometimes characterized by the skewness defined by $\langle x^3 \rangle / \langle x^2 \rangle^{3/2}$ and flatness defined by $\langle x^4 \rangle / \langle x^2 \rangle^2$. It is reported that, the PDFs obtained in the scrape off layers of various tokamaks have similar values of skewness~3 and flatness~10[13].

The mechanism of "blob" is illustrated in Fig.18:

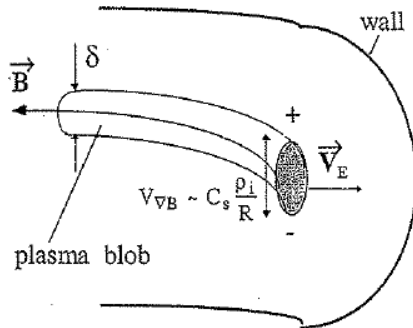


Fig.18

The charge accumulating in the tube is described by the following equation:

$$\rho_s^2 \nabla_{\perp} \cdot \{n \frac{d \nabla_{\perp} \phi}{dt}\} + \frac{2 \rho_s C_s}{R} \frac{\partial n}{\partial y} = \frac{2 C_s}{L_{con}} n \phi \quad (20)$$

The second term is caused by the curvature drift of particles and the first term is due to polarization current. These charges are balanced by the term on RHS which is caused due to the finite resistivity determined by the sheath effect. Equation (20) has been obtained by integrating the continuity equation along the tube. The potential ϕ is measured with respect to the wall or diverter plate, R

is the major radius, $C_s = (T_e / M)^{1/2}$ the sound velocity and, L_{con} is the connection length.

Equation 20 is associated with the continuity equation.

$$\frac{\partial n}{\partial t} + \vec{v}_{E \times B} \cdot \vec{\nabla} n = -\frac{2 C_s}{L_{con}} n \quad (21)$$

Neglecting of the polarization current, Eq.(20) is much simplified and gives the following solution:

$$\phi = -\frac{\rho_s L_{con}}{R} \frac{1}{n} \frac{\partial n}{\partial y} \quad (22)$$

Substituting Eq.(22) into Eq.(20), one obtains

$$\begin{aligned} & \frac{\partial n}{\partial t} - \frac{c}{B} \frac{\rho_s L_{con}}{R} \vec{\nabla} \left(\frac{1}{n} \frac{\partial n}{\partial y} \right) \cdot \vec{\nabla} n \\ &= \frac{\partial n}{\partial t} - \frac{c}{B} \frac{\rho_s L_{con}}{R} \left[\frac{\partial}{\partial y} \left(n \frac{\partial}{\partial x} \left(\frac{1}{n} \frac{\partial n}{\partial y} \right) \right) - \frac{\partial}{\partial x} \left(n \frac{\partial}{\partial y} \left(\frac{1}{n} \frac{\partial n}{\partial y} \right) \right) \right] = -\frac{2 C_s}{L_{con}} n \end{aligned} \quad (23)$$

The fist term of the bracket is nullified by integration over y and we assume the following form:

$$n(t, x, y) = n^{(x)}(t, x) n^{(y)}(y) \quad \text{with} \quad \tilde{n}(y) = e^{-\left(\frac{y}{\delta y}\right)^2} \quad (24)$$

Then, Eq. (23) allows the following solution.

$$n^{(x)}(t, x) = n^{(x)}(x - v_b t) \quad (25)$$

$$v_b = \frac{c}{B} \frac{2\rho_s L_{con}}{R} \frac{1}{(\delta y)^2} \quad (26)$$

Thus, the blob wave form may be summarized as follows:

$$n = n_b (x - v_b t) \tilde{n}(y) e^{-\frac{2C_s t}{L}} \quad (27)$$

and

$$\phi = -\frac{\rho_s L_{con}}{R} \frac{1}{n} \frac{\partial n}{\partial y} = \frac{\rho_s L_{con}}{R} \left(\frac{1}{\delta y}\right)^2 y \quad (28)$$

The blob is an interesting phenomena observed in the scrape off layer and streamers is regarded as one of the mechanism triggering the former. Though it occurs in the limited region of scrape off layer, it could affect transport of main body of the plasma due to nonlocal effects.

References for Section-VIII:

- [1] Y.Hamada, T.Watari, A.Nishizawa, K.Narihara, et al., PRL, 96(2007)11503,
"Streamers in the JIPP T-IIU Tokamak"
- [2] S.Champeaux, P.H.Diamond, Physics Letters, A-288(2001)214
"Streamer and zonal flow generation from envelope modulations in drift wave turbulence"
- [3] P.Bak, C.Tang, and K.Wiesenfield, Phys. Rev. Letters, 59(1987)381
"Self-organized criticality: An explanation of 1/f Noise"
- [4] P.A.Politzer, Phys. Rev. Letters, 84(2000)1192,
"Avalanche like phenomena in a Magnetically Confined Plasma"
- [5] X.Garbet, Y.Sarazin, P.Beyer, et al., Nuclear Fusion (special issue), 39(1999)2063,
"Flux driven turbulence in tokamaks"
- [6] P.Beyer, Benkadda, X.Garbet, and P.H.Diamond, Phys. Rev. Letters, 85(2000)4892,
"Non-diffusive transport in tokamaks: Three dimensional structure of bursts and role of zonal flow"
- [7] S.Benkadda, P.Beyer, et al., Nuclear Fusion, 41(2001)995,
"Bursty transport in tokamak turbulence: Role of zonal flows and internal transport barriers"
- [8] S.I.Krasheninnikov, Phys. Letters., A283(2001)368,
"On scrape off layer plasma transport"
- [9] J.A.Bodeo, et al., Phys. Plasmas, 8(2001)4826
"Transport by intermittent convection in the boundary of the DIII-D tokamak"
- [10] S.J.Zweben D.P. Stotler, J.L.Terry, et al., Phys. Plasmas 9(2002)1981,
"Edge turbulence imaging in the Alcator C-mod tokamak"
- [11] J.A.Bodeo, D.L. Rudakov, R.A. Moier, G.R. McKee, et al., Phys. Plasmas, 10(2003)1670,

"Transport by intermittency in the boundary of the D-III-D tokamak"

[12] N.Bian, S.Benkadda, J.-V. Paulsen, and Garcia, Phys. Plasmas, 10(2003)671

"Blobs and front propagation in the scrape-off layer of magnetic confinement devices"

[13] Ghassan Y. Antar, Glenn Counsell, Yang Yu, et al., Phys. Plasmas, 10(2003)419

"Universality of intermittent convective transport in the scrape-off layer of magnetically confined devices"

Acknowledgements:

This is the material used in the lecture at "JSPS-CAS Core University Seminar on Production and Control of High Performance Plasma with Advanced Plasma Heating and Diagnostics Systems". This work is largely supported by CUP as the seminar is entitled. I am very pleased that, in reviewing the works in the past, I was able to recognize that many international contributions were born in the activities under CUP.

Plasma shape control on EAST

B. J. Xiao, Q.P. Yuan, Z.P. Luo, R. R. Zhang, J.P. Qian, B. Shen, C. Y. Liu, L.Z. Liu, H.Z. Wang¹,
M.L. Walker, A. Hyatt, A. Welander, D.A. Humphreys, J.A. Leuer, B.G. Penaflor, D.A. Pigrowski, R.D.
Johnson², Dennis Mueller³

¹*Institute of Plasma Physics, Chinese Academy of Sciences, Hefei, China*

²*General Atomics, DIII-D National Fusion Facility, San Diego, CA, USA*

³*Princeton Plasma Physics Laboratory, Princeton, NJ, USA*

Advanced tokamak plasma operation relies on the exact control of the plasma shape in order to get better coupling to the heating RF waves, protect divertor by exact control of the striking points. For the shape control to be possible, the shape parameters must be known. Because the shape together with values of many plasma discharge parameters such as safety factor q , plasma poloidal β_p , can't directly measured, they can be evaluated from the available magnetic diagnostic data such as magnetic field and flux, plasma current and coil currents. These measured data can be used to fit the plasma current distribution in a combination of the solution of plasma force balance equation – Grad-Shafarany equation. Such procedure reconstructs the plasma equilibrium to give a full sets of the plasma equilibrium parameters and the plasma boundary as well. This full reconstruction of the equilibrium can be performed by using EFIT [1] code, which has been routinely done for EAST between adjacent shots. This kind of reconstruction was to be made sufficiently fast for the real-time shape control in DIII-D by using a fast loop and a slow loop calculations on separate CPUs[2]. The slow loop is responsible for the well-converged full reconstruction with enough accuracy performed at every longer time step while the fast loop only does one or a little more fixed number of loop iterations if faster CPU used. The fast loop calculates the shape control parameters such as flux error at given control points and thus the command to the power supplies. This algorithm was so called RTEFIT. While RTEFIT has been done at a control cycle, the control reference points was determined at first. Depending on the discharge, such reference point could be the point of the plasma touching the limiter if the separatrix was limited by the limiter or the X points for a diverted plasma. The flux at the reference point and thus calculated and the flux difference at pre-defined control points are calculated with reference to the flux at the reference point. The control would be conducted to make this flux difference to be zero and the reference points to be the predefined locations as sell. The overall shape control algorithm is called RTEFIT/ISOFLUX algorithm which was firstly realized in DIII-D[2].

Under the collaboration with DIII-D, EAST also adapted DIII-D plasma control software system[3]. One of the main missions for EAST 2008 summer campaign was to realized plasma shape control. The shape control algorithm is also RTEFIT/ISOFLUX.

Firstly, plasma must be well controlled for position and plasma current. This has been accomplished in the first two plasma campaigns of EAST [3]. When the current and position is well controlled, the real-time plasma equilibrium reconstruction was initiated with sufficient accuracy at fine enough time steps. After shots, this real-time reconstructed equilibrium was compared with off-line EFIT calculations and other diagnostic methods such as plasma CCD image. The left-hand side of Fig.1 shows the EAST coil configuration together with the limiter boundary(thinner black line), plasma shape target(thicker black line), control segments(red line) and control grids or areas(in shaded area) for the determination of X points. When in the limited control algorithm, the PFs 7-8 are

current-controlled. Their currents are increased against with their values at a circular plasma configuration, to strength the plasma in vertical direction. The currents of PFs5-6 were also increased but those of PFs1-2 drop more quickly in order to push the plasma harder to make the plasma more D-like. After carefully adjusting PFs 7-8 currents and the decoupling matrix for commanding PF1-6 coils, plasma shape can be approximately stable. Thus plasma shape at a typical time step can be used as the plasma shape for a shape control. Shown at the left of figure 1 was the plasma boundary determined by an offline EFIT reconstruction of the plasma equilibrium for the shot 7697 at 3.3 s. This shape was used as the basis shape to be controlled for an isoflux/double-null algorithm. After the shape control matrix and the PID control parameters have been carefully adjusted, the plasma shape can be well controlled at shot 8815 as shown at the right of figure 1. The control points were also shown in cross symbols together with the plasma shape and flux surfaces. The upmost and lowest points are the upper and lower X points, respectively. The other control points in the figure were chosen in such a way to mainly control the inner gap by the inmost point, outer gap by the outmost point, the upper and lower triangularities. In figure 2, we also showed the main controlled parameters at the isoflux control algorithm. It can be seen that the flux errors were well controlled below 5 mVs for most of the discharge time under shape feedback control which started from 3 s. The X point position control is rather good but in the range of several centimeters. In order for X positions to be well controlled with much lower error, the shape control has to be sufficiently consistent with the fast vertical position control. This leaves to be fulfilled at the next experimental campaign.

This work was partially supported by JSPS-CAS core-university program, China Nature Science Foundation with grant No. of 10835009 and the key project of knowledge innovation program of Chinese Academy of Sciences with grants No. of KJCX3.SYW.N4

References

- [1] LAO, L.L., et al., Nucl. Fusion **25** (1985) 1611.
- [2] J.R. FERRON, M.L. WALKER, L.L. LAO, H.E. ST. JOHN, D.A. HUMPHREYS, J.A. LEUER, NUCLEAR FUSION, Vol. 38, No. 7 (1998)
- [3] B.J. Xiao, D.A. Humphreys, M.L. Walker, A. Hyatt & J.A. Leuer, et al., “EAST plasma control system”, FUSION ENGINEERING AND DESIGN (2008)83–181

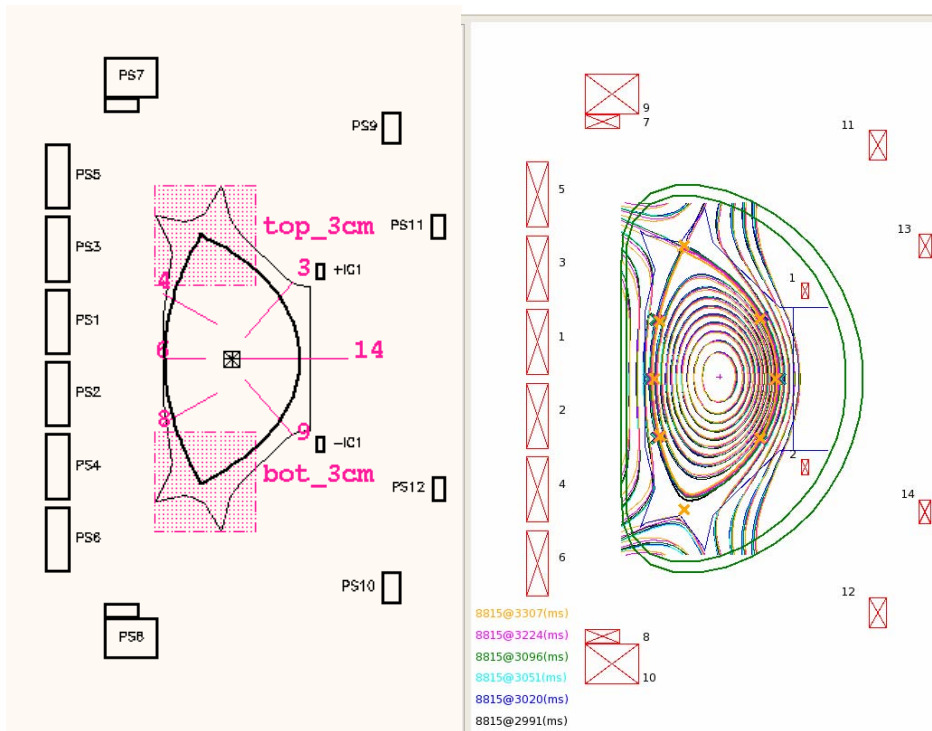


Figure 1, left: Plasma shape control points.

Right: the illustration of the achieved shape control at shot 8815.

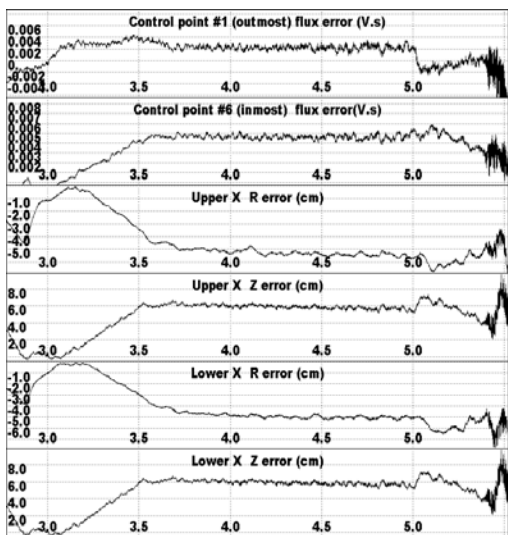


Figure 2 Control errors for the gap control point fluxes and X point positions.

Recent Results of JT-60 Experiments

Y. Koide and the JT-60 Team
Japan Atomic Energy Agency

Key words:

JT-60、JT-60SA, advanced tokamak, high beta, bootstrap current

Abstract:

JT-60 completed 24-year operation on 29th August, 2008 towards the construction of the next superconducting device JT-60SA. In this presentation, recent results of JT-60 for establishment of advanced tokamak concept for ITER and DEMO (i.e. development of plasmas with high beta, high confinement, high bootstrap-current fraction and high radiation fraction, as well as development of advanced diagnostics and high heating power technology) are presented. Status of JT-60SA programme is also reported where procurement has been already launched.

This work was partially supported by the JSPS-CAS Core-University program in the field of 'Plasma and Nuclear Fusion'.

Recent Progress of the HL-2A tokamak

X. R. Duan for the HL-2A Team

Southwestern Institute of Physics, P. O. Box 432, Chengdu 610041, China

E-mail address: duanxr@swip.ac.cn

Abstract

The HL-2A tokamak programme is to address key physics issues relevant to ITER. Since last FEC, recent experimental campaigns have been focused on studying and understanding the physics of turbulence, transport, MHD instabilities and energetic electron dynamics. Significant advances have been made in these fields. In particular, the three dimensional spectral structures of the theory and simulation predicted low frequency zonal flow (LFZF) and quasi-mode (QM) have been observed simultaneously for the first time. A spontaneous particle transport barrier (PTB) has been observed and evidenced for the first time in Ohmic discharges without any external momentum input or particle source. These advances have benefited from substantial improvements and developments of hardwares, including installation of modulated ECRH (2 MW/68 GHz), NBI (2 MW/45 keV), modulated SMBI system, plasma control and diagnostic systems.

1. Zonal Flows and Turbulence

The toroidal symmetry of the LFZF with $f < 4$ kHz is identified with toroidally distributed three-step Langmuir probes (TSLPs) in the edge plasma for the first time. The frequency and wave vector spectra of the flows are measured and analyzed in detail. High toroidal and poloidal coherences of the flows are simultaneously observed. The spectral averaged radial wave vector and width of the flows are estimated as $\bar{k}_r = 0.30\text{cm}^{-1}$ and $\Delta k_r = 3.2\text{cm}^{-1}$. Envelope analysis indicates that the high frequency ambient turbulence (HFAT) is regulated by the LFZF as is by geodesic acoustic mode (GAM), although the coherence in the frequency regime of the former is lower than that of the latter. In addition, the mode structure

of the density fluctuation at GAM frequency is identified. The transport induced by the large amplitude intermittent bursts in the scrape-off layer (SOL) is found to account for 45-50% of the total outward particle flux.

The distinct characteristics of low frequency QM fluctuations of several tens kilohertz and the HFAT of 100 kHz or higher are measured with high spatiotemporal resolution Langmuir probe arrays. Three dimensional wave number spectra and dispersion relations are investigated and compared between the QM and HFAT. Obvious differences, which reveal the existence of the two distinguishable regimes, are observed for the first time. The poloidal and toroidal correlation lengths of the QM are one order of magnitude longer than those of the HFAT. The timescale ratio of the QM and HFAT is of the same order. The nonlinear three wave coupling between the QM and HFAT turbulence is identified with bi-coherence analysis to be a plausible generation mechanism for the former.

2. Transport Study

Without momentum input, a spontaneous and quasi-steady state particle transport barrier (PTB), coincident with a velocity shear layer, has been evidenced by particle perturbation study using modulated SMBI technique and microwave reflectometry measurement. It is found that there is a threshold in line-averaged density for the PTB formation in these experiments, typically $n_c = 2.2 \times 10^{19} m^{-3}$. The threshold could be correlated to the TEM/ITG transition via the collisionality. The barrier is located around $r/a=0.6-0.7$ with a width of 1-2 cm. The particle diffusivity and the convective velocity have been determined simultaneously by analysing the propagation of particle perturbation across the barrier. The particle diffusivity is rather well-like than step-like with significant reduction inside the barrier. The convection is inward outside the barrier and outward inside the barrier. The measurement results by Doppler reflectometry show that the drastic change of the rotation velocity in the barrier is related to the steepness of the density gradient in the barrier.

The non-local transport (NLT) effect with new features induced by SMBI fuelling has been investigated. The results show that the duration of core T_e rise can be prolonged by changing the SMBI modulation frequency, duty cycle and gas pressure. Both the bolometric radiation and the H_α emission decrease when the NLT occurs in low density discharges. At higher density, the core T_e decreases fast in response to SMBI edge cooling, which is in contrast to fast increase at lower density. The Fourier analysis of temperature perturbation induced by modulated SMBI indicates that, electron heat transport has the similarity of the non-locality under both lower and higher density conditions.

3. MHD control

ECRH/ECCD is used to provide active control of the local current profile and then MHD activity. Stabilization of $m/n=2/1$ tearing modes has been achieved by depositing ECRH/ECCD power in the vicinity of the $q=2$ surface, resulting in an obvious increase in plasma density and stored energy. Moreover, it is found that the suppression of $m/n=2/1$ tearing mode can be sustained by ECRH modulated with low frequency of about 10 Hz. Continuous confinement improvement is obtained after the mode suppression, i.e. the plasma density, temperature, stored energy increase steadily. This may provide a low cost, effective means of controlling $m/n=2/1$ tearing mode and improving confinement. In addition, effective destabilization of large sawtooth has been demonstrated by using ECCD near $q=1$ surface.

4. Electron Fishbone

Strong bursts of the internal kink mode excited by energetic electrons of non-Maxwellian distribution have been observed and investigated by 10-channel CdTe hard X-ray detectors. This electron fishbone instability is found to correlate with the existence of energetic electrons of 30-70keV and can be excited with ECRH at high or low field sides. The mode has obvious features of the fishbone structure, which is characterized by the frequency chirping, and amplitude bursting. The mode is located around the $q = 1$ surface with frequency of 4-8 kHz. It propagates in the precession direction of the deeply trapped ions toroidally and electron

diamagnetic drift direction poloidally. The instabilities disappear when line-averaged density exceeds $4 \times 10^{19} \text{ m}^{-3}$ or the ECRH power is higher than 900 kW. The experimental results are coincident with the resonance condition of the fishbone instability excited by suprathermal trapped electrons.

Acknowledgements

This work was also partially supported by the JSPS-CAS Core-University program in the field of ‘Plasma and Nuclear Fusion’

Current Ramp-up by Microwave Power in the LATE Device

MAEKAWA Takashi (前川孝), TANAKA Hitoshi(田中仁), and UCHIDA Masaki(打田正樹)

Graduate School of Energy Science, Kyoto University, Kyoto 606-8502, Japan

E-mail:maekawa@energy.kyoto-u.ac.jp

Abstract. In the Low Aspect ratio Torus Experiment (LATE) device, plasma current is initiated and ramped up to 20 kA solely by microwave power at the electron cyclotron (EC) range of frequency with a ramp of the external vertical field B_v for the radial equilibrium of plasma loop at larger currents. Measurements suggest that a fast electron tail in the energy range of ~ 200 keV carries the current. The line averaged electron density is higher than the plasma cutoff density, suggesting that tail electrons might be driven by electron Bernstein waves mode-converted from the incident electromagnetic waves.

Keywords: Current ramp-up, Microwave, Electron cyclotron range of frequency

PACS: 52.55.Fa

1. Introduction

Removal of central solenoid from the core of tokamak reactors is beneficial^[1]. Reactors would be reduced in size, simplified in structure and improved in plasma performance via reduction of the aspect ratio, and, therefore, the construction cost could be significantly reduced. Without the central solenoid alternative methods for plasma initiation and current start up are required. The EC heating (ECH) is potentially an attractive candidate for this purpose in reactors since the microwaves for ECH can be launched with a simple small launcher positioned remote from the plasma surface. The resonance electrons in usual ECH are heated, however, primarily in the perpendicular direction to the magnetic field and, therefore, usual ECH is not useful for the current ramp-up, where there arises counter voltage from the self induction of plasma current loop that retards the resonance electrons towards backwards. Although the resonance electrons in the lower hybrid current drive (LHCD) are accelerated forwardly along the field line and can overcome the retarding voltage, LHCD needs a large complicated launcher at the plasma surface. In these circumstances, it is notable that electron Bernstein (EB) waves, which is an electrostatic mode at EC range of frequency, can potentially have high N_{\parallel} (parallel refractive index to the field line) much larger than 1^[2]. EC current drive (ECCD) by using such high N_{\parallel} waves may drive the resonance electrons forwardly along the field^[3].

In the LATE device plasma current can be initiated and ramped up to 20 kA solely by a microwave power (5 GHz, ~ 200 kW, ~ 100 msec) with a ramp of the external vertical field B_v for the radial equilibrium of plasma loop at larger currents. Measurements and analyses show that a fast electron tail in the energy range of ~ 200 keV is developed and carries the current. Furthermore, the line averaged electron density is higher than the plasma cutoff density, suggesting that tail electrons might be driven by EB waves mode-converted from the incident electromagnetic waves.

2. Experimental Apparatus

LATE is a tiny device^[4, 5] with a vacuum chamber made of stainless steel in the shape of a cylinder

with the diameter of 1.0 m and the height of 1.0 m as shown in figure 1. The center post is a stainless steel cylinder with the outer diameter of 11.4 cm, enclosing 60 turns of conductors for the toroidal field. The return conductors are grouped into 6 limbs and go around far from the vacuum vessel, which allows good accessibility to the vacuum chamber and suppresses toroidal field ripple at a low level (1.5 % at R=50 cm and 0.07% at R=30 cm). There are four sets of poloidal field coils. One is for feedback control of vertical position of the plasma loop, and the rest are for the vertical field for equilibrium and their currents are preprogrammed. There is no central solenoid for inductive current drive.

Three 2.45 GHz magnetrons, including two 5 kW CW tubes and a 20 kW 2 seconds tube, and a 5 GHz klystrons (~200 kW, ~100 msec) are used for ECH/ECCD. In all cases, microwaves are injected from radial ports with injection angles slightly deviate (about 15 degrees) from normal to the toroidal field as shown to avoid the direct reflection to the launcher from the plasma cutoff layer and also to ensure the good coupling to EB mode via the OXB mode-conversion process.

3. Experimental Results and Discussions

Figure 2 (a) shows a typical discharge by a 5 GHz microwave pulse. Breakdown takes place immediately after microwave injection and plasma current initiates and jumps up quickly to $I_p = 6$ kA and an initial closed flux surface is spontaneously formed under a steady vertical field of $B_v = 55$ G^[6]. After the spontaneous formation I_p ramps up at a rate of ~100 kA/s in accordance with a ramp of B_v for equilibrium of plasma loop, and reaches $I_p = 12$ kA at the end of the microwave pulse of 60 ms. This current amount to 13% of total toroidal coil currents that flow through the central post, forming a spherical torus with an aspect ratio of 1.4 and an elongation of 2 solely by microwave power as shown figure 2 (b). The line averaged electron density ($n \sim 4 \times 10^{11} \text{ cm}^{-3}$) exceeds the plasma cutoff density at 5 GHz ($n_c = 3.1 \times 10^{11} \text{ cm}^{-3}$), suggesting that EB waves mode-converted from the incident electromagnetic waves heat the plasma and drive I_p .

The parallel electron drift velocity is estimated as $v_{||} = I_p / S n e \sim 2.5 \times 10^6 \text{ m/s}$ by using values of $I_p = 12$ kA, S (cross section of plasma) $\sim 0.1 \text{ m}^2$, and the above density. This is comparable to the bulk electron thermal velocity $v_{th} = (T_e/m)^{1/2} \sim 3.2 \times 10^6 \text{ m/s}$ at $T_e \sim 60 \text{ eV}$. It is noted that the bulk electron temperature is estimated below $\sim 100 \text{ eV}$ since the radiation profile shows that the plasma does not yet go through the radiation barrier. This result excludes the possibility that present current is a bootstrap current and suggests that it is carried by a supra-thermal electron tail.

The poloidal beta $\beta_p = 8\pi S \langle p \rangle / \mu_0 I_p^2$ estimated by magnetics is ~ 1.5 ; essentially due to these current carrying tail electrons. Contribution of bulk electrons is only ~ 0.05 as estimated from the bulk density and temperature $T_e \sim 60 \text{ eV}$. The tail pressure can be written as $p \sim n m v^2$ for the typical velocity v and the current density as $j = I_p / S \sim n_e v$. Then, the factor $C_f = I_p \beta_p / I_A = (2e/mc)(\langle p \rangle / j) \sim \gamma v / c$ is a measure of the tail momentum range, where $I_A = 4\pi m c / \mu_0 e = 17 \text{ kA}$. The tail energy range estimated from C_f at $I_p = 12 \text{ kA}$ is as large as $\sim 200 \text{ keV}$, which exceeds the runaway critical energy $\sim 7 \text{ keV}$ for the present reverse voltage of $V_L \sim -0.015 \text{ V}$. Production of such a high energy tail at the energy range far beyond the critical energy, where the reverse electric force is much larger than the collisional friction force, is essential for efficient current ramp-up. This was already realized for LHCD^[7, 8] but not for ECCD. In the present case this might be realized by the forward driving force on tail electrons via EC absorption of high $N_{||}$ EB waves.

The velocity distribution of current-carrying fast electron tail has been investigated for the 2.45 GHz discharges at $I_p = 8$ kA with the pulse lengths of 2 seconds, where X-ray pulse height analysis has

been carried out in addition to the magnetic analysis by taking advantage of relatively long pulse length, showing that the X-ray photons at the energy range beyond ~ 100 keV are, indeed, emitted from the plasma^[4, 5].

Recently attained values of I_p has increased up to $I_p = 20$ kA^[4] and are plotted versus B_v together with the previous data in figure 3. By shifting the 2nd EC resonance layer to the center of the vacuum chamber from the previous position of inboard side by increasing the toroidal field, I_p becomes larger and being again proportional to B_v . This means that equilibrium with a large last closed flux surface such as shown in figure 2(b) at $B_v \sim 110$ G is recovered again at a higher B_v of ~ 200 G. It may be due to the better coupling of mode-converted EB waves to the fast tail electrons that is expected when the first propagation band of EB waves between the fundamental and the 2nd harmonic EC resonance layers expands towards the center of vacuum chamber by the replacement of the ECR layer towards outward.

Summary

In the Low Aspect ratio Toru Experiment (LATE) device, plasma current is initiated and ramped up against the counter voltage from the self induction solely by a microwave power at the EC frequency range, and reaches $I_p = 20$ kA. Thus a torus is formed without central solenoid by ECH/ECCD. Measurements and analyses show that a fast electron tail in the energy range of ~ 200 keV carries the current. These tail electrons might be driven by high N_{\parallel} electron Bernstein waves mode-converted from the incident electromagnetic mode.

Acknowledgement-This work is partly supported by JSPS-CAS Core University Program in the field of Plasma and Nuclear Fusion

References

- [1] Nishio S, et al., 2004, Technological and Environmental Prospects of Low Aspect Ratio Tokamak Reactor VECTOR, Proc. of 20th Fusion Energy Conf., IAEA-CN-116/FT/P7-35, Vilamoura
- [2] Maekawa T et al., 2001, Phys. Rev. Lett., 86: 3783.
- [3] Maekawa T et al., 1993, Phys. Rev. Lett., 70: 2561.
- [4] Tanaka H et al., 2008, Non-Solenoidal Formation of Spherical Torus by ECH/ECCD in LATE, Proc. 22th IAEA Fusion Energy Conf. 2008, EX/P6-8, Geneva
- [5] Tanaka H et al., 2006, Spherical Tokamak Startup and Formation by ECH without Central Solenoid on LATE, Proc. 21th IAEA Fusion Energy Conf. 2008, EX/P6-6, Chengdu
- [6] Yoshinaga T, et al., 2006, Phys. Rev. Lett., 96: 125005.
- [7] Jobes F C et al., 1985, Phys. Rev. Lett., 55: 1285.
- [8] Ogura K et al., 1990, Nuclear Fusion, 30: 611.

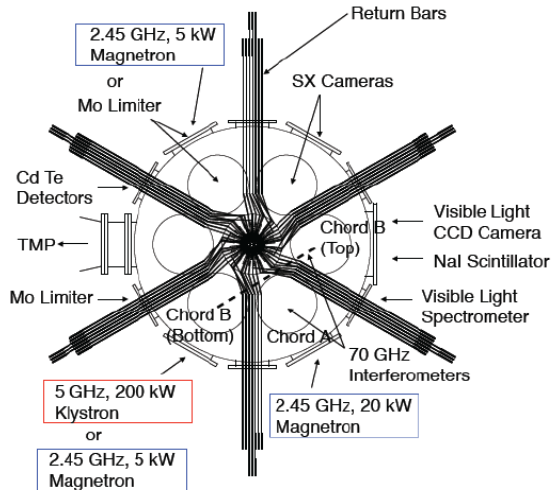


Figure 1 Top view of the LATE device

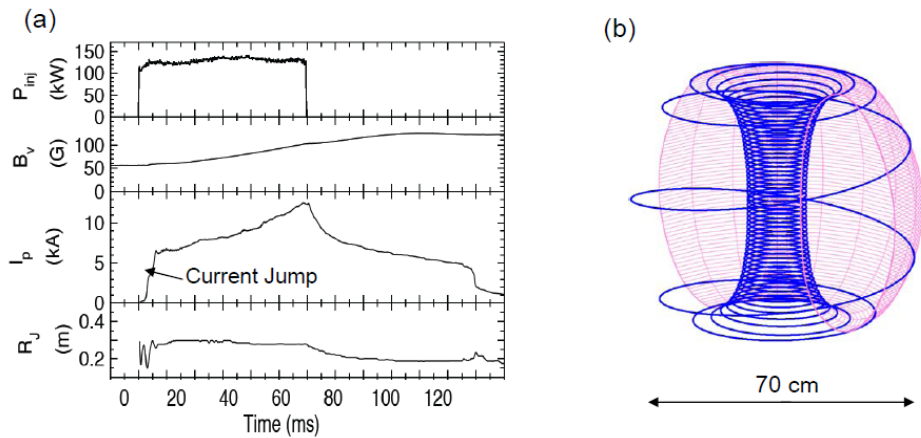


Figure 2. (a) Time trace of a 5 GHz discharge and (b) the field line on the last closed flux surface at the final stage of discharge. After the current jump under steady B_v the plasma current ramps up further by microwave power in accordance with a B_v ramp for equilibrium at larger current.

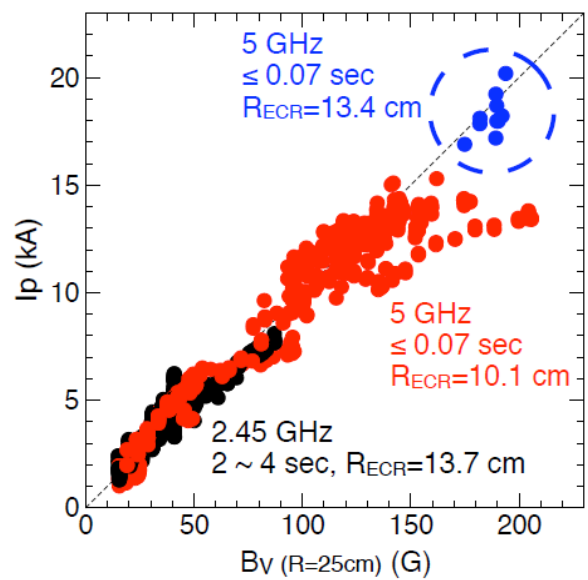


Figure 3. I_p (current just before the microwave turnoff) versus B_V

Research Activities and Plan of Electron Cyclotron Wave Startup and Alfven Wave Current Drive at SUNIST*

Zhe Gao (高喆),¹ Yexi He (何也熙),¹ **Yi Tan** (谭熠),¹ Wenhao Wang (王文浩),¹ Huiqiao Xie (谢会乔),¹ Lifeng Xie (解丽凤),¹ Long Zeng (曾龙),¹ Liang Zhang (张良),¹ Chunhuan Feng (冯春华),² Long Wang (王龙)² and Xuanzong Yang (杨宣宗)²

1) Department of Engineering Physics, Tsinghua University, Beijing, China

2) Institute of Physics, Chinese Academic of Science, Beijing, China

Electronic mail: tanyi@sunist.org

Abstract: Using electromagnetic waves to startup and sustain plasma current takes a important role in the research program of the SUNIST spherical tokamak. Electron cyclotron ware (ECW) current startup have been investigated and revealed two totally different regimes. In the regime of very low working pressure, a plasma current of about 2 kA is obtained with a steadily applied vertical field of 12 Gauss and 40 kW/2.45 GHz microwave injection. In addition, the physics of the transient process during ECW startup in the relatively high working pressure regime is analyzed. The hardware preparation for the experimental research of Alfven wave current drive is being performed. The Alfven wave antenna system consists of four models in toroidal direction and two antenna straps in poloidal direction for each module and the rf generator has been designed as a four-phase oscillator (4×100kW, 0.5~1Mhz).The impedance spectrum of the antenna system is roughly evaluated by 1-D cylindrical magneto-hydrodynamic calculation. To investigate the wave-plasma interaction in ECW startup and Alfven wave current drive, upgrade of the device, especially in equilibrium control and diagnostics, is ongoing.

1. Introduction

Non-inductive plasma startup and current drive are of great importance for spherical tokamak (ST), which is related its prospect in application of fusion plants. The SUNIST is a spherical tokamak with major/minor radius of 0.3m/0.23m, on-axis magnetic field of 1500Gauss and typical current of 30~50kA. Research activities at the SUNIST in recent years are concentrated on noninductive current startup and sustainment, especially in the range of high frequency electron cyclotron waves (ECWs) and that of low frequency Alfven waves (AWs).

ECW is utilized widely since its comprehensive abilities of plasma pre-ionization, startup and current drive [1-5]. It is also encouraging that ECW can be launched from a horn antenna remote from the plasma thus the deployment of ECW is very convenient. The preliminary experimental study of ECW startup at SUNIST [5] has shown a low efficiency. The spiky time trace of the driven current implied a bad coupling between microwave and plasmas. Here, the physics of the low efficiency is investigated and then the result of improved ECW startup is presented.

On the other limit, low frequency Alfven waves was considered as an attractive mechanism of driving plasma current because of its potential high efficiency, no density limit and the convenience of high power RF generating. [6] The difficulty due to high dielectric constants of ST plasmas is absent for Alfven waves. However, the trapping effect may dramatically decrease the

* This work is supported by the Major State Basic Research Development Program from MOST of China under Grant No. 2008CB717804, NSFC under Grant No. 10535020 , as well as the Foundation for the Author of National Excellent Doctoral Dissertation of PR China under Grant No. 200456.

current-driven (CD) efficiency. Ponderomotive force applied on bulk electrons provided by helicity injection was proposed [7]. However, this non-resonant drive force was theoretically proved to be canceled out when nonlinear stress forces were taken into account [8]. Although there were experiments [9,10] shown the CD efficiency is consistent with the Fisch-Carney theory,[6] both experiments are in the plateau regime, therefore, trapped electron effects cannot be verified. Spherical tokamak may be a good platform to study the behavior or contribution of trapped electrons in rf current drive. A preliminary plan of AWCD on the ETE device [11], in fact, has been proposed, but seems not to be actualized finally. Now, a research program on Alfvén wave current drive is ongoing at the SUNIST spherical tokamak. Experimental system preparation is being schemed. The Alfvén wave antenna system and the rf generator are preliminarily designed. The impedance spectrum of the antenna system is evaluated by 1-D cylindrical MHD calculation. To investigate the wave-plasma interaction in ECW startup and Alfvén wave current drive, upgrade of the device, especially in equilibrium control and diagnostics, is ongoing.

The paper is organized as follows. ECW current startup experimental results are presented in section 2 and the research plan of AWCD are presented in Section 3. Section 4 gives a brief introduction to the upgrade plan of the device and the present status.

2. Two different regimes of ECW current startup

2.1. Experimental setup

The experimental setup of ECW startup on SUNIST is shown in Fig. 1. The vacuum vessel of SUNIST consists of an inner cylinder and two semi spheres, which are electrically insulated from each other. The central solenoid is left open in order to avoid choking the toroidal plasma current. A microwave with 2.45 GHz, 100 kW, 10 ms is injected from the equatorial plane in the normal direction to the toroidal field with E field polarization parallel to toroidal field. The working gas, H₂, is puffed into the vessel through a piezo-valve installed on the top of vacuum chamber. Three pairs of vertical field (B_V) coils are connected in series thus the decay index of B_V is unchangeable. In our experiments, it is fixed to a quite small value (n~0.1 at R=50 cm). Main diagnostics in these experiments include one chord of 46 GHz (8 mm) microwave interferometer, 10 kfps fast visible light camera with the visual angle marked by dashed line in Figure 1(b), and a photodiode to pick up the overall light emission. The position of electron cyclotron resonance (ECR) layers are varied in the dashed region as shown in Fig. 1.

2.2. The high gas filling pressure regime

Only an unstable and small plasma current could be obtained in the experiments worked at a relatively high hydrogen gas pressure, P_{H2}=7x10⁻³~1.2x10⁻² Pa, with injected microwave power P_{inj} ~20 kW and a small vertical field BV ~14 G. [5] The waveforms of plasma current commonly consisted of a spiky head (<500 microseconds but up to 1 kA) and a quite low plateau (less than 300 A) in this high filling regime (Figure 2). The maximum attainable plasma current could not be further improved by increasing the power of microwave. Characters similar to that of plasma current are also found in the waveforms of the visible light emission and the line-averaged electron density. Typical waveforms of n_e is shown in Figure 3(a). Breakdown takes place at the beginning of discharge and n_e quickly rises to ~1x10¹⁷ m⁻³ exceeding the cut-off density of 2.45 GHz microwave, which is as low as 7x10¹⁶ m⁻³. In several hundred microseconds, however, n_e falls quickly forming the spiky head. The electron density at the plateau is about 5x10¹⁶ m⁻³ which is slightly lower than the cut-off density of the applied microwave. The time dependence of line

averaged electron density is quite similar to overall visible light emission, since both the ionization ratio and the electron temperature in this short term ECW driven plasmas are so low that the electron densities are roughly reflected by the intensity of visible light emission (mainly H alpha).

Figure 1. The experimental setup for ECW startup experiments on SUNIST: (a) Side view illustrating the radial positions of electron cyclotron resonance layers and the interferometer chord; (b) Top view showing the toroidal positions of main equipments and diagnostics.

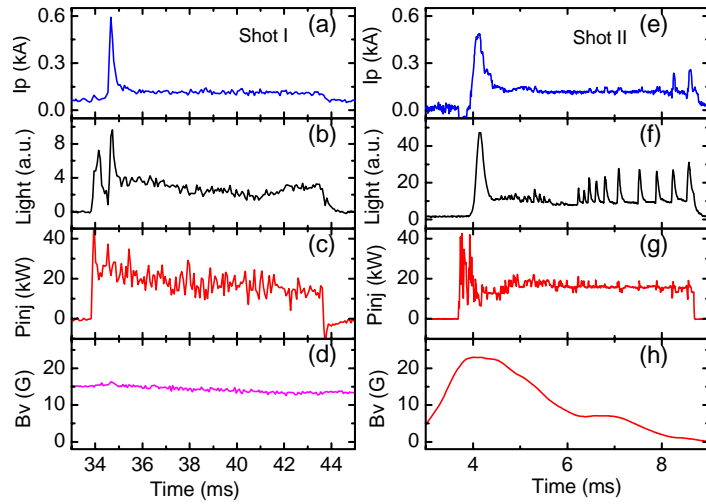


Figure 2. Waveforms of plasma current, (a) and (e), visible light emission, (b) and (f), power injection, (c) and (g), and vertical field, (d) and (h) for two shots in the high filling pressure regime ($P_{H2} \sim 7 \times 10^{-3}$ Pa).

Some properties of the spikes at the beginning of shots have been investigated by varying the position of ECR layer. A series of shots with the same experimental conditions except the ECR position is presented in Figure 4. From Figure 4 (b), we found the delay time is increased along with the distance between the launcher and ECR layer increases. This trend was supposed to be caused by the decreasing microwave power density. More interesting behaviors can be read from

Figure 4 (a). The slope of the traces of microwave reflection decreases when the distance between the launcher and ECR layer increases. But the eventual value of the microwave reflection are almost identical for different ECR positions. The characters of the microwave reflection imply a drift and/or diffusion process started from the ECR layer. Since the wavelength of the power microwave is large (about 12 cm in vacuum, $>a/2$ of SUNIST), the microwave will not be able to effectively heat the existing plasmas and ionize neutral gas until a layer of plasma with enough thickness (may be in the same order of the wavelength) near the ECR layer is formed. That's why the electron density at the beginning of discharge could exceeding two or three times larger than the cut off density of 2.45 GHz microwave. The spikes of electron density at the beginning of discharges have been widely observed in the experiments using low frequency ECW sources, such as LATE (2.45 GHz and 5 GHz), TST-2 (2.45 GHz), and CPD (8.2 GHz). However, the experiments using higher frequency power sources, e.g. WT-3 (40 GHz), CT-6B (20.1 GHz), JT-60U (60 GHz) are insulated with these spikes. The reflection ratio of the microwave, in addition, is sensitive to the position of the plasma layer that can effectively reflect the microwave. If the ECR layer in the inner region of vacuum vessel, it requires longer time to drift from the ECR layer to the position of microwave launcher. That's why the slope of microwave reflection is correlative to the position of ECR layer.

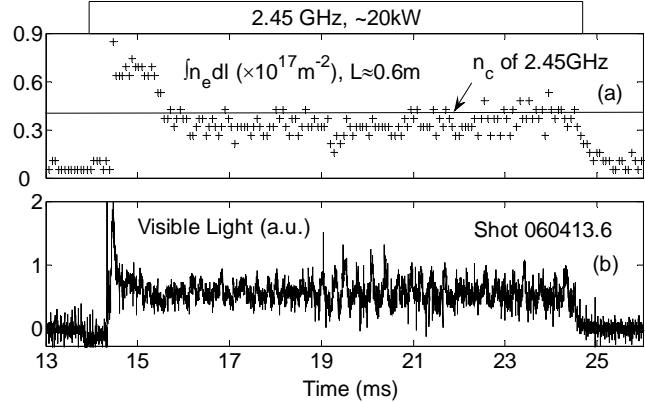


Figure 3. The traces of line averaged electron density (a) and visible light emission (b) of a high filling pressure shot.

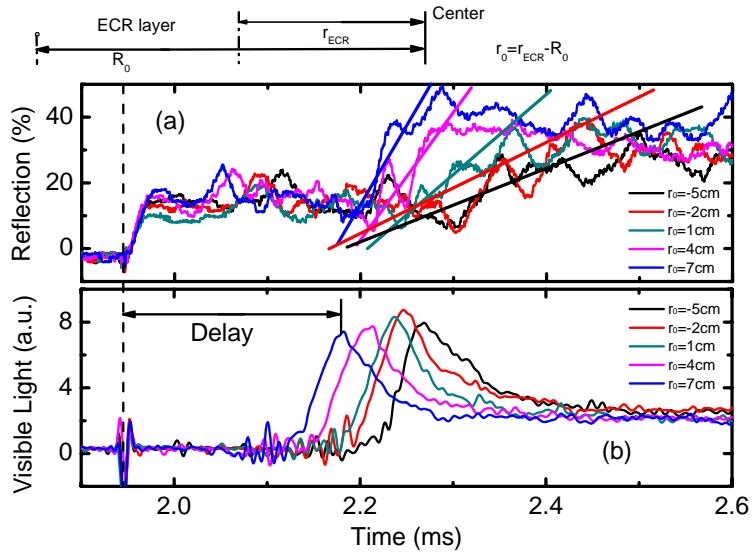


Figure 4. The traces of the microwave reflection ratio (a) and visible light emission (b) for a

series of high filling pressure shots with different ECR positions. The vertical dashed line indicates the beginning of microwave injection. The meaning of r_0 is illustrated at the top of the figure. The solid straight lines in (a) roughly denote the slope of the traces of microwave reflection having the same color.

The properties above requires a relatively high pressure of hydrogen that can be easily ionized. If the filling pressure is lowered to a very low level, these properties will be changed to a large extent.

2.3 The regime with gas filling pressure as low as 1×10^{-3} Pa

After extensive wall-conditioning, a typical discharge with relatively low gas filling pressure, $P_{H2} \sim 1 \times 10^{-3}$ Pa, is shown in Figure 5. From the visible light pictures, it can be noted that plasma is firstly generated near the fundamental ECR layer and hits the limiters at bottom and top along the field lines Figure 5(a) and (b). Then the plasma rapidly expands to a larger area Figure 5 (c) and (d) and generates a current peak. However, quite different from the high filling pressure discharge, neither visible light nor plasma current is attenuated too much in succession since microwave is not seriously blocked by the generated plasma. In fact, the reflection ratio ramps down dramatically when a substantial plasma current is generated. Plasma is more stable than in high filling pressure and almost constantly carrying a significant current ~ 2 kA in the remainder duration of microwave. All above suggest remarkable improvements on ECW coupling and current startup. In Figure 5 (e) and (f), it looks as if a closed field surface appears. The estimated poloidal field generated by plasma current (~ 15 Gauss) is bigger than the 12 Gauss externally applied vertical field. This also implies a closed field configuration. But it has not been confirmed yet by magnetic measurements since all magnetic probes are removed from the inside of vacuum vessel to prevent them from deteriorating the vacuum.

In the low filling pressure regime, no spikes in the trace of visible light emission was observed. Considering the correlation between the line-averaged electron density and visible light emission, we may conjecture that the spike in the electron density trace is also removed. That means the filling pressure in this regime is far from where ionization can quite easily occur. The longer delay time between the visible light emission and the onset of microwave reveals this too. But direct measurement of the electron density is still required to prove these conjectures.

Figure 6 shows these two different regimes: at high filling cases a low current follows a spiky head (discharge 071113.6 and 071113.10); and at low filling cases a high current follows a smooth head (discharge 071113.2 and 071113.3). The spiky head in the light signal can be served as a criterion for the operation regime.

In future studies of ECW startup, three approaches are planned. The first is still to precisely control the plasma density by wall conditioning and gas puffing control, but the most important is to measure the density and investigate its dependence on the discharge condition. The second is to increase the frequency and the duration time of the microwave source, which will be carried out once the budget for this purchasing is approved. The other is to modify the launcher from normal injection to oblique injection, which will increase not only the coupling of ECR to plasmas but also the possibility of the conversion to EBWs. A new launcher has been designed to increase the flexibility for the radial position of the launching face.

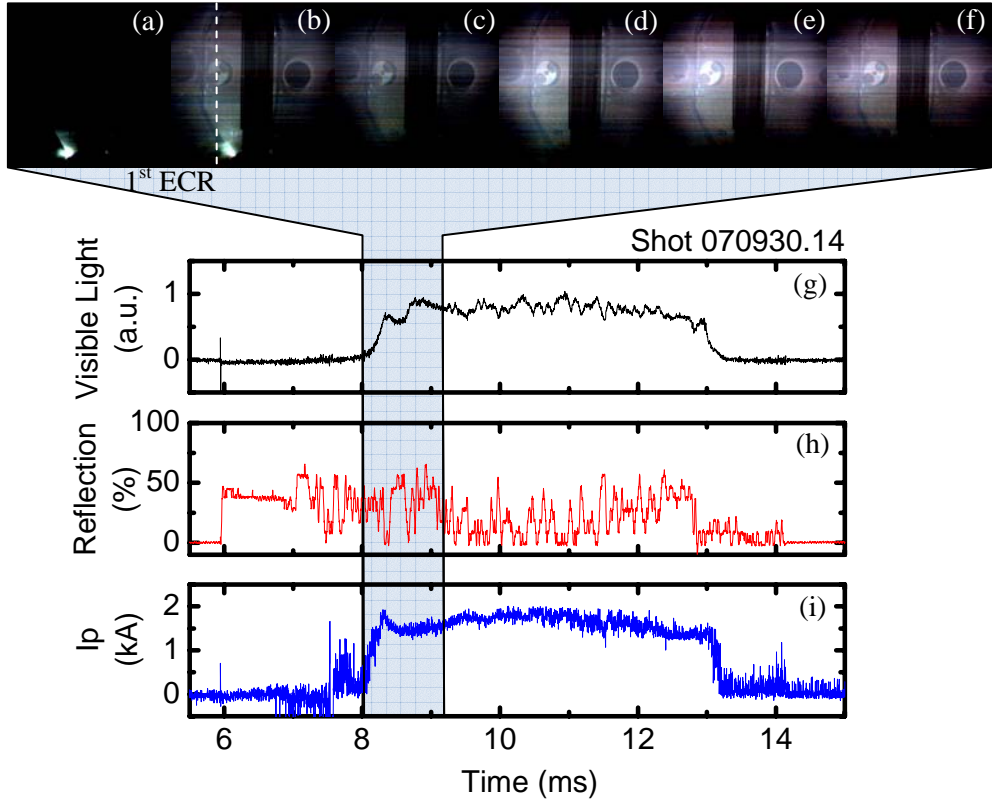


Figure 5. Pictures of visible light (a) ~ (f) and dependence of overall visible light emission (g), microwave reflection (h) and plasma current (i) on time in a typical discharge with filling pressure $P_{H_2} \sim 1 \times 10^{-3}$ Pa, vertical field $B_V \sim 12$ Gauss and microwave power ~ 40 kW. The pictures are taken with intervals of 0.2 ms.

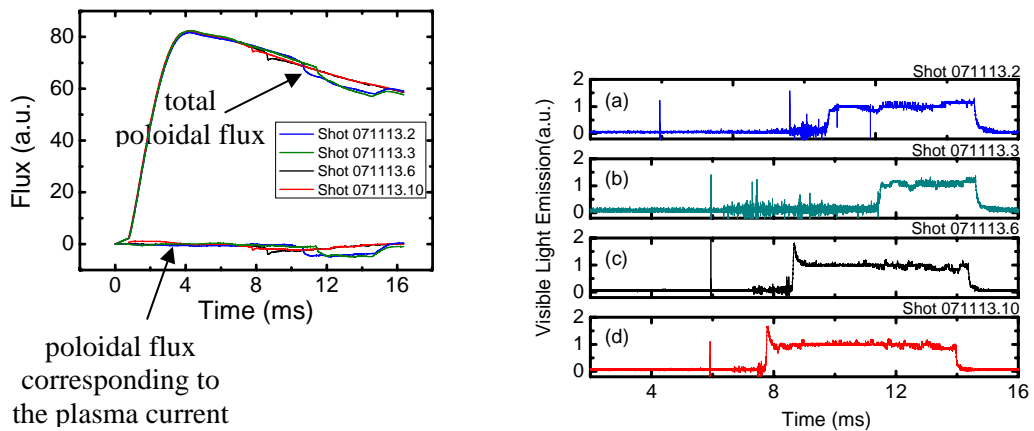


Figure 6. Comparing several shots in the two operation regimes. Shot 071113.2 and 071113.3: low filling pressure; Shot 071113.6 and 071113.10: high filling pressure.

3. Research plan of Alfvén wave current drive

3.1. Estimation of zones of Alfvén resonance and the impedances of the antenna

The zones of Alfvén resonance and the impedances of the antenna are analyzed in a simple 1-D MHD model. This model consists of a plasma cylinder, two sheathes carrying opposing current (the

folded antenna), and a metal cylinder wall (the wall of the vacuum vessel). S. Cuperman et al. have completed a series of numerical research [12-14] on Alfvén wave characters in ST plasmas and have found that the results varied by the shaping effects (in the range of $1.1 < A = R/a < 10$) is in the same order. Then, although this model is far different from the actual shape of a ST plasma, it is enough for us to do the analysis.

The dependences of impedances and resonant positions on frequency for $|N|=1$ modes and $|N|=2$ modes are shown in Figure 7. To obtain a higher efficiency (higher impedance), higher frequencies are needed. Higher frequencies, however, make Alfvén resonance move to the edge of the plasma column, which is not favorable for power deposition. Therefore, the frequency should be carefully chosen during experiments.

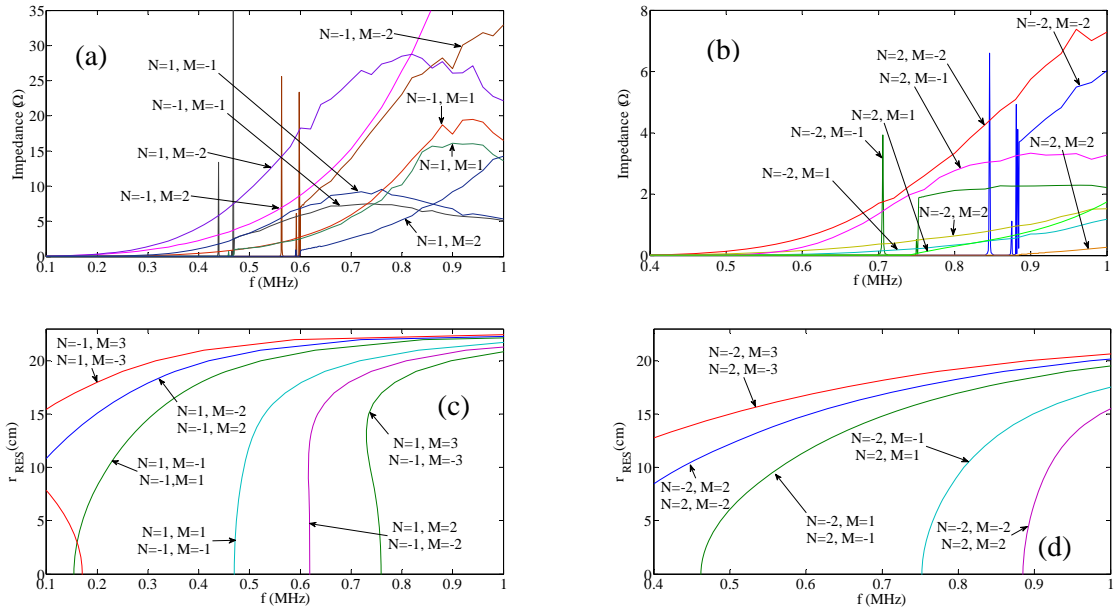


Figure 7. The dependences of impedances and resonant positions on frequency for $|N|=1$ modes (a and c) and $|N|=2$ modes (b and d).

3.2. The rf generator

As for the rf generator, we referenced to the design for the TCABR by Ruchko[15]. A four phase oscillator is designed, where each can deliver a 90 degree phase shift from its neighboring module and this phase shift between outputs does not depend on the variation of the antenna impedance. Therefore, the RF generator can deliver two possible phase shift, 90 degree or 180 degree, to nearby straps in either toroidal or poloidal direction. For experiments at the SUNIST, a rf generator with the power of 4×100 kW and the working frequency of $0.4 \sim 1$ MHz has been manufactured. Each separated module and the total integrated system has been tested.

3.3. Antenna system

The main task of the antenna in AWCD experiments is to excite a perturbation of magnetic field parallel to the equilibrium magnetic field with required spatial structures (called modes) in the plasma column. Typically, it is achieved by assembling poloidal current carrying loops surrounding the plasma column. However, loops with fully extension in poloidal direction cannot be implemented in STs because of the very tight configuration of central region. Then, according to the design of rf generator and referring to the design for the ETE [11], the antenna system consists of four modules in toroidal direction and two antenna straps in poloidal direction for each

module, which is shown in Figure 8. The reason of using this folded strap structure is considering the convenience in connecting to RF generator and less occupancies of windows (only 4 windows) although the impedance will decrease a lot.

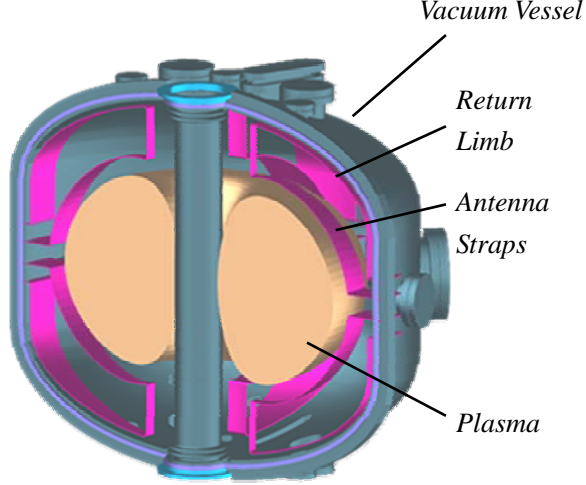


Figure 8. The concept design of the Alfvén wave antenna in the SUNIST device

The effect of the radial positions of the return limb and wall on the antenna's impedance is also studied. It is obvious that the coupling between antenna and plasmas is weakened when the return limb approaches the antenna strap. In our folded model, this effect is linear to all modes. For example, in the configuration of the radial position of return limb equals to 1.15 times of the radius of plasma column, the impedances of folded antenna decrease to about 27% of unfolded antenna's. That means we should bear an impedance loss of ~70% if the folded model is chosen to be manufactured. The detail of Alfvén wave antenna design can be seen in our recent paper.[16]

3.4. Engineering design and antenna shielding

We have mentioned in Sec. 3.3, we choose the folded structure since it occupies less windows than the unfolded structure, where twelve windows should be occupied. Besides this point, the engineering design of the antenna system follows the guideline below. Firstly, the return limb should be positioned as close as possible to the wall of vacuum vessel for improving coupling efficiency so the shape of the return limb and the antenna strap are simply defined by offsetting the shape of vacuum vessel and last closed flux surface of plasma column respectively. These shapes would have the most efficient utilization of limited space. Secondly, the width of the antenna strap is limited by the diameter of windows and the poloidal extension angle is reduced to avoid enveloping other diagnostic windows.

Figure 9 shows the engineering design of one strap of one module of the antenna system. Both return limb and antenna strap are made of 1 mm thick stainless steel. Two insulated bolts fix the antenna structure to the vacuum vessel. Two BN side limiters, which have been proven to have the ability of reducing edge power deposition [17], are installed directly on the antenna strap. The antenna is connected with RF generator by ceramic feeder through.

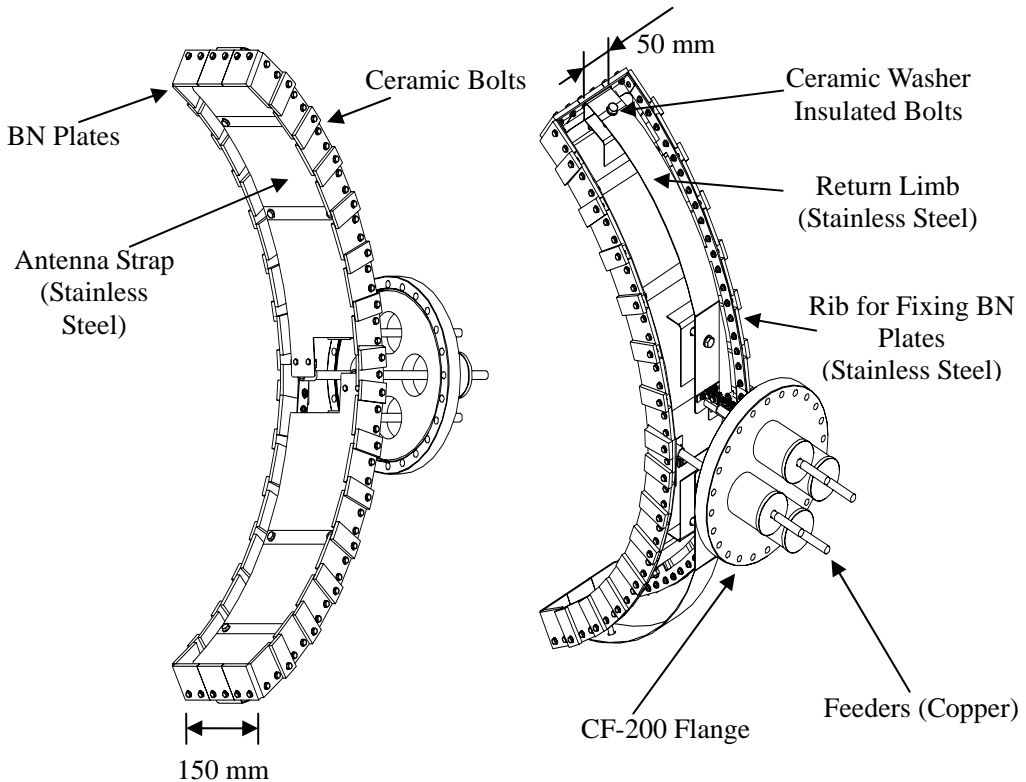


Figure 9. The engineering design of the Alfvén wave antenna in the SUNIST device

4. Upgrade of the SUNIST device

To investigate the wave-plasma interaction in ECR startup and Alfvén wave current drive, upgrade of the diagnostic system has been ongoing. A new well-shield magnetic probe system has been designed and manufactured to reconstruct equilibrium and to measure the excited mode. Microwave reflectometer and interferometer have been imported and soon installed to measure the density and its fluctuation. Microwave radiometer and Soft-X array have also been purchased and ICCD spectrometer is being purchasing for measuring electron temperature. Typical electrostatic probes will be designed to measure the flow and the density and potential fluctuation. To improve the control power of equilibrium field, a set of capacitor bank with 1200V and 270mF is being planned and an IGBT-based control scheme has been investigated preliminarily. In addition, a new manhole window is opened for convenience of in-vessel components installing and servicing. At present, the SUNIST device is decomposed to install the AW antenna and new diagnostic systems and to open a new window in vessel. It is expected to be re-assembled and start the experiment before November this year.

Acknowledgments: This work is supported by the Major State Basic Research Development Program of China (973 Program) under Grant No. 2008CB717804, the Foundation for the Author of National Excellent Doctoral Dissertation of China under Grant No. 200456 and the National Science Foundation of China under Grants No. 10405014, as well as the IAEA CRP on Joint research using Small Tokamaks.

References

- [1] Forest, C.B., et al., Phys. Rev. Letts., **68**(1992) 3559.
- [2] Ejiri, A., et al., Nucl. Fusion, **46**(2006)709.
- [3] Takase, Y., et al., Nucl. Fusion, **41**(2001) 1543.
- [4] Maekawa, T. ,et al., Plasma Sci. Tech., **8**(2006) 95.
- [5] He, Y., et al., Plasma Sci. Tech., **8**(2006) 84.
- [6] Fisch, N.J. and Karney, C.F.F., Phys. Fluids, **24**(1981) 27.
- [7] Ohkawa, T., Comments on Plasma Phys. and Control. Fusion, **12**(1989)165.
- [8] Gao, Z., Fisch, N.J. and Qin, H., Phys. Plasmas, **13**(2006) 112307.
- [9] Wukitch, S.,et al., Phys. Rev. Letts., **74**(1995) 2240.
- [10] Ruchko, L.F., et al., Bra. J. Phys., **32**(2002) 57.
- [11] Ruchko, L.F. and Galvao, R.M.O. , Bra. J. Phys., **34**(2004) 1722.
- [12] Cuperman, S., et al., Journal of Plasma Physics, **59**(1998) 461-498.
- [13] Cuperman, S., et al., Physics Letters A, **362**(2007) 305-323.
- [14] Cuperman, S., et al., Journal of Plasma Physics, **69**(2003) 15-43.
- [15] Ruchko, L.F.,et al., Fusion Eng. Design **43**(1998) 15.
- [16] Tan, Y., Gao, Z. and He Y., Fusion Eng. Design 2009, in press.
- [17] Sorensen, J., et al., Nucl. Fusion, **36**(1996)173.

Reconstruction of the TEXT-U tokamak in China

Zhuang Ge (庄革), **Ding Yonghua** (丁永华)^{*}, Zhang Ming (张明), Yu Kexun (于克训), Zhang Xiaoqing (张晓卿), Wang Zhijiang (王之江), Hu Xiwei (胡希伟), Pan Yuan (潘垣) and J-TEXT team

CEEE, Huazhong University of Science and Technology, Wuhan 430074, China

E-mail address of Ding Yonghua: yhding@mail.hust.edu.cn

Abstract:

The Joint TEXT (J-TEXT) tokamak, formerly named as the TEXT/TEXT-U tokamak, operated by the University of Texas at Austin in USA, has been reconstructed in Huazhong University of Science and Technology in China. The machine has been run for two experimental campaigns since 2007. And the discharges with plasma current more than 200 kA and duration of 300 ms have been obtained. At present all sub-systems, such as PF & TF power supplies, vacuum system, diagnostics systems etc, are successfully integrated into the routine operation. The plasma position can be elaborately controlled within two centimeters. All operating behavior and limits of the J-TEXT tokamak are typical of the machine and easy understandable compared to the former TEXT/TEXT-U experimental results.

Keywords: tokamak, J-TEXT, reconstruction

PACS:52.55.Fa

1. Introduction

The Joint Texas Experimental Tokamak (J-TEXT), formerly named as the TEXT-U tokamak, is a medium-sized conventional tokamak with iron core which is shown in figure 1. A typical section through a box is shown in figure 2. It was built and operated by the University of Texas at Austin and was specially designed for good experimental access and routine operation in 1980s. In 1990, the TEXT tokamak was upgraded to TEXT-U in attempt to obtain a H-mode confined plasma by adding ECRH power to a divertor plasma. [1] According to the agreement of UT Austin and Huazhong University of Science and Technology (HUST), the whole facility was moved to China in 2004 and renamed to Joint TEXT (J-TEXT) tokamak. The Joint TEXT Lab was established to cultivate fusion engineers and do some basal physical study such as disruption. The laboratory is open to world-wide fusion researchers and J-TEXT machine can serve as the complementary and pre-experimental device for large-size tokamaks in the future.

2. The structure of J-TEXT

The main parameters of J-TEXT are as follow: a major radius of 105 cm, a minor radius of 25~29 cm with a movable limiter configuration, a center-line toroidal field of 3 Tesla. The nominal plasma current can reach 400 kA and the firing period is about 2 minutes.

The tokamak facility consists of vacuum chamber and pumping system, various magnetic field coils and their power supplies, gas puffing system, diagnostic systems, data acquisition (DAQ) and data management system, etc, here are the details.

For the purpose of easily mounting, the vacuum vessel of J-TEXT tokamak can be parted and insulating rejoined in halves by two keystone sections at each end. Each part of the vessel has a single-walled frame welded by entirely stainless steel with seven sections and no insulating break. All port seals are metal, indium-coated copper wire but a few special ones with fluorine rubber O-rings. There have some TIC coated graphite tiles used to cover most of the inner wall surface. The vessel has a total volume of 3.25 m³ and its surface area is about 18 m². Due to the sealing materials, the design bake-out temperature is limited to 100°C.

The vessel is pumped by two turbomolecular pumps and two cryo-torr vacuum pumps with isolation valves and filled by gas supplies controlled with piezo-electric valves for rapid modulation. In addition to normal gauging, a residual gas analyzer is provided for monitoring vacuum cleanliness. Tailor discharge cleaning is provided by a 400 Hz generator. [2]

The toroidal field magnet of this machine consists of 16 near-round shape copper coils segments interlinked in series with 6 turns in per segment. Torodial field power supply fed by 100MW pulsed flywheel motor-generator have the ability to provide 500ms, 160kA flat current in torodial field magnet coils, hence the coils can produce a maximum toroidal field of 3T in the centre of the plasma. Refering to the original structure of TEXT-U TF power supply, we reform a new control and protection system for the grid difference between China and USA. [3]

The ohmic heating system relies on an iron-core transformer with two return legs and provides 1.6 V-sec. without saturation. The ohmic heating (OH) coil is 40 turns and galvanized by grid of 380V, capacitor banks, OH rectifier in sequence. OH rectifier is charged by 100MW pulsed flywheel motor-generator too and consumes about 2% of total energy in general.[4]

The plasma equilibrium is provided by auxiliary fields composed of 16-turn vertical field (VF) coil and 32-turn horizontal field (HF) coil. Each coils is electrified by the power grid of 380V via dissimilar distribution modes. These two field is comparitively small to TF and OH fields which is about 1% of the latter.

Nowdays J-TEXT diagnostics tools are simple and operated exclusively by the staff as a fixed reference for the success of discharge, It includes Plasma current, Loop voltage, Plasma position, ionization monitor, Hard x-ray monitor, Residual gas analyzer, plasma visible light CCD imaging system and results are recorded in the data log whenever the device is operating. Other diagnostic tools will be developed for individual experiments. The ongoing projects covers MHD coil arrays, Langmuir probes arrays, X-ray diodes, bolometer array, etc, which will offer windows for the observation of more subtle process in tokamak plasma and assist us catch on the essence of MHD, turbulence and other impalpable topic.

J-TEXT data acquisition system (DAQ) is designed for the acquisition, storage, and analysis of experimental data. The system is constructed on C/S (Client / Server) model via the physical media of high-speed Ethernet and the sample rate is 500 kHz now with 16bits in accuracy. All data is stored in MdsPlus and it affords good service with the stable and reliable operation plus

flexible data access. DAQ is proved to satisfy the demand of the J-TEXT. [5]

Central control system (CCS) of J-TEXT is the brain of the organism and is most important in J-TEXT framework. It is a multi-mission system that can function as a supervisor, operation pilot, data manager, etc to pilot J-TEXT behaviour in each period. There are three major aspects highlighted for the CCS system: integrate subsystems for the discharge operation, respond to emergencies and implement experimental scenarios by real-time feedback control, and each is achieved by basic functions such as timing sequence control, status cruise, safety control, discharge waveforms design and Post-shot service. The CCS contains two datalinks consisting of Ethernet and Point to Point (P to P) twisted pair to improve the system safety. In the routine life of J-TEXT, the CCS works well and sustains the progress of forthcoming research project.[6]

3. The experiment result

After years of hard work, the J-TEXT was reconstructed and all subsystem was adjusted to their optimal work condition. To vacuum system, with one week of cleaning discharge, the base pressure can reach 7.6×10^{-6} Pa and the partial pressure of gases except hydrogen is less the 5×10^{-6} Pa. The mass spectra of the residual gases in the vacuum chamber before and after Taylor discharge cleaning was shown in Fig.3. It dictates the main contaminates are water and N2 or CO (mass 28) in J-TEXT and the percentage of water can decrease from 90% to 45 % with heating bellows to nearly 100°C by cleaning.

TF coils and the power supply is another system that needs to examination. For the progress of technologies, we replaced the modulation part of the power supply with digital components instead of ancient analog module and the change of grid frequency to 50Hz (60Hz in USA) constitutes other reasons for system updating. Fig. 4 is the current waveform of the TF coils, the current platform up to 100kA is obtained and the flat time is longer than 500ms. With some simple calculation, the toroidal magnetic field was up to 2 Tesla, which is sufficient for the generation of first plasma. The 100MW motor-generator double-fed varying speed system is on schedule and will exploit the potential of the power supply with maximal TF to 3 Tesla.

Comparing to TF, the OH power supply is much complex for the function as plasma generation, plasma current formation plus Ohmic heating. To increase Volt-seconds, the OH coils is electrified with -100A by grid and a negative voltage of -25V is formed 100ms before discharge. The capacitor bank for ionization fired at time $t=0$ ms with $V=1300$ V and the filling gas stream into plasma by Townsend discharge. Capacitor bank C1 to C3 works one by one which corresponding to the latter 3 peaks in OH voltage form and the pour into the energy to lift plasma current. At time $t=60$ ms, the energy in the Capacitor bank is released and the voltage drops sharply to 300V which is below the rectified voltage, then OH rectifier induces the energy from motor-generator to maintain the current. When $t=400$ ms comes, the main process of tokamak discharge is completed, we invert the working phase of converters to reduce the current and release the energy of the TF coils in order to protect the TF power supply and the coils. The evolvement of the OH current also reflect the course of the OH power supply with the -100A reversed current, ramp-up to 4kA and the sudden fall after inversion. Fig 5 give the evolution of current and voltage added to the OH field coils.

Like all present conventional tokamaks, J-TEXT depends on OH field to produce first plasma.

The better discharge and the typical waveform are displayed by figure 6. At the shot the toroidal field is 1.5T and the gas filling pressure is 0.02Pa. The rate of plasma current rise is 6kA/ms, the plasma current is more than 150 kA ($q \sim 3.5$) and the duration is more than 400 ms. The plasma loop voltage (V_{loop}) decrease from the peak 35V to less than 2V. The H_{α} is the most distinctive sign of breakdown and its spike clearly indicates the breakdown. The operating behavior and limits are understandable and typical of the machine.

4. Summary

J-TEXT has been successfully commissioned as an operating fusion plasma experiment. All engineering systems are working to rated capacity under the control of the central control system after 1400 shots test. The device is producing tokamak discharges as it did formerly and the operating behavior and limits are understandable and typical. It now runs with more than 150 kA plasma current ($q \sim 3.5$) and a duration of 400 ms. All data is archived and available in the standard MdsPlus format, like the operation of other modern tokamaks. With the reinforcement of planned diagnostics, the machine will be fully capable of productive research.

5. Acknowledgements

The authors are grateful to the help from the Southwestern Institute of Physics and the Institute of Plasma Physics, Chinese Academy of Science. This work is supported national 973 project of China (No 2008CB717805). This work was partially supported by the JSPS-CAS Core-University program in the field of 'Plasma and Nuclear Fusion'.

References

- 1) Text User Handbook, Fusion Research Center in The University of Texas at Austin, 1989
- 2) Ding Yonghua, Zhuang Ge, Wang Weijun et al Vacuum system of J-TEXT.(in submiting)
- 3) Zhang Ming. 2005, Simulation and Applicaton of Interlligent PID Control. [PHD Thesis]. Wuhan: Huazhong University of Science & Technolgy (in chinese)
- 4) Zhang Ming, Zhuang Ge, Yu Kexun et al The power supply system for the J-TEXT poloidal field, Plasma Science and Technology, (in press)
- 5) Zhoujun Yang, Ge Zhuang, Xiwei HU et al Design and realization of the J-TEXT tokamak central control system (in submiting)
- 6) Hong Zelong, Zhuang Ge, Qu Lianzhen et al MARINE ELECTRIC & ELECTRONIC TECHNOLOGY, VOL27, NO2

Figures



Fig.1 J-TEXT bird-view

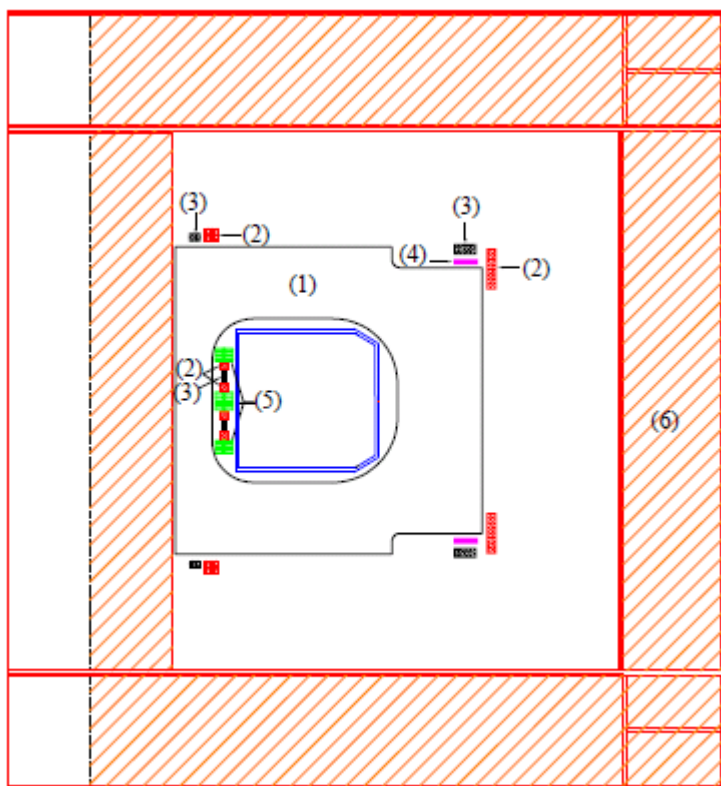


Fig.2. A typical section through a box.

- (1)TF Coil (2) OH Coil (3) VF Coil
- (4) HF Coil (5) DIV Coil (6) Iron Core

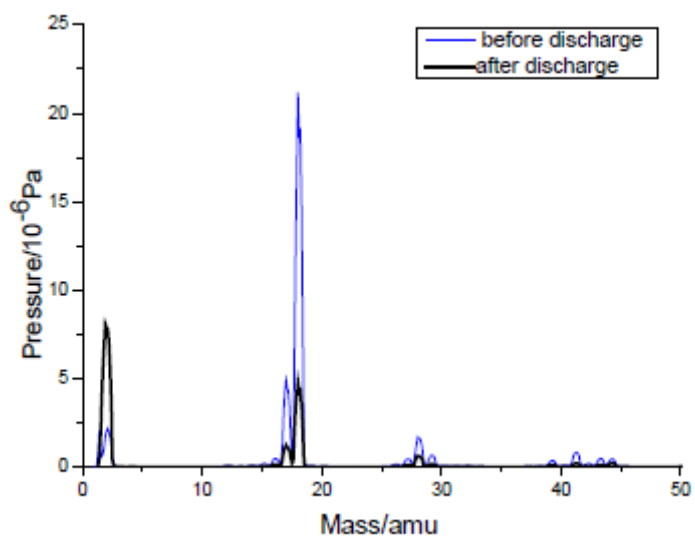


Fig.3. Mass spectrometer before and after Tarlordischarge cleaning

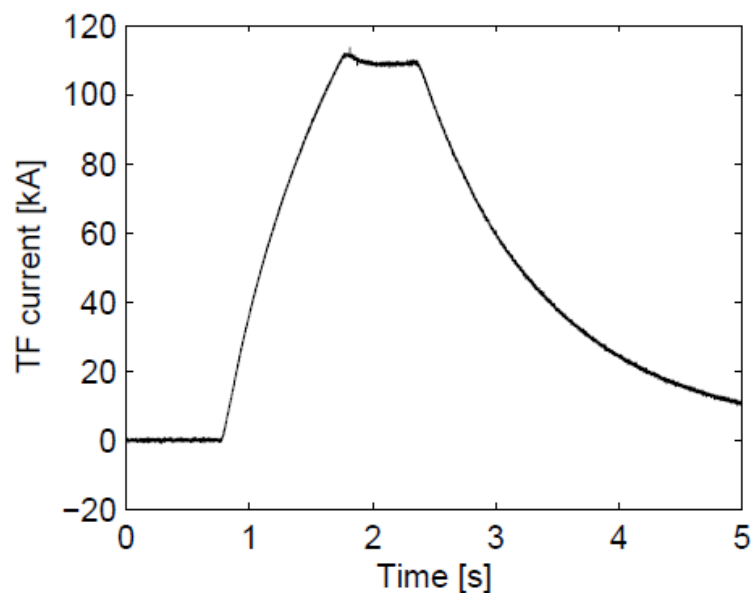


Fig.4. The waveform of TF coil current

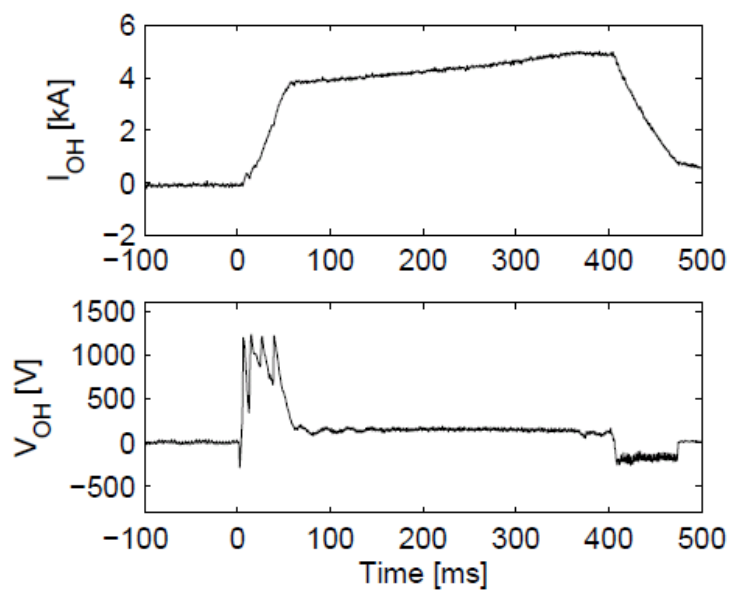


Fig.5. The waveform of OH current and voltage

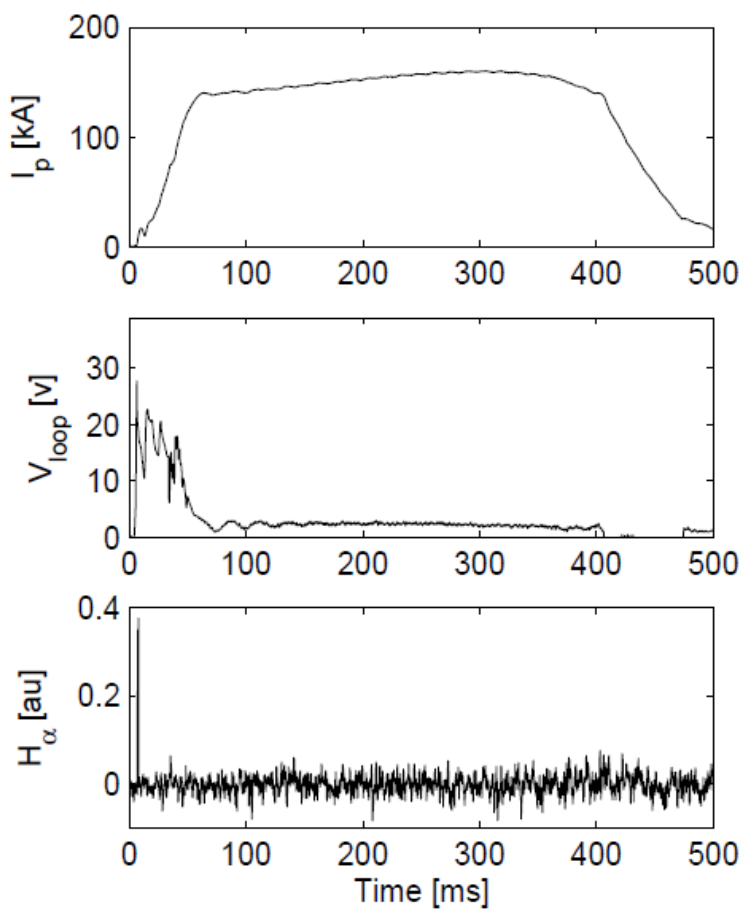


Fig.6. A typical OH discharge on J-TEXT tokamak

Contribution of the Large Helical Device Plasmas to Alfvén Eigenmode Physics in Toroidal Plasmas

K. Toi[#], M. Isobe, M. Osakabe, F. Watanabe*, K. Ogawa*, T. Tokuzawa, A. Shimizu, T. Ido,
K. Ida, T. Ito*, S. Morita, K. Nagaoka, K. Narihara, M. Nishiura, S. Ohdachi,
S. Sakakibara, K. Tanaka and LHD Experimental Group

National Institute for Fusion Science, Toki, Japan

*Department of Energy Engineering and Science, Nagoya Univ., Nagoya, Japan

[#]E-mail address: toi@lhd.nifs.ac.jp

Abstract

In the Large Helical Device (LHD) having three dimensional configuration, Alfvén eigenmodes (AEs) destabilized by energetic ions are widely investigated using plasmas with monotonic and non-monotonic rotational transform ($\iota/2\pi$) profiles. In a plasma with monotonic $\iota/2\pi$ -profile, core-localized toroidicity-induced Alfvén eigenmode (TAE) as well as global one are often observed. With the increase in the averaged toroidal beta value (=total plasma pressure/toroidal magnetic pressure), core-localized TAE with low toroidal mode number becomes global type but usually consists of two dominant Fourier modes. In a relatively high beta plasma with monotonic $\iota/2\pi$ -profile, two TAEs with different toroidal mode number often interact nonlinearly and generate another modes through three wave coupling. In a plasma with non-monotonic $\iota/2\pi$ -profile produced by intense counter neutral beam current drive, reversed shear Alfvén eigenmode (RSAE) and geodesic acoustic mode (GAM) excited by energetic ions have been observed for the first time in a helical plasma. Nonlinear coupling has also been observed between RSAE and GAM.

Key words: alpha particles, Alfvén eigenmodes, TAE, GAM, nonlinear coupling,
helical/stellarator, tokamak

PACS : 52.35.Bj, 52.55.Pi, 52.55.Tn, 52.55.Hc, 52.55.Fa

1. Introduction

In a burning plasma, alpha particles play an essential role in sustaining D-T burn. However, there is a concern that energetic alphas would destabilize Alfvén eigenmodes, in particular, toroidicity induced Alfvén eigenmode (TAE) and, in turn, they enhance radial transport of energetic alphas and lead to damage of plasma facing components. Accordingly, Alfvén eigenmodes excited by energetic ions are intensively investigated in many large tokamaks toward International Thermonuclear Experimental Reactor (ITER) [1]. This research is also important for helical/stellarator devices to investigate impacts of AEs in three dimensional plasmas [2-4]. In a two dimensional magnetic configuration such as tokamak, poloidal mode coupling among shear Alfvén continua having different poloidal mode number m generates various spectral gaps. TAE has lower gap frequency and is thought to be more dangerous for confinement of energetic ions. Many experiments on AEs in tokamaks are addressed to TAEs and their impacts on energetic ion transport. On the other hand, in a helical/stellarator plasma, toroidal mode coupling as well as poloidal mode coupling are possible. In this three dimensional configuration, Fourier components with n' which satisfy the relation $n \pm n' = kN$ can interact with the Fourier mode with the toroidal mode number n , where $k=0, \pm 1, \pm 2, \pm 3, \dots$ and N is the toroidal field period number. However, toroidal mode coupling is very small for low n TAE in a helical plasma with large N such as CHS ($N=8$) [3] and LHD ($N=10$) [5]. That is, TAEs in CHS and LHD have almost same character of TAEs in tokamaks. The LHD can contribute to comprehensive understanding of AE physics in toroidal plasmas. This paper presents new results on AEs observed in LHD plasmas with two characteristic $\nu/2\pi$ -profiles.

2. Energetic-ion driven MHD modes in a plasma with monotonic $\nu/2\pi$ -profile

A core-localized TAE as well as a global TAE can be excited in a tokamak plasma with monotonic safety factor ($q=2\pi/\iota$) profile. The eigenfunction of the former is localized in the plasma core region and is composed basically by two Fourier modes [6]. If the TAE gaps are well aligned across the plasma minor radius, the latter TAE is most typically excited having an eigenfunction radially extended from the core to the plasma peripheral region. The latter TAE is thought to induce appreciable loss and spatial redistribution of energetic ions. The former core-localized TAE often induces redistribution of energetic ions in spite of no significant energetic ion loss.

In a low beta LHD plasma, the TAE gap frequency increases toward the plasma edge, because the $\nu/2\pi$ -profile is a monotonically increasing function of the minor radius. Accordingly, a core-localized TAE is most likely excited without large continuum damping in such LHD plasma. Actually, core-localized TAE as well as global TAE were observed in CHS [3, 7] and LHD [5]. With the increase in the averaged toroidal beta (=total plasma pressure/toroidal magnetic pressure),

core-localized TAE with low n becomes global type but usually consists of two dominant Fourier modes. A typical discharge waveform of a relatively high beta plasma where AEs are strongly excited is shown in Fig.1(a). The magnetic configuration of LHD always exhibits large Shafranov shift even in the range of $\sim 1.5\%$ averaged toroidal beta, as seen from an electron temperature profile measured with Thomson scattering (Fig.1(b)). In the quasi-stationary phase ($t \sim 2.5$ s), two TAEs having $n=1$ ($=n_1$; $f_1=58$ kHz) and $n=2$ ($=n_2$; $f_2=99$ kHz) have been clearly detected, as shown in Fig.2. Interestingly, these TAEs interact nonlinearly and generate other two global modes with $n=3$ ($=n_1+n_2$) ($f_{31}=f_2+f_1=157$ kHz) and $n=1$ ($=n_2-n_1$) ($f_{32}=f_2-f_1=41$ kHz). Selection rules for toroidal wave number and frequency are satisfied exactly for these modes. Large Shafranov shift will enhance the nonlinear mode coupling.

3. Energetic ion driven MHD modes in a reversed magnetic shear plasma

A reversed magnetic shear (RS) tokamak has received much attention, because this configuration is one of promising candidate operation scenarios for ITER. Moreover, an interesting AE: reversed shear Alfvén eigenmode (RSAE) is often excited by energetic ions and exhibits a characteristic frequency sweeping related to time evolution of the minimum of the safety factor q_{min} [1]. Time evolution of the RSAE frequency is a good diagnostic tool for q_{min} in the RS-tokamak. It is worthwhile to investigate energetic ion driven modes in a RS-configuration of helical/stellarator plasmas, for drawing a general picture of RSAE in a toroidal plasma. The RS-configuration was realized for the first time by using intense counter neutral beam current drive (NBCD) on the condition that energetic ion contribution is significant. Figure 3 shows an example of the waveforms of plasma parameters in the RS configuration. During the rise in the net plasma current, a characteristic frequency sweeping mode was observed while line averaged electron density is kept almost constant, as shown in Fig.4 [8]. The mode numbers are $n=1$ and $m \sim 2$ around $t \sim 2.3$ s, and $n=1$ and $m \sim 3$ around $t \sim 3$ s. These modes have been identified to be RSAE through comparison between these data and the eigenmode frequencies and eigenfunctions calculated by AE3D code which is an MHD code for analysis of AEs in an incompressible low beta plasma[9]. The time when the RSAE frequency reaches the minimum indicates that the minimum value $(1/2\pi)_{min}$ of the rotational transform profile has passed through the rational value $(1/2\pi)_{min}=1/2$ at $t \sim 2.3$ s or $1/3$ at $t \sim 3$ s. The minimum value of RSAE frequency is close to the geodesic acoustic mode (GAM) frequency, which is consistent with the theory developed for a tokamak [10]. The $n=0$ mode having the frequency just below the minimum frequency in RSAE is also observed. The frequency agrees well with the GAM frequency derived from kinetic theory for a helical plasma [11, 12]. This mode is thought to be GAM excited by energetic ions and global mode accompanying strong magnetic fluctuations.

In this RS plasma of LHD where RSAE and GAM coexist, RSAE and GAM interact

nonlinearly and generate other frequency sweeping modes through three wave coupling, as shown in Fig.4. Thus generated driven modes again interact with GAM sequentially and generate a multitude of frequency sweeping modes. This fact is more clearly seen in the spectrogram of a signal of microwave interferometer/reflectometer. Effects of RSAE, GAM and driven modes on energetic ion transport are left for a future important work.

4. Summary

In three dimensional plasmas of LHD, RSAE have been observed for the first time in a helical plasma, in addition to usual TAEs. These observations in LHD indicate possibilities of direct comparison of the data with those in tokamaks and comprehensive understanding of Alfvén eigemode physics in a toroidal plasma. In addition, LHD is also a unique platform to study AEs observed only in three dimensional plasmas. Comparison study of LHD results with data that will be obtained near future in the Chinese tokamaks such as EAST and HL-2A is surely one of most interesting and fruitful collaboration researches between China and Japan.

Acknowledgements

Authors thank the LHD technical teams for their support. One of authors (K.T.) acknowledges D. Spong, Y. Todo and T. Watari for their fruitful discussions. This work is partly supported by LHD project budget (NIFS08ULHH508) and the Grant-in-aid for Scientific Research from MEXT, No. 16082209. This research is also supported by the JSPS-CAS Core-University Program in the field of “Plasma and Nuclear Fusion”.

References

- [1] A. Fasoli, C. Gormezano, H.L. Berk et al., Nucl. Fusion **47**, S264 (2007).
- [2] A. Weller, M. Anton, J. Geiger et al., Phys. Plasmas **8**, 931 (2001).
- [3] K. Toi, M. Takechi, M. Isobe et al., Nucl. Fusion **40**, 1349 (2000).
- [4] K. Toi, S. Yamamoto, N. Nakajima et al., Plasma Phys. Control. Fusion **46**, S1 (2004).
- [5] S. Yamamoto, K. Toi, S. Ohdachi et al., Nucl. Fusion **45**, 326 (2005).
- [6] G.Y. Fu, C.Z. Cheng, R. Budny et al., Phys. Rev. Lett. **75**, 2336 (1995).
- [7] M. Takechi, K. Toi, S. Takagi et al., Phys. Rev. Lett. **83**, 312 (1999).
- [8] K. Toi, F. Watanabe, T. Tkuzawa et al., submitted to Phys. Rev. Lett.
- [9] D.A. Spong and Y. Todo, Bull. American Phys. Soc., Vol.52, No. 11(2007) pp8.00098.
- [10] B. N. Breizman, M.S. Pekker, S.E. Sharapov, Phys. Plasmas **12**, 112506 (2005).
- [11] H. Sugama and T.H. Watanabe, Phys. Plasmas **13**, 012501 (2006).
- [12] T. Watari, Y. Hamada, T. Notake et al., Phys. Plasmas **13**, 062504 (2006).

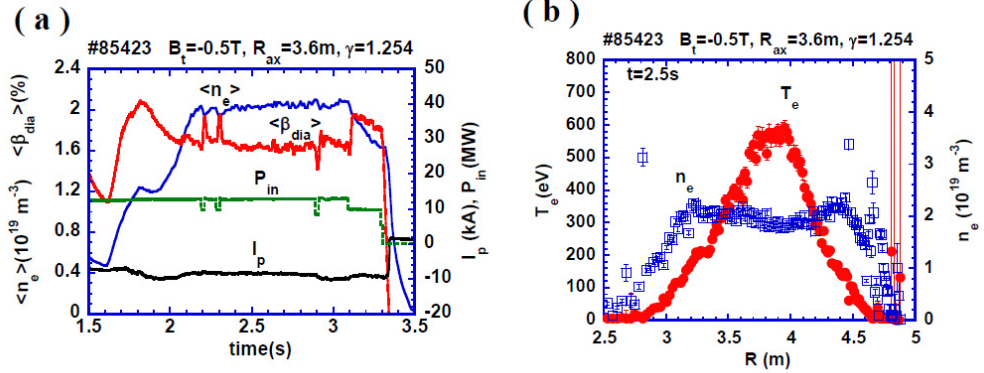


Fig.1 (a) A typical discharge waveform with relatively high averaged-toroidal-beta value($\sim 1.5\%$), where absorbed NBI power is inferred to be more than 8MW. The quantities $\langle n_e \rangle$, $\langle \beta_{dia} \rangle$, I_p and P_{in} are respectively the line averaged electron density, averaged toroidal beta derived from diamagnetic measurement, plasma current and NBI power through injection port. (b) Electron temperature and density profiles measured with Thomson scattering at $t=2.5\text{s}$. The peak position of electron temperature is shifted outward appreciably to $R\sim 3.9\text{m}$ from the vacuum position of $R_{ax}=3.6\text{m}$.

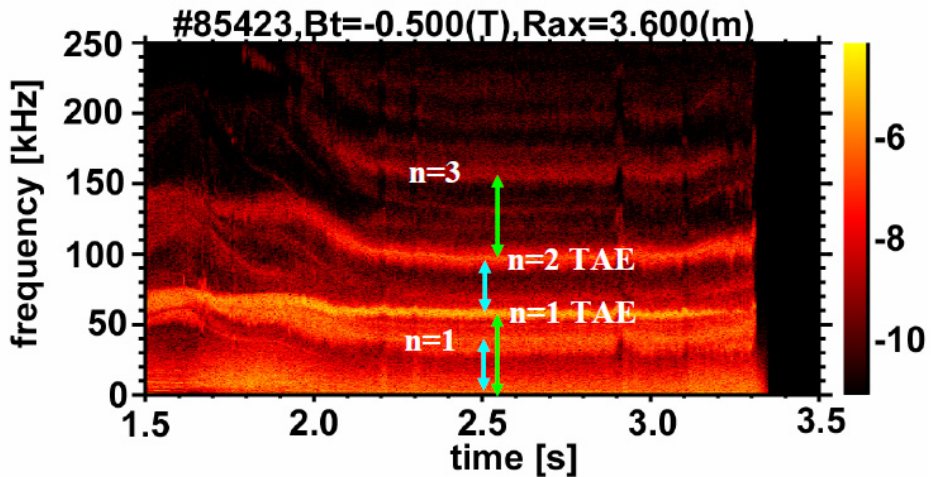


Fig.2 Spectrogram of magnetic probe signal obtained in the plasma shown in Fig.1. Coherent modes marked with “ $n=1$ TAE” or “ $n=2$ TAE” are energetic ion driven TAEs. Other coherent modes with $n=3$ and $n=1$ are driven modes through nonlinear coupling between these two TAEs. The arrows show a measure of frequency.

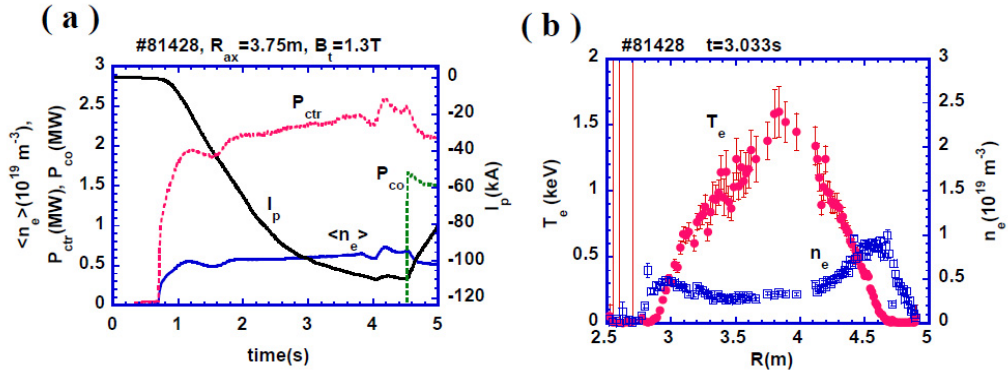


Fig.3 (a) A typical waveform of the RS plasma obtained by counter NBCD, where neon is puffed into a target plasma, to minimize shine-through of NBI and electron return current in NBCD. P_{ctr} and P_{co} stand for absorbed power of counter- and co-NBI powers, respectively. (b) Electron temperature and density profile at $t=3.033s$.

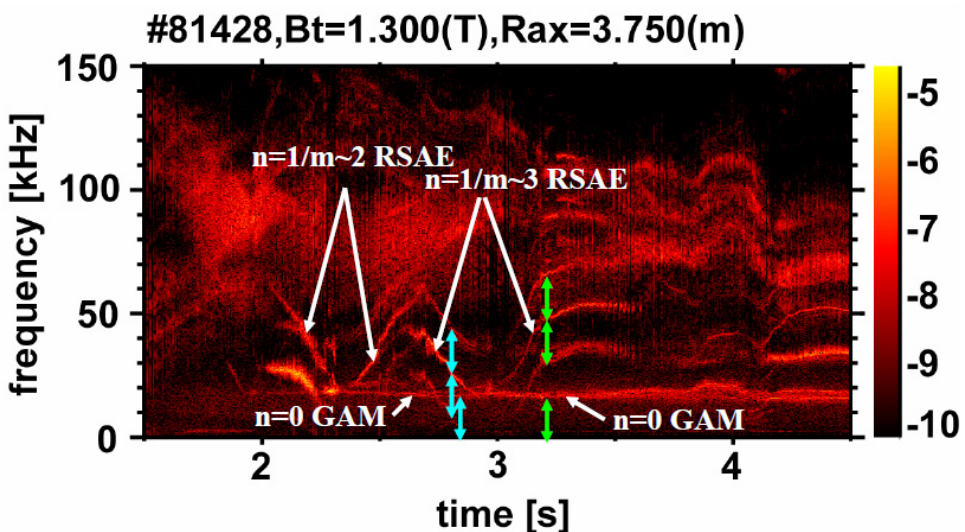


Fig.4 Spectrogram of magnetic probe signal obtained in the plasma shown in Fig.3. The arrows show a measure of frequency. The frequency sweeping modes of which frequency is shifted additive and subtractive are driven through nonlinear coupling between RSAE and GAM, for instance, at $t \sim 3.2s$ in this figure.

Progress on edge and core impurity transport study with development of spectroscopic instruments in LHD

Shigeru MORITA, Motoshi GOTO, Masahiro KOBAYASHI, Sadatsugu MUTO,
Malay Bikas CHOWDHURI¹⁾, Chunfeng DONG¹⁾, Hangyu ZHOU¹⁾,
Zhengying CUI²⁾, Keisuke FUJII³⁾, Akihiro FURUZAWA⁴⁾, Masahiro HASUO³⁾,
Atsushi IWAMAE³⁾, Yinxian JIE⁵⁾, Mohammed KOUBITI⁶⁾, Ikuya SAKURAI⁴⁾,
Yuzuru TAWARA⁴⁾, Baonian WAN⁵⁾ and Zhenwei WU⁵⁾, Naohiro YAMAGUCHI⁷⁾

National Institute for Fusion Science, Toki 509-5292, Gifu, Japan

¹⁾Department of Fusion Science, Graduate University for Advanced Studies,
Toki 509-5292, Gifu, Japan

²⁾Southwestern Institute of Physics, Chengdu 610041, China

³⁾Department. of Engineering Physics, Kyoto University, Kyoto 606-8502, Japan

⁴⁾EcoTopia Science Institute, Nagoya University, Nagoya 464-8603, Japan

⁵⁾Institute of Plasma Physics Chinese Academy of Sciences, Hefei 230031, China

⁶⁾Physique des Interactions Ioniques & Moleculaires, Universite de Provence,
Av. Escadrille Normandie-Niemen, F-13397 Marseille Cedex 20, France

⁷⁾Physics Laboratory, Graduate School of Medicine and Pharmaceutical Sciences,
Toyama 930-0194, University of Toyama

Abstract

Impurity transport has been investigated at edge and core regions in Large Helical Device with developing spectroscopic instruments which can measure one- and two-dimensional distributions of impurities. The edge impurity behavior has been recently studied using four carbon resonance transitions in different ionization stages of CIII (977Å), CIV (1548Å), CV (40.3Å) and CVI (33.7Å). When the line-averaged electron density, n_e , is increased from 1 to $6 \times 10^{13} \text{ cm}^{-3}$, the ratio of $(\text{CIII}+\text{CIV})/n_e$ increases whereas the ratio of $(\text{CV}+\text{CVI})/n_e$ decreases. Here, CIII+CIV (CV+CVI) expresses the sum of CIII (CV) and CIV (CVI) intensities and CIII+CIV indicates the carbon influx and CV+CVI indicates the emissions through the transport in the ergodic layer. The result thus gives experimental evidence on the impurity screening by the ergodic layer in Large Helical Device (LHD), which is also supported by 3-dimensional edge particle simulation. The core impurity behavior is also studied in high-density discharges ($n_e \leq 1 \times 10^{15} \text{ cm}^{-3}$) with H₂ multi-pellets injection. It is found that the ratio of V/D (V: convection velocity, D: diffusion coefficient) decreases after pellet injection and Z_{eff} profile shows a flat one at values of 1.1-1.2. These results confirm no impurity accumulation occurs in high-density discharges. As a result, the iron density, n_{Fe} , is analyzed to be 6×10^{-7} ($= n_{\text{Fe}}/n_e$) of which the amount can be negligible as radiation source even in such high-density discharges. One- and two-dimensional impurity distributions from spatial-resolved VUV and EUV spectrometers newly developed for further impurity transport study are also presented with their preliminary results.

Keywords: impurity transport, screening effect, VUV spectroscopy

PACS number: 52.70.-m, 52.70.Kz, 52.25.Vy

E-mail address: morita@nifs.ac.jp

Present address (M.B.Chowdhuri): Institute for Plasma Research, Near Indira Bridge,

Bhat, Gandhinagar, Gujarat, India, 382428

Present address (A.Iwamae): Naka Fusion Institute, JAEA, Naka 311-0193, Ibaraki,

Japan

1 Introduction

Large Helical Device (LHD: $R/\langle a \rangle = 3.6\text{m}/0.64\text{m}$, $B_t < 3\text{T}$, $V_p = 30\text{m}^3$, $P_{\text{NBI}} \sim 23\text{MW}$) is characterized by the presence of edge stochastic magnetic field surrounding the core plasma, so called ‘ergodic layer’. The intermediately closed magnetic field lines in the ergodic layer mainly consist of ones with 10-1000m. The size of the ergodic layer typically varies between 2 and 30cm in thickness, basically depending on poloidal angle and magnetic axis position ($3.5 \leq R_{\text{ax}} \leq 4.1\text{m}$). The electron temperature in the ergodic layer is widely distributed at $T_e \leq 500\text{eV}$ and the electron density at last closed flux surface (LCFS) is typically ranged in 10-100% to line-averaged density. The transport study of the ergodic layer thus becomes very important in viewpoint of plasma performance improvement in addition to the confinement improvement. Impurity transport is one of major topics in relation to studies on the role of the ergodic layer and density limit. In the ergodic layer, especially, the understanding of parallel impurity transport along magnetic field lines is a key issue as well as perpendicular transport.

In LHD, on the other hand, variety of density profiles have been observed until now such as peaked, flat and hollow ones. The study of impurity transport in the plasma core gives useful information to solve the physical mechanism on density profile formation in addition to the study on the relationship between the impurity transport and density profile. Recently, high-density discharges ($n_e(0) \leq 1 \times 10^{15}\text{cm}^{-3}$) using multi-pellets injection have been successfully performed in LHD. The study of impurity transport in such high-density plasmas becomes also important in terms of Z_{eff} and reactor orientation.

In the present paper, some results on the edge and core impurity transport studies recently done in LHD are presented in connection with above mentioned motivation.

The progress on spatial-resolved spectroscopy newly developed for further impurity transport study is also interpreted with some preliminary results.

2 Edge impurity transport

When the impurity transport along magnetic field lines is simply expressed by the momentum equation of

$$m_z \frac{\partial V_{z\parallel}}{\partial t} = -\frac{1}{n_z} \frac{\partial T_i n_z}{\partial s} + m_z \frac{V_{i\parallel} - V_{z\parallel}}{\tau_{zi}} + ZeE_{\parallel} + 0.76Z^2 \frac{\partial T_e}{\partial s} + 2.6Z^2 \frac{\partial T_i}{\partial s}, \quad (1)$$

two forces based on friction between impurity and background ions (second term) and ion temperature gradient (fifth term) become dominant in the parallel transport, because other terms are estimated to be negligibly small. Here, the subscripts of z and i define impurity ion with charge state of z and background ion as fuel. The symbol of s is the coordinate along magnetic field line. Other variables mean usually used ones. The eq.(1) is then rewritten by

$$V_{z\parallel} = V_{i\parallel} + 2.6Z^2 \frac{\tau_{zi}}{m_z} \frac{\partial T_i}{\partial s}. \quad (2)$$

The ions basically flow downstream if the ion temperature gradient can be negligible. In this case the impurities also flow downstream due to the friction force, i.e., ‘impurity screening’.

In order to make it clear, four resonance carbon transitions of CIII (977Å), CIV (1548Å), CV(40.3Å) and CVI(33.7Å) have been observed using VUV and EUV spectrometers^{1,2}, which are absolutely calibrated with bremsstrahlung emission. Here, the CIII (47.9eV) and CIV (64.5eV) define the carbon influx and the CV (392eV) and CVI (490eV) express emissions through the transport in the ergodic layer due to their

higher ionization energies. Therefore, the intensity ratio of CV+CVI to CIII+CIV can give a degree of impurity screening. The ratios are analyzed with several experimental parameters which modify the magnetic field structure in the ergodic layer. A typical example of the carbon intensities measured from LHD standard configuration ($R_{ax}=3.6m$) is shown in Fig.1(a). Two groups of CIII+CIV and CV+CVI behave in contrast each other against the electron density. Taking the ratio of $(CIII+CIV)/(CV+CVI)$ from Fig.1(a), we find a very simple relation with the density, as shown in Fig.1(b). The ratio monotonically decreases against the density and varies in two orders between 1 and $7\times 10^{13}\text{cm}^{-3}$.

The intensities of CIII-CV are calculated using three-dimensional edge transport code, EMC3-EIRENE, which is a combination of fluid equation solver, EMC3³, and particle transport solver, EIRENE⁴. The results are shown in Figs.1 (c) and (d). The CVI is not calculated in the code, since it is generally localized just inside the LCFS. The calculated results are plotted for typical two cases, i.e., with (Fig.1(c)) and without (Fig.1(d)) friction force. Seeing the clear difference between two cases in the CV behavior, the importance of the friction force can be easily understood in the mechanism of edge impurity transport. The impurity screening has been experimentally verified by the present study as a role of the ergodic layer in LHD.

In the simulation code, on the other hand, the perpendicular transport is treated to be the extension of core plasma⁵. However, the real magnetic field structure of the ergodic layer is, of course, considerably different from the assumption. Detailed impurity structure is necessary for further understanding of the edge impurity transport study. Therefore, a new method on one- and two-dimensional edge impurity structure measurement has been developed using a 3m VUV spectrometer in LHD^{6,7}. As an

example of the measurement, radial profiles of CIII-CV are plotted in Fig.2. Since data are obtained from local island diverter experiment in $R_{ax}=3.75\text{m}$ where a carbon plate (1m^2 in size) is inserted into a large $m/n=1/1$ island at plasma edge, the carbon emissions are quite strong. Asymmetric poloidal structures are seen in CIII and CIV profiles^{8,9}. When the toroidal magnetic field direction is inverted, the CIV profile is also inverted, i.e., the peak of CIV moves to $Z=-0.4\text{m}$. Ions in the diverter region generally flow downstream toward opposite direction to magnetic field lines due to grad-B drift. The CIV profile seems to express the grad-B drift of the impurity ions. Such an asymmetric feature is completely disappeared in the CV profile, and it expresses to be a function of magnetic surface, since the CV is located near LCFS because of its high ionization energy (392eV).

Two-dimensional edge impurity structure is tried to measure from horizontal mid-plane. A typical result obtained from $R_{ax}=3.6\text{m}$ configuration is shown in Fig.3. Figure 3 (a) shows a view angle of the 3m normal incident VUV spectrometer, which is denoted with square solid line. Two pairs of diverter carbon plates at inboard side are also seen from top-right to bottom-left. The zero-th order light in Fig.3(b) means emissions integrated from VUV to visible range (300-7000Å). It is seen that the strong emissions are localized near inboard X-point and rotate poloidally along the diverter plates. These emissions are specially enhanced in inward-shifted configuration like $R_{ax}=3.5-3.6\text{m}$ where magnetic field lines connecting to divertor plates are concentrated at the inboard side. The CIV emissions are further localized near the inboard X-point at some toroidal position near horizontally elongated cross section.

3 Core impurity transport

Recently, high-density discharges up to $1 \times 10^{15} \text{ cm}^{-3}$ have been successfully achieved using multi-pellets injection under outwardly shifted configurations ($3.8 \leq R_{\text{ax}} \leq 4.0 \text{ m}$) with relatively better MHD stability of magnetic well formation over wider range of plasma radius. Peaked density profiles are seen after the pellet injection and sustained during several hundred milliseconds with appearance of the maximum diamagnetic energy. Impurity transport study becomes important in such a high-density operation in relation to the impurity accumulation. The core impurity transport study in LHD has been done until now using a combination of visible bremsstrahlung and impurity pellet injection^{10, 11}. In the present high-density discharges, however, the electron temperature remarkably changes as a function of time and the enhancement of visible bremsstrahlung emission from small-sized impurity pellet ($\sim 0.5 \text{ mm}$ in diameter) ablated at plasma edge is too small compared to the background emission before the impurity pellet injection. A classical method using passive spectroscopy is then applied to the present core impurity transport study.

A typical waveform in high-density discharges is traced in Fig.4. Nine H_2 pellets are repetitively injected during 0.7-0.9s (see Fig.3(c)). Line-averaged density evaluated from density profiles measured with Thomson scattering continuously increases during the pellet injection and reaches $4 \times 10^{14} \text{ cm}^{-3}$. Electron temperature at plasma center quickly decreases down to 0.3keV according to the density rise. Li-like resonance transition of FeXVI (335.4Å) suddenly appears after the pellet injection and the intensity takes its maximum at the final pellet injection ($t=0.95 \text{ s}$). In LHD almost all the parts of vacuum vessel are covered with protector plates made of stainless steel, although the carbon plates are installed only in the divertor section (see Fig.3(a)). A

small amount of iron always exists in the discharges. The FeXVI is then used for the present core impurity transport study.

The impurity transport is studied with traditional method using impurity transport code. In a diffusive/convective model the impurity ion flux is expressed by

$$\Gamma_q = -D_q(r) \frac{\partial n_q}{\partial r} + V_q(r) n_q, \quad (3)$$

where Γ and q are the impurity ion flux and the q^{th} charge state of impurity ions, respectively. Values of diffusion coefficient, D , and convective velocity, V , have been already examined in usual NBI discharges¹⁰. For FeXVI, then, $D=0.2\text{m}^2/\text{s}$ and $V=-3\text{m/s}$ are used for the analysis. Here, it is confirmed from the impurity transport simulation that the FeXVI (Fe^{15+}) exists in the plasma center after pellet injection, whereas it is located at plasma edge before pellet injection. Result is shown in Fig.5 as a parameter of iron impurity density normalized by electron density. The impurity density is thus determined to be 6×10^{-7} to the electron density. The total radiation loss from iron is also estimated to be 200kW from the analysis of FeXVI under $T_e(0)=0.3\text{keV}$ and $n_e=5 \times 10^{14}\text{cm}^{-3}$. Since the input NBI power is 15-20MW and the total radiation loss is 1.5MW after pellet injection, the amount of iron radiation loss can be entirely neglected even in such high-density discharges of LHD.

The time behavior of FeXVI is analyzed as parameters of D and V . It is impossible to obtain two parameters separately from usually used passive spectroscopy. A typical result is shown in Fig.6 for V dependence. The value of D is fixed as $0.2\text{m}^2/\text{s}$. The inward velocity has to be changed after the pellet injection at $t=0.95\text{s}$ in order to describe well such a quick reduction of the FeXVI signal. In the calculation the reduction of the inward velocity to -1.5m/s makes the best fit to the measurement.

In the same way we obtain a change in D from 0.2 to $0.4\text{m}^2/\text{s}$, if the V is fixed as -3m/s .

After all, the ratio of V/D has to be reduced to half the value after the pellet injection.

The electron diffusion coefficient analyzed from electron density profiles does not show any change in both cases before and after the pellet injection. If the impurity ions behave a similar diffusion to the electrons, the change in the iron transport is caused by the convective velocity. Anyway, the present analysis concludes no impurity accumulation is occurred in high-density discharges with multi-pellets injection of LHD.

In order to study core impurity/particle transport one- and two-dimensional spectroscopy has been developed as well as the edge diagnostics. A new system using an optimized visible spectrometer for radial profile measurement of Z_{eff} has been installed on LHD instead of former system with interference filter¹². The effect of line radiation mixing into the visible bremsstrahlung signal can be completely avoided by the new system. A typical result from high-density discharges is shown in Fig.7. The density profile seen in Fig.7(a) is peaked as described above and then the emissivity of visible bremsstrahlung is also further peaked because it is basically proportional to the square of electron density. The analyzed Z_{eff} , as shown in Fig.7(d), suggests roughly a flat profile with values of 1.1-1.2 except for edge region of $\rho \geq 1$. Error bars are originated in fitting curves of temperature and density profiles and uncertainty on detailed structure of magnetic surfaces deformed by the plasma pressure. At least now it is difficult to analyze the data in flat and hollow density profiles because of a large amount of poloidally non-uniform visible bremsstrahlung emitted from the ergodic layer. Further effort is being paid for resolving this problem.

A spatial-resolved EUV spectrometer has been also developed in range of 50-500Å to measure one- and two-dimensional structures of edge and core impurity emissions. One-dimensional distribution of the impurity profile is preliminarily obtained as the first data (see Fig.8). At present the spectrometer observes half the LHD plasma along vertical direction ($\Delta Z=50\text{cm}$) at horizontally elongated plasma cross section. Radial images of several iron lines in highly ionized states are shown in Fig.8(a). Figure 8(b) shows a vertical profile of FeXXIII (132.9Å), which is taken from the 4th horizontal line of EUV image in Fig.8(a). The profile clearly informs us that the FeXXIII is located in the plasma center. The result certifies that the present system is sufficiently applicable to the core and edge impurity transport studies.

4 Summary

The impurity screening by the ergodic layer in LHD and the behavior of the convective (inward) velocity in high-density LHD discharges are presented with analytical results using transport simulation codes as part of edge and core impurity transport studies. Through the present impurity transport studies the impurity screening is experimentally verified as a role of the ergodic layer in LHD and it is confirmed that no impurity accumulation occurs in high-density LHD discharges. Several spectroscopic diagnostics have been newly developed, e.g., spatial-resolved VUV and EUV spectrometers for one- and two-dimensional measurements for the purpose of edge and core impurity transport studies. These instruments are aimed for further understandings on perpendicular and parallel particle transports in edge plasmas, impurity behaviors based on three-dimensional magnetic structure and magnetic surface modification due to the increased plasma pressure. Finally, it should be noted that

edge plasma diagnostics using polarization spectroscopy¹³ and magnetic dipole forbidden transition^{14, 15} have been newly carried out in visible range and charge state distribution of iron have been studied using K α x-ray lines for core impurity transport¹⁶,¹⁷. Spectroscopy on ablation cloud of impurity pellet has been also started as part of particle diffusion study¹⁸.

Acknowledgements

The authors thank all members of LHD experimental group for their technical supports. This work is partially carried out under the LHD project financial support (NIFS08ULPP527). This work is also partially supported by the JSPS-CAS Core-University program in the field of ‘Plasma and Nuclear Fusion’.

References

- 1 Chowdhuri M B, Morita S, Goto M, et al. 2007, *Rev. Sci. Instrum.*, 78: 023501
- 2 Chowdhuri M B, Morita S, Goto M. 2008, *Appl. Optics*, 47: 136
- 3 Feng Y, Sardei F, Kisslinger J, et al. 2004, *Contrib. Plasma Phys.*, 44: 57
- 4 Reiter D, Baelmans M, Borner P. 2005, *Fusion Sci. Tecnol.*, 47: 172
- 5 Kobayashi M, Feng Y, Masuzaki S, et al. 2008, *Contrib. Plasma Phys.*, 48: 255
- 6 Morita S, Goto M. 2003, *Rev. Sci. Instrum.*, 74: 2036
- 7 Katai R, Morita S, Goto M. 2006, *Rev. Sci. Instrum.*, 77: 10F307
- 8 Yamazaki H, Goto M, Morita S, Watanabe T H. 2007, *Plasma Fusion Res.*, 2: S1115
- 9 Goto M, Morita S. 2007, *Plasma Fusion Res.*, 2: S1053
- 10 Nozato H, Morita S, Goto M, et al. 2004, *Phys. Plasmas*, 11: 1920
- 11 Nozato H, Morita S, Goto M. 2006, *Phys. Plasmas*, 13: 092502
- 12 Zhou H Y, Morita S, Goto M, Chowdhuri M B. 2008, *Rev. Sci. Instrum.*, 79: 10F536
- 13 Iwamae A, Hayakawa M, Atake M, et al. 2005, *Phys. Plasmas*, 12: 042501
- 14 Katai R, Morita S, Goto M. 2007, *J. Quant. Spectr. Rad. Trans.* 107: 120
- 15 Iwamae A, Atake M, Sakaue A, et al. 2007, *Phys. Plasmas*, 14: 042504
- 16 Sakurai I, Tawara Y, Matsumoto C, et al. 2007, *Plasma Fusion Res.*, 2: S1068
- 17 Muto S, Morita S. 2008, *Plasma Fusion Res.*, 3: S1086
- 18 Goto M, Sakamoto R, Morita S, 2007, *Plasma Phys. Control. Fusion*, 49: 1163

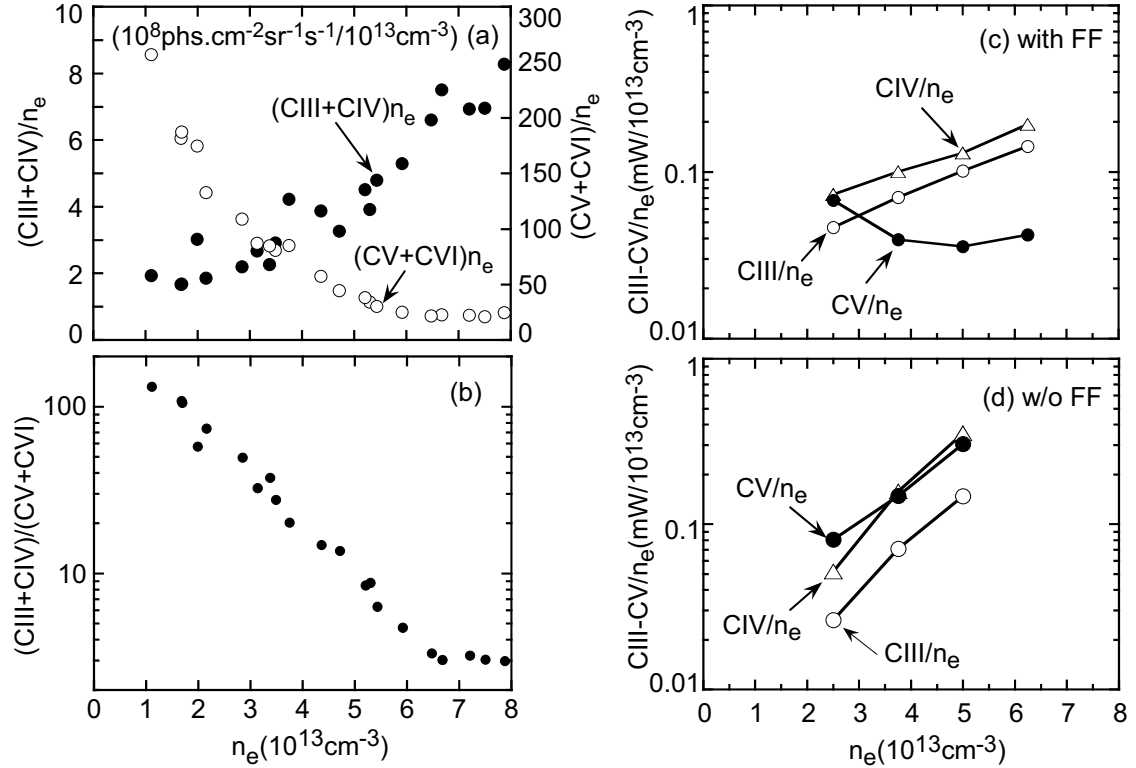


Fig.1 (a) Intensity summation of CIII (977Å) + CIV (1548Å) (closed circles) and CV (40.3Å) + CVI (33.7Å) (open circles) normalized to electron density, (b) intensity ratio of CIII+CIV to CV+CVI and calculated carbon intensities normalized to electron density with (c) and without (d) friction force (CIII/n_e: open circles, CIV/n_e: open triangles, CV/n_e: closed circles). All figures are plotted as a function of electron density.

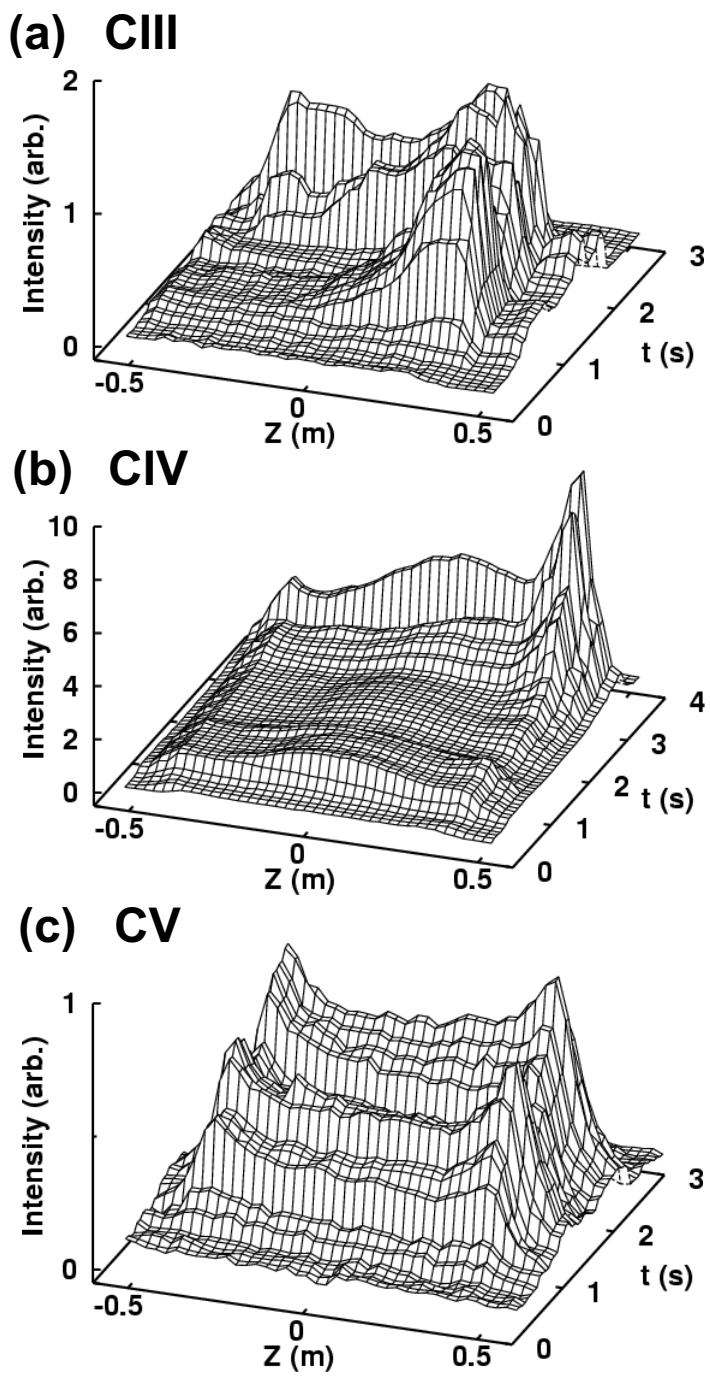


Fig.2 (a) Vertical (top-to-bottom) profiles of (a) CIII: 977Å, (b) CIV: 1548Å and (c) CV: 40.3Å as a function of discharge time. Profiles are obtained at local island diverter experiment in $R_{ax}=3.75$ m configuration.

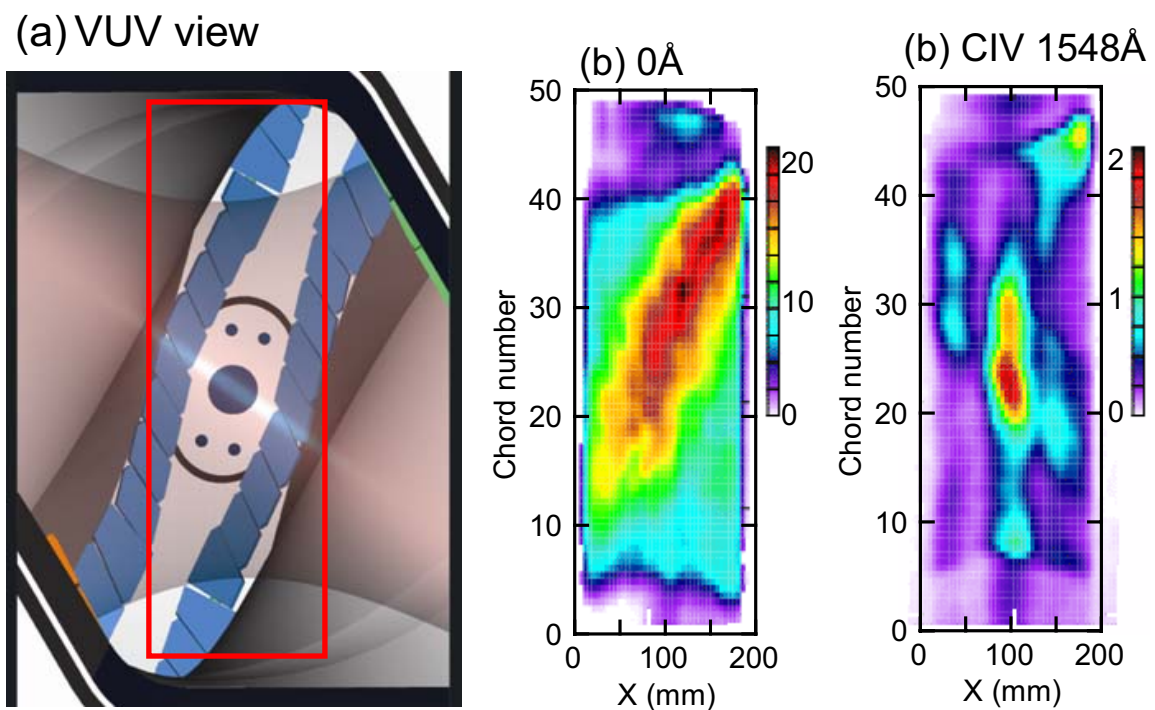


Fig.3 (a) View of 3m VUV normal incidence spectrometer denoted with square solid line and two dimensional image of (b) 0th order light 0Å and (c) CIV 1548Å.

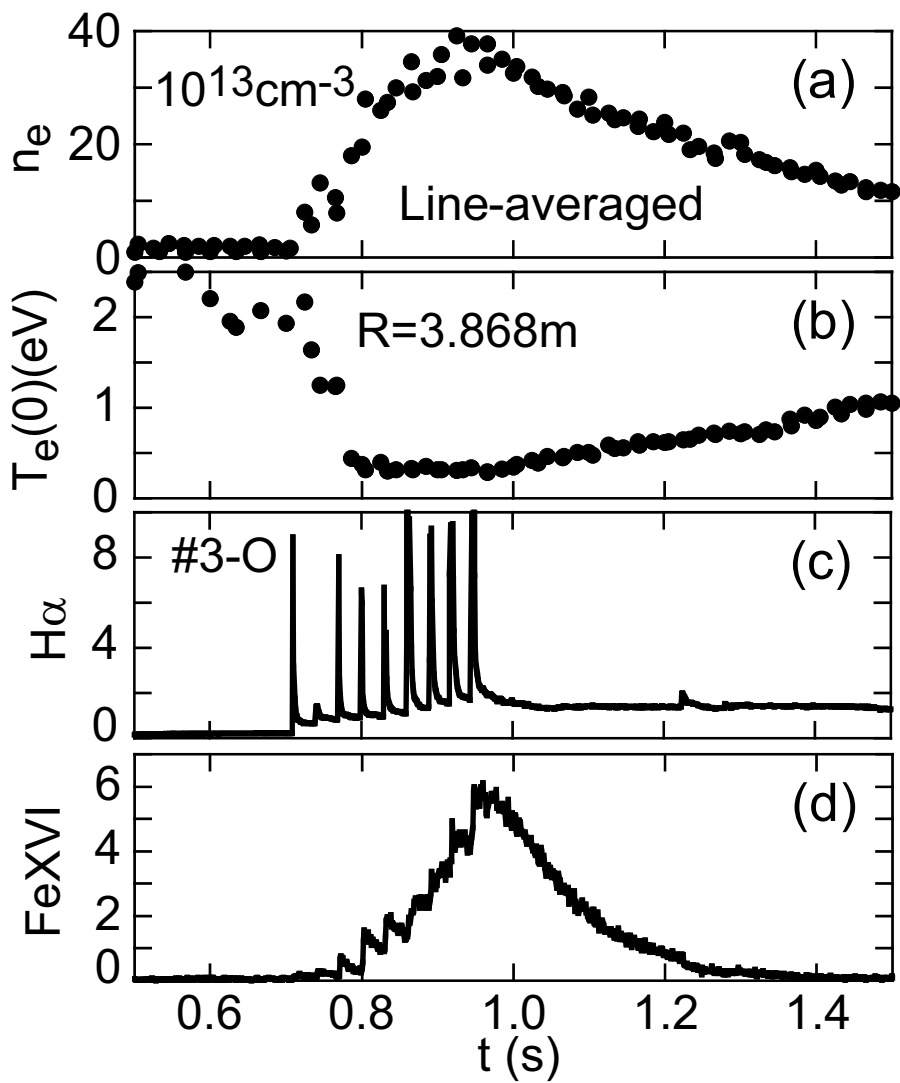


Fig.4 High-density discharge with multi-pellets injection; (a) line-averaged electron density, (b) central electron temperature and (c) H α and (d) FeXVI (335.4Å) intensities.

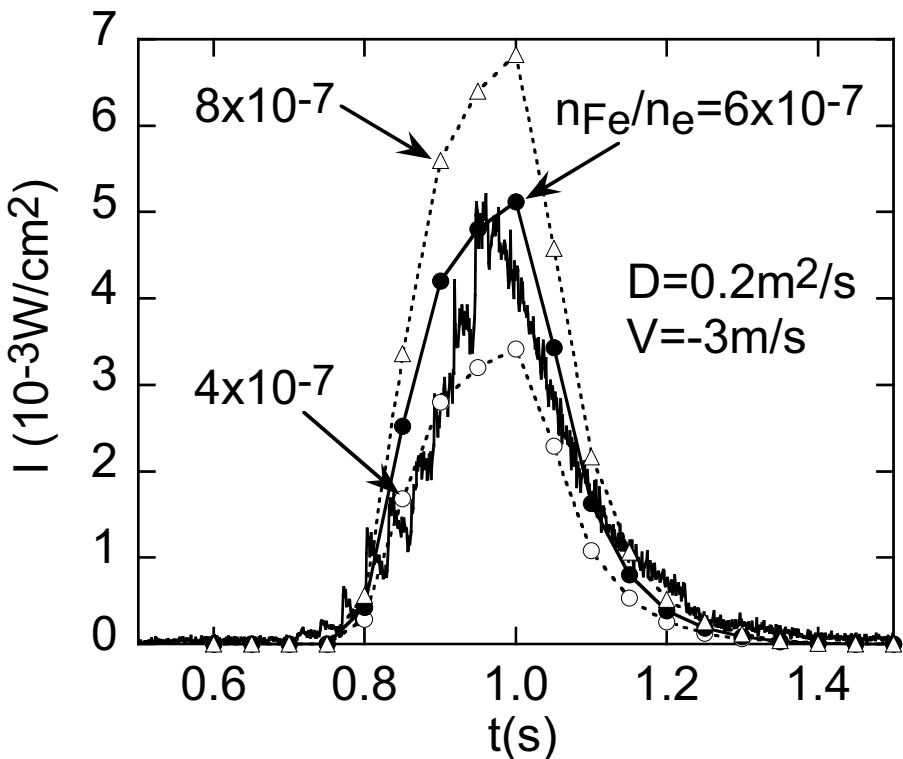


Fig.5 Iron density analysis under constant D of $0.2 \text{m}^2/\text{s}$ and V of -3m/s as a parameter of ratio of iron to electron densities (solid line: FeXVI, dashes line with open triangles: $n_{\text{Fe}}/n_{\text{e}}=8 \times 10^{-7}$, solid line with closed line: $n_{\text{Fe}}/n_{\text{e}}=6 \times 10^{-7}$ and dashed line with open circles: $n_{\text{Fe}}/n_{\text{e}}=4 \times 10^{-7}$).

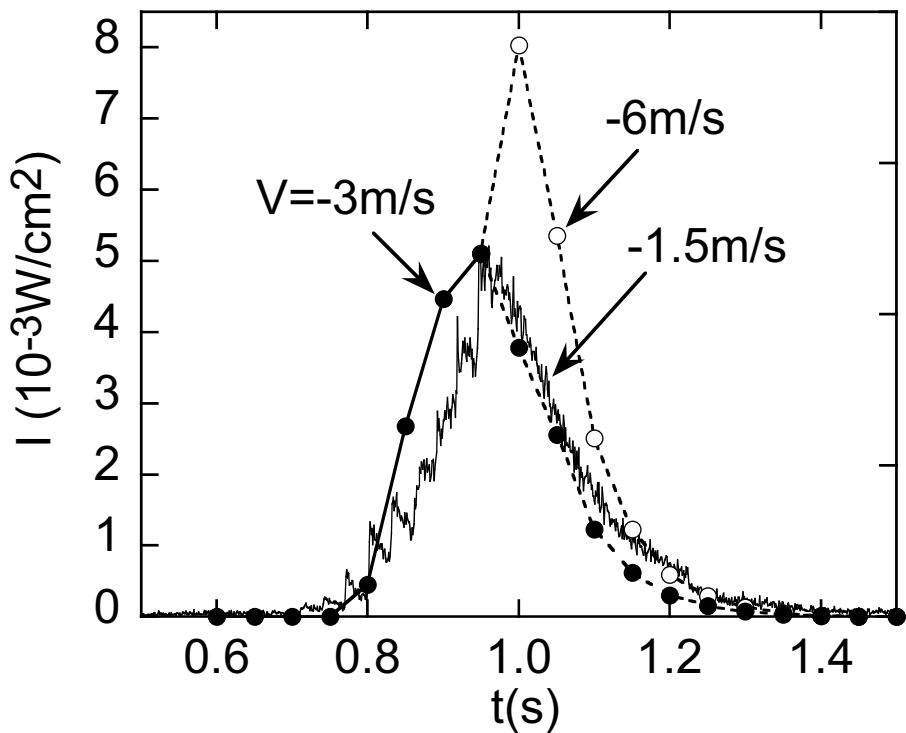


Fig.6 Impurity transport analysis of FeXVI (335.4Å) as a parameter of inward velocity of V (solid line with closed circles: $V = -3\text{m/s}$, dashed line with open circles: $V = -6\text{m/s}$ and dashed line with closed circles: $V = -1.5\text{m/s}$). Inward velocities are changed from -3m/s to -6m/s or -1.5m/s at $t = 0.95\text{s}$ when pellet injections are finished.

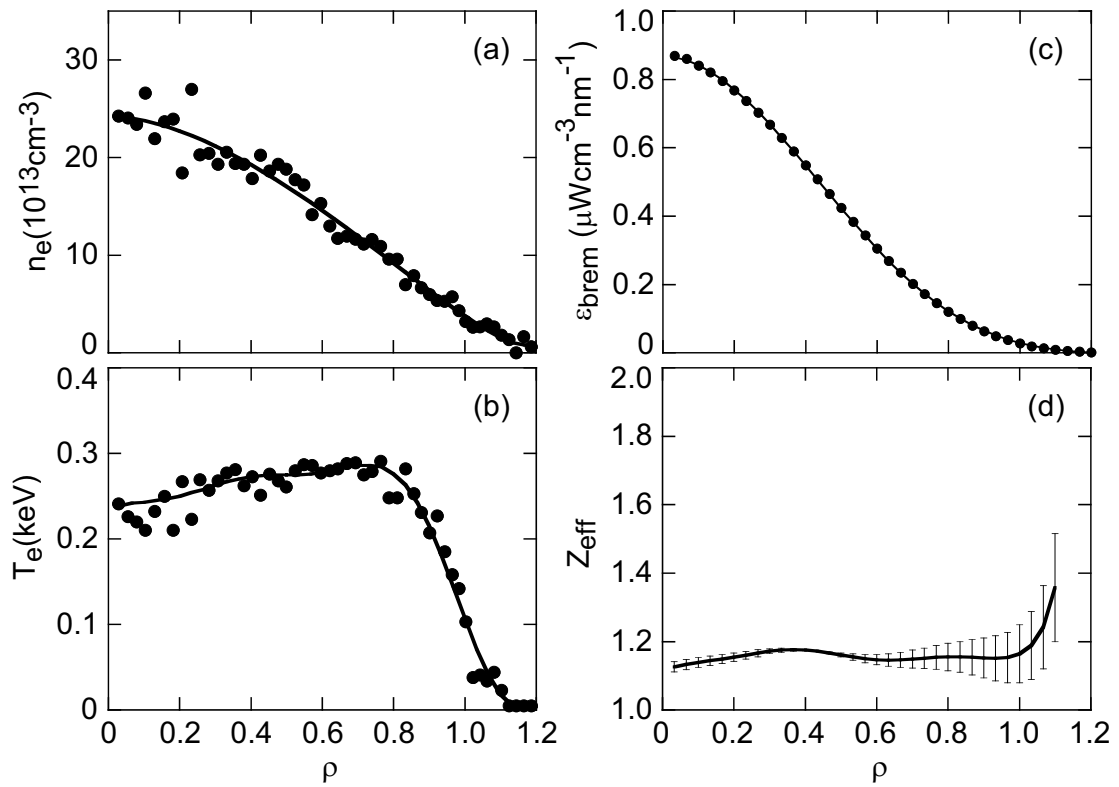


Fig.7 Typical example of Z_{eff} profile measurement in high-density discharges with multi-pellets injection; (a) electron density, (b) electron temperature, (c) visible bremsstrahlung emissivity and (d) Z_{eff} profiles as a function of averaged minor radius.

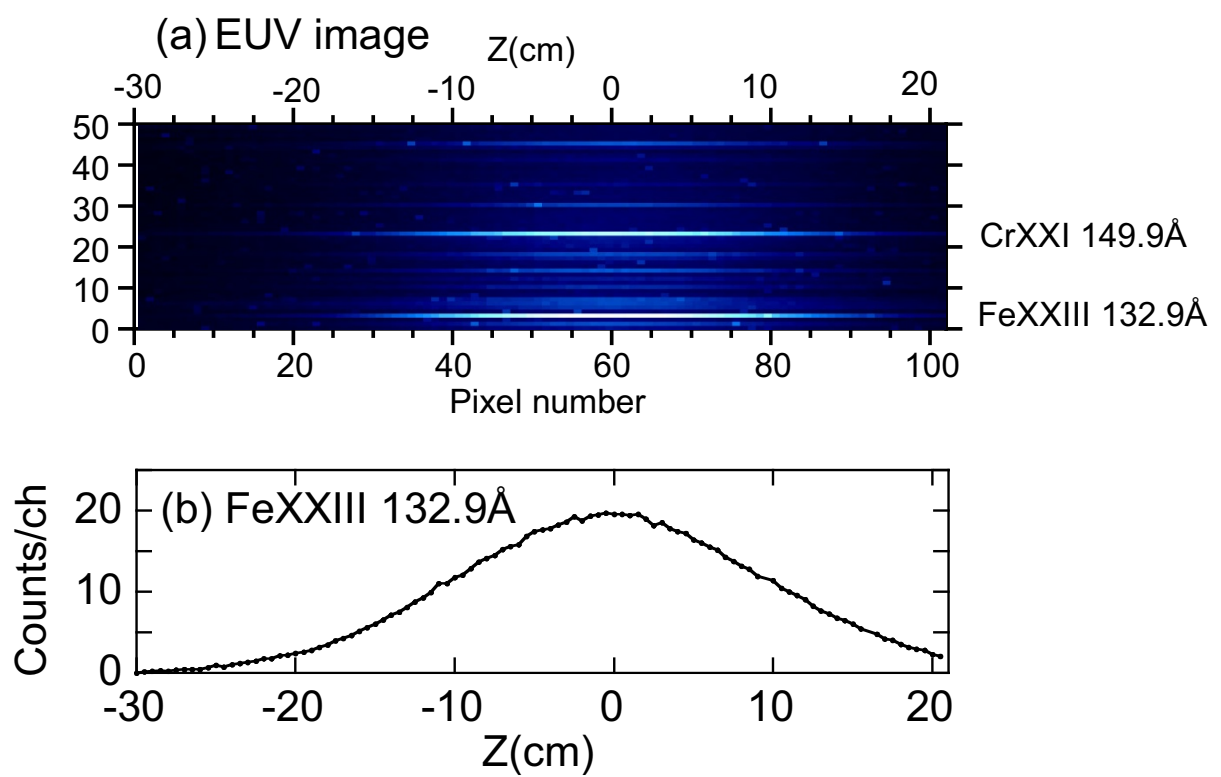


Fig.8 (a) Spectral image of spatial-resolved EUV spectrometer and (b) vertical profile of FeXXIII (132.9Å).

Plasma sheath resistance measurement by reference probe in PECVD coating machine

Qing WANG¹, De-Chun BA¹, Hua-bing Xu², and Xiang-kun Xu³

1. School of Mechanical Engineering & Automation; Northeastern University; Shenyang 110004, China
2. Department of Dynamic Engineering; Bohai Shipbuilding Vocational College; Huludao 125000, China
3. School of Application Technology; Shenyang Ligong University; Fushun 113122, China

Abstract

Plasma space potential is constant theoretically in plasma diagnostic using Langmuir probe. However plasma space potential often changes in low-frequency besides in rf-frequency when Langmuir probe potential is varied to obtain a sweeping I-V characteristic curve. The change leads to measure incorrectly plasma parameters. In this research a home-made rf compensated Langmuir probe with reference probe was used to measure and analyse the low-frequency change of plasma potential in PECVD coating machine. The plasma bulk in PECVD coating machine is capacitance coupled plasma (CCP) driven by radio-frequency power supply. We find that the sheath resistance of plasma to ground is about 345 ohm and is quite high. The change of plasma potential causes a flattening of I-V characteristic curve due to the high resistance.

1 Introduction

The Langmuir probe, as an important plasma diagnostic tool, is biased by sweeping power supply to absorb electron and positive ion flow. Plasma key parameters such as plasma space potential, electron temperature, electron density or ion density, floating potential, electron energy distribution function EEDF, can be deduced through analyzing I-V characteristic curve of Langmuir probe [1-6]. However in practice, it is not easy to analyze I-V characteristic curve due to all kinds of disturbances as follows:

(1) contamination of probe surface [7]: Langmuir probe tip is inserted into plasma and easy to be bombarded by ions or electrons. So its effective collecting area is changed, which leads to measurement error. Sometimes the surface of Langmuir probe can be coated a non-conducting film during depositing film, which also affects data acquisition and analyzing of I-V curve.

(2) radio frequency interference [8-10]: Langmuir probe used in radio frequency plasma sources are subject to rf pickup which can greatly distort the I-V characteristic and give erroneous results. The "V" is actually the potential difference, is DC potential applied to probe, and is a potential that can fluctuate at the rf frequency and its harmonics. Without proper rf compensation, Langmuir probe data in rf discharges can give spurious data on Te and Vf.

(3) lower frequency interference (noise) [11-13]: Langmuir probe, sometimes, is also subject to lower frequency signal pickup which can distort the I-V characteristic due to driving by sweeping power supply. For example in a capacitively coupled rf plasma the DC resistance of the plasma to wall sheath can be quite high, 100-1000 ohms. Similarly in plasmas with poor return to ground this resistance may be the same order or higher. Biasing the probe tip causes a DC shift in the

plasma potential due to this resistance. If this DC shift is not compensated the calculated parameters will be incorrect.

In this paper, lower fluctuation of radio frequency non-equilibrium plasma is studied. Plasma sheath resistance is measured in plasma enhancement chemical vapour deposition(PECVD) coating machine using rf- compensated langmuir probe and plasma floating probe. The results show that the capacitively coupled rf plasma sheath resistance is very high. The low-frequency fluctuation effects plasma diagnostic with langmuir probe.

2 Experimental setup

2.1 plasma discharge device

In this research, plasma discharge device, as shown in Fig.1, is rf plasma enhancement chemical vapour deposition(PECVD) coating machine. Principally it is a capacitively coupled RF plasma source[14-15].

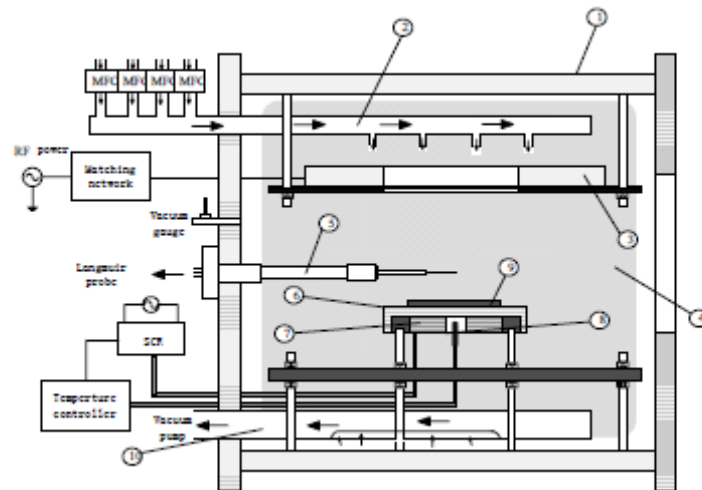


Fig.1 Structure sketch of RF-500 CVD coating machine

- ①vacuum wall;②gas inlet;③rf electrode;④plasma;⑤langmuir probe;⑥substrate holder;⑦substrate heater; ⑧thermocouple; ⑨ substrate; ⑩gas outlet.

Mass flow controllers(MFC) are used to adjust gas flow. Thermocouple temperature controller and silicon-controlled rectifier(SCR) control substrate temperature together. Radio frequency power supply(500W) and network matcher are used to excite plasma. Langmuir probe as plasma diagnostic tool are mounted 55mm from the substrate.

2.2 Langmuir probe and floating reference probe

The structure sketch of langmuir probe used in this research is shown in Fig.2.

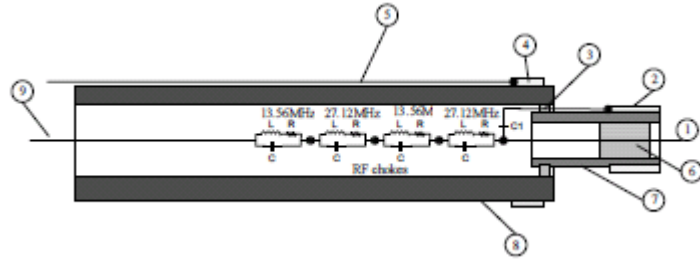


Fig.2 Structure sketch of Langmuir probe

①langmuir probe tip($mm175.0=\phi$);②rf compensation electrode ($mm5=\phi$);③lock ring;④floating reference electrode;⑤lead wire of reference electrode;⑥probe holder;⑦short ceramic tube (AL_2O_3mm2 in outer diameter,25mm in long);⑧long ceramic tube ($AL_2O_3, mm8=\phi$ in outer diameter and $mm6=\phi$ in inner diameter);⑨conducting wire

Langmuir probe is contact measuring device and is immersed in plasma directly. So special techniques must be used to protect it from the plasma and to ensure that the circuitry gives the correct I-V values. The langmuir probe tip is made of a high-temperature material, a tungsten wire 0.175mm in diameter. The tungsten wire is threaded into a short ceramic tube to insulate it from the plasma except for a short length of exposed tip, 5mm long. To avoid disturbing the plasma, the ceramic tube should be as thin as possible. The probe tip should be centered in the tube and extend out of its end without touching it, so that it would not be in electrical contact with any conducting coating that may deposit onto the insulator. Cylindrical rf compensated electrode(5mm in outer diameter,4.5cm² in area) is connected to probe tip through a shunt capacitor(4.7nF).

The rf chokes are threaded into a long ceramic tube. Two pairs chokes(high Q, high impedance at 13.56MHz and 27.12MHz) are used in series to reduced rf effects. The floating reference electrode(stainless steel) is adopted for measure low-frequency fluctuation of plasma floating potential. The measurement principle of langmuir probe is shown in Fig.3.

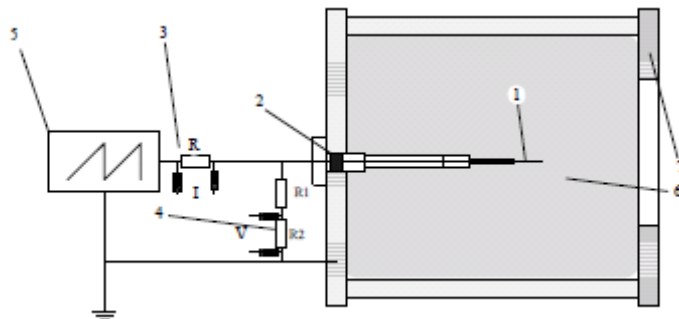


Fig.3 Measurement principle of Langmuir probe

1langmuir probe;2 vacuum ceramic seal;3 sampling resistance $R=100\Omega$;4 sampling resistance $R1=100K\Omega,R2=10K\Omega$;5 sweeping voltage source (sawtooth wave);6 plasma;7 vacuum house.

The DC sweeping voltage source($\pm 100V$) is electrically connected by sampling resistance R to langmuir probe and is electrically connected to ground(vacuum wall). The sampling resistor R is used to collect current flow I of probe and sampling resistor R1,R2 is used to acquir voltage V of probe. The resistor R1,R2 is much more large than plasma sheath. The circuit principle of

Langmuir probe used in the research is shown in Fig.4. The circuit is made of sweeping voltage source circuit and signal acquisition circuit.

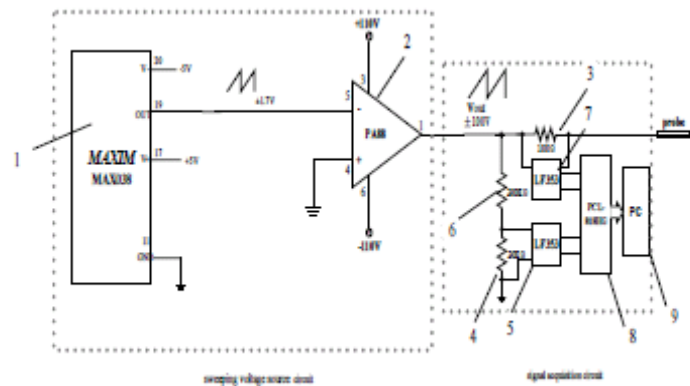


Fig.4 Circuit principle of Langmuir probe

The signal generator (MAX038, Maxim Integrated Products, Inc. USA) generate sawtooth wave signal($\pm 1.7V$) and is electrically connected to power amplifier(PA88 Apex Cirrus Logic, Inc. USA). PA88 amplify sawtooth wave signal($\pm 1.7V$)from MAX038,connected to langmuir probe by sampling resistor3. The signal acquisition circuit is used to obtain current I and voltage V of circuit of Langmuir probe. The differential amplifier7(LF353, national semiconductor corporation) is applied to measure voltage of resistor3 for obtaining current I of langmuir probe. The output of amplifier7 is connected to data acquisition card 8(PCL818HG,Advantech Co., Ltd.Taiwan).The card is inserted into Industrial Standard Architecture (ISA) slot of industrial control computer. The differential amplifier5(LF353, national semiconductor corporation) is applied to measure voltage of resistor4 for obtaining voltage V of langmuir probe. The PCL818HG card transmits I-V Data to computer based on Direct memory Acess(DMA). The floating potential is voltage at which the probe draws no current. The floating reference probe ,in this research, is applied to measure the floating potential. The traditional measurement circuit is shown in Fig.5.

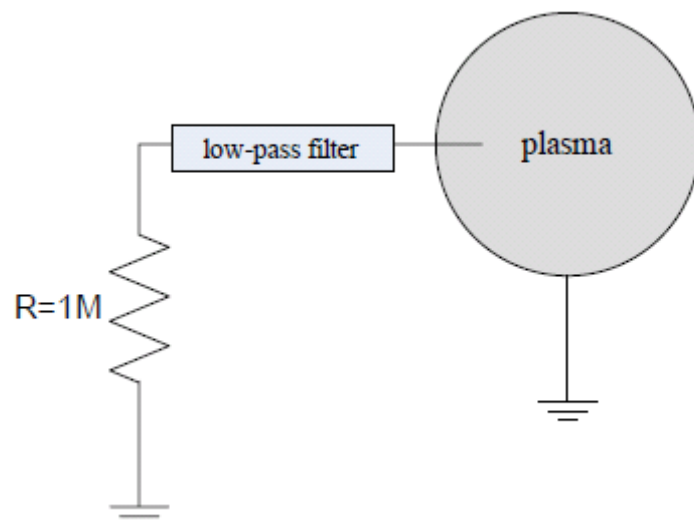


Fig.5 Traditional circuit principle of floating reference probe

The resistor $R(1M\Omega, \text{high resistance})$ is connected to probe tip by low-pass filter, and connected to ground electrode. The differential voltage of the resistor R is equal to floating potential approximately. In practically, it is not easy to measure directly the differential voltage due to the resistor's high resistance. In this paper a unity gain transimpedance amplifier instead of the resistor R is used to obtain the floating potential, as shown in Fig.6.

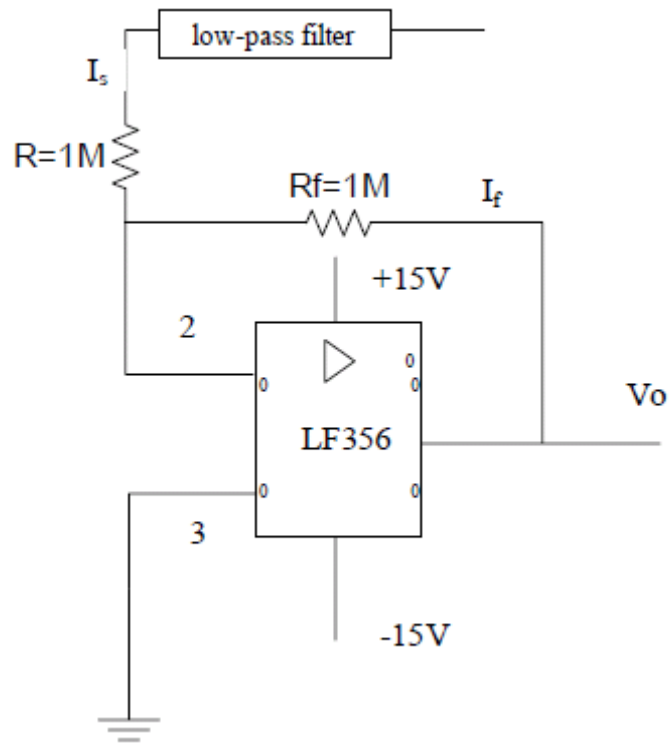


Fig.6 Circuit of plasma floating reference probe

The unity gain trans-impedance amplifier is made of resistor $R(1M\Omega, \text{high resistance})$ and I-V converter (high input impedance $1M\Omega$, low output impedance 50Ω) based on LF356 (dual JFET input operational amplifier, national semiconductor corporation, USA). The low-pass filter (cut-off frequency 1MHz) is used to block radio frequency signals.

3 Sheath resistance measurement

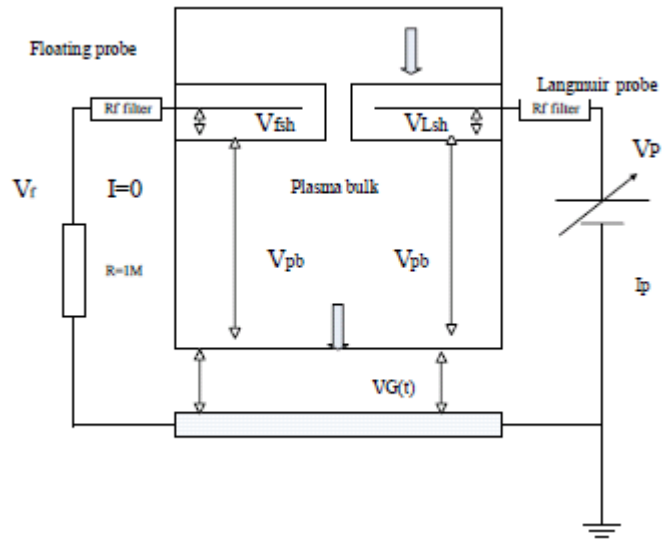


Fig.7 Circuit model of experiment system

The sheath is generated around langmuir probe tip, which is driven by sweeping voltage source. The sheath between plasma and vacuum wall(ground) voltage can be given. The radio-frequency part of sheath voltage can be neglected due to a passive rf compensated technology applied to probe. The change of can be expressed. Therefore, the probe current must be equal to the current through the grounded electrode sheath. In this paper, is measured by floating reference probe and by langmuir probe shown in Fig.8.

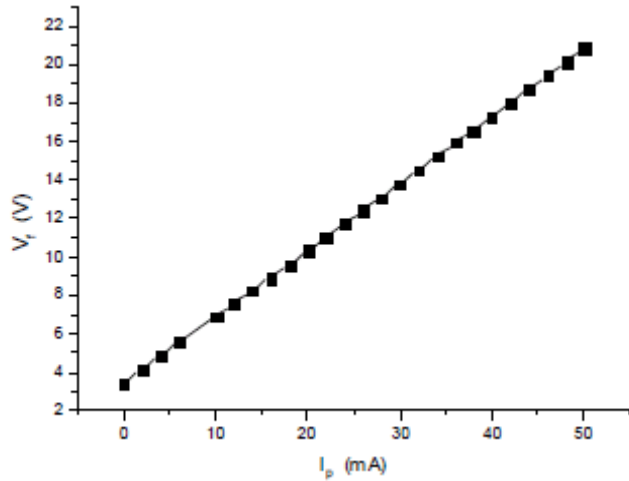


Fig.8 V_f as function of I_p

The slope of this line gives the sheath resistance, a value of $=349\Omega$. This would produce a 17.45V offset of the plasma potential at the 50mA electron saturation current. So the plasma sheath resistance effects langmuir probe I-V characteristic curve. The corrected I-V characteristic curve is shown in Fig.9.

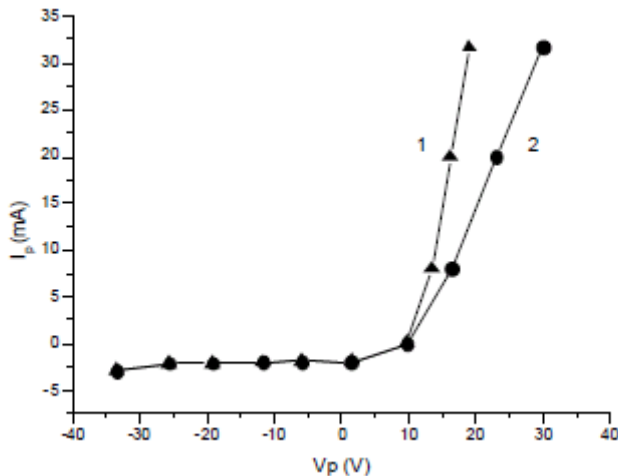


Fig.9 I-V characteristic curve(1 corrected ;2 uncorrected)

In Fig.9 I-V characteristic curve 1 deviates from exponential distribution and lead to DC shift in the plasma space potential due to the high sheath resistance. In curve 2 the DC shift in the plasma space potential is compensated.

4 Conclusion

The sheath resistance describes how the plasma space potential and floating potential increase with increasing electron current collected by a langmuir probe. The plasma potential rises in order to maintain current continuity because the increased current carried by electrons to the langmuir probe must be balanced by a decreased current carried by electrons to the grounded electrode or a net ion current there. If the sheath resistance is very high and the DC shift is not compensated, the calculated parameters will be incorrect by langmuir probe method.

5 Acknowledgement

This work was partially supported by the JSPS-CAS Core-University program in the field of 'Plasma and Nuclear Fusion'.

References

- 1 Francis F. Chen, Lecture Notes on LangmuirProbe Diagnostics, Mini-Course on Plasma Diagnostics, IEEE-ICOPS meeting,Jeju, Korea, June 5, 2003
- 2 Francis F.Chen,Jane P.Chang. Lecture Notes on Principles of Plasma Processing .Los Angeles: Kluwer/Plenum, 2002
- 10 I. H.Hutchinson, Principles of Plasma Diagnostics,2nd ed. London:Cambridge University Press, 2002
- 3 Francis F.Chen. Plasma Diagnostic Techniques(Chapter 4, 113–200) ed R H Huddlestone and S L Leonard . New York:Academic press , 1965.
- 4 J.D. Swift and M.J.R. Schwar, Electric Probes for Plasma Diagnostics. London: Ilife Books Ltd.,1970
- 5 Francis F.Chen. Probe Techniques, Plasma Physics Summer Institute Notes. Princeton :Princeton University ,1962.

- 6 Annemie Bogaerts,Erik Neyts,Renaat Gijbels,Joost van der Mullen.Gas discharge plasmas and their applications.spectrochimica acta part B,2002,57(4):609-658
- 7 Edward P.Szuszczewice.Area influences and floating potentials in langmuir probe measurements. Journal of Applied Physics,1972, 43(3):874-880.
- 8 Isaac D Sudit,Francis F Chen.RF compensated probes for high-density discharges. Plasma Sources Science and Technology,1994,3(2):162-168.
- 9 Magdalena Aflor,J.L.Sullivan.Langmuir probe measurements in an asymmetrical rf discharge.romanian reports in physics,2005,57(1):71-77
- 10 M.Hannemann,F.Sigeneger.Langmuir probe measurements at incomplete rf-compensation.Czechoslovak journal of physics,2006,56(10):B740-B748
- 11 M.B.Hopkins langmuir probe measurwments in the gaseous electronics conference rf reference cell.journal of research of the national institute of standards and technology,1995,100(4):415-425
- 12 E.V.Shun'ko.Influence of ohmic resistance of a cylindrical langmuir probe on its I-V characteristic. review of scientific instruments,1991,62(12):3110-3111
- 13 Francis F Chen.Double-probe method for unstable plasma.review of scientific instruments,1964,35(9):1208-1212
- 14 H Conrads M Schmidt.Plasma generation and plasma sources. Plasma Sources Science and Technology,2000,9(4):441-454
- 15 N St J Braithwaite.Introduction to gas discharges. Plasma Sources Science and Technology,2000,9(4):517-527
- 16 RobertN.Carlile,Tucson, Ariz.Langmuir probe system for radio frequency execited plasma processing system. United States Patent:US5339039B2,1994-08-16
- 17 Hopkins et al.Radio frequency langmuir probe[P].United States Patent:US7015703B2,2006-03-21
- 18 Ricky Marsh,Satanley siu. plasma probe and method for making same.United States Patent:US6553853B2,2003-04-29
- 19 Yuancai Ye,R.Kenneth Marcus.Application of a tuned langmuir probe for the diagnostic study of radio frequency glow discharges:instrumentation and theory.spectrochimica acta part B,1995,50(12):997-1010
- 20 Yuancai Ye,R.Kenneth Marcus.Harware and software systems for the determination of charged particle parameters in low pressure plasma using impedance-tuned langmuir probes.spectrochimica acta part B,1997,52(14):2025-2041
- 21 N.St.J.Braithwaite.Electron energy distribution functions in processing plasmas. Pure and Applied Chemistry,1990,62(9):1721-1728
- 22 G.J.H.Brussaard,M.van der Steen,M.Carrere,M.C.M.van de Sanden, and D.C.Schram.Langmuir probe measurement in an expanding magnetized plasma.physical review E,1996,54(2):1906-1911.
- 23 A.D.Cheetham,L.Davidson,J.Jakobsen,T.Lund,J.P.Rayner.Stand-alone microprocessor controlled fast sweep langmuir probe driver..review of scientific instruments,1997,68(9):3405-3411
- 24 Klaus Wiesemann.Characterisation of plasmas by advanced diagnostic methods[J]. Pure and Applied Chemistry,1996,68(5):1029-1034
- 25 M.Klick,M.Kammeyer,W.Rehak,et al.Innovative plasma diagnostics and control of process in reactive low-temperature plasma.surface and Coatings technology ,1998,98:1395-1399
- 26 P. Awakowicz, R. Schwefel, P. Scheubert and G. Benstetter. Deposition of a-C:H films with an ECWR-reactor.
- 27 Jennifer LKleber, Lawrence J Overzet.Sheath resistance measurements in the GEC reference reactor. Plasma Sources Science and Technology,1999,8(4):534-543.
- 28 Henry M.Musal,JR. Electrostatic Probe and Electronic Circuit for Low-Temperature Plasma Measurements. Journal of Applied Physics,197041(6): 2605-2609.

Progress of Long Pulse and LHCD Discharges on HT-7 Tokamak

GAO Xiang (高翔)^{1*}, GONG Xianzu (龚先祖)¹, HU Liqun (胡立群)¹, SHAN Jiafang (单家方)¹, K.Toi², S.Morita², LIU Jin (刘瑾)³, HU Jianshen (胡建生)¹, YANG Jianhua (杨建华)¹, and HT-7 team¹

¹*Institute of Plasma Physics, Chinese Academy of Sciences,*

P.O.Box 1126, Hefei, Anhui 230031, P.R.China

²*National Institute for Fusion Science,*

322-6 Oroshi-cho, Toki-city, Gifu 509-5292, Japan

³*Yunnan University, Kunming, Yunnan 650091, P.R.China*

***E-mail:** xgao@ipp.ac.cn

Abstract

Long pulse plasma (up to 400 s) has been achieved by lower hybrid current drive (LHCD) in the HT-7 superconducting tokamak. High power lower hybrid wave (LHW) was performed (P_{LHW} \sim 800 kW at 2.45 GHz) recently. Lower hybrid current drive efficiency was studied for different injected powers and for different plasma current. Electron temperature and Z_{eff} were measured and studied in LHCD discharges. Improved particle confinement was observed by the application of LHCD as characterized by an increase in the central line averaged electron density and the decrease in D_α emission. The particle confinement time (τ_p) was increased from 15 ms to 22 ms.

Keywords: LHCD, long pulse, confinement

PACS: 52.50.Sw, 52.55.Fa

1. Introduction

Progress has been achieved experimentally in many tokamaks since the 1980s using lower hybrid current drive (LHCD) [1, 2]. In the Tore Supra tokamak [1], up to 0.5 MA full non-inductively driven current with 6 min pulse length has been achieved. In the TRIAM-1M tokamak [2], a long-pulse discharge has been sustained by LHCD for over 2 h.

Lower hybrid wave (LHW) experiments have been oriented towards the exploration of current drive (CD) and current profile control applicability for steady-state operation of tokamak plasmas. Efforts to further optimize plasmas will benefit from the following aspects: (1) higher power, longer duration, (2) the development of feedback control of the current profile and (3) high LHCD efficiency. Experiments in many tokamaks such as Tore Supra [1], TRIAM-1M [2], FTU [3], JET [4], JT-60U [5] and HT-7 [6–10] have shown that LHCD is one of the most efficient methods to drive non-inductive current in tokamak plasma.

The LHCD experiment has been conducted on the HT-7 tokamak since 1999 [7]. Recently, the main objectives of developing LHCD technology on HT-7 have been to sustain long pulse discharges and improve plasma confinement [6, 13, 14]. Long-pulse plasmas up to 400 s were achieved by LHCD in the HT-7 superconducting tokamak in 2008. A high power (0.8 MW at 2.45 GHz) LHCD experiment was recently performed on the HT-7 tokamak. In this paper, the experimental progress in LHW experiments concerning long pulse, confinement, and LHCD

efficiency at high power is summarized.

2. Long-pulse experiment progress

The HT-7 superconducting tokamak has a major radius of $R = 1.22$ m and a minor radius of $a = 0.27$ m in the circular cross-section. There are two layers of thick copper shells, and between them are located 24 superconducting coils which can create and maintain a toroidal magnetic field (B_t) of up to 2.5 T. The HT-7 tokamak with the limiter configuration is normally operated under the basic parameters: $I_p = 100\text{--}250$ kA, the toroidal magnetic field $B_t = 2$ T, the central line-averaged plasma density is $(1\text{--}6) \times 10^{19} \text{ m}^{-3}$, central electron temperature $T_e = 0.5\text{--}3.0$ keV and central ion temperature $T_i = 0.2\text{--}1.5$ keV. The plasma current, position and central line averaged electron density were feedback controlled during discharges. A stainless-steel liner was installed in the vacuum chamber at the radius of 0.32 m [7].

Figure 1 shows the progress of long-pulse operation ($t = 400$ s) in the HT-7 superconducting tokamak from 1994 to 2008. It is a great advancement in the study to sustain discharge under quasi-steady state operation. Before the 2003 experimental campaign, HT-7 was equipped with one high field side belt limiter and two poloidal graphite limiters with an active coolant stainless-steel heat sink. Several technical improvements were made based on the understanding of plasma–surface interactions. GBST1308 doped graphite was used as a limiter material. It has high thermal conductivity up to $180 \text{ W}(\text{mK})^{-1}$, whose good thermal shock resistance can withstand 6 MW m^{-2} high heat loads for 60 s. All carbon tiles were coated with $100 \mu\text{m}$ SiC functional gradient coating, which was also used for the limiter and the Faraday screen of the IBW antenna. 24 pieces of a ferromagnetic material (ferritic steel) were installed inside the vacuum

chamber, to be used as plasma facing components (PFCs) and for the reduction of the magnetic ripple [8]. About 1 min duration of long-pulse plasmas was achieved on HT-7 in 2003 as shown in figure 1. In 2004, actively cooled toroidal double-ring graphite limiters at the bottom and the top of the vacuum vessel were developed and tested for long-pulse operation on the HT-7. The grill of the LHW was improved into a 3×16 multi-junction and coated with TiN film. The width of the main lobe of the wave power spectrum was about $\Delta n_{\parallel} = 0.6$. The power spectrum of the launched wave could be adjusted in the range $n_{\parallel}^{\text{peak}}$ of 1.25–3.45 by means of feedback control of the phase difference between adjacent wave-guides of the coupler, where $n_{\parallel}^{\text{peak}}$ is the peak value of the parallel refractive index of the launched wave. The radial position of the antenna was adjusted with respect to the last closed flux surface (LCFS) in order to optimize the RF coupling. With the purpose of protecting the LHW antenna from high heat flux of thermal and non-thermal particles, the guard limiters were set at both sides of the LHW antenna in the 2005 experiment campaign.

Figure 2 shows a typical LHCD discharge with 400 s pulse duration achieved on the HT-7 tokamak in 2008, where the plasma current is $I_p = 60$ kA, the central electron temperature is 1 keV, and the central line average density is 0.6 in units of 10^{19} m^{-3} . In the HT-7 long-pulse experiment, the plasma current I_p is feedback-controlled by means of center solenoid coils during LHCD discharges [13–15]. The horizontal displacement and the vertical displacement are well feedback controlled in Fig. 2.

3. LHCD efficiency

Full non-inductive CD discharges for several seconds have been reported on the HT-7 superconducting tokamak [6, 10]. For non-zero loop voltage pulses, the residual electric field

accelerates the fast electrons consequently enhancing the CD efficiency according to Fisch's theory of electric conductivity in hot plasmas [11–16]. In LH power scan experiments for CD efficiency, the plasma current was maintained at a constant value during LHCD. Neglecting the small contribution of bootstrap current and assuming that the sum of the LHW driven current I_{rf} and the inductively driven current I_{oh} is unchanged, then the experimental value of CD efficiency can be calculated by the formula:

$$\eta = -\frac{\Delta V}{V_{OH}} \frac{\bar{n}_e R I_p}{P_{LHW}},$$

where P_{LHW} is the LHW power, \bar{n}_e is the line-averaged electron density, R is the plasma major radius, and the plasma current is $I_p = I_{rf} + I_{oh}$, $I_{rf} = (-\Delta V/V_{OH})I_p$, and $\Delta V = V_{LHW} - V_{OH}$. High power (up to 800 kW) lower hybrid current drive experiment was performed on HT-7 tokamak. The result of the LH power scan experiment is shown in figure 3.

It is observed that the LHCD efficiency decreases with increasing LHW power. The normalized value of the reduced loop voltage ($-\Delta V/V_{OH}$) increases almost linearly with the LHW power, but saturates at a critical power ($P_{LHW} \sim 300$ kW) as shown in figure 4. It was observed in JT-60U that the LHCD efficiency is proportional with the electron temperature and is against to the Z_{eff} [5]. Therefore, the electron temperature and Z_{eff} were measured and studied recently in HT-7 tokamak. The diagnostics of soft-X ray PHA system (central electron temperature T_e) in HT-7 shows that the electron temperature is weakly increased at $P_{LHW} = 300$ –600 kW in figure 5. The visible bremsstrahlung radiation for Z_{eff} measurement shows that the Z_{eff} is strongly enhanced at $P_{LHW} = 300$ –600 kW in figure 6. Therefore, this result is major caused by an impurity behaviour at a high power of LHW on HT-7 tokamak.

4. Confinement study

Improved particle confinement is observed during LHCD as characterized by the increase in the central line-averaged electron density and decrease in D_a emission. Figure 7 illustrates a typical discharge at the plasma parameters: $I_p = 130$ kA, $B_t = 1.95$ T, $\bar{n}_e = 1.5 \times 10^{19} \text{ m}^{-3}$, $T_e = 0.8$ keV, $T_i = 0.3$ keV, $P_{LHW} = 300$ kW, $n_{//}^{\text{peak}} = 2.35$. When the LHW is injected, the electron temperature in the central region increases from 0.6 to 0.8 keV (as shown in figure 7(b)), and the plasma loop voltage drops from 1.5 to 0.4 V (see figure 7(d)). Figure 7(e) shows a feedback signal of gas puff injection and (f) the injected LHW power. It is seen that particle confinement enhancement is observed clearly during the LHCD phase, which is characterized by the slight increase in the central line averaged electron density (figure 7(b)) and by the decrease in the D_a emission (figure 7(a)). It is calculated that the particle confinement time ($\tau_p = N_e / (S_e - dN_e / dt)$, where N_e is sum of particles, S_e is particle source flux) is 1.5 ms for the ohmic heating phase. The calculated particle confinement time is $\tau_p = 22$ ms during the LHCD phase, and it increased by about 1.5 times. It is observed that the energy confinement time for LHCD plasmas is lower than that of ohmic discharges [17]. The impurity behaviours enhanced the plasma radiation power, and it decreased the energy confinement time.

5. Summary

Long pulse plasma (~ 400 s) has been achieved by lower hybrid current drive (LHCD) in the HT-7 superconducting tokamak. The current drive efficiency experiment with an LHW was performed on the HT-7 tokamak at a high power $P_{LHW} \sim 800$ kW. It is observed that the LHCD efficiency decreases with increasing LHW power. The normalized value of the reduced loop

voltage ($-\Delta V/V_{OH}$) increases almost linearly with the LHW power, but saturates at a critical power ($P_{LHW} \sim 300$ kW). It is nearly constant at higher power (300–600 kW) due to the increase of the Z_{eff} . It is observed that the particle confinement time is increased by LHCD. The energy confinement time is not improved during high power LHW experiments. Dynamic impurity control may be a key issue in the high power LHCD experiments on the HT-7 tokamak in the future.

Acknowledgments

This work was partly supported by the JSPS-CAS Core-University Program on Plasma and Nuclear Fusion.

References

- [1] Houtte D V et al 2004 Nucl. Fusion 44 L11
- [2] Itoh S et al 1999 Nucl. Fusion 39 1257
- [3] Angelini B et al 2005 Nucl. Fusion 45 S227
- [4] Pamela J et al 2003 Nucl. Fusion 43 1540
- [5] Ide S et al 1996 Plasma Phys. Control. Fusion 38 1645
- [6] Liu J et al 2006 Phys. Lett. A 350 386
- [7] Kuang G L et al 1999 Nucl. Fusion 39 1769
- [8] Li J G et al 2003 Phys. Plasmas 10 1653
- [9] Ding B J et al 2003 Nucl. Fusion 43 558
- [10] Gao X et al 2005 J. Nucl. Mater. 337 835

- [11] Giruzzi G et al 1997 Nucl. Fusion 37 673
- [12] Fisch N J 1987 Rev. Modern Phys. 59 175
- [13] Chen Z Y et al 2006 Plasma Phys. Control. Fusion 48 1489
- [14] Shi Y J et al 2004 Rev. Sci. Instrum. 75 4930
- [15] Gao X et al 2008 Nucl. Fusion 48 035009
- [16] Goniche M et al 2004 Plasma Phys. Control. Fusion 46 899
- [17] Gao X et al 2008 Plasma Phys. Control. Fusion 50 035006

Figure's Captions:

Fig.1 The progress of long-pulse plasma operation on HT-7 tokamak in the past ten years. Up to 400 s of long-pulse LHCD plasmas have been achieved in 2008.

Fig.2 A typical long-pulse LHCD discharge on HT-7 tokamak, where plasma current is $I_p = 60$ kA, the center electron temperature is about 1 keV, and center line average density is $\bar{n}_e(0) = 0.6$ in unit of 10^{19} m^{-3} .

Fig.3 LHCD efficiency versus different injected LHW power on HT-7 tokamak, where plasma current is 120 – 150 kA, and average density is $1.3 – 1.8 \times 10^{19} \text{ m}^{-3}$.

Fig.4 Reduced loop voltage versus injected LHW power, where plasma current is 120 – 150 kA, and average density is $1.3 – 1.8 \times 10^{19} \text{ m}^{-3}$ for all shots.

Fig.5 The dependence of electron temperature on injected LHW power.

Fig.6 The dependence of the Z_{eff} on injected LHW power.

Fig.7 The waveforms of a typical high power LHW ($>300\text{KW}$) discharge (shot 78673). (a) $H_{\alpha}(D_{\alpha})$ radiation; (b) line average electron density and central electron temperature; (c) plasma current; (d) plasma loop voltage; (e) gas puffing; (f) LHW power.

Figures:

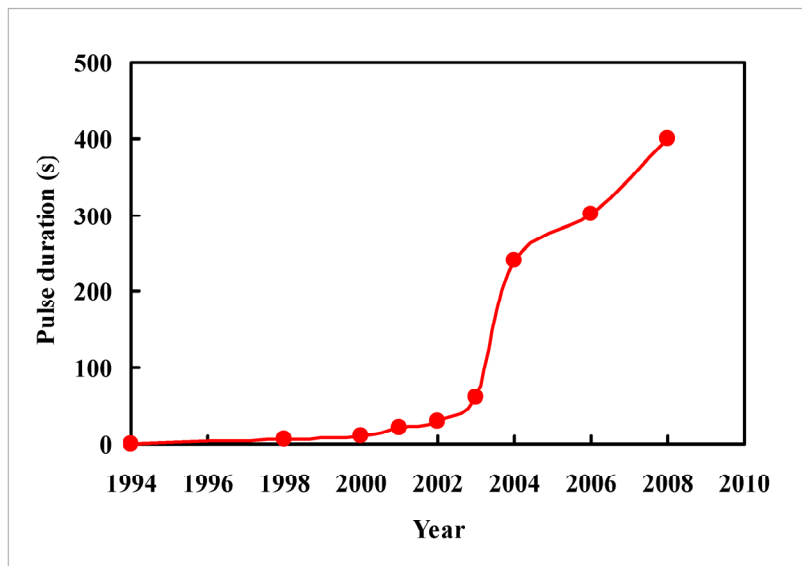


Fig.1

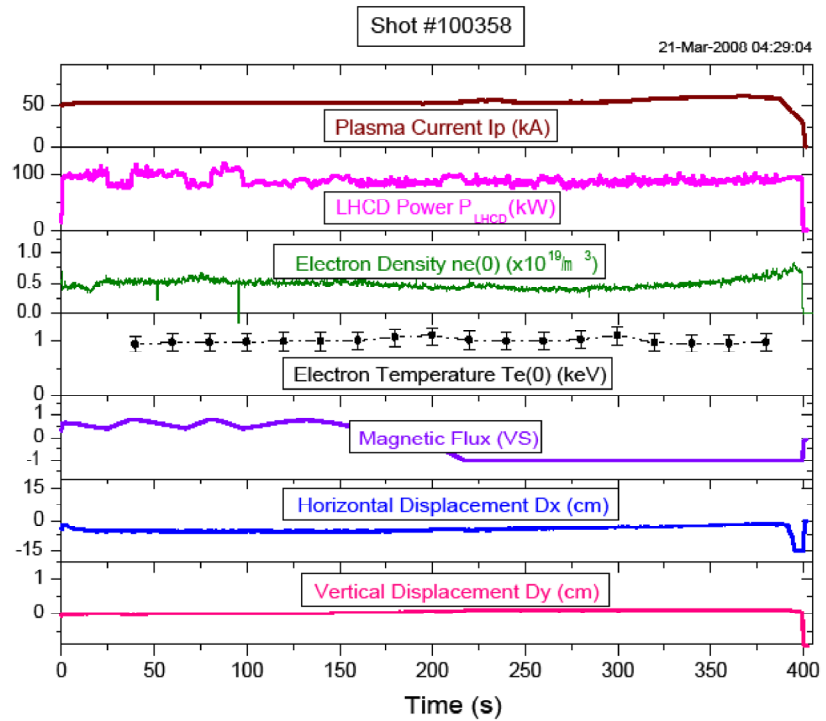


Fig.2

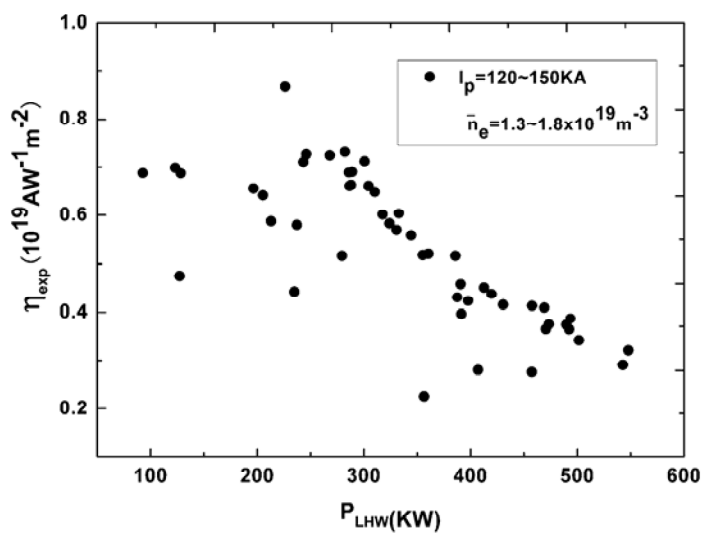


Fig.3

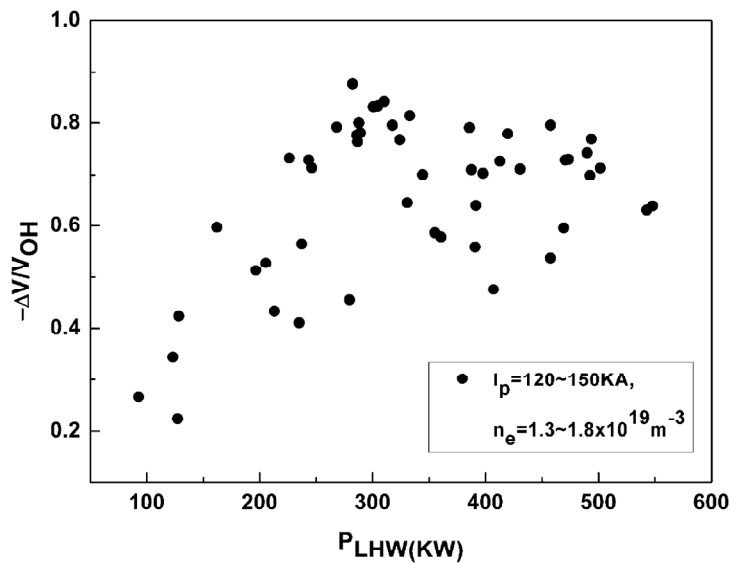


Fig.4

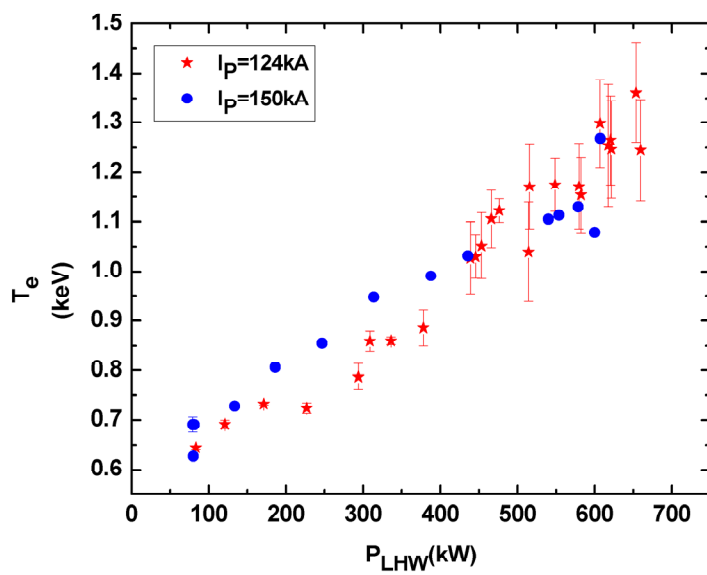


Fig.5

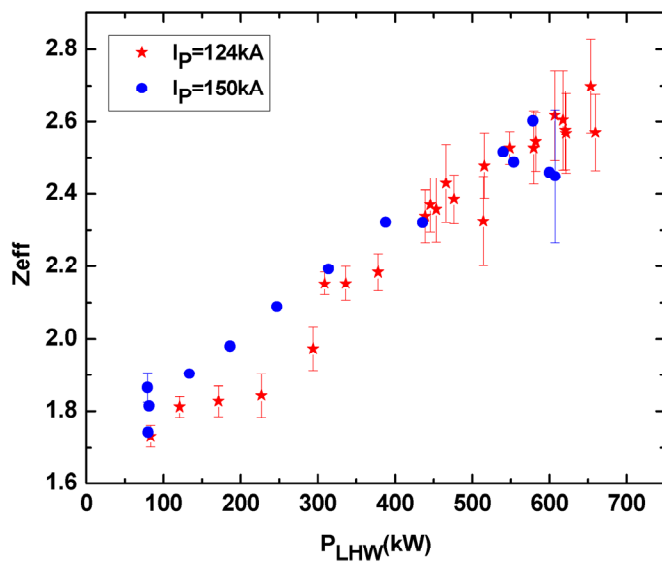


Fig.6

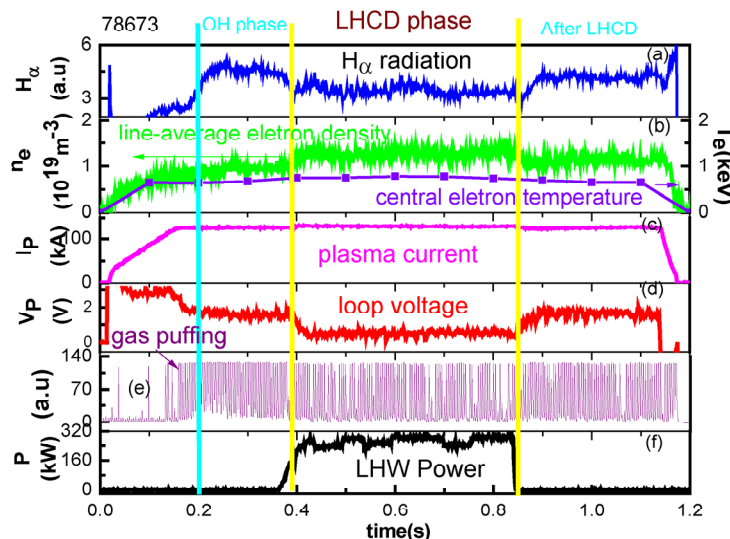


Fig.7

(END)

Present Progress of Plasma Transport Study on HL-2A

X.T. Ding¹, W.W. Xiao¹, X.L. Zou², H.J. Sun¹, Yi Liu, L.H. Yao¹, J. Rao¹, B.B. Feng¹, Z.T. Liu¹, Y. Zhou¹,
Q.W. Yang¹, L.W. Yan¹, J.Q. Dong¹, X.R. Duan¹ and HL-2A team

¹*Southwestern Institute of Physics, P.O. Box 432, Chengdu, China*

²*Association Euratom-CEA, CEA/DSM/IRFM, CEA/Cadarache, 13018 St Paul-lez-Durance, France*

Abstract. The recent experiments of HL-2A tokamak have been focused on studying the physics of turbulence and transport. A spontaneous particle transport barrier has been observed in Ohmic discharges without any external momentum input. The barrier was evidenced by density perturbation study using modulated supersonic molecular beam injection (SMBI) and microwave reflectometry. The new features of the non-local transport effect induced with SMBI have been analyzed. The suppression of $m/n = 2/1$ tearing modes may be sustained by ECRH modulation at a frequency about 10 Hz. Continuous confinement improvement was observed after the mode suppression.

1. Introduction

The understanding of transport physics and plasma confinement is an important subject for the design of future fusion reactors, especially the physics for particle transport^[1-4], electron heat transport^[5-8] and the internal transport barrier formation^[9-11]. The recent experiments of HL-2A tokamak ($R=1.65$ m, $a=0.4$ m) have been focused on studying the physics of turbulence, transport, MHD instabilities and energetic electron dynamics. This paper presents some new experimental results for transport on HL-2A, including the spontaneous particle transport barrier, the non-local phenomena triggered by SMBI and the confinement features during modulated ECRH.

2. Present Status of the HL-2A Tokamak The main operation parameters of the device are as follows: the toroidal magnetic field is 1.2-2.7 T, the plasma current is 150-450 kA and the plasma density is $(1 - 6) \times 10^{19}$ m⁻³. ECRH system with four 68 GHz / 500 kW / 1 s gyrotrons has been built up in HL-2A. The ECRH power with both fundamental O-mode and second harmonic X-mode up to 2 MW is injected from the low field side of the device. The deposit position of ECRH is determined by the toroidal magnetic field. When toroidal magnetic field varies from 2.43T to 2.2T for O-mode, the resonance point can be replaced from the plasma core to the point at $r=16$ cm. The wave energy deposits in a range of 3cm. The efficiency of the transmission system is more than 80 %, so at least 1.6 MW power can be injected into plasmas. The electron and ion temperatures are 5 keV and 1.5 keV during 2MW ECRH respectively.

The supersonic molecular beam injection (SMBI) system has been improved with the modulation frequency reaching 50 Hz. Particles of the gas are accelerated by imposed pressure through the nozzle to get into the vacuum chamber of the tokamak. It is an attempt to enhance the penetration depth and fuelling effect. The penetration depth is very important to trigger the non-local transport phenomena. H_α intensity profile measured by H_α detector array and the density profiles measured by microwave reflectometry indicate that the penetration depth of the SMBI is more than $\rho = 0.7$. The SMBI injection has deeper penetration and better locality than conventional gas puffing. The system is not only an advanced technology for fuelling, but also a powerful tool (combined with microwave reflectometer or ECE) for particle as well as electron thermal transport studies.

The device is equipped with extensive and advanced diagnostics for transport study, including ECE and microwave reflectometry with high spatial and temporal resolution. There are also the Thomson scattering for electron temperature measurement, the 8 channel HCN laser interferometer for density profile, the five soft x-ray arrays for MHD study and the Doppler reflectometry for plasma rotation and core turbulence measurements.

3. Experimental results

3.1 Spontaneous internal particle transport barrier

On HL-2A tokamak, spontaneous particle transport barriers were observed in purely Ohmic heating plasmas without any external momentum input. The internal particle transport barriers (pITBs) were found to be formed when the line averaged electron density increases to a critical value in HL-2A experiments. Figure 1 shows the temporal evolution of the density profile measured by a broadband O-mode reflectometer for a representative discharge with a transition to pITB formation. The pITB developed gradually around $r = 29$ cm. The critical line-averaged electron density corresponding to this transition is $n_c = 2.2 \times 10^{19} \text{ m}^{-3}$. The width of the barrier is 1-2 cm. There is a drastic change in the density gradient through the barrier: $L_n \sim 10 \text{ cm}$ at the barrier, $L_n \sim 50 \text{ cm}$ for $r=20-28 \text{ cm}$ and $L_n \sim 25 \text{ cm}$ for $r=30-36 \text{ cm}$.

To study the transport features of the

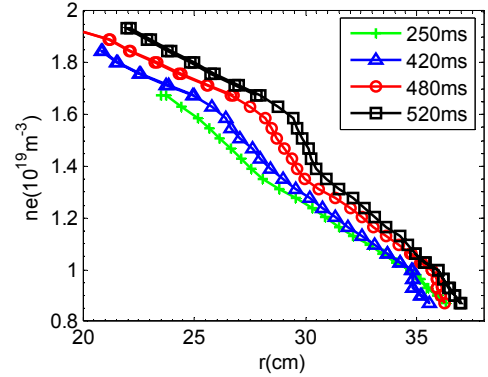


Fig.1. Temporal evolution of the density profile at selected moments: before the appearance of the barrier (250 ms); at the beginning of the appearance of the barrier (420 ms); strong barrier (480 ms); just after a particle pulse injection by SMBI (520 ms).

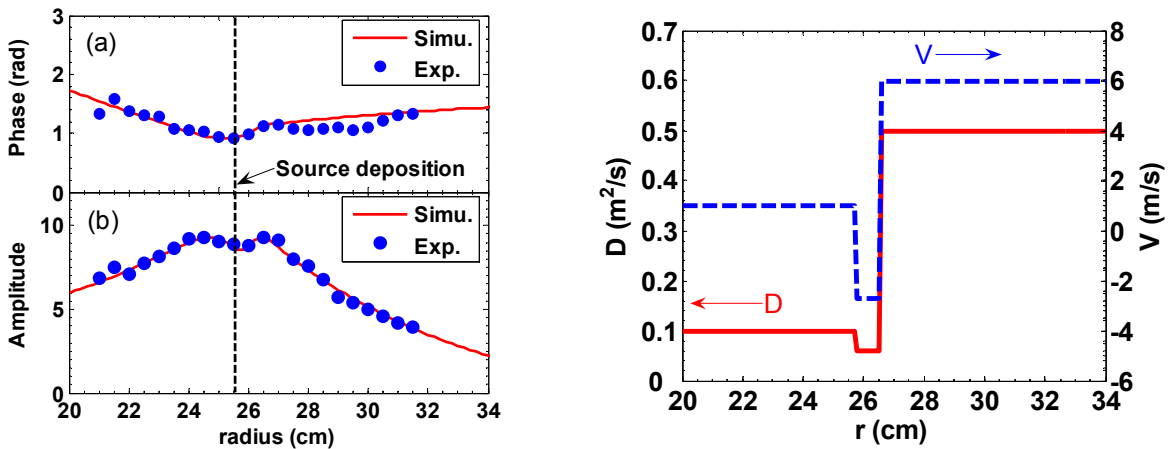


Fig. 2. Profiles of the phase (a) and amplitude (b) of the 1st Fourier harmonic of the modulated density. (c) Profiles of the diffusivity D and convective velocity V for the simulation.

pITB, the density modulation generated by SMBI has been employed. The modulation frequency

and the pulse duration of the SMBI are 9.6 Hz and about 6 ms, respectively, while the gas pressure is 1.3 MPa in the experiments. The simulation with an analytical model for particle transport was carried out to characterize this barrier quantitatively. The phase and the amplitude of the 1st harmonic of the modulated density are displayed in Figs. 2 (a) and (b), where the solid lines and closed circles are the simulation and experimental results, respectively. The model diffusivity D and convective velocity V employed in the simulation are presented in Fig. 2(c): $D_1 = 0.1 \text{ m}^2/\text{s}$, $V_1 = 1.0 \text{ m/s}$ in the domain I ($r < x_1$); $D_2 = 0.045 \text{ m}^2/\text{s}$, $V_2 = -2.7 \text{ m/s}$ in the domain II ($x_1 < r < x_2$), and $D_3 = 0.5 \text{ m}^2/\text{s}$, $V_3 = 6.0 \text{ m/s}$ in the domain III ($r > x_2$). The model apparently represents the experiment quite well. In comparison, a SMBI modulation experiment has also been performed for a discharge with a density ($n_e = 1.9 \times 10^{19} \text{ m}^{-3}$) lower than the critical density n_c . In this case, no barriers have been observed and the diffusivity obtained with the same method is $D = 0.25 \text{ m}^2/\text{s}$ for $r = (28-31) \text{ cm}$. In addition, a negative convective velocity has been found as $V = -2.2 \text{ m/s}$ for $r = (28-31) \text{ cm}$ and $V = -4.2 \text{ m/s}$ for $r = (31-33) \text{ cm}$. From the density modulation experiments, it may be concluded that the convective velocity is negative when the density is lower than the threshold and positive when the density exceeds the threshold, except inside the barrier where the particle convective velocity remains negative. The diffusivity D is rather well-like instead of step-like.

The sign change of the convective velocity can be explained with the TEM/ITG turbulence regimes [10, 11]. The density threshold may correlate with the TEM/ITG transition via the collisionality. However, the mechanism leading to the pITB formation remains unclear at present. On the other hand, the formation of the barrier may coincide with the TEM/ITG transition. Thus, it is not excluded that the transport barrier is created initially by the discontinuity or jump in the convective velocity during the TEM/ITG transition, or more precisely, by two convective velocities in opposite direction (inward/outward) at the barrier. This speculation needs, of course, further experiments to be confirmed.

2.2 Non-local transport with SMBI

Since the first observation of the non-local electron thermal transport on TEXT-U in 1995 [12], a variety of edge cooling techniques [13- 15] have been widely used in studying the effect, including impurity injection by laser ablation, ice pellet injection, carbon-based molecule injection, etc. The effect has been observed after supersonic molecular beam being injected the HL-2A tokamak.

Shown in Fig.3 is the time evolution of electron temperature T_e , measured with ECE at different radii during modulated SMBI of 4 ms duration. The electron temperature sharp dropping in the edge and fast rising in the core after each SMB pulse are clearly shown. In addition, the duration of the core electron temperature rise may be prolonged by adjusting the time separation between two successive SMB pulses, which are 20 ms, 20 ms and 15 ms, respectively, for the three successive series here. Besides, both the thermal radiation and the $\text{H}\alpha$

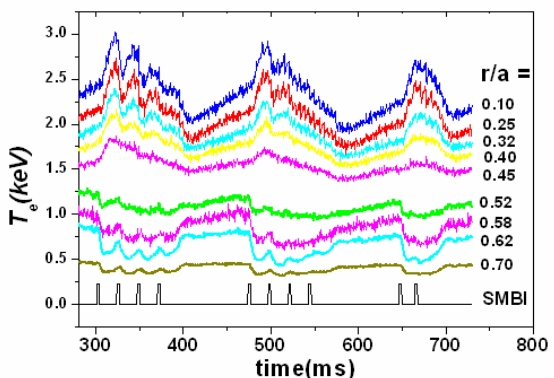


Fig. 3. Temporal evolution of T_e measured by the ECE at different radii.

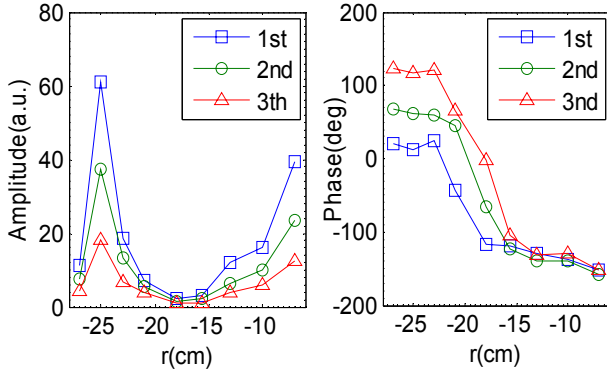


Fig. 4. Amplitudes and phases of the first three harmonics after FFT of the Te measured by ECE (shot 8337, $B_t = 1.4$ T, $n_e = 0.7 - 1.0 \times 10^{19}$ m $^{-3}$, $I_p = 180$ k.).

takes place. The two peaks in each amplitude profile and the two corresponding troughs in each phase profile are apparent for all harmonics. These may indicate that two perturbation sources exist in the regions outside and inside the inversion radius, respectively. The position of the outer initial heat pulse was found to be at $r \sim -25$ cm, depending on the deposition location of SMBI. The behaviour of the perturbation shows usual propagation features of SMBI cold pulse in this region. The value of χ_{eHP} deduced from the Fourier analysis, showing agreement with the result from sawtooth pulse propagation, is in the range of (2 – 3) m 2 /s. In the inner region, the initial perturbation was found to be in the core. The profiles of the amplitude and the phase of the first three harmonics are independent of the SMBI modulation frequency. The steeper profiles around the interface mean a reduction of heat transport and indicate formation of an internal transport barrier in this region. With the good flexibility and easy controllability of the SMBI parameters (gas pressure, modulation frequency, duty cycle, etc.), modulated SMBI has been proven to be an effective tool for studies of the non-local effect. Further investigation on the mechanism of the effect is undertaken on HL-2A.

3.3 Improved Confinement during Off- Axis ECRH The investigation on the suppression of $m = 2/n = 1$ tearing mode by off-axis ECRH has been performed. With the instability suppression, obvious increase of the plasma density and stored energy has been observed. A transient improved confinement was obtained after ECRH switch-off in the experiments with the ECRH power in the range of $0.6 < P_{ECRH}/P_{ohm} < 1$. The interesting feature of the confinement after ECRH switch-off motivated us to apply successive ECRH pulses for sustaining MHD-free phase and obtaining a continuous confinement improvement.

The ECRH power must be deposited just around the flux surface where the $m/n=2/1$ magnetic islands were located in order to achieve perfect mode stabilization. The frequency and depth of the modulation were about 10 Hz and 100%, respectively, with a duty cycle of 50%. In this operation mode the maximum power that the gyrotron could deliver was limited to 250kW. The results from two identical discharges with the ECRH power deposited at (#8207) and 3 cm inside (#8236) the $q = 2$ surface, respectively, are shown and compared in Figure 5. The behaviors of the line averaged density, the central electron temperature (soft x-ray), and the stored energy are the same in the two shots. The amplitude of the $m/n=2/1$ magnetic fluctuations begins to decrease after the injection of modulated ECRH at 425ms in discharge #8207. Concurrently with the suppression of the tearing

emission decrease when the non-local effect appears.

The transport properties of the non-local phenomena were analyzed with Fourier transformation of the modulated Te measured with ECE. The results for the modulation of SMBI at $f = 10$ Hz are given in Fig. 4. A strong decrease in amplitude and a clear phase jump for all harmonics occur at $r \sim -18$ cm, where the reverse of the electron temperature change

mode the plasma density, the stored energy, and the energy confinement time increase $\sim 80\%$, $\sim 50\%$, and $\sim 40\%$, respectively, indicating a significant confinement improvement. Thus, the experimental results clearly show that indeed a better suppression may be achieved with such a lower frequency modulated ECRH in the vicinity of the $q = 2$ surface. The suppression event is characterized by a feature of the continuous improvement of confinement, i.e. the steady increases of the plasma density, temperature, stored energy and energy confinement time throughout the modulated ECRH period. This provides an alternative way to control the $m=2/n=1$ tearing mode in addition to the continuous ECRH or modulated ECRH with a high frequency in phase with the O-points of the islands.

4. Conclusions

A natural particle transport barrier has been evidenced firstly in the ohmic plasmas in HL-2A without any auxiliary heating and external momentum input. The barrier is located around $r/a=0.6-0.7$ with a width of 1-2 cm. A threshold in central line averaged density has been found for the observation of the particle transport barrier with $n_c=2.2\times 10^{19} \text{ m}^{-3}$. By analysing the propagation of a particle wave, it is found that the diffusivity D is rather well-like than step-like with important reduction inside the barrier. The convection is found to be inward outside of the barrier, and outward inside the barrier.

The non-local phenomena triggered by SMBI have been observed on HL-2A firstly. The core electron temperature T_e rise increases from 18% to more than 40% and the duration of the T_e rise could be prolonged by changing the conditions of SMBs injection. Repetitive non-local effect induced by modulated SMBs allows Fourier transformation of the temperature perturbation, yielding detailed investigation of the pulse propagation. The suppression of $m=2/n=1$ tearing mode has been realized with heating located around $q=2$ surface. The continuous improvement of confinement increase steadily throughout the modulated off-axis ECRH.

Acknowledgement

This work was supported by the National Natural Science Foundation of China (Grant No.10335060) and supported partially by the JSPS-CAS Core University Program in the field of 'Plasma and Nuclear Fusion'.

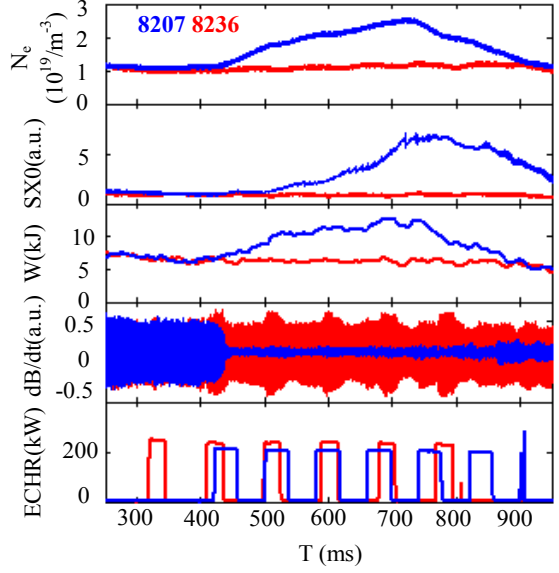


Fig.5 Time traces of the density, the SXR intensity, the stored energy, the time derivative of the poloidal magnetic field and the power of ECRH deposited at (the blue traces) and inside (the red traces) the $q=2$ surface.

References:

- [1] F. Wagner, G. Faussmann, D. Grave *et al.*, Phys. Rev. Lett. **53**, 1453 (1984)
- [2] M.J. Greenwald, D.A. Gwinn, S. Milora *et al.*, Phys. Rev. Lett. **53**, 352 (1984)
- [3] C.L. Fiore, J.E. Rice, P.T. Bonoli *et al.*, Phys. Plasmas **8**, 2023 (2001)
- [4] E.J. Doyle, G.M. Staebler, L. Zeng *et al.*, Plasma Phys. Controlled Fusion **42**, A237 (2000)
- [5] Ryter F, Leuterer F, Pereverzev G, Fahrbach H U, Stober J, Suttrop W and ASDEX Upgrade Team 2001 *Phys. Rev. Lett.* **86** 2325
- [6] Ryter F. et al, *Plasma Phys. Contr. Fus.* **48** B453 (2006)
- [7] Garbet B. et al, *Plasma Phys. Contr. Fus.* **46** B557 (2004)
- [8] Jacchia A, De Luca F, Cirant S, Sozzi C, Bracco G, Bruschi A, Buratti P, Podda S, Tudisco O 2002 *Nucl. Fusion* **42** 1116
- [9]"Electron heated ITB in JET" G.M.D.Hogewij, et.al *Plasma Physics & Control. Fusion* **44** (2002) 1155
- [10] Garbet X, Garzot L, Mantica P. et al. 2003 *Phys. Rev. Lett.* **91**, 035001
- [11] Bourdelle C, Garbet X, Imbaux F. et al 2007 *Phys. Plasmas* **14**, 112501
- [12] Callen J. D. 1992 *Phys. Fluids* **B4** 2142
- [13] Gentle K. W. et al 1995 *Phys. Rev. Lett.* **74** 3620
- [14] Hogeweij G. M. D. et al 2000 *Plasma Phys. Contr. Fusion* **42** 1137
- [15] Zou X.L. et al 2000 *Plasma Phys. Control. Fusion* **42** 1067

Particles Behavior in Quasi-steady-state AC Plasmas

on HT-7 Tokamak

Yinxian Jie (揭银先)¹, Xiang Gao (高翔)¹, Kenji Tanaka², Yao Yang (杨曜)¹,
Qiang Xu (徐强)¹, Wei Gao (高伟)¹, Jiangang Li (李建刚)¹

1. Institute of Plasma Physics, Chinese Academy of Sciences, PO Box 1126, Hefei, Anhui 230031, People's Republic of China
2. National Institute for Fusion Science, Toki 509-5292, Japan

Abstract

A quasi-steady-state alternating current (AC) operation assisted by LHW was achieved recently on a HT-7 superconducting tokamak. It is found in ac plasmas that the particle confinement time of the positive current plasma is lower than that of the negative current plasma. The particle transport coefficients are investigated in ac plasmas by the gas puff modulation method. It is observed that the particle diffusion coefficient for the positive plasma current case is almost the same as for the negative one, but the absolute value of inward pinch velocity of the positive current plasma is much lower than that of the negative one. The result of the particle transport model study is in agreement with the experimental confinement study. The intensity of H_α emission and impurities emission of CIII, OII and OV for the negative current plasma are much lower than for the positive current plasma. The radiations from H α, OII, CIII and ECE signals from the negative to the positive current phase showed less ionization and lower parameters than those from the positive to the negative one. The difference of particle transport and confinement in ac plasmas is not predicted by the current theory.

Keywords: ac plasma, particle transport coefficients, particle confinement time

PACS numbers: 52.55.Fa, 85.25.Hr

1 Introduction

Steady-state alternating current (AC) operation has been studied recently on the HT-7 superconducting tokamak with a plasma current of $I_p = 125$ kA, line-averaged density of $1.5 \times 10^{19} \text{ m}^{-3}$, electron temperature of $T_e = 500 \text{ eV}$ and $30 - 50 \text{ s}$ plasma duration [1]. Plasma discharges were sustained and smoothly transferred from one direction to the other without losing plasma ionization. AC operation of a tokamak reactor is an attractive scenario to generate a continuous output of electric energy without the need for a complicated non-inductive current driven system. The use of ac inductive current drive for a tokamak fusion reactor allows the reactor to operate with a minimum plant re-circulating power. Compared with non-inductive current drive operation,

ac discharges are technically simpler and have higher cost efficiency.

It was observed that the plasma properties are different when the plasma current crosses zero alternately. In the HT-7 ac discharges, the plasma kept a finite density when the plasma current was zero [1]. Plasma ionization was fully maintained by LHCD. One carefully compared the zero current plasma properties between the plasma current transition from positive to negative and from negative to positive current that the different plasma property is obviously observed. The radiations from H α , OII, CIII and ECE signals from the negative to the positive current phase showed less ionization and lower parameters than those from the positive to the negative one. It is found that the particle confinement of plasma is different for two plasma current directions. The particle confinement time τ_p is about 29 - 31 ms for negative current plasma, and it is about 16 - 17 ms for positive current plasma. It is very important to study the particle confinement and transport in ac plasmas.

To investigate the particle transport coefficients in ac plasmas, the method of gas puff modulation [2-5] is used to determine the particle diffusion coefficient (D) and the convection velocity (V) on HT-7 tokamak in 2007. The density modulation experiment shows that the particle diffusion coefficient (D) of positive current plasma is almost same as of negative one, but the inward pinch velocity (V) of positive one is much lower than of negative current plasma. The result of particle transport study in ac plasmas is agreed experimentally with the particle confinement time study in the HT-7 superconducting tokamak.

2. Experimental set-up

HT-7 superconducting tokamak is a middle size device for the research of high performance and long pulse discharge. HT-7 has a circular cross section with limiter configuration. The major radius is 1.22 m and minor radius is 0.27 m. HT-7 operated usually with plasma current $I_p = 100\text{-}250$ kA, toroidal magnetic field $B_t = 1\text{-}2$ T, central average electron density $(0.5\text{-}6) \times 10^{19} \text{ m}^{-3}$, central electron temperature $T_e = 0.3\text{-}2.0$ keV.

The key issue of AC operation is the control of ionization at the current transition, which require a short dwell time and maintain of ionization. In HT-7 tokamak, this issue was solved by modification of the PF power supply, the intensified gas puffing, the LHW assistance, and the careful control of the plasma displacement. The plasma position is calculated from the signals of magnetic loop coils, which is not valid for the plasma current transition point ($I_p = 0$ kA), so the vertical field was preset to control the position both for the positive current phase and negative phase when the plasma approaches zero ($-20 \text{ kA} < I_p < 20 \text{ kA}$). To keep the ionization, the gas puffing pulse and the LHW were applied at the current transition. The current directions are defined in the bird-eye view. The negative current is clockwise direction and the positive current is anticlockwise direction. The toroidal field direction is kept in clockwise direction during all of AC discharges.

Fig.1 gives location of the limiters, the plasma cross section, and the diagnostics systems involved in this article. The limiters include the upper toroidal limiter, the bottom toroidal limiter and the belt limiter. A 35-channel H α ($\lambda = 656.3\text{nm}$) photodiode array is mounted on the top port to monitor the plasma, with the component including a lens, an interference filter, a 35-channel photo diode chip, and the pre-amplifiers. The chord-averaged electron density is measured through 5 channels of far infrared laser interferometers. 9 channels of CIII line emission ($\lambda = 464.7 \text{ nm}$)

monochromators are used to observe the lower half part of plasma from the horizontal port. 7 channels of visible bremsstrahlung emission ($\lambda = 578.0$ nm) interference filter systems are designed to observe the lower half part of plasma. A channel of O_{II} line emission ($\lambda = 441.5$ nm) monochromator and a channel of O_V line emission ($\lambda = 278.1$ nm) monochromator are arranged to observe the central chord from the horizontal port .

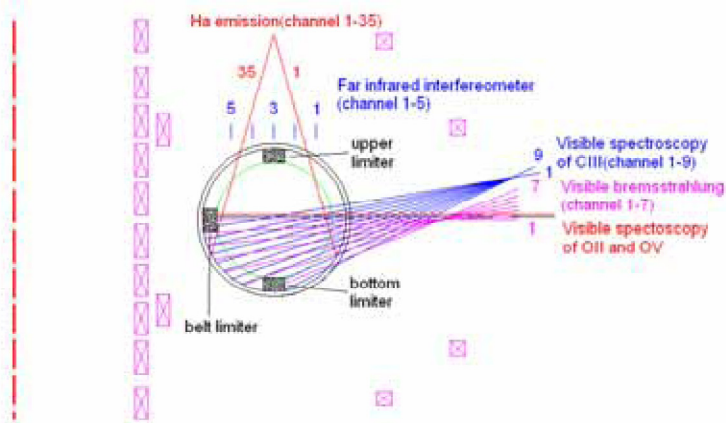


Fig.1 Diagnostic chord distribution on the HT-7 tokamak for AC discharge.

3. Particle behaviors in AC plasma

Figure 2 shows a typical steady state ac operation with about $t_d = 35$ s duration in the HT-7 superconducting tokamak. The waveforms from top to bottom in figure 2 are plasma current, loop voltage, magnetic flux, line-averaged density, LHCD power, H α signal and CIII radiation. The H α signals and CIII intensities are increased due to plasma wall interaction in ac plasma discharges [1]. The plasma performance showed a relatively stable behavior for 35 s. It is found that the particle confinement of plasma is fully different for two plasma current directions. It is observed that the intensity of CIII radiation during positive current plasma is always higher than negative current plasma as shown in bottom of Fig.2. The average density of positive current plasma is almost same as of negative current plasma, but the particles recycling of H α signal during positive current plasma is higher than negative current plasma obviously in Fig.2.

Fig.3 is another typical AC discharge with duration of 4.8s (the shot number is 99552#) on HT-7 tokamak. The plasma current is fixed at about 110 kA for both current directions; the electron density is about $1.25 \times 10^{19} \text{ m}^{-3}$. From Fig.3 (e), it can be found that the H α emission is lower during the negative phase than that of the positive phase with a factor of 0.5 (from 0.38 to 0.19 in a.u.), the difference of particle confinement time can be confirmed . A detailed analysis is shown in Fig.4. The spatial and temporal evolution of the 35-channel H α emission intensity is contoured. All the channels show the same trend that the H α emission decreases in the negative current phase and it increases in the positive current phase. It means that the global particle confinement is different in AC plasmas. Calculation of τ_p shows that the particle confinement time is improved a factor of two in the negative current plasma.

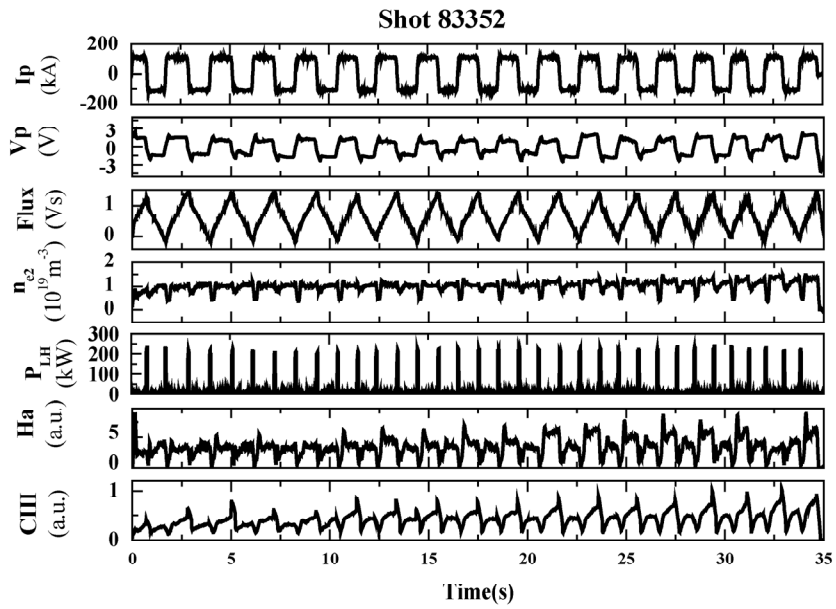


Figure 2 A typical AC plasma operation (plasma current I_p is from +125 kA to -125 kA, $B_t = 1.9$ T, central line-averaged density $\langle n_e \rangle = 1.5 \times 10^{19} \text{ m}^{-3}$ and central electron temperature $T_e = 500$ eV, shot number 83352#) in the HT-7 superconducting tokamak

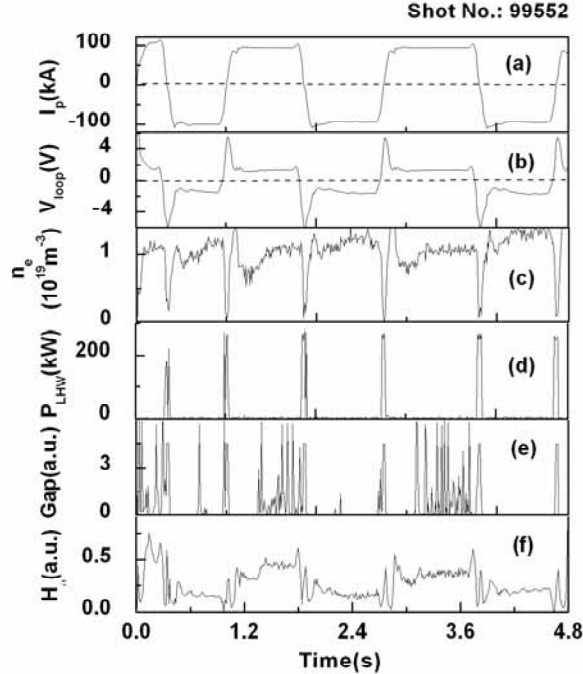


Fig.3 Typical AC discharge (shot number 99552): (a) plasma current; (b) loop voltage; (c) central line average electron density; (d) power of LHW wave; (e) gas puffing controlled by electron density feedback; (f) H_α line emission of channel 17

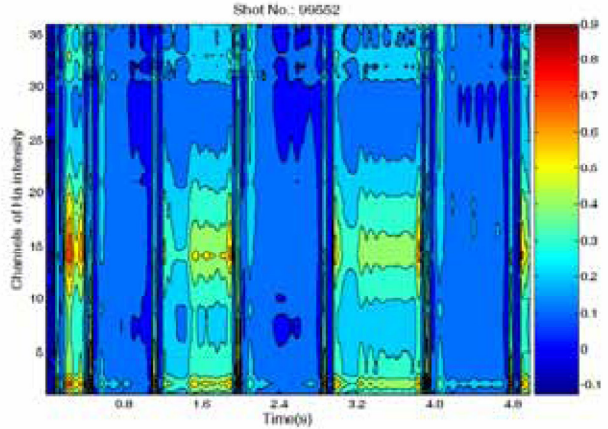


Fig.4 Spatial and temporal evolution of the 35-channel H_α emission line intensity, where the spatial distribution is plotted in Fig. 1.

The difference of emission behaviour during the positive and negative current phase is interesting and of great physics connotation. In Fig.5, the density slightly increases from $1.1 \times 10^{19} \text{ m}^{-3}$ to $1.35 \times 10^{19} \text{ m}^{-3}$. From Fig.5 (c), (d), (e), the emission of the CIII, OII, OV is much higher in the positive phase than in the negative phase, considering the same behaviour of the H_α emission, an increase of impurity recycling in positive current plasma can be deduced.

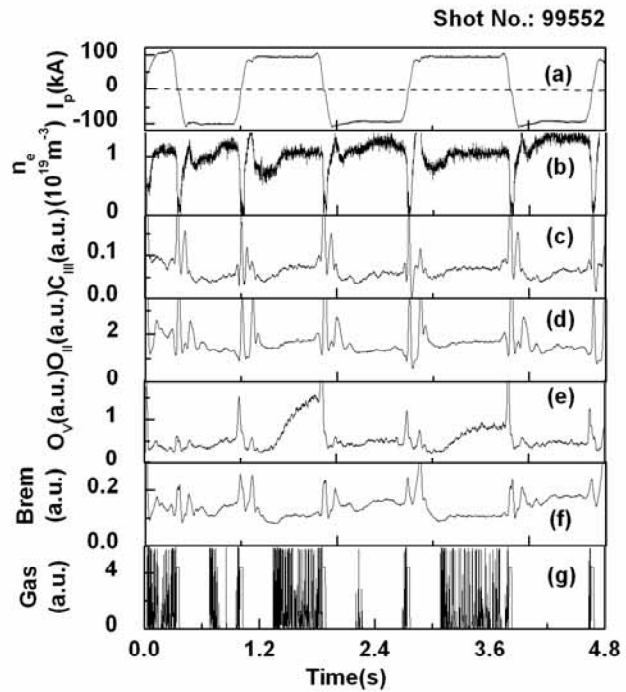


Fig.5 The trace of emission signal in shot 99552: (a) plasma current; (b) line average electron density; (c) CIII emission of channel 1; (d) OII line emission; (e) OV line emission; (f) bremsstrahlung emission of channel 1; (g) gas puffing .

The modulation of electron density [2-5] has been studied to determine the particle diffusion coefficient (D) and the convection velocity (V) on HT-7 tokamak since 2004. The particle diffusion coefficient and the convection velocity were studied based on the density modulation using D2 gas puffing on the HT-7 tokamak. The density was measured by a five-channel FIR laser interferometer [6,7]. The density modulation amplitude was 10% of the central chord averaged background density and the modulation frequency was 10 Hz in the experiments. It was observed that the influence of density modulation on the main plasma parameters was very weak. The particle diffusion coefficient (D) and the convection velocity (V) during the discharge of gas puff modulation can be obtained by a computer code calculation. The density modulation experiments are performed for ac plasma operation in the HT-7 tokamak recently. The averaged density is about $1.0 \times 10^{19} \text{ m}^{-3}$, $B_t = 1.9 \text{ T}$, electron temperature $T_e = 500 \text{ eV}$, and the plasma current is 110 kA. The calculated particle diffusion coefficient is $D = 0.30 \text{ m}^2/\text{s}$ and convection velocity is $V = -0.95 \text{ m/s}$ in “positive” case, where symbol of “-” means direction of inward pinch velocity. However the particle diffusion coefficient is $D = 0.37 \text{ m}^2/\text{s}$ and convection velocity is $V = -3.40 \text{ m/s}$ in “negative” case. It is observed that the particle diffusion coefficient ($D = 0.3 \text{ m}^2/\text{s}$) for positive plasma current case is almost same as for negative one ($D = 0.37 \text{ m}^2/\text{s}$). However, the absolute value of convection velocity ($V = -0.95 \text{ m/s}$) of positive current plasma is much lower than of negative one ($V = -3.40 \text{ m/s}$). The difference of inward convection velocity would take an important rule in the difference of particles confinement in ac plasmas. This result has been confirmed in other similar ac shots.

4. Particle behaviors at current transition

The AC plasma is a serial of the current cycles. At the current transition, the plasma has important properties due to the unique characteristic of zero current and the small electron density. In fact the zero current is composed of both positive and negative currents on the low field side and the high field side, so the impurity behaviour may vary with the plasma current, which has not been testified in AC plasma. In HT-7 AC discharge, the lower hybrid wave and the gas puff is employed to maintain the ionization at the current transition, the impurity and H_α emission intensity is a good measure to evaluate the quality of the zero current plasma. In Fig. 6 and 7, the intensity of OII, OV, CIII, H_α have a trend of decrease when the plasma current is approaching zero before the gas puffing and lower hybrid wave is launched. The application of gas puffing and lower hybrid wave stops the decrease of the radiation, after a spike just before the $I_p = 0 \text{ kA}$, the intensity enters a relative stable phase around the $I_p = 0 \text{ kA}$ (marked with the vertical line), which maintained till after the loop voltage makes effect. Comparison of these two graphics shows that the emission intensity at the stable stage is higher in the Fig. 7 than in the Fig. 6, which shows a better ionization for the positive to negative transition.

The evolution of density profile is studied in detail in ac plasmas (shot number 83352#). Figure 8 shows that density from the positive current to the negative one is about $(2.9-3.5) \times 10^{18} \text{ m}^{-3}$ at $I_p = 0$ in $t = 2.9 \text{ s}$ with a sustained hollow profile. After the transition ($I_p = 0$), the hollow density profile is kept for about 60 ms as shown in Fig.8. Figure 9 shows that central line-averaged plasma density at zero current (in $t = 4 \text{ s}$) from the negative to the positive phase is about $(0.5-1.2) \times 10^{18} \text{ m}^{-3}$. After the transition, the hollow density profile changes in a peaking profile quickly as shown in Fig.9. Finally the density profiles are observed to become almost the same profile at

plasma current $I_p = \pm 120$ kA phase in both cases. It should be clarified that lower hybrid wave plays different role for the co-driven and anti-driven directions. LHW play an anti-drive mode for the current transiting from positive to negative, the heating effect play a role, which provide a good interpretation for different behaviours of particle.

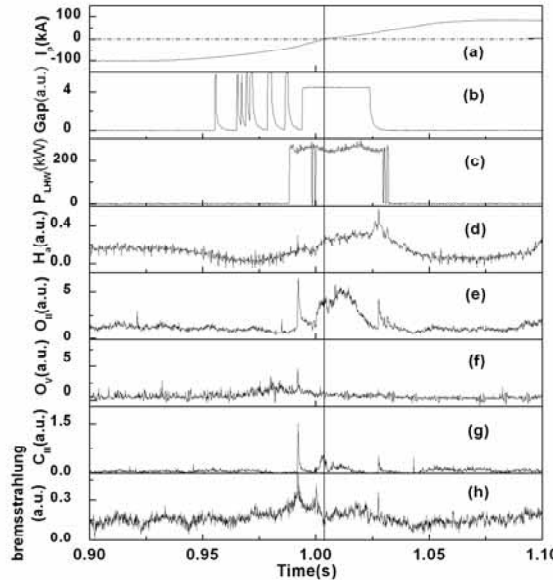


Fig.6 The trace at around $t = 1.0$ s: (a) plasma current; (b) gas puffing; (c) power of LHW; (d) H_α line emission of channel 17; (e) OII line emission; (f) OV line emission; (g) CIII line emission of the channel 1; (h) bremsstrahlung emission of channel 1

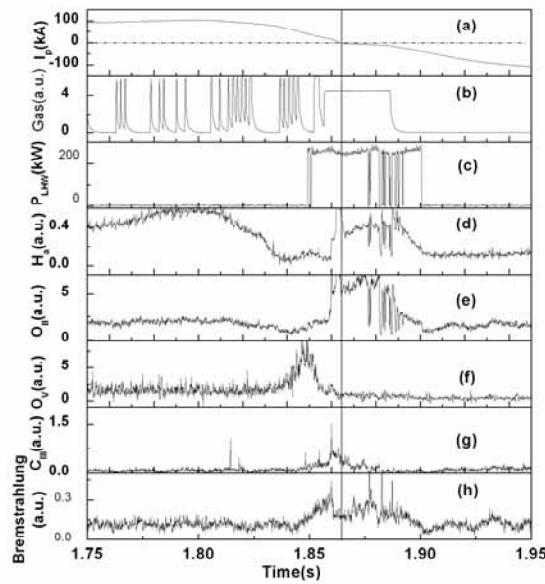


Fig.7 The trace at around $t = 1.85$ s: (a) plasma current; (b) gas puffing; (c) power of LHW; (d) H_α emission of Channel 17; (e) OII line emission; (f) OV line emission; (g) CIII line emission of channel 1; (h) bremsstrahlung emission of channel 1.

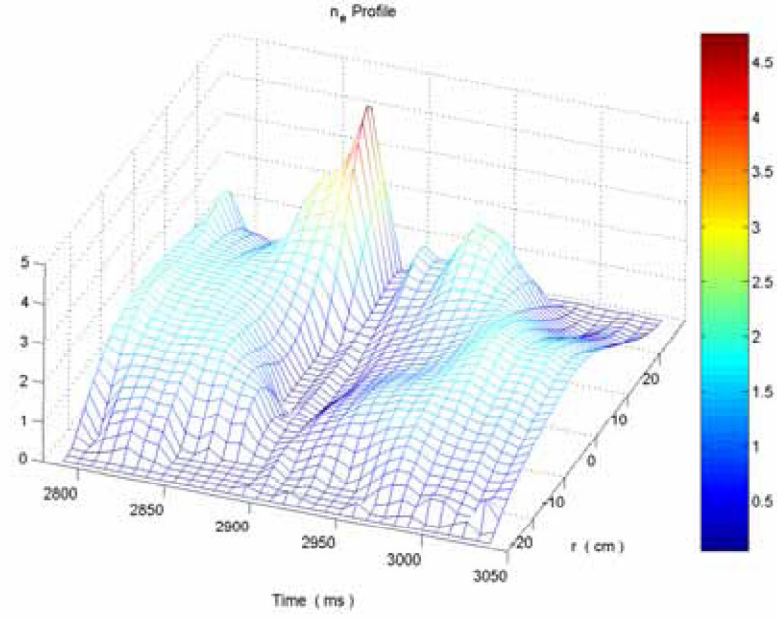


Figure 8 Space-time evolution of density profile (83352#) from case “positive” to case “negative”, where $I_p = 0$ at $t = 2.9$ s, the unit of electron density n_e is 10^{19} m^{-3} .

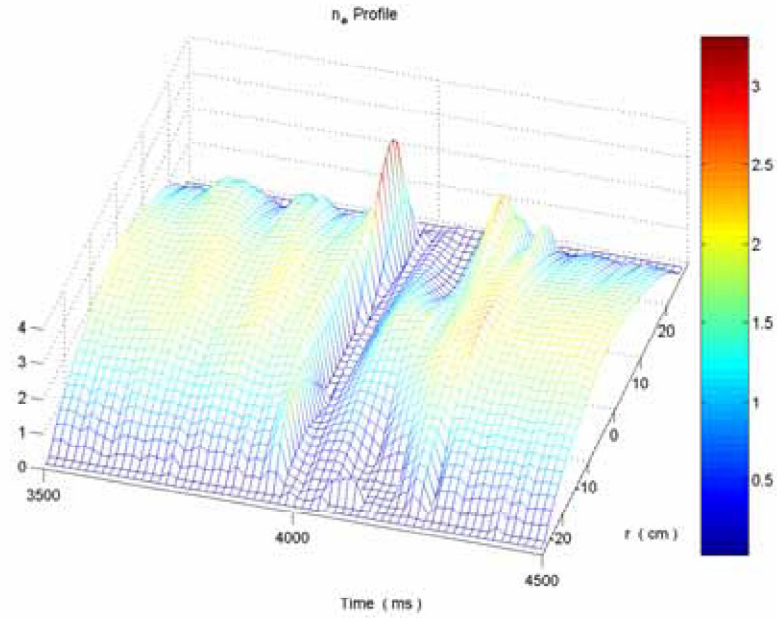


Figure 9 Space-time evolution of density profile (83352#) from case “negative” to case “positive”, where $I_p = 0$ at $t = 4$ s, the unit of density n_e is 10^{19} m^{-3} .

5. Conclusion

In conclusion, the quasi-steady-state alternating current plasma operation was achieved successfully on the HT-7 superconducting tokamak. It is found in AC plasmas that the H_α emission is lower during the negative current phase than that of the positive phase with a factor of 2. The increase of impurity recycling in positive current plasma was observed by the intensity

of CIII, OII and OV emissions. The particle confinement time of positive current plasma is lower than that of negative current plasma. The particle transport coefficients are investigated in AC plasmas by the gas puff modulation method. It is observed that the particle diffusion coefficient ($D = 0.3 \text{ m}^2/\text{s}$) for positive plasma current case is almost same as for negative one ($D = 0.37 \text{ m}^2/\text{s}$), but the absolute value of inward pinch velocity ($V = -0.95 \text{ m/s}$) of positive current plasma is much lower than of negative one ($V = -3.40 \text{ m/s}$). The result of particle transport model study is agreed with the experimental confinement study. The particle behaviors is different at different current transitions. The difference of particles transport and confinement in ac plasmas is not predicted by current theory.

6. Acknowledgments

The authors would like to thank Dr. K. Tanaka for joint study of density modulation experiments in the HT-7 tokamak. This work was funded by National Nature Science Foundation of China with contract No.10675127, No.10675125. This work was partly supported by JSPS-CAS Core-University Program on Plasma and Nuclear Fusion.

References

- 1 Li J. *et al* 2007 *Nucl. Fusion* 47 1071
- 2 Gentle K W, *et al* 1987 *Plasma Phys. Contr. Fusion* 29: 1077
- 3 Gentle K W, *et al* 1992 *Nucl. Fusion* 32: 217
- 4 Tanaka K. *et al* 2004 *Chin. Phys. Lett.* 21 2458
- 5 Jie Y.X. *et al* 2006 *Plasma Sci. Technol.* 8 129
- 6 Gao X. *et al* 1995 *Rev. Sci. Instrum.* 66 139
- 7 Jie Y.X. *et al* 2000 *Int. J. Infrared Millim. Waves* 21 1375

E-mail address of Jie Yinxian: yx_jie@ipp.ac.cn

Investigation of experimental configuration for electron Bernstein wave heating on LHD

IGAMI Hiroe¹, IKEDA Ryosuke¹, TAKAHASHI Hiromi¹, YOSHIMURA Yasuo¹, SHIMOZUMA Takashi¹, KUBO Shin¹, TANAKA Hitoshi,² NAGASAKI Kazunobu³, MUTOH Takashi¹ and the LHD experimental group¹

¹National Institute for Fusion Science. 509-5292, Toki, Japan

²Graduate School of Energy Science Kyoto University, 606-8502, Kyoto, Japan

³Institute of Advanced Energy, Kyoto University, 611-0011, Uji Japan

Abstract

Investigation of experimental configuration for electron Bernstein wave (EBW) heating with use of existing electron cyclotron heating (ECH) antennas on LHD has been performed. With use of antennas installed in a bottom port, direct oblique launching of the extraordinary (X-) mode from the high magnetic field side (HFS) is available. Since the parallel component of the refractive index (N_{\parallel}) varies with the wave orbit because of the inhomogeneity of the magnetic field, N_{\parallel} is able to become zero when the launched X-mode crosses the electron cyclotron resonance (ECR) layer even N_{\parallel} is not 0 at first. In such condition, the obliquely launched X-mode is not completely damped out in the ECR layer and can be mode converted EBW that is absorbed at the Doppler shifted ECR layer. With use of an antenna installed in a horizontal port, oblique launching from the low magnetic field side (LFS) toward the over-dense plasma is available. Excitation of EBW via ordinary(O)-extraordinary(X)-electron Bernstein wave(B) mode conversion process is expected with the O-mode launching toward an appropriate direction. The O-X-B mode conversion rate can be calculated at the cutoff however, for certain launching direction, the O-mode cannot reach the cutoff because of refraction. Therefore effective O-X-B mode conversion window narrows. In an experimental configuration where effective O-X-B mode conversion rate can be obtained, mode conversion to EBW takes place around $\rho = 0.9$ and excited EBW can propagate into the inner region

of the plasma and be absorbed in the Doppler shifted ECR layer.

Keywourds : LHD, electron cyclotron heating (ECH), electron Bernstein wave (EBW), high density plasma

PACS : 52.35.Hr, 52.50.Sw

1 Introduction

In extreme high density core region and low temperature peripheral region of the plasma, electron cyclotron heating (ECH) and current drive (ECCD) by normal electromagnetic (EM) mode are not available. In such regions, ECH/ECCD by electron Bernstein wave (EBW) has been expected as promising substitutes since it does not have density limit for propagation and be strongly absorbed even in the low temperature region. Since EBW is an electrostatic mode, it is required to be excited via the mode conversion process from the extraordinary (X-) mode of electromagnetic (EM) wave in the upper hybrid resonance (UHR) layer. Since the UHR layer is shielded by the evanescent region lying between the UHR layer and the right handed cyclotron cutoff in the low magnetic field side (LFS), getting accessibility of the X-mode to the UHR layer is important and complex problem.

One straightforward way to excite EBW is launching the X-mode from the high magnetic field side (HFS), that is so called slow X-B method. If the launched X-mode is not completely damped out in the electron cyclotron resonance (ECR) layer that lies HFS of the UHR layer, it can reach the UHR layer and excite EBW^[1]. In LHD, direct oblique launching of the X-mode from HFS with use of existing antennas installed in a bottom port is available. Some experimental results about the direct oblique launching were reported^[2,3]. Another way is launching EM mode from LFS with appropriate polarization and launching angle so that it couples well to the slow X-mode that propagates toward the UHR layer in HFS. The optimum polarization and angle are different for the density gradient in the mode conversion region^[4].

In LHD, since the scale length of the density gradient in the mode conversion region is extremely gentle in comparison of the wavelength of the EC wave, launching of the ordinary (O-) mode, so called O-X-B method ^[5]. Theoretical investigation pointed out a possibility that the O-mode launched from the horizontal port can be efficiently mode converted to EBW, then reaches the inner region of the plasma and is absorbed there ^[6]. With use of existing ECH antennas installed in a bottom port which has flexibility of launching direction, O-mode can be launched appropriately to obtain sufficient mode conversion rate ^[7]. Recently high power 77GHz gyrotron was installed in a transmission line connected to a horizontal antenna and investigation of experimental configuration for O-X-B method with this transmission line has been required.

We have developed additional function to existing 3-D ray tracing code for LHD ^[8]. For existing ECH antenna, appropriate setting of the launching direction for EBW excitation has been able to be investigated. In this paper, examples of investigation are reported. In section 2, current ECH system of LHD is shortly introduced. In section 3, examples of investigation for slow X-B method by direct oblique launching from a bottom port is reported. In section 4, an example of investigation for O-X-B method with use of a horizontal antenna is reported. In section 5, discussion and summary are presented.

2 Current ECH system in LHD

Figure 1 shows a schematic view of the ECH system in 2008. Two 82.7GHz (500kW/2sec., GYCOM), two 84GHz (800kW/3sec., GYCOM) and two 168GHz (500kW/1sec., TOSHIBA), gyrotrons are used as microwave sources in high power, short pulse (usually ≤ 2 sec) experiments. One 84GHz (200kW/CW., GYCOM) gyrotron has been used in long pulse experiment. Recently two 77GHz (1MW/5sec. and 300kW/CW, TOSHIBA) has been developed in collaboration with Tsukuba University and installed. There are eight transmission lines for ECH. For one of them, long part of the line is shared by a 84GHz gyrotron used in short pulse experiments and a 84GHz gyrotron used in long pulse experiments. Two antennas installed in a bottom port (L-port antenna)

and two antennas installed in a horizontal port (O-antenna) have flexibility of the launching angle and are expected to be used for EBW excitation and heating. For slow X-B experiment, L-port antennas are available. For O-X-B experiment, L-port antennas and O-port antennas are available.

3 Investigation for slow X-B method

Figure 2 presents a schematic view of the relationship between the launching direction and the plasma cross-section in LHD. For the case of launching of 84GHz electron cyclotron (EC) wave from the bottom port, the launching direction (angle) is set by the launching parameter (R_f, T_f) that is a coordinate point on the virtual target plane located on the equatorial plane. Figure 3 shows an example of oblique cross section of the LHD plasma along the straight EC wave beam launched from one of the antennas installed in a bottom port. The launching parameter is $(R_f, T_f) = (3.25m, -0.4m)$ in this case. The obliquely launched wave first encounters the fundamental ECR layer and if the wave is not completely damped out there, it can reach the UHR layer and excite EBW. Actually the orbit of the wave is not straight since the wave is refracted in the plasma. Figure 4 shows the result of ray tracing calculation for the case of X-mode launching with launching parameter $(R_f, T_f) = (3.25m, -0.4m)$. In the region where $(\omega_{pe}/\omega)^2 < 0.02$, dispersion equation in the cold plasma is solved, and in the region where $(\omega_{pe}/\omega)^2 \geq 0.02$, dispersion equation in the hot plasma is solved since the ECR layer and the UHR layer are located close to the edge of the plasma and finite temperature effect is not negligible even in the peripheral region (See Appendix). ω_{pe} is the plasma angular frequency. The absorption coefficient is obtained directly from the imaginary part of the wave vector for both cases of EM wave propagation and EBW propagation (also see Appendix). The electron density profile and the electron temperature profile are given as $n_e(\rho) = n_{e0} (1 - (\rho/1.1)^8)$, $n_{e0} = 2 \times 10^{19} \text{ m}^{-3}$ and $T_e(\rho) = T_{e0} (1 - (\rho/1.1)^4)$, $T_{e0} = 2 \text{ keV}$. In this case, the parallel component of the refractive index varies along the orbit because of the inhomogeneity of the magnetic field and becomes almost 0 when the X-mode crosses the ECR layer. In the low density region, the absorption of the fundamental X-mode is weak if $N_{\parallel} \sim 0$ but it is strong as N_{\parallel} deviates 0. Therefore

it is important that the launching direction is optimized so that N_{\parallel} becomes 0 when the launched X-mode cross the ECR layer that is located in the plasma peripheral region. If N_{∞} does not become 0 when the X-mode crosses the ECR layer that is located in the low density and low temperature peripheral region, strong absorption as the fundamental X-mode occurs and the X-mode cannot pass through the ECR layer^[3].

4 Investigation for O-X-B method

Recently 77GHz(1MW/5sec. and 300kW/CW, TOSHIBA) gyrotron has been installed in a transmission line connected to a horizontal O-port antenna that has flexibility of launching direction. It is well known that N_{\parallel} should be $N_{\parallel\text{opt}} = \{\beta/(1+\beta)\}^{1/2}$, where $\beta = \omega_{ce}/\omega$ in the mode conversion region so that the plasma cutoff and the left handed cyclotron cutoff coincide and the evanescent region between them is vanished. If N_{\parallel} deviates $N_{\parallel\text{opt}}$, a part of the wave is reflected because of the existence of the evanescent region. The mode conversion rate T_{OXB} is analytically given as follows^[9]

$$T_{\text{OXB}} = \exp\{-\pi(\omega/c) L_n (\beta/2)^{1/2} [2(1+\beta)(N_{\parallel} - N_{\parallel\text{opt}})^2 + N_v^2]\} \quad (1)$$

where N_v is the component of the refractive index along the direction that is perpendicular to the external magnetic field and density gradient, $L_n = n_e/(dn_e/dr)$ is the scale length of the density gradient in the mode conversion region, r direction is parallel to the density gradient. A survey of the launching direction to search appropriate one for efficient O-X-B mode conversion and EBW heating has been performed. The electron density profile and the electron temperature profile are given as $n_e(\rho) = n_{e0} (1 - (\rho/1.0)^8)$, $n_{e0} = 1 \times 10^{20} \text{ m}^{-3}$ and $T_e(\rho) = T_{e0} (1 - (\rho/1.0)^4)$, $T_{e0} = 0.5 \text{ keV}$. For the launching from the horizontal antenna, the launching direction is defined as launching parameter (T_f, Z_f) , that is a coordinate point on the virtual target plane placed as shown in Figure 5. The direction of the T_f axes is along the toroidal direction at the origin $(T_f, Z_f) = (0,0)$ that is placed at $R=3.9\text{m}$, $Z=0.0\text{m}$ on the horizontally long cross section. The direction of Z_f axes is the vertical direction. For various sets of (T_f, Z_f) , the point where the minimum perpendicular refractive index

N_∞ is obtained by ray tracing and T_{OXB} is calculated at the point. Figure 6-(a) shows a contour plot of the minimum N_∞ as a function of (T_f, Z_f) . Note that if the minimum N_∞ is not close to 0 it means that the wave is refracted before it reaches the cutoff and in such a case, to calculate T_{OXB} at the minimum N_∞ point is meaningless. In Figure 6-(b), T_{OXB} is plotted if the minimum N_∞ is less than 0.1 and in Figure 6-(c), T_{OXB} is plotted if the minimum N_∞ is less than 0.05. Taking into account of the refraction, effective mode conversion window narrows. The location of the O-X-B mode conversion window on the (T_f, Z_f) launching parameter plane, its effective width shifts if the external magnetic configuration and/or the electron density profile vary. Investigation of the shift is required for obtaining effective mode conversion in real experiments.

For a setting $(T_f, Z_f) = (-0.9\text{m}, 0.25\text{m})$, result of the ray-tracing is shown in Figure 7. The electron density and temperature profile is the same as the case of Figure 6. Since T_{OXB} is 0.985, narrow evanescent region appears and the ray is reflected in front of the left handed cyclotron cutoff. We consider that N_{\parallel} and N_v in eq. (1) are conserved through the evanescent layer and solve the dispersion equation at the HFS of the evanescent region and obtain the initial value to restart the ray tracing. The re-started ray reaches the UHR layer located in peripheral region, then the wave is mode converted to EBW. The EBW is finally absorbed around $\rho=0.77$.

5 Discussion and summary

Investigation for experimental configuration for EBW heating by existing ECH antennas have been performed. EBW excitation and heating are possible by direct oblique launching of 84GHz EC wave with the X-mode from HFS, with use of an antenna installed in a bottom port. For excitation of EBW, the X-mode should be launched so that N_{\parallel} becomes 0 when the X-mode crosses the ECR layer or else, the X-mode is damped out in the ECR layer and cannot reach the UHR layer where mode conversion process to EBW takes place. Since the orbit of the X-mode in the peripheral region in HFS is strongly affected by the electron density profile, information of the density profile in the edge region is important to adjust the launching direction so that N_{\parallel} becomes 0 when the

wave crosses the ECR layer. In an over dense plasma, with use of ray-tracing calculation, the width of O-X-B mode conversion window is obtained in the case where 77GHz EC wave is launched from an antenna installed in a horizontal port. Taking into account of the refraction of the launched wave, the effective O-X-B mode conversion window narrows. Since the location of the O-X-B mode conversion window shifts on the (T_f, Z_f) launching parameter plane, and its effective width varies as the external magnetic configuration and/or the electron density profile varies, investigation of the shift is required and more, construction of some feedback system of launching parameter moving on with variation of the plasma parameters is desirable in future for obtaining effective O-X-B mode conversion rate. One example of ray tracing calculation shows that EBW is excited in the UHR layer located in peripheral region and EBW is absorbed around $\rho=0.77$. In our investigation the effect of the collisional damping is not included, however it should be included to estimate power absorption more correctly in the edge region where the electron density $T_e < 100\text{eV}$.

Acknowledgment

This work was mainly performed under the budget codes NIFS07ULRR501-3,518, NIFS07KLRR303 and partially supported by a grant-in-aid for scientific research of MEXT JAPAN, 2008 19740347 and the JSPS-CAS Core-University program in the field of 'Plasma and Nuclear Fusion'.

Appendix : Method of calculation

A-1 Dispersion equation of EM wave and EBW in hot plasmas

We have added the function to treat the X-B and the O-X-B mode conversion process and EBW propagation and absorption to the existing 3-D ray tracing code for LHD^[8]. In the region where the density and electron temperature are sufficiently low, the dispersion equation in the cold plasma^[10] is used for calculation. Near the ECR layer and the region between the ECR and the UHR layer the dispersion equation of electromagnetic (EM) wave in hot plasma^[11] is used since the finite

temperature effect is not negligible there.

$$G_{HOT}(\omega, \mathbf{k}) = \det \square (c/\omega)^2 (\mathbf{k} \cdot \mathbf{k} - k^2 \delta_{ij}) + \epsilon_{ij} \square \quad (2)$$

where c is the velocity of light and ω is the angular frequency of the wave, \mathbf{k} is the wave vector.

ϵ_{ij} is the dielectric tensor of the hot plasma given as follows,

$$\epsilon_{ij} = \delta_{ij} + (\omega_{pe}/\omega)^2 [\sum i\pi\xi_0 Z(\xi_n) \prod^{(n)}_{ij} + 2\xi_0^2 b_i b_j] \quad (-\infty \leq n \leq \infty), \quad \xi_n = (\omega - n\Omega_{ce})/(k_{\parallel} v_t) \quad (3)$$

where ω_{pe} is the plasma angular frequency, Ω_{ce} is the electron cyclotron angular frequency,

$Z(\xi_n)$ is the plasma dispersion function, $v_t = (2T_e/m_e)^{1/2}$ is the thermal velocity of the electron ,

k_{\parallel} is the parallel component of the wave vector. $\mathbf{b} = (b_x, b_y, b_z)$ is the unit vector along the magnetic field. $\prod^{(n)}_{ij}$ is given as follows.

$$\prod^{(n)}_{ij} = \begin{pmatrix} (n^2/\lambda)A_n, & i A'_n n, & (2/\lambda)^{1/2} n \xi_n A_n \\ -i A'_n n, & (n^2/\lambda)A_n - 2\lambda A'_n & -i(2\lambda)^{1/2} \xi_n A'_n \\ (2/\lambda)^{1/2} n \xi_n A_n, & i(2\lambda)^{1/2} \xi_n A'_n, & 2\xi_n^2 A_n \end{pmatrix} \quad (4)$$

$A_n \equiv eI_n(\lambda), \quad A'_n = dA_n/d\lambda, \quad \text{sgn}(\lambda) = -1$

$\lambda = k_{\perp}^2 T_e / m_e \Omega_{ce}^2 = (k \rho_e)^2 / 2$, k_{\perp} is the perpendicular component of the wave vector, $\rho_e = v_t / \Omega_{ce}$ is the Larmor radius of the thermal electron, I_n is the n th modified Bessel function, $Z(\xi_n)$ is the plasma dispersion function. The dispersion equation of EBW is given as follows^[8].

$$G_{EBW}(\omega, k) = 1 + 2(\omega_{pe}/k v_t) 2[1 + \xi_0 Z(\xi_n) e^{\lambda} I_n(\lambda)] = 0 \quad (5)$$

In the calculation we take summation over n up to $n \pm 5$ for both of dispersion equation of EM in hot plasmas and dispersion equation of EBW.

A-2 Absorption coefficient

The optical thickness τ is obtained by integrating the imaginary part of the wave vector.

$$\tau = 2 \int \mathbf{k}_i \oplus d\mathbf{s} \quad (6)$$

Where s means a vector along the trajectory. In the case of weak damping, the dispersion equation can be expanded

$$G(\omega, \mathbf{k}) = G_0(\omega, \mathbf{k}) + i(\partial G_0/\partial \mathbf{k})\mathbf{k}_i + iG_I(\omega, \mathbf{k}_0) = 0 \quad (7)$$

$$G_0 = Re[G(\omega, \mathbf{k}_0)] \sim 0, G_I = Im[G(\omega, \mathbf{k}_0)], \quad \mathbf{k} = \mathbf{k}_0 + i\mathbf{k}_i$$

With use the relation $(dr/ds) = (\partial G/\partial \mathbf{k})$ and eq. (7), eq. (6) can be rewrite as follows.

$$\tau = -2 \int G_I ds \quad (9)$$

Where s is the measure of distance along the trajectory. In the calculation, G_I is calculated at each step and the absorbed power P_{abs} is obtained, $P_{abs} = P_0(1 - \exp(-\tau))$ where P_0 is the launched power of the wave.

References

- 1 Maekawa T., Kobayashi T., Yamaguchi S. et al. (2001) Phys. Rev. Lett. **86** pp. 3783~
- 2 Igami H., Shimozuma T., Kubo S. et al. (2006) Plasma and Fusion Res. **1** pp.52~
- 3 Igami H., Yoshimura Y., Kubo S. et al. (2008) Proceedings of 22nd IAEA Fusion Energy Conference, 13-18 Oct. Geneva, Switzerland, EX/P6-13
- 4 Igami H., Tanaka H., Maekawa T. (2006) Plasma Phys. Control. Fusion **48** pp.573
- 5 Laqua H. P, Erckmann V., Hartfuss H. J. et al. (1997) Phys. Rev. Lett. **78** pp.3467-
- 6 Nagasaki K., and Yanagi N. (2002) Plasma Phys. Control. Fusion **44** pp.409
- 7 Igami H., Kubo S. Laqua H. P et al. (2006) Rev. Sci. Instrm. **77** 10E931
- 8 Kubo S et al., (2002) Journal of Plasma Fusion Research SERIES **5** pp.584
- 9 Mjølhus E. (1984) J. Plasma Phys. **31** pp.7
- 10 Stix T. H. (1992) "Waves in Plasmas" McGraw-Hill, New York, Chap.1, 2 and 13
- 11 Akhiezer A. I., Akhiezer I. A., Polovin R. V., Sintenko A. G. and Stepanov K. N., (1975), "Plasma Electrodynamics" English Ed., Pergamon Press Chap.5
- 12 Maekawa T. Tanaka S. and Hamada Y. (1980) J. Phys. Soc. Japan **48** pp.247

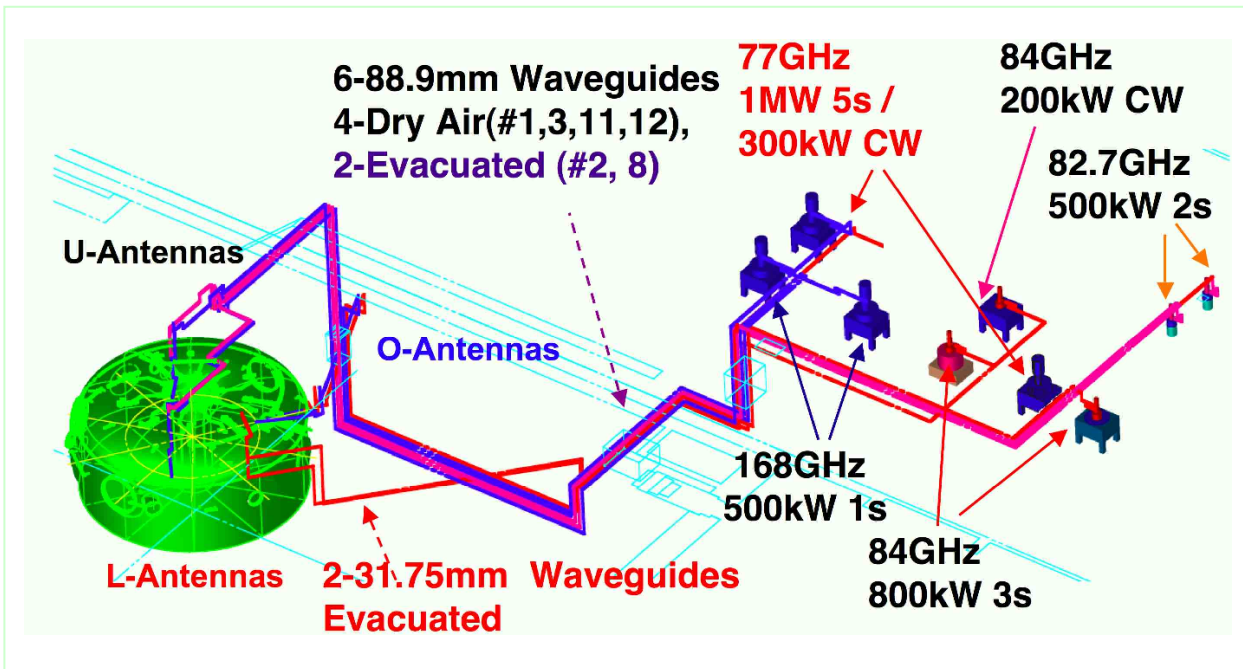


Figure 1 : ECH system in LHD in 2008

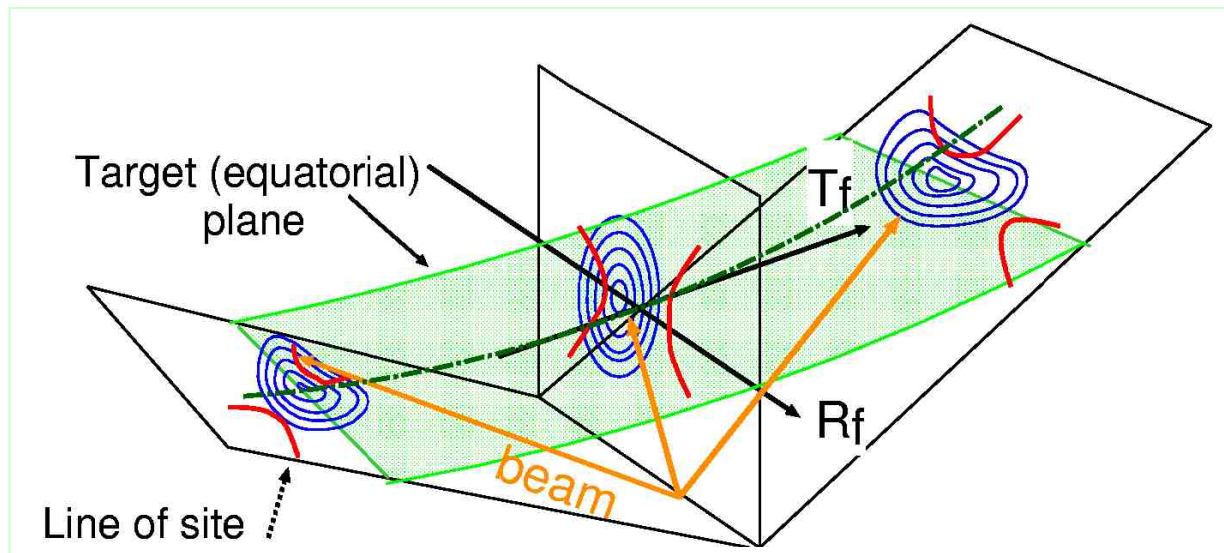


Figure 2 : Schematic view of plasma cross sections and virtual target plane to define the launching parameter (R_f, T_f). The origin of the orthogonal axes of R_f and T_f is defined at $(R, z, \phi) = (3.9\text{m}, 0.0\text{m}, 0.0^\circ)$, where R is the distance from the center of the torus, z is the vertical distance from the equatorial plane and ϕ is the toroidal angle from the vertically long cross section.

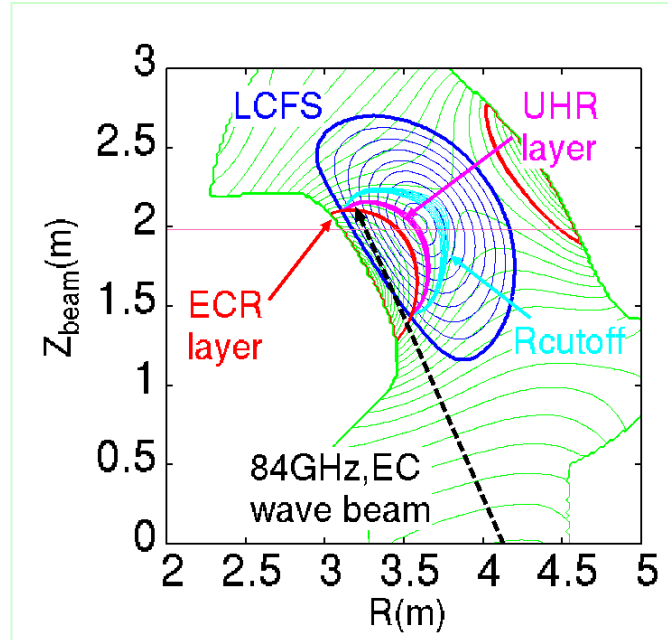


Figure 3 : An example of oblique cross section of LHD along the straight EC wave beam launched from one of L-antennas installed in a bottom port. The wave can access the UHR layer through the ECR layer from HFS.

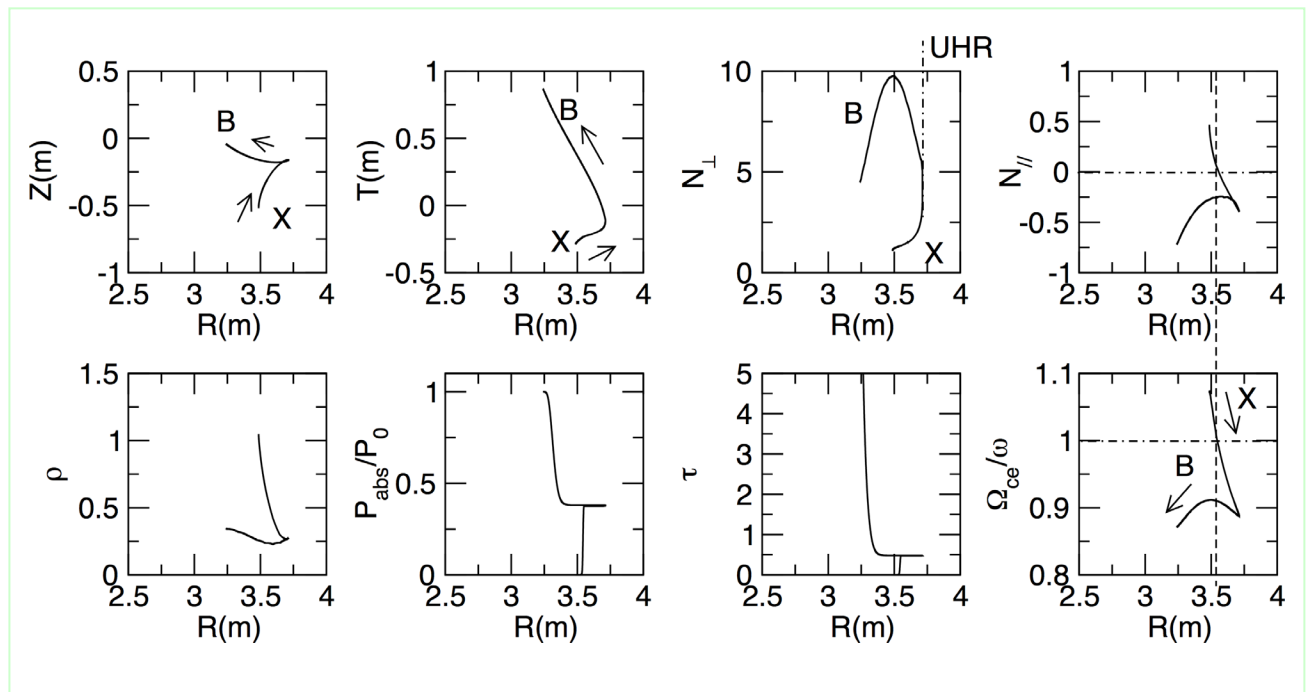


Figure 4 : Result of ray tracing in the case of direct oblique launching from HFS. The launching parameter is $(R_f, T_f) = (3.25\text{m}, -0.4\text{m})$. $n_e(\rho) = n_{e0} (1 - (\rho / 1.1)^8)$, $n_{e0} = 2 \times 10^{19} \text{ m}^{-3}$ and $T_e(\rho) = T_{e0} (1 - (\rho / 1.1)^4)$, $T_{e0} = 2 \text{ keV}$. (From the left on the upper column) orbit projected on the vertically long

cross section. Orbit projected on the equatorial plane. Perpendicular component of the refractive index, N_∞ . Parallel component of the refractive index, N_{\parallel} . Normalized small radius, ρ . Normalized absorbed power, P_{abs}/P_0 where P_0 is the launched power. Optical depth, τ . Normalized electron cyclotron angular frequency, Ω_{ce}/ω .

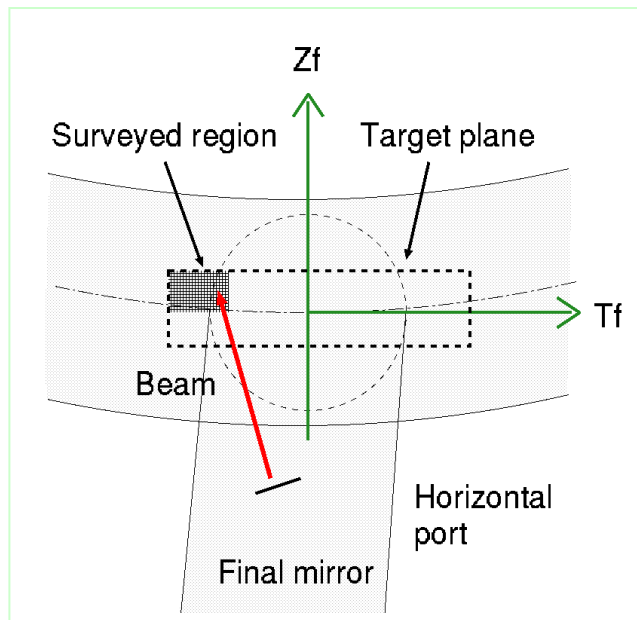


Figure 5 : Schematic view of the virtual target plane to define the launching direction in the horizontal port. The T_f axis is along the toroidal direction at $R=3.9m$, $Z=0.0m$ on the horizontally long cross section. The Z_f axis is along the vertical direction.

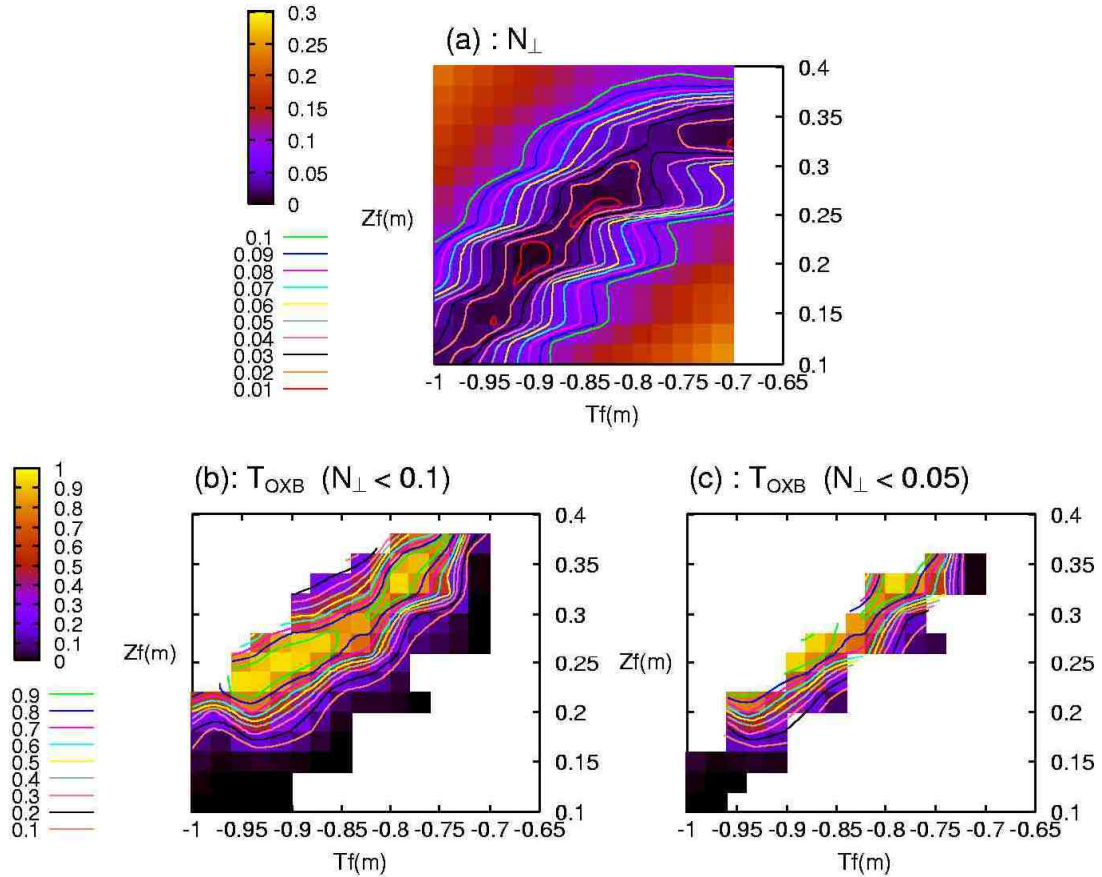


Figure 6 : (a): Minimum value of the perpendicular refractive index N_{\perp} , in the orbit of the launched O-mode, (b) : T_{OXB} calculated at the point where the minimum N_{\perp} is obtained, only for the cases where the minimum $N_{\perp} < 0.1$, (c) : T_{OXB} , only for the cases $N_{\perp} < 0.05$, are plotted as functions of launching parameter (T_f , Z_f) inside the "survey region" drawn in Figure. 5. The magnetic configuration is $(R_a, B_a) = (3.75\text{m}, 2.4\text{T})$ where R_a is the position of the magnetic axis and B_a is magnetic field strength on the axis. $n_e(\rho) = n_{e0} (1 - (\rho / 1.0)^8)$, $n_{e0} = 1 \times 10^{20} \text{ m}^{-3}$ and $T_e(\rho) = T_{e0} (1 - (\rho / 1.0)^4)$, $T_{e0} = 0.5 \text{ keV}$.

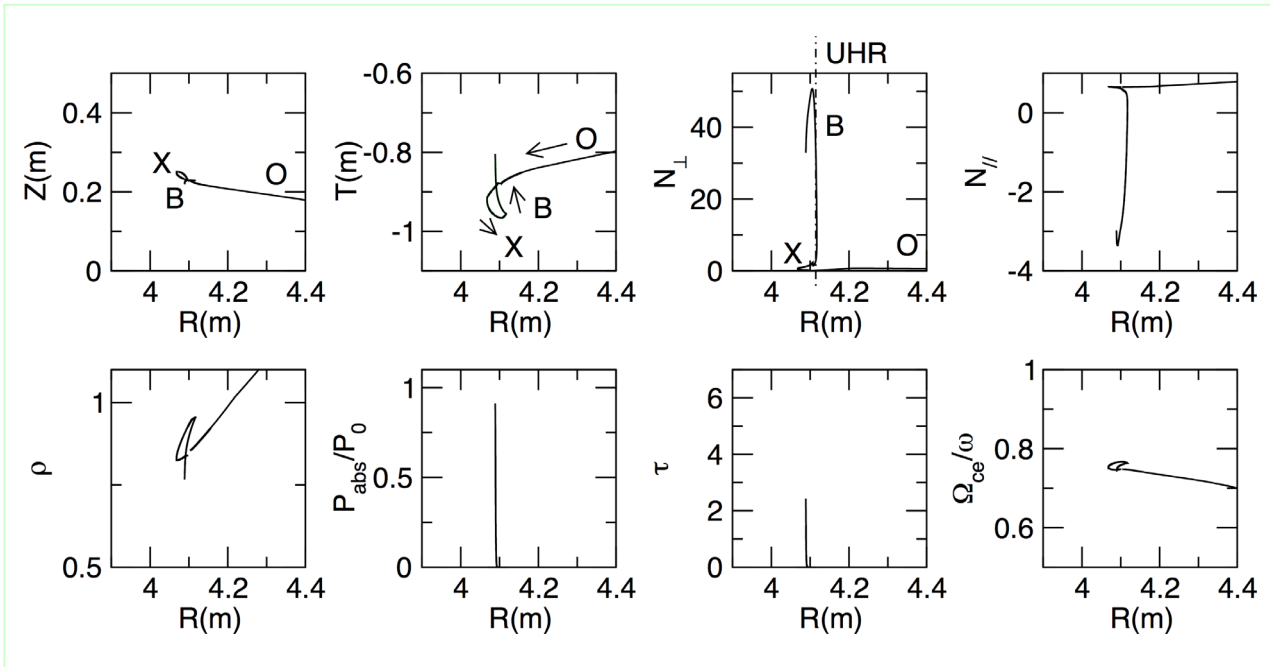


Figure 7 : Similar plot as figure 4. O-mode is launched from low field side so that EBW is excited via O-X-B mode conversion process. The launching parameter is $(T_f, Z_f) = (-0.9m, -0.25m)$. $n_e(\rho) = n_{e0} (1 - (\rho / 1.0)^8)$, $n_{e0} = 1 \times 10^{20} \text{ m}^{-3}$ and $T_e(\rho) = T_{e0} (1 - (\rho / 1.0)^4)$, $T_{e0} = 0.5 \text{ keV}$.

Study of high power ICRF antenna design in LHD

Hiroshi Kasahara¹⁾, Tetsuo Seki¹⁾, Kenji Saito¹⁾, Ryuhei Kumazawa¹⁾, Takashi Mutoh¹⁾,
Goro Nomura¹⁾, Fujio Shimpo¹⁾, Shin Kubo¹⁾, Takashi Shimozuma¹⁾, Yasuo Yoshimura¹⁾,
Hiroe Igami¹⁾, Hiromi Takahashi¹⁾, Yangping Zhao²⁾, Takuya Oosako³⁾, Yuichi Takase³⁾
and LHD experimental group¹⁾

¹⁾*National Institute for Fusion Science, Gifu 509-5292, Japan*

²⁾*Academia Sinica Plasma Physics Institute, Hefei 230031, People's Republic of China*

³⁾*University of Tokyo, Kashiwa 277-8561, Japan*

(Nov. 4, 2008)

In Large helical device (LHD), the antenna loadings are different from minority ion cyclotron heating (MICH)(38.47MHz) and mode converted ion Bernstein wave heating (MC-IBW)(28.4MHz), and there is necessary to improve antenna loading at different reasons. To design a new ion cyclotron range of frequencies (ICRF) antenna in LHD, simple antenna model is calculated using three-dimensional electrical magnetic code (High Frequency Structure Simulator, HFSS), and strap width and strap height are very important parameters to design the ICRF antenna. Antenna loading strongly depend on strap width, and the capacitance between strap and Faraday shield is important. Strap height changes peaked antenna loading frequency around 40 MHz, and the active electrical length is controlled by the strap height.

Keywords: ICRF, minority heating, mode conversion heating, antenna design, LHD

PACS: 52.50.Qt, 87.55.tg, 84.40.Ba

1 Introduction

In tokamak experiments, radio frequency wave with ion cyclotron range of frequencies (ICRF) has been investigated all over the world, and minority heating ^[1] and mode converted ion Bernstein wave heating ^[2] with good heating efficiency are demonstrated. In recent toroidal plasma experiments using ICRF, high energy particles impact to wall and inside of vacuum vessel ^[3] and they are terrible problems to sustain plasma discharge ^[4]. During long pulse operation hot spot is observed ^[5], and metal impurity flux is suddenly increased. After that radiation collapse is caused by the impurities, and plasma is terminated. The similar collapses at the end of long pulse discharges are reported in the LHD, magnetic axis sweeping is useful to decrease the hot spot temperature. However heating power is increased, the appearance time of hot spots is short and the hot spot temperature is rapidly increased. After strong hot spots are appeared, metal penetration usually happens and radiation collapse is caused. High energy particle which is accelerated on ion cyclotron resonances cause these impacts, and the ion tail handling is difficult in long pulse operation.

Mode-converted ion Bernstein wave (MC-IBW) heating is promising to direct electron heating, and weak ion tail enhancement is expected than minority heating. On initial heating experiment in LHD, direct electron heating is observed with negligible ion tail enhancement, and electron heating efficiency is larger than 80 %. MC-IBW is candidate for a heating tool of steady-state operation as a post minority heating. Though MC-IBW is very powerful heating tools with small ion tail enhancement and relative high heating efficiency, the loading resistance of MC-IBW is much smaller than that of minority heating in LHD(see Fig. 1). In typical low electron density plasmas in MC-IBW experiments, the loading resistance (less than $1 \times 10^{19} \text{ m}^{-3}$) is smaller than 2Ω , and in unmatched antenna impedance region between ICRF antenna and stub tuners ^[6] a voltage standing wave ratio (VSWR) is high ($|\Gamma| \sim 0.92$ with 2Ω , and $\text{VSWR} \sim 25$ without vacuum loading). In MC-IBW experiments the maximum voltage on transmission line is easily exceed 35 kV, and a transmission line protection circuit from arching often works. To avoid the work of a protection circuit with high power injection, higher loading resistance is needed.

In these ICRF heating scenarios aiming at steady-state operation, there are some techniques to increase loading resistance, and newly antenna design is one of the solution for high power ICRF injection with lower VSWR in the transmission line. In section 2, I would discuss about the ICRF antenna design and parameters (strap width, height, loop length and back faraday shield) using three-dimensional electromagnetic calculation code, HFSS. These characteristics are summarized in section 3.

2 Three dimensional simple model calculation of ICRF antenna

In LHD, each ICRF antenna has a single-loop strap (antenna width of 30 cm, antenna height of 60 cm), and they consist of one center conductor for fast wave excitation, Faraday shields for unexpected wave removing, many side carbon protectors for antenna protection from the plasma contacts and one back plate for return-current. Figure 2 shows the simple antenna model in the study of ICRF antenna design, though this simple antenna model does not have side carbon protectors to simplify the calculation. The simplifying the model is very useful to save calculation time and memory. Many calculation time is saved, and a few hours are needed in this simple mode calculation using 64 bit personal computer with Xeon CPU (3.4 GHz) and 64 GB Memory.

2.1 Strap width, strap height and loop length

Figure 3 shows the frequency dependence of $|S_{11}|$ for three kinds of strap width (30 cm, 60 cm, 80 cm), and the other typical parameters are same in Fig. 2. $|S_{11}|$ is return loss at feeder port in this antenna model, and $|S_{11}| = -3$ dB means that half of injection power is excited in fresh-water and vacuum regions. As strap width is increased, $|S_{11}|$ is strongly increased from -3dB to -8dB around frequency of 40 MHz, the maximum frequency is gradually decreased from 50 MHz to 45 MHz. Frequency dependence of $|S_{11}|$ around the peaked frequency becomes narrow over the frequency of 35 MHz, and $|S_{11}|$ around frequency of 28 MHz is not improved.

Figure 4 shows the frequency dependence of $|S_{11}|$ for three kinds of strap height (60 cm, 80 cm, 100 cm), and the other typical parameters are same in Fig. 2 and strap width is 60 cm. As strap height is increased, $|S_{11}|$ is weakly increased from -5dB to -6dB around frequency of 50 MHz, the peaked frequency around 50 MHz is strongly decreased from 60 MHz to 40 MHz. At lower frequency regions (~ 30 MHz), $|S_{11}|$ with strap height of 100 cm is obviously improved. This is not different in the dependence of strap width though that $|S_{11}|$ around the peaked frequency is narrow is similar to the characteristic of strap width. In LHD experiments, minority heating is carried out at frequency of 38.47 MHz (magnetic field of 2.75 T at major radius R of 3.6 m), and mode converted ion Bernstein wave is carried out at frequency of 28.4 MHz (magnetic field of 2.75 T at R of 3.6 m). The Improvement of $|S_{11}|$ in these two frequencies (38.47 MHz and 28.4 MHz) is necessary in LHD, and the increase of strap height is useful in these heating scenarios. When strap height is increased, electrical length between grounded point and feeder point is changed. The increases of strap height makes that this actual electrical length is close to

$\lambda/4$.

Figure 5 shows the frequency dependence of $|S_{11}|$ for three kinds of loop length (9.5 cm, 6.5 cm, 3.5 cm), and the other typical parameters are same in Fig. 2 except the strap width of 30 cm and the strap height of 80 cm. As loop length is decreased from 9.5 cm to 3.5 cm, peaked frequency is increased and $|S_{11}|$ is gradually decreased. Considering loop length is strongly related to with a cross section of magnetic filed excitation, they suggest that loop length is not only the increase of a cross section but also the increase of antenna capacitance. In this model, back Faraday shield exists and that distance is 1 cm, and the back Faraday shield could inhibit the effect of the increase of cross section to the increased of loop length.

2.2 Angle of Faraday shield

Figure 6 shows the frequency dependence of $|S_{11}|$ for four kinds of the Faraday shield angle to y direction ($0^\circ, 8^\circ, 16^\circ, 32^\circ$). and the other typical parameters are same in Fig. 2 except strap width of 20 cm, strap height of 100 cm. In this calculation, the antenna width is narrow than that of actual LHD antenna, and I would aim at the design for manufacturability with good accuracy. For these reasons, the strap width of 20 cm and the strap height of 100 cm is selected. When the angle of Faraday shield is increased from 0° to 32° , peaked frequency is slightly increased. The differences of peaked frequencies are negligible, and there is necessary to consider about the angle of Faraday shield in the optimization of $|S_{11}|$ and excitation frequencies.

2.3 Back Faraday shield

Figure 7 shows the frequency dependence of $|S_{11}|$ for four kinds of the distance between back plate and strap (1 cm, 3 cm, 5 cm, 8 cm), and the other typical parameters are same in Fig. 2 except strap width of 20 cm and strap height of 100 cm. As the gap between back Faraday shield and back plate is increased, peaked frequency is increased though the $|S_{11}|$ is roughly same. The gap between front Faraday shield and strap is 1 cm, and back Faraday shield work as a capacitance around the back Faraday shield gap of 1 cm. Though Back Faraday shield is useful when the back Faraday shield gap is less than the gap of front Faraday shield, many trouble are prospected since high voltage is induced around back Faraday shield.

2.4 Current profile on the surface of strap and Faraday shield effect

Current profile on the strap surface is very important to excite fast wave in the plasma, since excited wave pattern is strongly determined that RF current profile. For effective fast wave heating experiments, RF current had better go to the vertical direction (z direction), to magnetic field (y direction), and strong electrical field with the radial direction of plasma is excited at that time. Figure 8 shows the current profile on the strap surface at the front side (close to plasma) and the back side (close to back plate). In these figures, Most of RF current goes along the edge of center conductor on the front side, and RF current profile is favorable to excite fast wave. The difference between edge current and center current is approximately 10 times, and the difference of power is 100 times. They suggests that edge cooling is important than the center cooling, and the edge of strap is usually damaged rather than the center of strap. When the material temperature is high, the secondary electron emission coefficient is increased. There is a high possibility that the damage is caused by the concentration current at the edge of strap.

3 Summary and discussion

For steady-state operation using ICRF with high power, higher loading resistance antenna is needed in minority heating and mode converted ion Bernstein wave heating, though the reason of necessary for high loading resistance is different. In minority heating case there are necessary to decrease impurity ratio and ion tails, and in mode converted ion Bernstein wave heating case there are necessary to decrease the maximum voltage in the transmission line.

Using three dimensional electrical magnetic simulator code, HFSS, parameter dependences of ICRF antenna design are shown, and they (strap width, strap height, loop length and back Faraday shield) are summarized in the table 1. In these calculation strap width is useful to increase $|S_{11}|$, and the other parameter are not sensitive at the increase of $|S_{11}|$. For ion Bernstein wave experiments, the peaked frequency around 40 MHz have to be moved to lower frequency region (28 MHz), and three kinds of ways (strap height, loop length and back Faraday shield) exist. The increase of strap height is strong candidate for the adjustment parameter of the peaked frequency, since back Faraday shield is induced high RF voltage in the vacuum vessel.

4 Acknowledgment

This work was partially supported by the JSPS-CAS Core-University program in the field of 'Plasma and Nuclear Fusion'.

5 References

- 1 Start D, Jacquinot J, Bergeaud V, *et al.* 1998, Phys. Review Letters **80**: 3102
- 2 Majeski R, Rogers J H, Batha S H, *et al.* 1996, Phys. Review Letters **76**: 764
- 3 Saito K, Kumazawa R, Mutoh T, *et al.* 2002, Plasma Phys. Control. Fusion, **44**: 103
- 4 Kasahara H, Seki T, Saito K, *et al.* 2008, Fusion Eng. Des., **83**: 253
- 5 Bremond S, Agarici G, Beaumont B, *et al.* 2003, Fusion Eng. Des., **22**: 1253
- 6 Kumazawa R, Mutoh T, Seki T, *et al.* 1999, Rev. Sci. Inst., **70**: 2665

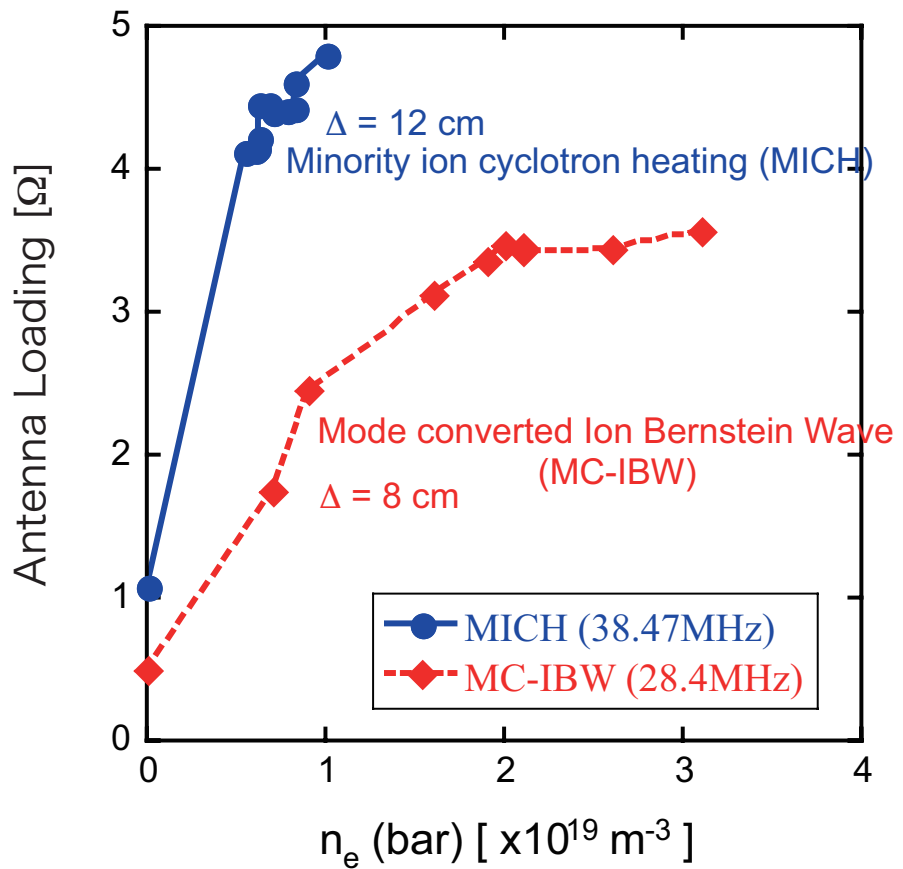


Fig. 1 Loading resistance depends on plasmas density, and that of minority heating in steady-state operation is higher than that of mode-converted IBW heating. This antenna is design to excite fast wave for minority heating, and neutral beams are additionally injected the higher electron density of MC-IBW ($> 1 \times 10^{19} m^{-3}$).

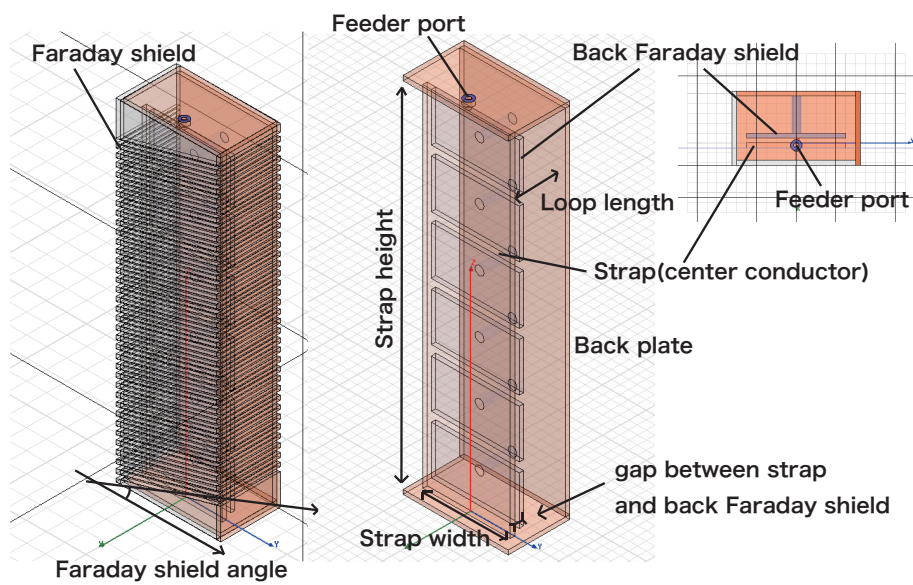


Fig. 2 Three dimensional simple ICRF antenna model. Typical design parameters are as follows: strap width of 20 cm, strap height of 80 cm, loop length of 9.5 cm, the distance between plasma(fresh-water) and antenna is 5 cm, the distance between back plate and metal wall is 3 cm. Antenna exists on vacuums region, and fresh-water exists in front antenna. The size to each direction of imaginal plasma region is 2.5 m, and the size of each direction of vacuum region is similar to imaginal plasma except the size of the loop direction (less than 20 cm, and there are different in each loop lengths).

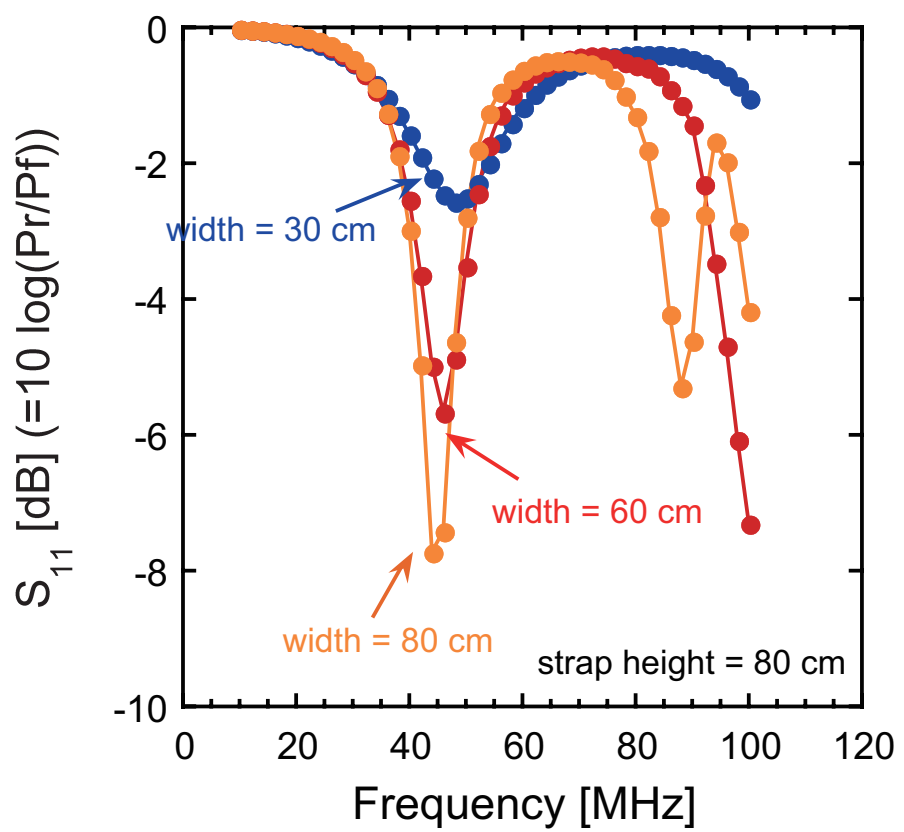


Fig. 3 Frequency dependence for various strap width without back Faraday shield. $|S_{11}|$ is very useful to increase loading resistance.

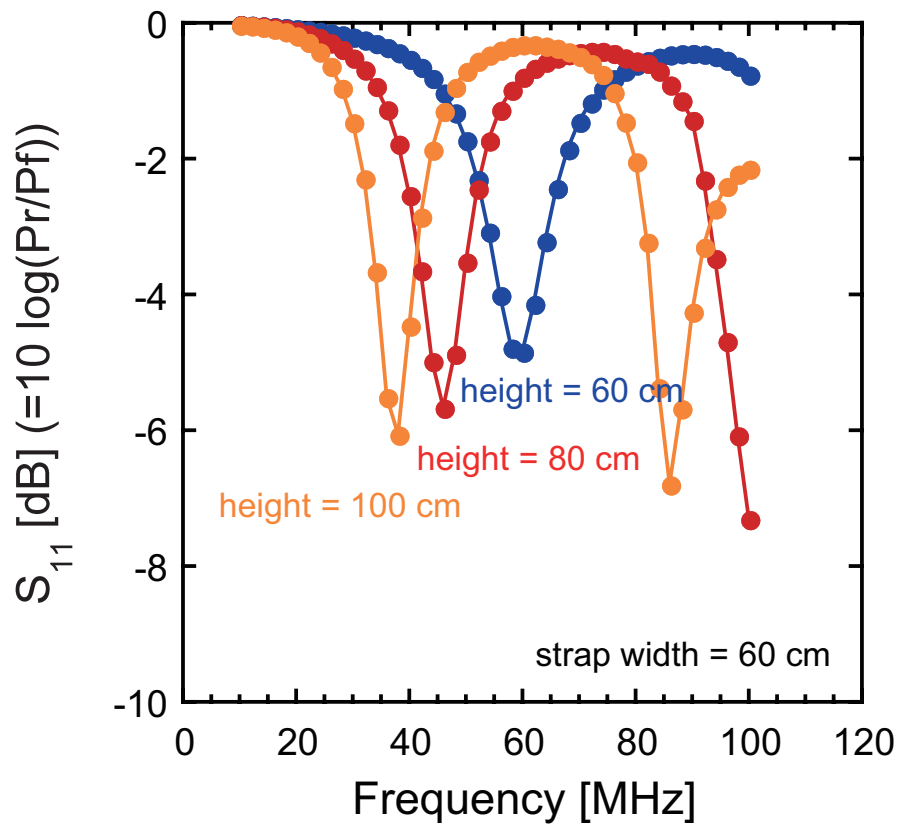


Fig. 4 Frequency dependence for various strap height without back Faraday shield. The peaked frequency obviously is decreased, as the strap height is increased.

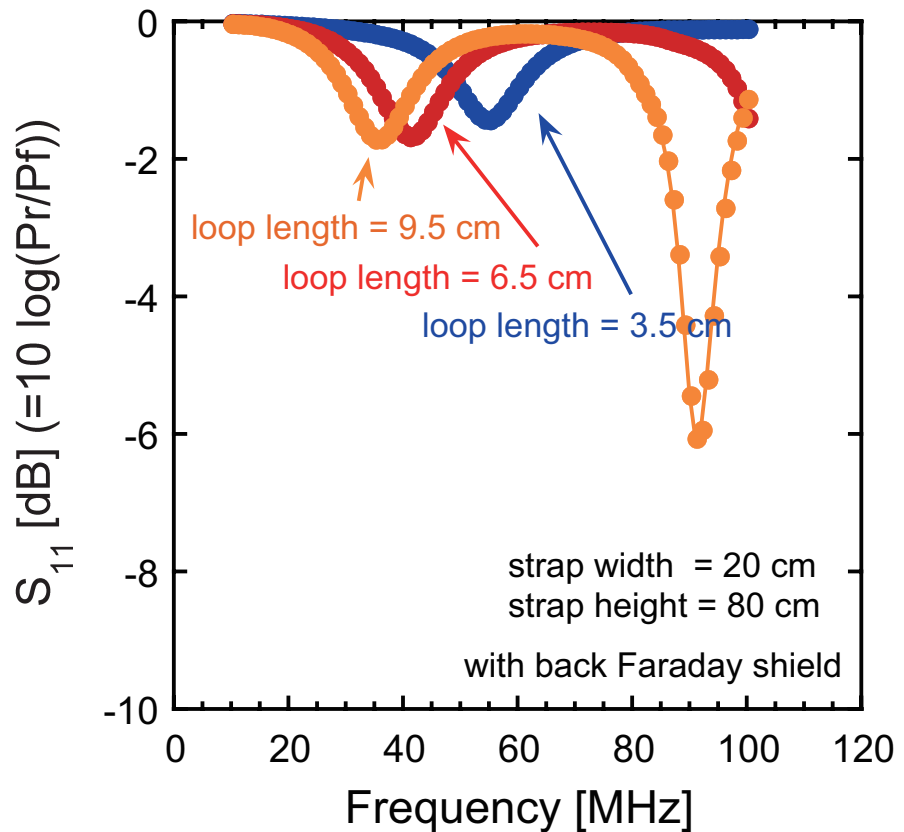


Fig. 5 Frequency dependence for various loop length with back Faraday shield. The distance between back Faraday shield and strap is 1 cm.

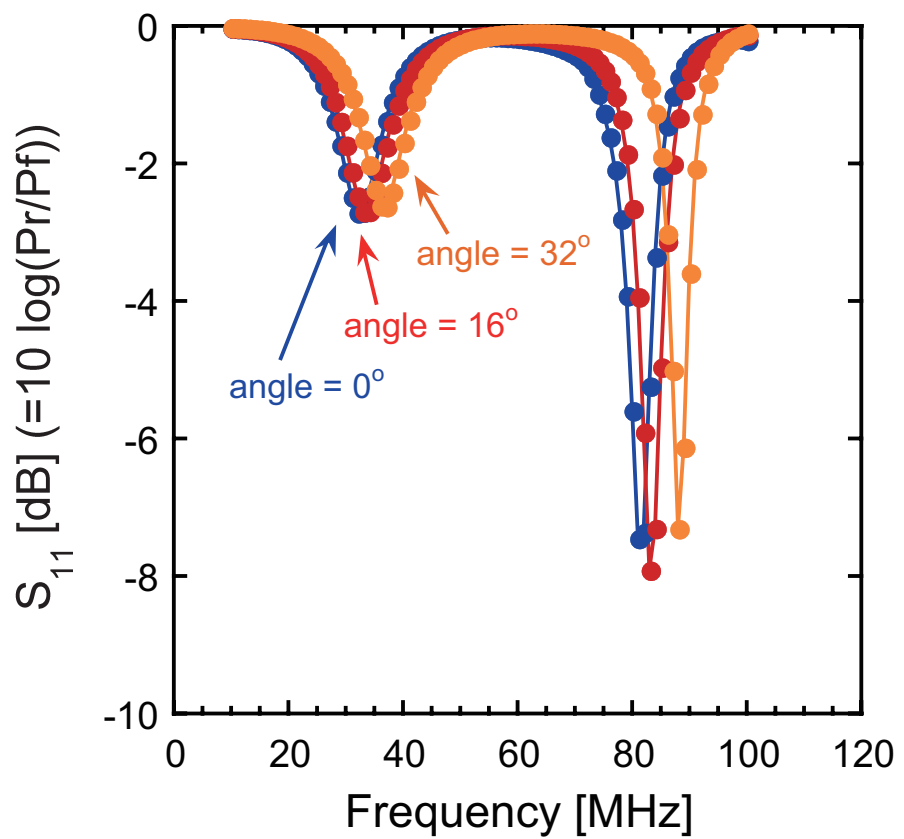


Fig. 6 Frequency dependence for angles of Faraday shield without back Faraday shield. Peaked frequencies are roughly same in various angles.

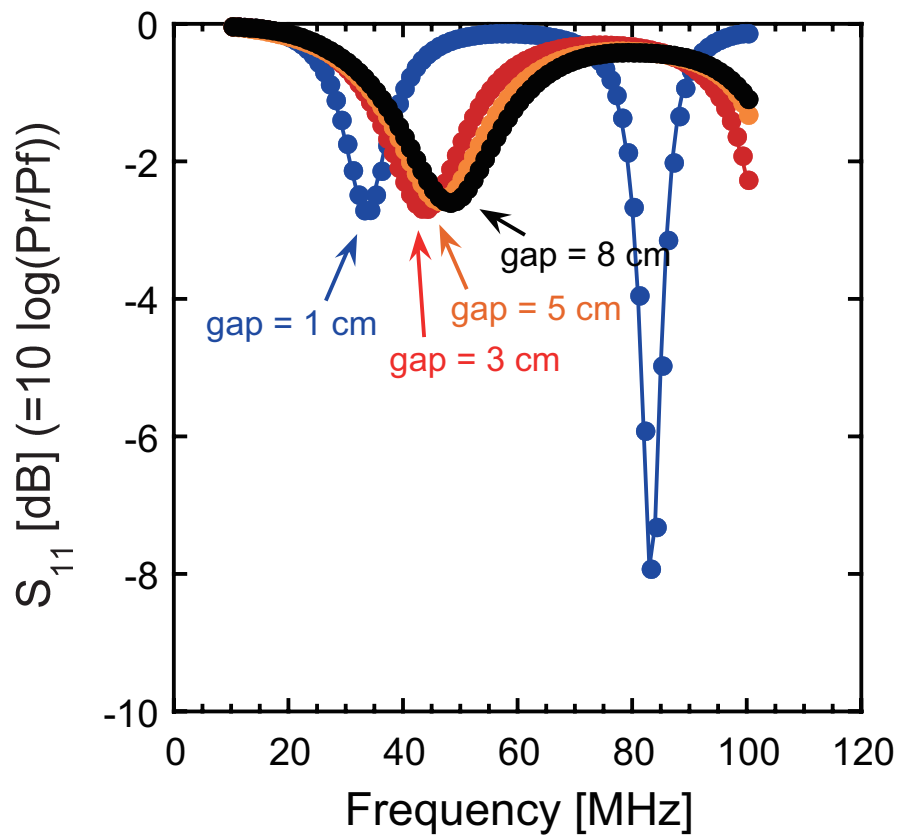


Fig. 7 Frequency dependence for back Faraday shield. Loop length of 9.5 cm. The distance between the front Faraday shield and strap is 1 cm. The gap is only less than 3 cm, the peaked frequencies are decreased and there are negligible.

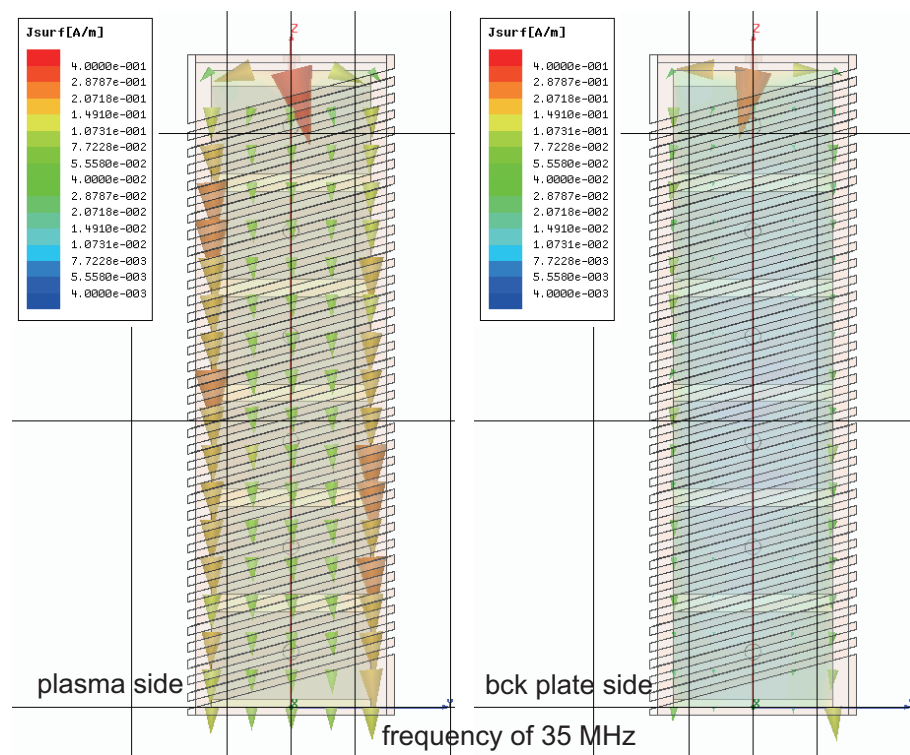


Fig. 8 Current profile of the center conductor at the front side (plasma side) and back side (back plate side) at the frequency of 35 MHz ($|S_{11}|$ is peaked). RF current is concentrated on the edge of antenna.

Table 1 Characteristics for the design parameters. C: capacitance, L: inductance, $l_{\text{electrical}}$: electrical length, \bigcirc : strong dependence, \times : weak or negligible dependance

Parameters	$ S_{11} $	Frequunecy	Contens
Strap width	\bigcirc	\times	C, L
Strap height	\times	\bigcirc	$l_{\text{electrical}}$
Loop length	\times	\bigcirc	L
Back Faraday shield	\times	\bigcirc	C

Energetics of resistive wall modes in flowing plasmas

M. HIROTA

Japan Atomic Energy Agency, Naka, Ibaraki, 311-0193, Japan

Stability of magnetohydrodynamic (MHD) waves subject to Alfvén and sound resonances and small resistivity at a conductive wall is analytically discussed in terms of wave energy (or, more precisely, wave action). Negative energy wave, which may exist in the presence of mean flow, is shown to be destabilized by the resistive wall, where its growth rate is characterized by the energy dissipation rate. The effect of resonance is examined as well based on a recent knowledge of wave energy for Alfvén and sound continuum modes. Resonant coupling between an eigenmode and a continuum mode having the same sign of energy results in phase mixing (or continuum) damping. In contrast, if their signs are opposite, such resonance triggers an instability.

PACS numbers: 52.55.Tn, 52.65.Kj, 52.35.Py

Keywords: MHD stability, resistive wall mode, flowing plasma, wave energy

I. INTRODUCTION

Stabilization of resistive wall modes by plasma rotation is one of the key issues in modern fusion experimental devices (such as tokamaks) toward improved confinement. This phenomenon is in itself of physical significance since the well-known energy principle¹, which also serves to resistive wall modes², is no longer expedient for stability analysis of flowing plasmas, and a solid analytical footing is still lacking.

Recently, wave energy is drawing attention as a suitable quantity that characterizes stability of flowing plasmas³, even in the presence of a resistive wall^{4,5}. However, it is proposed^{6,7} that, in addition to flow, the continuum damping due to Alfvén or sound resonance is necessary for stabilizing resistive wall mode (as far as in the MHD model). In order to incorporate the effect of resonance into the energetics, wave energy for the continuum modes must be specified. Its formulation has been recently developed in a general manner⁸ and applied to the MHD continuous spectrum⁹.

In this paper, we present wave energy for the case of cylindrical plasmas, following the recent works^{8,9}, and discuss stability in terms of it. We shall investigate whether a stable oscillatory mode (= wave) in a flowing plasma will be destabilized or not by introducing the effects of both resonance and wall resistivity as perturbation. Our result systematically generalizes earlier works^{4,6}

and provides an unified view by making use of wave energy.

II. CYLINDRICAL PLASMA

We consider cylindrical equilibria illustrated in FIG. 1 (where the length L is introduced just for reference). The plasma in $r < a$ may have arbitrary flow $\mathbf{v} = (0, v_\theta(r), v_z(r))$, magnetic field $\mathbf{B} = (0, B_\theta(r), B_z(r))$ and mass density $\rho(r)$ (the equilibrium force balance then determines a pressure profile). The outer region $a < r$ is vacuum except that a thin conductive wall is placed at $r = b$. For simplicity, the total pressure (i.e., kinetic plus magnetic pressure) is supposed to be smooth at $r = a$.

We focus on linear perturbations with a single Fourier harmonics $\exp(im\theta + ikz - i\Omega t)$ for fixed wavenumbers $m, k \in \mathbb{R}$. The frequency $\Omega \in \mathbb{C}$ is to be sought by the eigenvalue problem^{10,11},

$$\begin{pmatrix} \frac{\Pi_2}{\Pi_0} & \frac{\Pi_3}{\Pi_0} - \frac{\partial}{\partial r} \\ \frac{\Pi_3}{\Pi_0} + \frac{\partial}{\partial r} & \frac{\Pi_1}{\Pi_0} \end{pmatrix} \begin{pmatrix} r\xi \\ p \end{pmatrix} = 0 \quad (1)$$

where ξ denotes the radial component of the Lagrangian displacement, and p denotes the perturbed total pressure. The function $\Pi_0(r, \Omega)$ is given by

$$\Pi_0 = [(\Omega - \mathbf{k} \cdot \mathbf{v})^2 - \omega_A^2][(\Omega - \mathbf{k} \cdot \mathbf{v})^2 - \omega_S^2],$$

where $\mathbf{k} \cdot \mathbf{v} = mv_\theta/r + kv_z$, and $\omega_A(r)$ and $\omega_S(r)$, respectively, denote the local Alfvén and slow magneto-sonic frequencies. Other functions $\Pi_{1,2,3}(r, \Omega)$ are also given explicitly, and they satisfy a well-known relation $\Pi_1\Pi_2 - \Pi_3^2 \propto \Pi_0$ (see Bondeson *et al.*¹¹ for details).

Equation (1) should be solved in $0 < r < a$ under the boundary condition $\lim_{r \rightarrow 0} r\xi = 0$ at the origin. On the other hand, the perturbed magnetic field in the vacuum region can be solved analytically. By invoking the thin resistive wall approximation², the boundary condition at the plasma surface $r = a$ is expressed as

$$\frac{p(a)}{\xi(a)} = \frac{f_b + \frac{i}{\tau_w \Omega} f_\infty}{1 + \frac{i}{\tau_w \Omega}}, \quad (2)$$

where $\tau_w \in \mathbb{R}$ denotes the resistive wall diffusion time (inversely proportional to the resistivity)⁶. If an ideal wall ($1/\tau_w \rightarrow 0$) were to be located at $r = b$ (or $r = \infty$), then $f_b \in \mathbb{R}$ (or $f_\infty \in \mathbb{R}$) would represent the ratio of surface pressure change $p(a)$ to surface displacement $\xi(a)$, and an inequality $f_b \geq f_\infty \geq 0$ holds. It is more conventional to use the perturbation energy W_b (or W_∞) stored in the vacuum magnetic field;

$$W_{b,\infty} = 2\pi a L \frac{|\xi(a)|^2}{2} f_{b,\infty}. \quad (3)$$

For later use, we denote the 2×2 operator in Eq. (1) by $\mathcal{E}(\Omega)$. For any $\Omega \in \mathbb{C}$, let $\Xi(r, \Omega)$ and $P(r, \Omega)$ be the solution of

$$\mathcal{E}(\Omega) \begin{pmatrix} \Xi \\ P \end{pmatrix} = 0 \quad \text{with} \quad \begin{cases} \Xi(0, \Omega) = 0, \\ P(0, \Omega) = 1. \end{cases} \quad (4)$$

Note that $\mathcal{E}(\Omega)$ is real except for the parameter Ω , i.e. $\mathcal{E}(\Omega) = \overline{\mathcal{E}(\overline{\Omega})}$, where the overbar denotes complex conjugate. This fact implies that $\Xi(r, \Omega) = \overline{\Xi(r, \overline{\Omega})}$ and $P(r, \Omega) = \overline{P(r, \overline{\Omega})}$.

We can solve Ξ and P numerically, for example, by the shooting method. Then, the other boundary condition

$$D(\Omega) := \frac{P(a, \Omega)}{\Xi(a, \Omega)} - \frac{f_b + \frac{i}{\tau_w \Omega} f_\infty}{(1 + \frac{i}{\tau_w \Omega}) a} = 0 \quad (5)$$

can be regarded as a dispersion relation, namely, the point spectrum (eigenvalues) of $\mathcal{E}(\Omega)$ is the set of ω_n , $n = 1, 2, \dots$, satisfying $D(\omega_n) = 0$. The corresponding eigenmodes are given by

$$\text{Re}[(\hat{\xi}_n, \hat{p}_n) e^{im\theta + ikz - i\omega_n t}] \quad (6)$$

where $r\hat{\xi}_n(r) = c_n \Xi(r, \omega_n)$ and $\hat{p}_n(r) = c_n P(r, \omega_n)$ with some amplitude $c_n \in \mathbb{C}$.

It is also well-known that $\mathcal{E}(\Omega)$ has the continuous spectrum associated with Alfvén (ω_A) and slow magneto-sonic (ω_S) waves;

$$\sigma_A^\pm = \{\mathbf{k} \cdot \mathbf{v}(r) \pm \omega_A(r) \in \mathbb{R} : r \in [0, a]\}, \quad (7)$$

$$\sigma_S^\pm = \{\mathbf{k} \cdot \mathbf{v}(r) \pm \omega_S(r) \in \mathbb{R} : r \in [0, a]\}. \quad (8)$$

When Ω belongs to any of them, the term $1/\Pi_0$ in $\mathcal{E}(\Omega)$ becomes singular. One can derive singular (or improper) eigenfunction $\hat{\xi}(\omega), \hat{p}(\omega)$ for every $\omega \in \sigma_c := \sigma_A^+ \cup \sigma_A^- \cup \sigma_S^+ \cup \sigma_S^-$.

III. WAVE ACTION

For the moment, we restrict ourself to the case of ideal wall ($1/\tau_w \rightarrow 0$) at $r = b$, for which the operator $\mathcal{E}(\Omega)$ is symmetric and the dynamical system has the Hamiltonian property⁸. Wave energy is then represented by the normal form; $\omega_n \mu_n$ for eigenmodes and $\int \omega \mu(\omega) d\omega$ for continuum mode, where μ_n and $\mu(\omega)$ denote wave actions attributed to each wave.

A. Point spectrum

Let us consider an oscillatory mode (6) with a real frequency $\omega_n \in \mathbb{R}$. The corresponding wave action is given by⁸

$$\mu_n = \pi L \int_0^a \overline{\begin{pmatrix} r\hat{\xi}_n & \hat{p}_n \end{pmatrix}} \frac{\partial \mathcal{E}}{\partial \Omega}(\omega_n) \begin{pmatrix} r\hat{\xi}_n \\ \hat{p}_n \end{pmatrix} dr. \quad (9)$$

Now, let us differentiate an identity,

$$0 = \int_0^a \begin{pmatrix} \Xi(\Omega) & P(\Omega) \end{pmatrix} \mathcal{E}(\Omega) \begin{pmatrix} \Xi(\Omega) \\ P(\Omega) \end{pmatrix} dr, \quad (10)$$

with respect to Ω . By exploiting the symmetry of $\mathcal{E}(\Omega)$, we obtain

$$\begin{aligned} 0 = & \int_0^a \begin{pmatrix} \Xi(\Omega) & P(\Omega) \end{pmatrix} \frac{\partial \mathcal{E}}{\partial \Omega}(\Omega) \begin{pmatrix} \Xi(\Omega) \\ P(\Omega) \end{pmatrix} dr \\ & - \left[\Xi^2(\Omega) \frac{\partial}{\partial \Omega} \left(\frac{P}{\Xi} \right) (\Omega) \right]_{r=a}. \end{aligned} \quad (11)$$

By substituting $\Omega = \omega_n$ into this identity, we can derive an alternative form of (9) as

$$\mu_n = \pi L |a\hat{\xi}_n(a)|^2 \frac{\partial D_b}{\partial \Omega}(\omega_n), \quad (12)$$

where $D_b(\Omega) := (P/\Xi)(a, \Omega) - f_b/a = 0$ is the dispersion relation. The similar expression for wave energy $(\omega_n \mu_n)$ has been observed in many literatures^{12,13}. The wave energy can be negative in the presence of flow^{8,14}.

B. Continuous spectrum

For the sake of completeness, we exhibit only the result^{8,9} for the continuous spectrum. For each $\omega \in \sigma_c$, the wave action is represented by

$$\begin{aligned} \mu(\omega) = & \pi L \int_0^a \pi \left[|\hat{\psi}(\omega)|^2 + |\hat{\psi}^\dagger(\omega)|^2 \right] \\ & \times \text{Im}[\Lambda(\omega + i0)] dr \end{aligned} \quad (13)$$

where we have put $\hat{\psi}(\omega) = -(\Pi_3/\Pi_1)(\omega)r\hat{\xi}(\omega) - \hat{p}(\omega)$ and $\hat{\psi}^\dagger(\omega)$ is the Hilbert transform of $\hat{\psi}(\omega)$. Moreover, $\Lambda(\Omega) = \Pi_1(\Omega)/\Pi_0(\Omega)$, which yields four Dirac's delta functions in the limit of $\Omega \rightarrow \omega + i0$,

$$\begin{aligned} \text{Im}[\Lambda(\omega + i0)] = & \frac{\pi r}{2\rho} \left\{ \frac{k_\perp^2}{\omega_A} [\delta(\omega - \mathbf{k} \cdot \mathbf{v} - \omega_A) \right. \\ & - \delta(\omega - \mathbf{k} \cdot \mathbf{v} + \omega_A)] \\ & + \frac{k_\parallel^2 \omega_S^3}{\omega_A^4} [\delta(\omega - \mathbf{k} \cdot \mathbf{v} - \omega_S) \\ & \left. - \delta(\omega - \mathbf{k} \cdot \mathbf{v} + \omega_S)] \right\}, \end{aligned}$$

where $k_\parallel = (mB_\theta/r + kB_z)/|\mathbf{B}|$ and $k_\perp = (-kB_\theta + mB_z/r)/|\mathbf{B}|$.

IV. BIFURCATION THEORY

Let $\omega_n \in \mathbb{R}$ be an eigenvalue discussed in Sec. III A. Now, we put $c_n = 1$ for simplicity, so that both $\hat{\xi}_n$ and \hat{p}_n are real functions. We consider stability of this wave by assuming that (i) a slight modification of the equilibrium fields occurs like

$$\Pi_j \rightarrow \Pi'_j \quad (j = 0, 1, 2, 3), \quad (14)$$

so that the wave undergoes *weak resonance* with some continuum and (ii) the wall actually has a small resistivity $1/\tau_w \omega_n \sim O(\epsilon)$. Let $\omega'_n \in \mathbb{C}$ and $(\hat{\xi}'_n, \hat{p}'_n)$ be the resultant solution of the eigenvalue problem,

$$\begin{aligned} \mathcal{E}'(\omega'_n) \begin{pmatrix} r\hat{\xi}'_n \\ \hat{p}'_n \end{pmatrix} = 0, \quad \left[r\hat{\xi}'_n \right]_{r=0} = 0, \\ \left[\hat{p}'_n - \frac{f'_b + \frac{i}{\tau_w \omega'_n} f'_\infty}{1 + \frac{i}{\tau_w \omega'_n}} \hat{\xi}'_n \right]_{r=a} = 0, \end{aligned} \quad (15)$$

while their deviations, $\delta\omega = \omega'_n - \omega_n$ and $(\delta\hat{\xi}, \delta\hat{p}) = (\hat{\xi}'_n - \hat{\xi}_n, \hat{p}'_n - \hat{p}_n)$, are supposed to be small $\sim O(\epsilon)$.

We are now interested in whether an instability $\text{Im}(\delta\omega) > 0$ occurs or not. To see this, it is useful to expand the following identity,

$$0 = \int_0^a \begin{pmatrix} r\hat{\xi}'_n & \hat{p}'_n \end{pmatrix} \mathcal{E}'(\omega'_n) \begin{pmatrix} r\hat{\xi}'_n \\ \hat{p}'_n \end{pmatrix} dr. \quad (16)$$

By denoting $\delta\mathcal{E} = \mathcal{E}' - \mathcal{E}$ and exploiting the symmetry of $\mathcal{E}(\omega_n)$ again, one can obtain, to leading order,

$$\begin{aligned} 0 = & \delta\omega \int_0^a \left(r\hat{\xi}_n \ \hat{p}_n \right) \frac{\partial\mathcal{E}}{\partial\Omega}(\omega_n) \begin{pmatrix} r\hat{\xi}_n \\ \hat{p}_n \end{pmatrix} dr \\ & + \int_0^a \left(r\hat{\xi}_n \ \hat{p}_n \right) \delta\mathcal{E}(\omega'_n) \begin{pmatrix} r\hat{\xi}_n \\ \hat{p}_n \end{pmatrix} dr \\ & + \left[\hat{p}_n r \delta\hat{\xi} - r\hat{\xi}_n \delta\hat{p} \right]_{r=a}, \end{aligned} \quad (17)$$

Note that, from (15), the expansion of the boundary condition at $r = a$ gives

$$\left[\delta\hat{p} - f_b \delta\hat{\xi} - \left(\delta f_b - i \frac{f_b - f_\infty}{\tau_w \omega_n} \right) \hat{\xi}_n \right]_{r=a} = 0$$

with $\delta f_b = f'_b - f_b$, which can be used in the boundary terms of (17). Let us multiply (17) by πL and take its imaginary part, which leads to

$$\text{Im}(\delta\omega)\mu_n = -\delta\mu_n - \frac{W_b - W_\infty}{\tau_w \omega_n} \quad (18)$$

where (3) and (9) has been used and the remaining term

$$\delta\mu_n := \pi L \int_0^a \left(r\hat{\xi}_n \ \hat{p}_n \right) \text{Im} [\delta\mathcal{E}(\omega'_n)] \begin{pmatrix} r\hat{\xi}_n \\ \hat{p}_n \end{pmatrix} dr,$$

manifests the resonance effect.

The resonance implies that ω_n belongs to the continuous spectrum after the modification (14), namely, $\Pi'_0(r, \omega_n) = 0$ occurs at some resonant points. Recall that $\text{Im}[\Lambda'(\omega_n + i0)]$ include four delta functions, and their coefficients are supposed to be small $\sim O(\epsilon)$ (weak resonance). Since $\hat{\xi}_n$ and \hat{p}_n are smooth functions, $\text{Im} [\delta\mathcal{E}(\omega'_n)]$ in $\delta\mu_n$ can be approximated by

$$\text{Im} [\delta\mathcal{E}(\omega'_n)] \simeq \begin{pmatrix} \frac{\Pi'_2}{\Pi'_1} & \frac{\Pi'_3}{\Pi'_1} \\ \frac{\Pi'_3}{\Pi'_1} & 1 \end{pmatrix} (\omega_n) \text{Im}[\Lambda'(\omega_n + i0)].$$

By introducing $\hat{\psi}_n = -(\Pi'_3/\Pi'_1)(\omega_n)r\hat{\xi}_n - \hat{p}_n$, we obtain

$$\begin{aligned} \delta\mu_n = & \pi L \int_0^a \left[\hat{\psi}_n^2 + \frac{\Pi'_1 \Pi'_2 - \Pi'^2_3}{\Pi'^2_1} (r\hat{\xi}_n)^2 \right] \\ & \times \text{Im}[\Lambda'(\omega_n + i0)] dr \\ = & \pi L \int_0^a \hat{\psi}_n^2 \text{Im}[\Lambda'(\omega_n + i0)] dr \end{aligned} \quad (19)$$

where the use of the relation, $\Pi'_1 \Pi'_2 - \Pi'^2_3 \propto \Pi'_0$, has been made. Since this expression is similar to (13), the sign of $\delta\mu_n$ corresponds to that of the wave action of the continuum mode, $\mu(\omega_n)$, at ω_n .

V. DISCUSSION

We have analytically investigated stability of an oscillatory eigenmode (or wave) subject to weak resonance in the plasma and small resistivity at the wall. The subsequent growth rate, $\text{Im}(\delta\omega)$, is estimated by (18), where wave actions and vacuum field energy are well-defined in this work. The wall resistivity dissipates the wave energy $\omega_n\mu_n$ at a rate of $(W_b - W_\infty)/\tau_w > 0$, which damps any wave with positive energy, but conversely destabilizes negative energy waves. The latter may exist only when the plasma is flowing. Simultaneously, the resonance causes the continuum damping of the wave if wave actions for point and continuous spectra have same sign $\delta\mu_n/\mu_n > 0$, whereas a resonant instability occurs if they have opposite sign. The eventual growth rate, as well as the marginal condition, is determined by these factors.

Acknowledgments

This work was partially supported by the JSPS-CAS Core-University program in the field of 'Plasma and Nuclear Fusion'.

-
- ¹ Bernstein I B, Frieman E A, Kruskal M D, Kulsrud R M. 1958, Proc. Roy. Soc. London, A244: 17
 - ² Haney S W, Freidberg J P. 1989, Phys. Fluids B, 1: 1637
 - ³ Khalzov I V, Smolyakov A I, Ilgisonis V I. 2008, Phys. Plasmas, 15: 054501
 - ⁴ Lashmore-Davies C N. 2001, Phys. Plasmas, 8: 151
 - ⁵ Lashmore-Davies C N. 2005, J. Plasma Phys., 71: 101
 - ⁶ Betti R, Freidberg J P. 1995, Phys. Rev. Lett., 74: 2949
 - ⁷ Zheng L-J, Kotschenreuther M, Cheu M S. 2005, Phys. Rev. Lett., 95: 255003
 - ⁸ Hirota M, Fukumoto Y. 2008, J. Math. Phys., 49: 083101
 - ⁹ Hirota M, Fukumoto Y. to appear in Phys. Plasmas.
 - ¹⁰ Appert K, Gruber R, Vaclavik J. 1974, Phys. Fluids, 17: 1471
 - ¹¹ Bondeson A, Iacono R, Bhattacharjee A. 1987, Phys. Fluids, 30: 2167
 - ¹² Stix T H. 1962, *The Theory of Plasma Waves*. McGraw-Hill, New York.
 - ¹³ Cairns R A. 1979, J. Fluid Mech., 92: 1
 - ¹⁴ Sturrock P A. 1960, J. Appl. Phys., 31: 2052

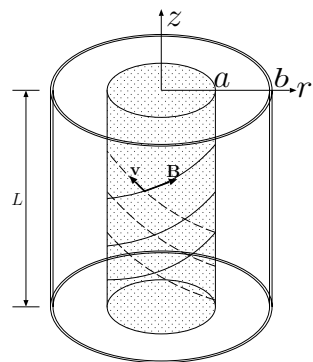


FIG. 1: Cylindrical geometry

Recent Progress of Neutral Beam Injector and Beam Emission Diagnosis in LHD

IKEDA Katsunori , NAGAOKA Kenichi, TAKEIRI Yasuhiko, OSAKABE

Masaki, TSUMORI Katsuyoshi, KANEKO Osamu, and LHD Experimental

Group

National Institute for Fusion Science, Toki, Gifu 509-5292, Japan

November 4 2008

Large size hydrogen neutral beam injectors (NBI) used a negative ion source (NNBI) and a proton source (PNBI) have been developed for the Large Helical Device. The injection power from NNBI and PNBI have reached $16MW$ and $6.8MW$, respectively. These injection powers have outstripped the nominal beam powers. A diagnostic system of beam emitted hydrogen visible spectrum has been installed along the beam injection axis to estimate the energy fraction on PNBI. The full energy beam component is about half which is equivalent to 70% injection beam power. The beam attenuation of high energy neutral beam is also observed on NNBI. The peak density distribution is effective to increases beam deposition power.

PACS: 52.50.Gj, 52.40.Mj, 52.70.Kz

Keywords: NBI, spectroscopy, LHD

author's e-mail: ikeda.katsunori@lhd.nifs.ac.jp

1. Introduction

The operation of Large Helical Device (LHD) has been executed successfully in 10 years. A neutral beam injector (NBI) as a main heating device has closely related to production of high temperature and/or high density plasma [1-3]. Especially, the operation result of negative ion based NBI system (NNBI) which spans 10 years [4] contributes to assess the possibility of a future NNBI system for ITER (International Thermonuclear Experimental Reactor) [5]. Hydrogen negative ion (H^-) source is a necessity tool in order to generate a high energy NB such as 180 keV, because the neutralization efficiency used gas cell keeps 60% in H^- case, although that efficiency drops under 10% in proton (H^+) case [6]. There are several important topics on NNBI to generate a high power beam and to do a stable operation as follows; improvement of efficiency to product H^- ions with or without Cs vapor, and improvement of the beam uniformity in a large size ion source, and decreasing of the heat loading into grid systems.

Used only high energy NBIs, we had achieved 13keV ion temperature (T_i) in an argon discharge plasma, since ion heating power increased in the high-Z discharge effectively [1, 2]. In the same heating condition, T_i rose about 2keV in hydrogen discharge due to the only 40% ion heating fraction by 180keV neutral beam. The ion heating fraction can be upped to 80% by decreasing 40keV beam energy in hydrogen discharge. So we have installed 40keV low energy PNBI system used a high current proton source for the purpose of improvement of T_i in hydrogen discharge [7].

In the following, we present NBI systems used a negative hydrogen ion source and a proton source for LHD experiment. The progress of the NB heating power is shown in the next section. We also show the beam emission diagnosis to obtain energy fraction of neutral beam in PNBI and to obtain beam attenuation along the beam injection axis in NNBI.

2. Neutral Beam Injectors in LHD

LHD-NBI system consists three tangential beam lines (BL1, BL2 and BL3) and the perpendicular beam line (BL4) arranged as shown in Fig. 1. The nominal beam energy and injection beam power of the tangential NNBI is 180keV and 5MW, respectively in each beam line used two H^- ion sources. In the ion source, H^- ions are produced on a surface of plasma grid faced to arc discharge by using cesium (Cs) vapor. The inner size of the arc chamber of this ion source is 145cm height, 35cm width and 20cm depth. H^- ions are extracted by five segments

of the grid systems composed by plasma grids ($-180kV$), extraction grids ($-170kV$) and grounded grids ($0kV$). H^- beam is neutralized in $3m$ long neutralizer with hydrogen gas, and then H^- and H^+ ions are removed on an ion beam dump by an ion bending magnet. Each NB is tilted 1.8° from the beam injection axis in order to pass through a injection port. Beam protection armor plates are equipped on a inner surface of the LHD vacuum vessel at the crossing position of the beam injection axis. The nominal beam durations is $10sec$ with high power beam, $2 \sim 5sec$ NB is usually used for LHD operation now.

Figure 2(a) shows the history of total NB injection power from three NNBI. NB power increases year by year, and it has reached $16MW$ in 2007. The total NB power jumped up at 2001 when the BL3 operation was started. In the BL3, we have adopted the individual twelve power supplies for arc discharge in order to control a beam distribution. The beam uniformity was improved by changing the arc discharge distribution [8,9]. The total NB power was exceed $13MW$ at 2003 when the multi-slot grounded grid (MSGG) was installed in BL1 [10]. The heat load into the MSGG with the transparency of 67% was suppressed to about a half compared to the conventional multi-aperture grounded grid (MAGG) with the transparency of 35%. The acceleration voltage was improved to $190keV$ by the reduction of the gas pressure in the acceleration gap. The difference of the optimum condition for the beamlet convergence between parallel and perpendicular directions to the slot was appeared [10]. This disagreement has been fixed now by a steering grids with racetrack shaped apertures [11].

The operation of the forth beam line (BL4) was started successfully at 2005 as shown in Fig. 2(b) [7,12,13]. We have adopted an arc discharge H^+ ion source with $200mA/cm^2$ high H^+ current density in BL4. Two ion sources was installed in the A side at the beginning of the operation, and additional two ion sources was installed in the B side at 2006. A grid system is conventional MAGG with 35% transparency. The beam extraction area is $21cm$ width and $50cm$ height with the circle apertures of $8mm$ diameter. Neutral beams from BL4 is injected to the LHD plasma perpendicularly as shown in Fig 1. The nominal beam energy and the beam power is $40keV$ and $6MW$, respectively. We have achieved $6.8MW$ beam injection with $0.2sec$ short pulse duration in 2007. In usual $5MW$ beam operation, beam duration can be extended by $0.9sec$. This PNBI is designed for ion heating to improve the ion temperature in LHD plasma. And also this NB is used for a charge exchange recombination spectroscopy (CXRS) [14] to measure radial profile of ion temperature. The specification of beam energy and focal length of PNB was optimized for both a CXRS measurement and an efficiency of the beam power gone into the protection armor plates.

3. Neutral Beam Emission Diagnosis for NBI Heating

Hydrogen NB particle emits visible Balmer- α spectrum ($H\alpha$) by an interaction of plasma particles [15]. We have investigated beam attenuation and energy fraction used a beam emission [16]. Figure 1 also shows the arrangement of two optical sight lines for beam emission diagnosis on BL3 and BL4. A quartz optical fiber coupled with small lens installed with the 5-o port and the 6-o port to observe the downstream position and the upstream position, respectively. The angles of the beam injection axis and the two sight lines are 62.4° and 134.7° . The end of the optical fibers are connected to the $25cm$ spectrometer (Bunkoh-Keiki M25-TP). A spectrum is detected by an intensified charge couple device detector (ICCD: ANDOR DH720) set on the focal plane of the spectrometer. The spectral resolution of spectrometer system is $0.21nm$ in totally. We have used the $40ms$ frame sampling time with the $20ms$ exposure time of the ICCD detector.

Figure 3 shows the observed spectrum in hydrogen discharge. Strong $H\alpha$ spectrum emitted from plasma discharge is located at $656.3nm$. Weak $H\alpha$ spectra emitted from high energy ($167keV$) NB of BL3 have been observed around $647nm$ and $662nm$ on the downstream position and the upstream position, respectively. These spectra are shifted by the Doppler effect by NB velocity and the observation angle. The beam emission spectrum splits two components due to the two ion sources with different beam injection angle. We have also observed strong $H\alpha$ spectra located between $659nm$ and $663nm$ on the downstream sight line. These spectra are emitted from low energy PNB of BL4. In a proton source, molecular hydrogen ions such as H_2^+ and H_3^+ are also extracted by the acceleration potential. The velocity of beam particle is expressed $\sqrt{2E/m}$, where E and m is beam energy and particle mass, respectively. So the energy of NB which is separated from H_2^+ or H_3^+ becomes $20keV$ or $13.3keV$, respectively in the $40keV$ beam acceleration.

Figure 4 shows the time evolution of this hydrogen discharge used four NBIs with the configuration of magnetic field strength $B = 2.769T$ and magnetic field axis of $R = 3.575m$. This plasma is built up by an electron cyclotron heating (ECH) at first, and it is sustained by $40keV$ low energy NB as shown in Fig. 4(a). The averaged electron density measured by a far infrared ray (FIR) laser interferometer increases to $\langle n_e \rangle = 2 \times 10^{19}m^{-3}$ as shown in Fig 4(b). The signal intensity of beam emission from BL4 is similar behavior of the product of $\langle n_e \rangle$ and NB power as shown in Fig. 4(e). Three energy components are almost same fraction during discharge. The full energy NB particles exist about half of the NB particles, and the number of third energy NB particle is larger than second energy beam particles. In this case, the power fraction of NB with the energy of $40keV$, $30keV$ and $13.3keV$ is

70%, 16% and 14%, respectively as shown in Fig 4(f). Power fraction is also constant during the discharge, and most of power is supplied by full energy particles in BL4.

Plasma stored energy (W_p), electron temperature (T_e) and T_i increase after the additional 13MW NB injection after $t = 0.9sec$ as shown in Fig. 4(b) and 4(c), here T_e and T_i is measured by a Thomson scattering system and Doppler broadening of ArXVII used a X-ray crystal spectrometer, respectively. Beam emission signal in the downstream position becomes minimum value at $t = 1.00s$, and it increases at time increases as shown in Fig 4(d). This behavior indicates that the number of penetration beam particles changes with time, because the beam emission intensity proportional to a beam density n_{beam} , n_e , and emission coefficient. The difference of density distribution between $t = 1.00sec$ and at $t = 1.27sec$ is appeared as shown in Fig. 5. In the case of hydrogen discharge, a beam stopping coefficient (S_{cr}) of central peak density ($n_e = 2.2 \times 10^{19} m^{-3}$) and central hollow density ($n_e = 1.4 \times 10^{19} m^{-3}$) obtained by ADAS (Atomic Data and Analysis Structure) database [17, 18] is $S_{cr} = 7.8 \times 10^{-8} cm^3 s^{-1}$ and $S_{cr} = 7.5 \times 10^{-8} cm^3 s^{-1}$, respectively. So the penetration beam particles passing through plasma with peak density is less than the case with hollow density due to the beam attenuation function as $n_{beam}(L) = n_{beam}(0) \exp(-\int_0^L n_e(l) S_{cr}(l) / v dl)$, where v is the velocity of beam particle, respectively. According to the beam stopping coefficient in both cases, the absorption beam power in the peak density is 11% larger than in the hollow density. The beam emission diagnosis is utilized to understand the beam attenuation directly.

In conclusion, 180keV tangential NNBIs and 40keV PNBI are operated successfully in the last 10 years at LHD. High power beams are achieved 16MW totally in the three NNBIs and 6.8MW in the PNBI, respectively, which have outstripped the nominal beam powers now. The beam emission diagnostic system have run in both PNBI ad NNBIs. These optical diagnosis is utilized for understand of beam quality and beam heating along the beam injection axis.

ACKNOWLEDGMENTS

The authors would like to acknowledge the LHD and NBI staff for their operational and diagnostic support. We would like to thank Dr. Yoshihide Oka for development of LHD-NBI. We also thank Dr. Allan Whiteford (University of Strathclyde) for useful discussions on the beam attenuation measurement and ADAS application. This work is also supported by the budget for NIFS08ULBB501. This work is also partially supported by the JSPS-CAS Core-University program in the field of Plasma and Nuclear Fusion.

References

- 1 Ikeda K, Osakabe M, Takeiri Y, *et al.* 2006, J. Korean Phys. Soc., **49**: 6S96
- 2 Takeiri Y, Morita S, Ikeda K, *et al.* 2007, Nucl. Fusion, **47**: 1078
- 3 Ohyabu N, Morisaki T, Masuzaki S, *et al.* 2006, Phys. Rev. Lett., **97**: 055002
- 4 Takeiri Y, Kaneko O, Tsumori K, *et al.* 2006, Nucl. Fusion, **46**: S199
- 5 Hemsworth R S, Feist J -H, Hanada M, *et al.* 2007, Rev. Sci. Instrum., **67**: 1120
- 6 Berkner K H, Pyle R V, Stearns J W. 1975, Nucl. Fusion, **15**: 249
- 7 Nagaoka K, Yokoyama M, Takeiri Y, *et al.* 2008, Plasma and Fusion Research **3**: S1013
- 8 Ikeda K, Takeiri Y, Kaneko O, *et al.* 2004, Rev. Sci. Instrum., **75**: 1744
- 9 Y. Takeiri Y, O. Kaneko O, K. Tsumori K, *et al.* 2006, Nucl. Fusion, **46**: S199
- 10 Tsumori K, Nagaoka K, Osakabe M, *et al.* 2004, Rev. Sci. Instrum., **75**: 1847
- 11 Tsumori K, Osakabe M, Kaneko O, *et al.* 2008, Rev. Sci. Instrum., **79**: 02C107
- 12 Nagaoka K, Ikeda K, Osakabe M, *et al.* 2007, Plasma and Fusion Research, **2**: S1051
- 13 Osakabe M, Nagaoka K, Tsumori K, *et al.* 2007, Development of radial neutral beam injection system on LHD, 17th International Toki Conference, Toki, P2-079
- 14 Yoshinuma M, Ida K, Yokoyama M, *et al.* 2008, Plasma and Fusion Research, **3**: S1014
- 15 Mandl W, Wolf R C, *et al.* 1993, Plasma Phys. Control. Fusion, **35**: 1373
- 16 Ikeda K, Osakabe M, Whiteford A, *et al.* 2007, Transactions of Fusion Sci. and Tech., **51**: 2T283
- 17 Summers H P. 2004, The ADAS User Manual, version 2.6, <http://www.adas.ac.uk/>
- 18 Summers H P, Anderson H, Kato T, *et al.* 1999, Research Report NIFS-DATA Series, Nagoya, National Institute for Fusion Science, No. 55

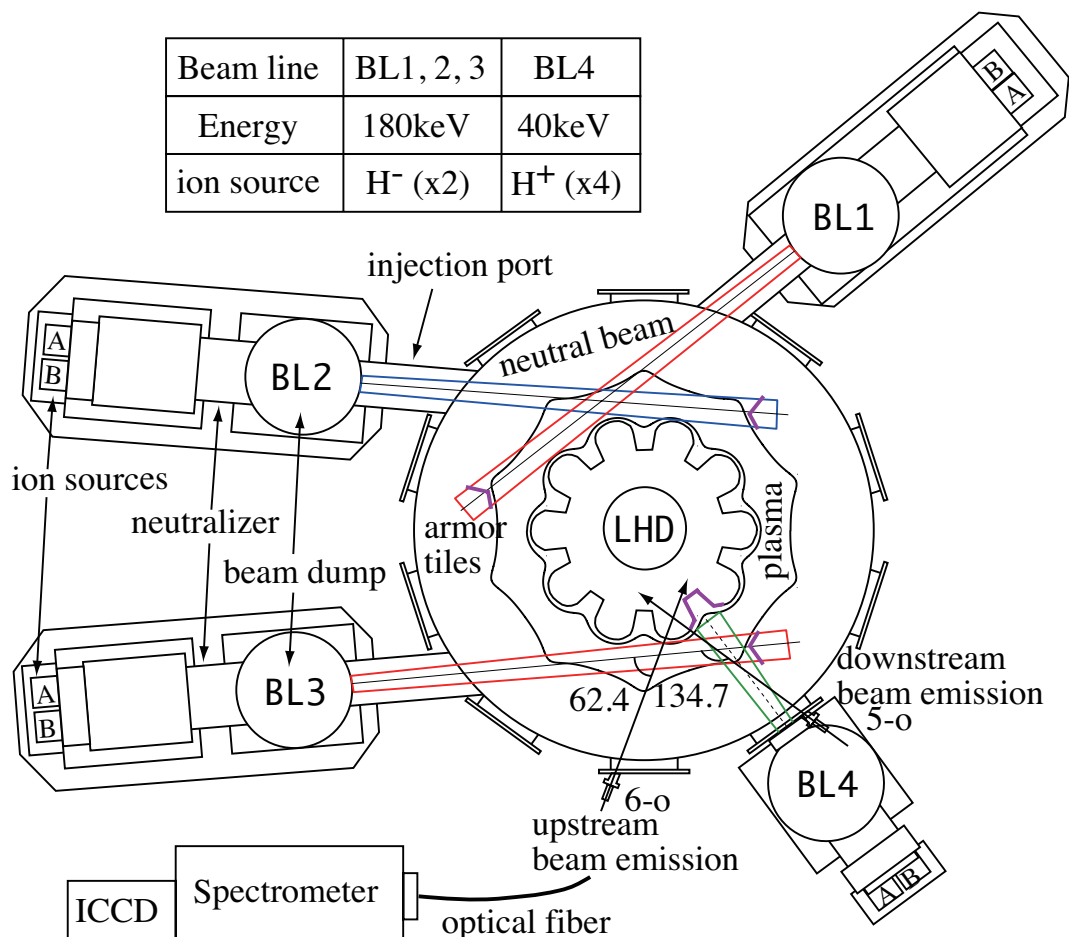


Fig. 1 Schematic drawing of LHD and arrangement of four NBIs. Two optical sight lines to observe beam emission H α spectrum are set on the side ports.

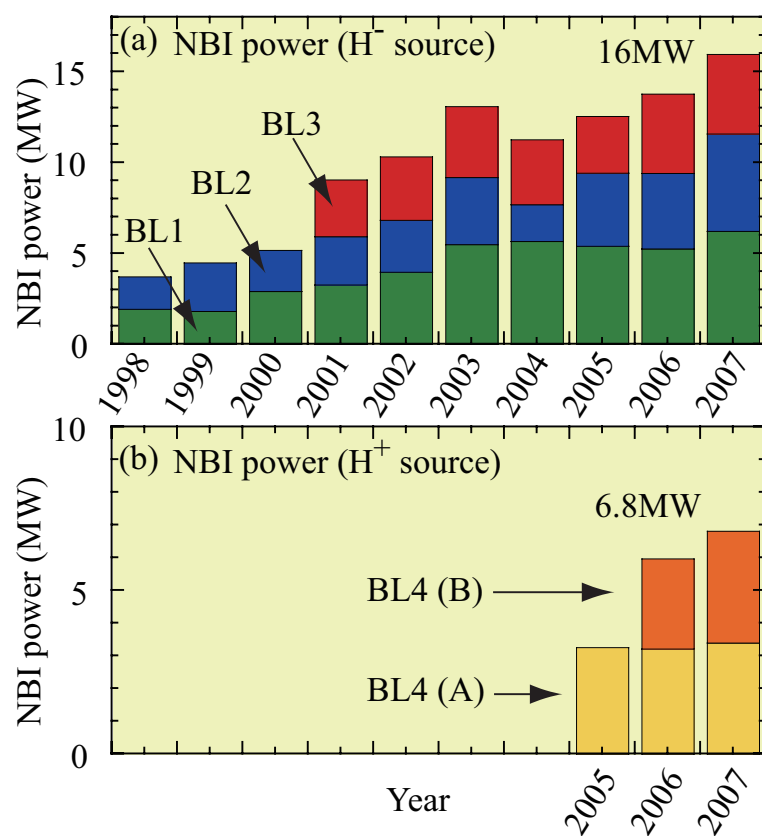


Fig. 2 History of NB injection powers used H^- source (a) and H^+ source (b).

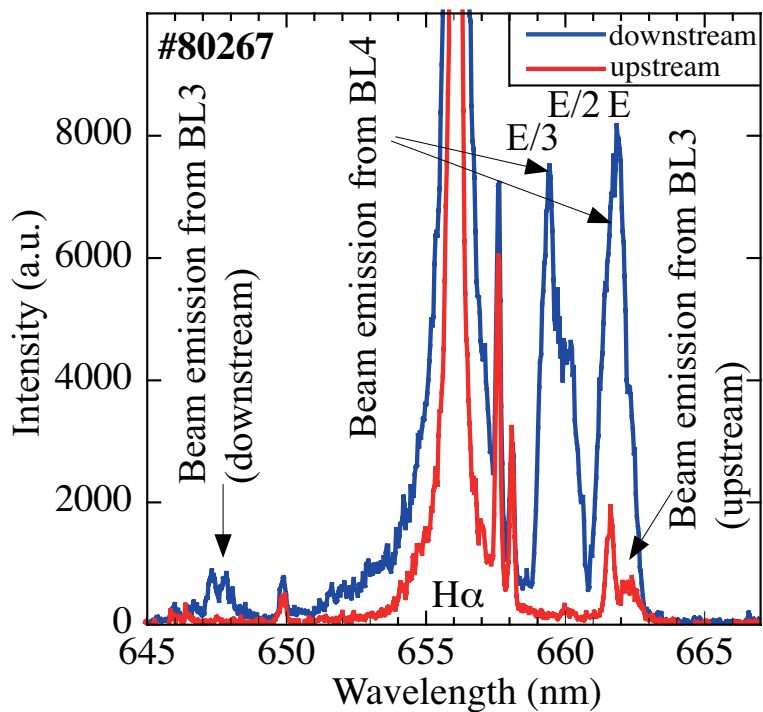


Fig. 3 H α spectra from plasma discharge without Doppler shift are observed at the center, and beam emission H α spectra with Doppler shift located at the both side.

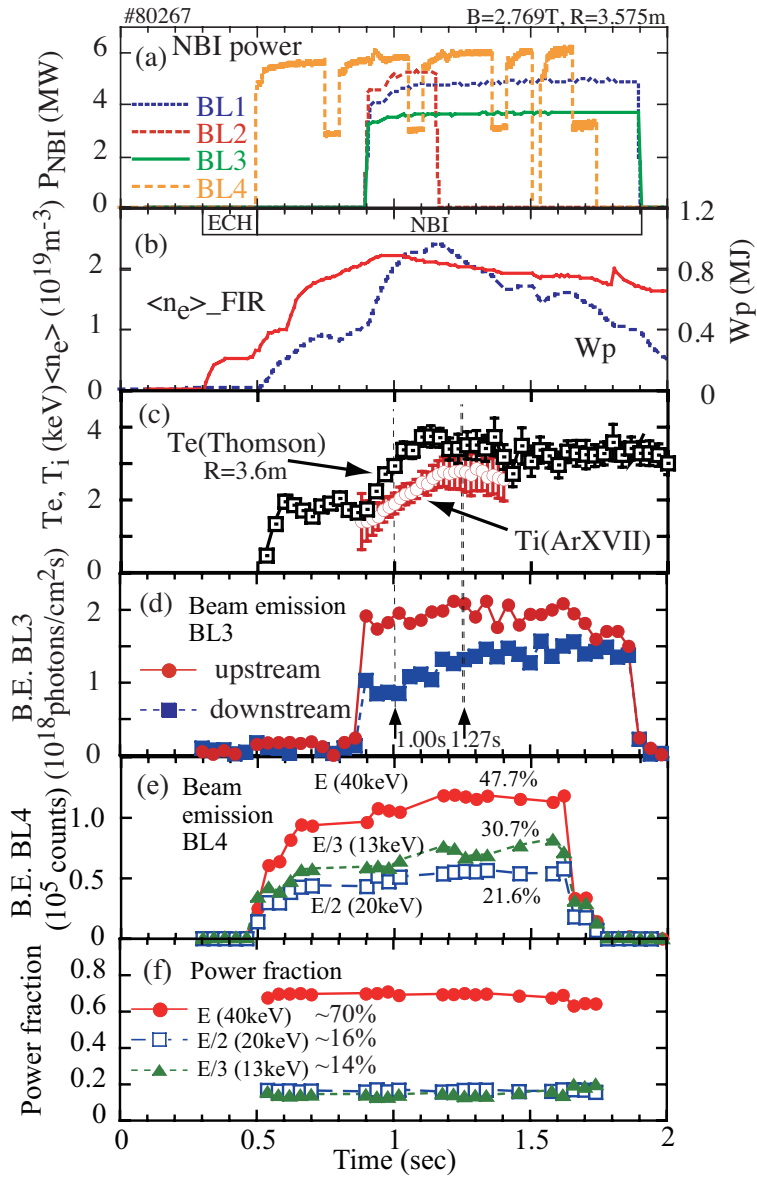


Fig. 4 Hydrogen plasma discharge used four neutral beams (a), $\langle n_e \rangle$ and W_p (b), T_i and T_e (c), beam emission flux from BL3 (d), intensity of beam emission from BL4 (e) and power fraction of PNBI (f).

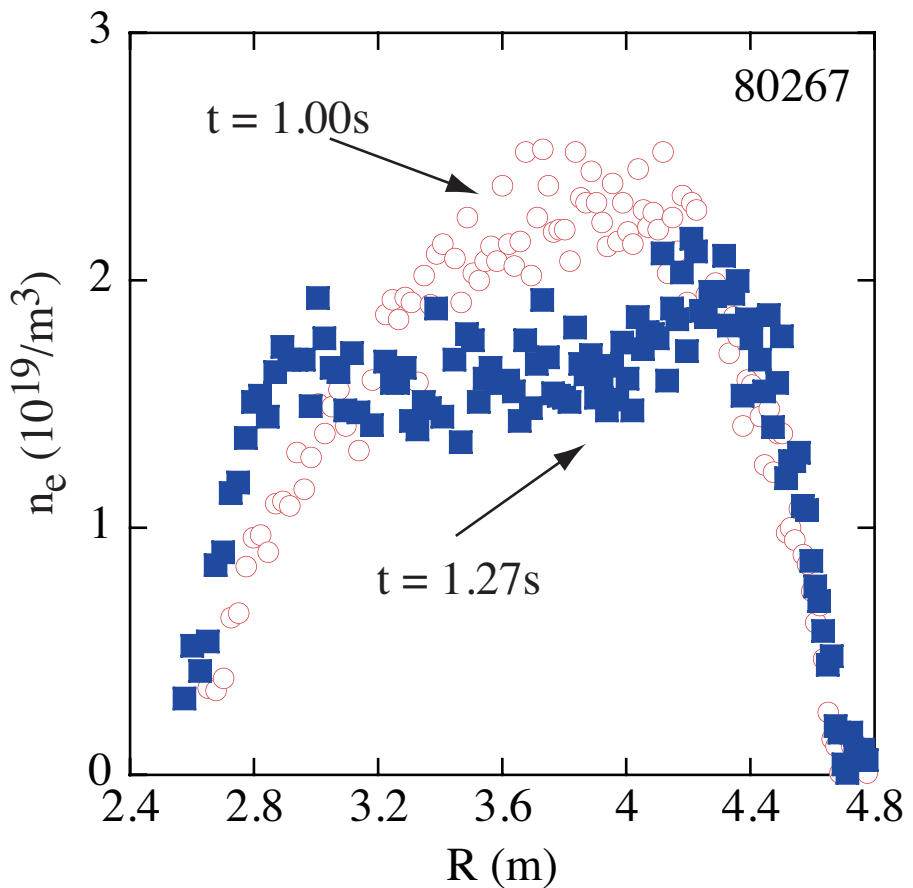


Fig. 5 Radial profile of n_e obtained by Thomson scattering calibrated by FIR interferometer at $t = 1.00s$ (circle) and $t = 1.27s$ (square) on the discharge shown in Fig 4 .

Density limits with different fuelling methods in the HL-2A tokamak

YAN Longwen (严龙文), ZHOU Yan (周艳), Chen Chengyuan (陈程远), CAO Zhen (曹曾), SONG Xianming (宋显明), LI Wei (李伟), DONG Yunbo (董云波), HONG Wenyu (洪文玉), YANG Qingwei (杨青巍), DUAN Xuru (段旭如)

Southwestern Institute of Physics, Chengdu 610041, China

Abstract Density limits with different fuelling methods have been compared in HL-2A, i.e. direct gas puffing and supersonic molecular beam injection (SMBI) from low field side, divertor gas fuelling. The maximum densities for low current discharges are $3.4 \times 10^{19} \text{ m}^{-3}$, $4.3 \times 10^{19} \text{ m}^{-3}$ and $4.7 \times 10^{19} \text{ m}^{-3}$ for the 3 kinds of fuelling methods. The density ratios to Greenwald density limit are 0.9, 1.1, 1.2, respectively. The behavior of density limit disruption is analyzed as well.

Key words: Density limit; Fuelling method; Supersonic molecular beam injection; Disruption

PACS: 52.55.Dy, 52.50.Nr, 52.55.Rk

1 Introduction

It is well known that stable plasma operation in a tokamak is limited by three basic limits, i.e. maximum plasma current, electron density and maximum normalized plasma pressure ^[1].

Generally, the density limit should not appreciably exceed the empirical Greenwald density limit, $n_G (10^{20} \text{ m}^{-3}) = I_p (\text{MA}) / \pi a^2 (\text{m}^2)$ ^[2], which is caused by too high radiating power fraction and the underlying deterioration of particle confinement ^[3,4]. Furthermore, high density operation is

effective to achieve detachment ^[5], which reduces the divertor heat load since the edge plasma temperature naturally decreases as the edge density increases. The density limit due to high radiating power is more easily identified in the stellarator due to no MHD instability driven by plasma current ^[6], which is proportional to the absorbed power density. The deterioration of particle confinement is imposed another density limit ^[7], which may have a more indirect MHD origination that in turn leads to an MHD initiated disruption ^[8].

The density limit experiments have been performed in the HL-2A tokamak with different refueling methods for low current discharges, including direct gas puffing (GP) and supersonic molecular beam injection (SMBI) from outer midplane, bulk and noble gas injection in divertor chamber. Maximum density is obtained with the SMBI fuelling.

The remained parts in this paper are arranged as follows. The experimental setup is described in Sec.2. The main results of density limit experiments are presented in Sec.3. The final part is for conclusions.

2. The experimental setup

HL-2A is a medium size tokamak with two rather closed divertor chambers ^[9,10]. Its device parameters are the major radius $R = 1.65$ m, the minor radius $a = 0.4$ m, the toroidal magnetic field $B_t = 2.8$ T and the flux swing of 5.0 V.s. Its present operation parameters are the plasma current $I_p = 100\text{-}450$ kA, current duration $t = 4$ s, the line- averaged electron density $n_e = (0.2\text{-}6) \times 10^{19}$ m⁻³, the electron temperature $T_e = 5$ keV, the ion temperature $T_i = 1.2$ keV, the maximum energy confinement 120 ms and so on. So far, there is the ability of 5 MW auxiliary heating ($P_{ECRH} = 2$ MW, $P_{NBI} = 2$ MW, $P_{LHCD} = 1$ MW). The electron density profile is obtained by 8-channel HCN interferometer. Electron temperature profile can be measured by Thomson

scattering, fast electron cyclotron emission (ECE) and energy spectrum of X-rays, while ion temperature is given by the energy spectrum of neutral particles. Plasma radiation can be observed from 4 bolometer arrays, 5 soft X-ray arrays, hard X-rays, vacuum ultraviolet (VUV) spectrometer, visible spectrometer and so on. The electron temperature and density profiles at divertor target plates are given by 7 fixed Langmuir probe arrays ^[11], while outer target temperature is monitored by an FIR camera. The edge electron temperature and density profiles are measured by a reciprocating probe system ^[12]. The arrangement of relevant diagnostics and fuelled systems is shown in Fig.1. The direct GP and SMBI fuelling is from at outer midplane, while the divertor is fuelled with deuterium and noble gases.

3. Main results of density limit experiments

The density limits of 3 kinds of fuelling methods are compared with low current discharges, typically $I_p = 185$ kA, magnetic field $B_t = 1.4$ T and safety factor $q_a = 3.3$. At first, we analyze the density limit of direct GP from outer midplane. Figure 2 shows main parameter evolutions of a density limit discharge with the GP. The maximum density is only $3.4 \times 10^{19} \text{ m}^{-3}$. Bolometer and H_α emissions continuously increase with density rising. The ratio of attainable density with Greenwald density limit (Q_{ne}) is 0.9. The radiating power fraction to Ohmic input power (Q_{rad}) slightly rises before density limit disruption. The disruption process of the density limit discharge with gas puffing is described in Fig.3. The Q_{rad} gradually rises to above 1 before density limit disruption, which means that high radiation fraction is the main cause to form the density limit. The density gradually drops in minor disruptions. The soft X-rays (SXR) abruptly decrease during major disruption, while plasma current rises a little due to its redistribution.

The parameter evolutions of a density limit discharge with divertor fuelling are manifested in

Fig.4. The maximum density is $4.3 \times 10^{19} \text{ m}^{-3}$. The bolometer and H_α emissions continuously increase with density as well. The maximum density ratio rises to $Q_{ne}=1.1$. The radiating power fraction is $Q_{rad}<0.3$ before major disruption, implying that the density limit may be caused by the MHD instability excited by highly radiating power fraction. The detached plasma appears with rather low electron temperature at outer target with $T_{edd6}<3 \text{ eV}$. Figure 5 illustrates the disruption process of the density limit discharge with divertor fuelling. The radiating power fraction in main plasma is $Q_{rad}<0.2$ before a major disruption. There are 4 minor disruptions on soft X-rays and Mirnov signals, which mean that plasma confinement continuously degenerates due to MHD instability before the major disruption. Density gradually decreases with minor disruptions before density limit disruption. Plasma current abruptly rises during the major disruption.

Figure 6 presents main parameter evolutions of a density limit discharge with the SMBI fuelling from out midplane. The maximum density reaches $4.7 \times 10^{19} \text{ m}^{-3}$. The bolometer and H_α emissions gradually increase with density. The maximum density ratio is $Q_{ne}=1.2$ in current flattop, which is higher in current ramping down. The radiating power fraction in main plasma is $Q_{rad}<0.3$ before a major disruption. The detached plasma is observed with very low electron temperature of target plate ($T_{edd6}<2 \text{ eV}$). The $Q_{rad}<0.4$ is observed before the major disruption even if so high plasma density. There are 3 minor disruptions appearing on SXR and Mirnov signals. Plasma density drops step by step due to minor disruptions. Plasma current suddenly rises during the major disruption.

Figure 7 is soft X-ray profile evolutions during density limit disruption. The inversion radius of sawtooth oscillations is about $r = 12 \text{ cm}$, which is localized at the normalized radius about $r/a = 0.30$. Three minor disruptions appear before the major disruption, whose inversion radius is larger than 23.8 cm , implying that minor disruptions should be taken place near the $q=2$ rational

surface. The SXR intensity at central chord may be recovered after a minor disruption. The SXR intensities at outer chords cannot be revived after a minor disruption. All SXR intensities abruptly drop after the major disruption, indicating that global particle confinement is almost lost.

In contrast, a completely detached discharge produced by 5 helium pulses in divertor is shown in Fig.8. The electron temperatures at the targets are below 2.0 eV. The maximum density exceeds $5.6 \times 10^{19} \text{ m}^{-3}$ at $t=850 \text{ ms}$ before current ramping down. Electron temperatures and pressures at target plates, radiation power in divertor and the compression ratio of neutral gas pressures between divertor and main chamber obviously drop during the detachment. There is no disruption appearance though the radiation power fraction in main plasma is higher than 50% of input power, which indicates that the profile of radiating power is rather significant to trigger MHD instability and then density limit disruption.

4. Conclusions

Density limits with different fuelling methods have been obtained in HL-2A, including direct gas puffing and SMBI fuelling from outer midplane, bulk and noble gas injection in divertor. Highest density is achieved with the SMBI fuelling. Highly radiating power fraction and MHD instability are two main causes to produce density limit. Minor disruptions are often observed before the density limit disruption. They may originate from the $q = 2$ rational surface of safety factor. The profile of radiating power has significant impact on exciting the MHD instability and then leading to density limit disruption.

Acknowledgement

This work is partly supported by the JSPS-CAS Core-University Program in the field of

Plasma and Nuclear Fusion, a Grant-in-Aid for scientific research from Ministry of Education, Science and Culture of Japan (No. 19055005), and by the National Science Foundation of China under the grant of Nos. 10675041, 10775044.

References

- [1] Hender T C, Wesley J C, Bialek J, et al. 2007, Nucl. Fusion, 47: S128
- [2] Greenwald M et al. 1988, Nucl. Fusion, 28: 2199
- [3] Loarte A, Lipschultz B, Kukushkin A S, et al. 2007, Nucl. Fusion, 47: S203
- [4] ITER Physics Basis 1999, Nucl. Fusion, 39: 2137
- [5] Pitcher C S and Stangeby P C. 1997, Plasma Phys. Control. Fusion, 39: 779
- [6] Miyazawa J, Sakamoto R, Masuzaki S, et al. 2008, Nucl. Fusion, 48: 015003
- [7] Greenwald M. 2002, Plasma Phys. Control. Fusion, 44: R27
- [8] Yan L W, Yao L H, Zhou Y, et al. 2000, Plasma Science and Technology, 2 : 431
- [9] Yang Q W, Liu Y, Ding X T, et al. 2007, Nucl. Fusion, 47 : S635
- [10] Yan L W, Cheng J, Zhao K J, et al. 2007, Nucl. Fusion 47: 1673:
- [11] Hong W Y, Yan L W, Zhao K J, et al. 2006, Chinese Physics, 15 : 556
- [12] Yan L W, Hong W Y. Zhao K J, et al. 2006, Rev. Sci. Instrum. 77: 113501

Figure Captions

Fig.1 The arrangement of divertor diagnostics and fuelling systems

The direct GP and SMBI fuelling is from outer midplane, while the divertor is fuelled with deuterium and noble gases. Seven sets of triple flush probes give electron temperature and density profiles at inner and outer divertor targets with spatial resolution of 1 cm. Two fast ionization gauges measure neutral particle pressures in main chamber and divertor. Movable probes provide electron temperature and density profiles in divertor through shot by shot. An IR camera observes the surface temperature at outer target.

Fig.2 Parameter evolutions of a density limit discharge with direct gas puffing

The curves are the gas pulses at outer midplane (a), bolometer and H_α emissions (blue) passing through X-point (b), near central chord soft X-rays (c), central line-averaged density (d), the ratio of line-averaged density with Greenwald density limit (Q_{ne}) and radiating power fraction (Q_{rad}) to Ohmic power (e), and plasma current (f).

Fig.3 Density limit disruption with gas puffing

The curves are the Mirnov fluctuations at outer midplane (a) and inner one (b), near central chord soft X-rays (c), line-averaged electron density (d), radiation power fraction (e), and plasma current $I_p=185$ kA (f).

Fig.4 Parameter evolutions of a density limit discharge with divertor fuelling

The curves are, the electron temperature at outer target (a), H_α emission passing through X-point (b), central chord soft X-rays and bolometer via X-point (c), central line-averaged density and gas pulses in divertor (d), the ratio of line-averaged density with Greenwald density limit (Q_{ne}) and radiating power fraction (Q_{rad}) to Ohmic power (e), and plasma current (f).

Fig.5 Density limit disruption with divertor fuelling

The parameters are the same as in Fig.3.

Fig.6 Parameter evolutions of a density limit discharge with SMBI fuelling

The curves are the same as in Fig.4 except SMBI pulses in Fig.6 (d).

Fig.7 The SXR profile evolutions during density limit disruption

The curves of (a)-(f) are the soft X-ray intensities through the chord radii of $r = 23.8, 20.2, 16.3, 12.0, 7.3, -2.5$ cm.

Fig.8 The completely detached plasma discharge with helium puffing in divertor

The curves are, (a) the ratio ($R_{p0} = P_{0d}/P_{0m}$) of neutral particle pressures between divertor and main chamber, radiation power in divertor (P_{div}), (b) electron pressures at inner and outer targets, (c) electron temperatures at inner and outer targets, (d) radiation power in main plasma (P_{rad}) and plasma current (I_p), (e) line-averaged electron density (n_e) and deuterium GP pulses in divertor.

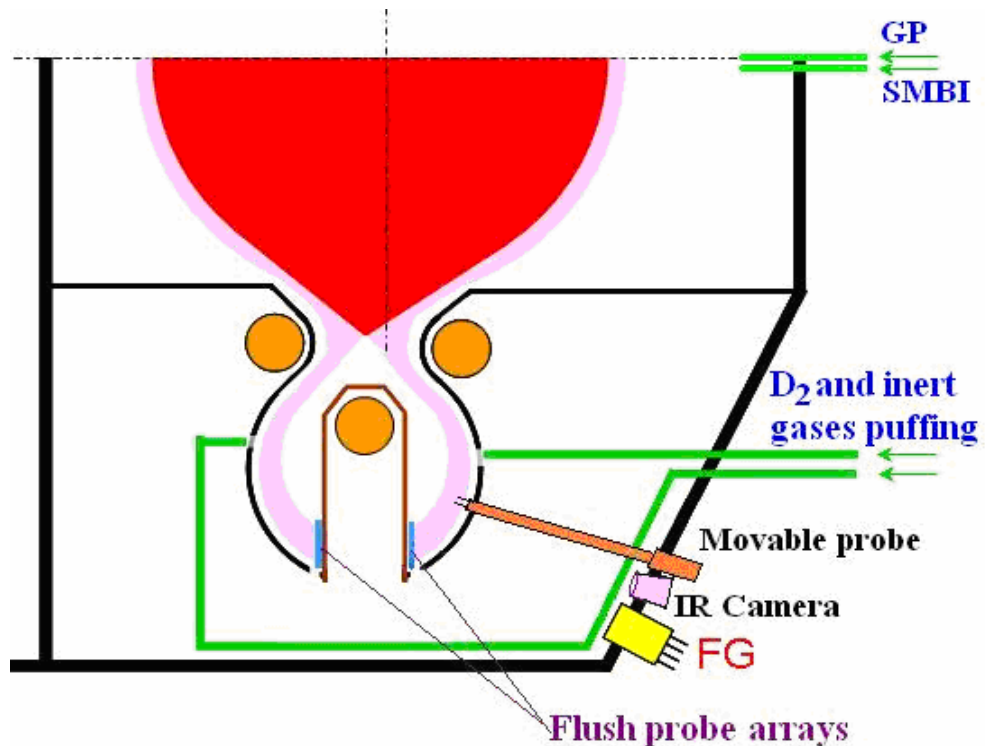


Fig.1 The arrangement of divertor diagnostics and fuelling systems

The direct GP and SMBI fuelling is from outer midplane, while the divertor is fuelled with deuterium and noble gases. Seven sets of triple flush probes give electron temperature and density profiles at inner and outer divertor targets with spatial resolution of 1 cm. Two fast ionization gauges measure neutral particle pressures in main chamber and divertor. Movable probes provide electron temperature and density profiles in divertor through shot by shot. An IR camera observes the surface temperature at outer target.

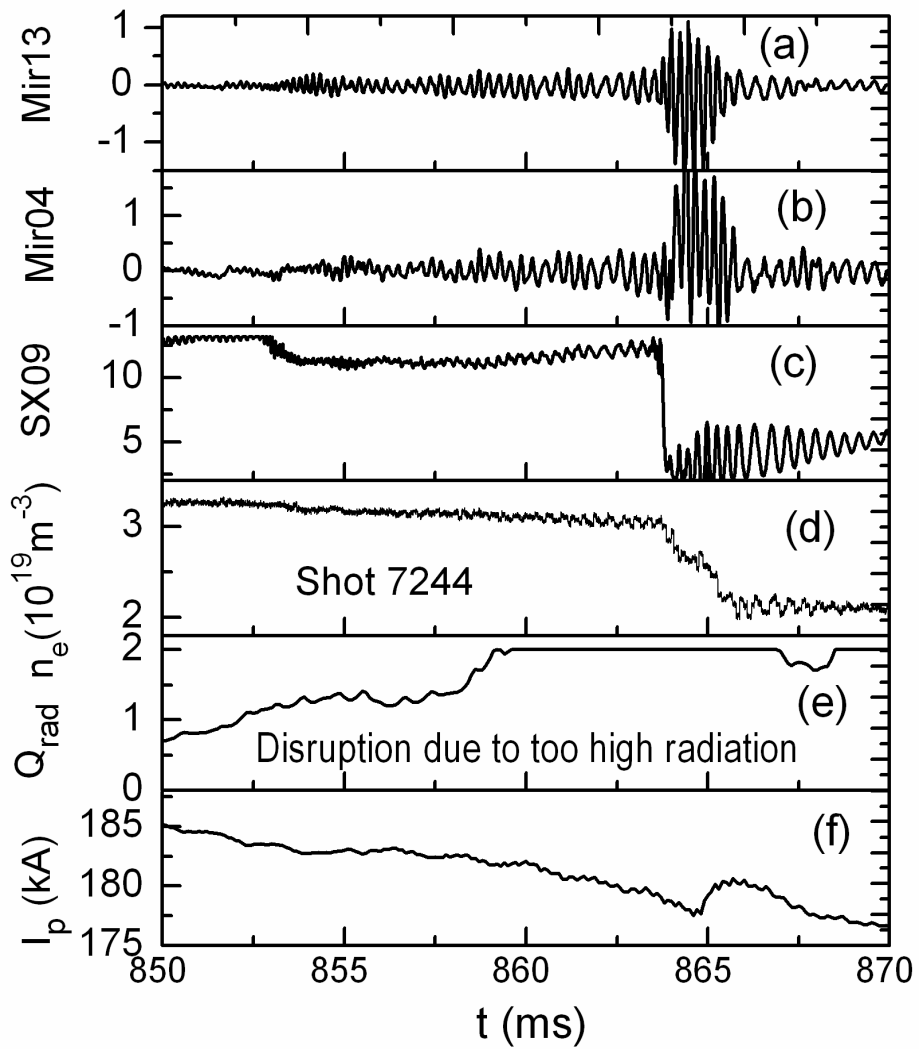


Fig.2 Parameter evolutions of a density limit discharge with direct gas puffing

The curves are the gas pulses at outer midplane (a), bolometer and H_α emissions (blue) passing through X-point (b), near central chord soft X-rays (c), central line-averaged density (d), the ratio of line-averaged density with Greenwald density limit (Q_{ne}) and radiating power fraction (Q_{rad}) to Ohmic power (e), and plasma current (f).

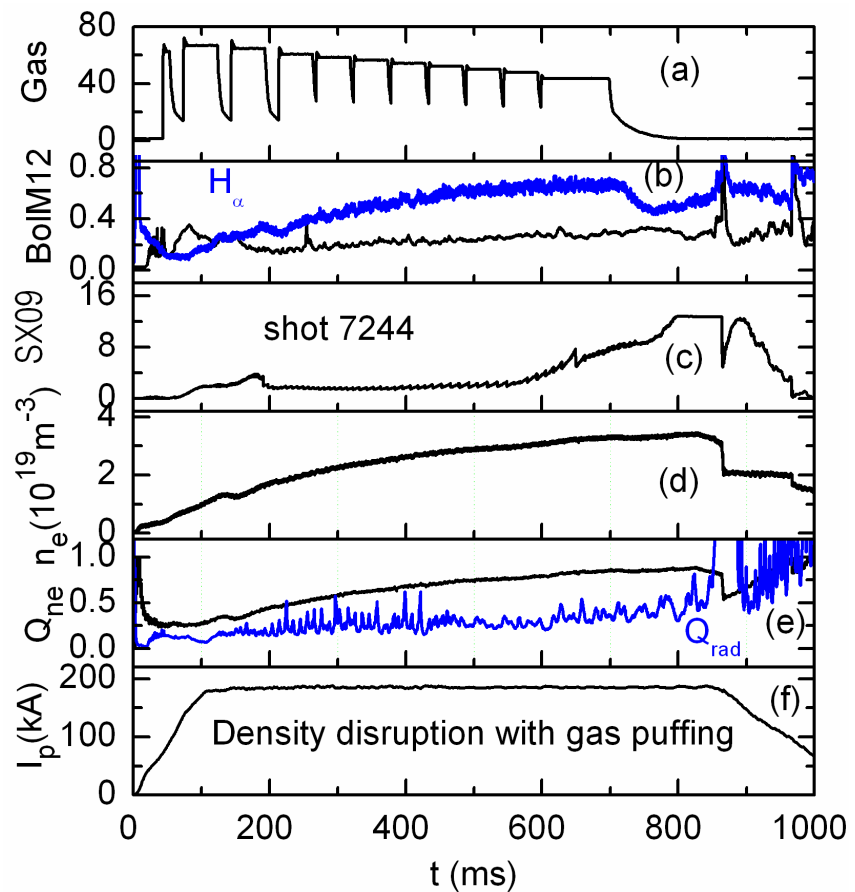


Fig.3 Density limit disruption with gas puffing

The curves are the Mirnov fluctuations at outer midplane (a) and inner one (b), near central chord soft X-rays (c), line-averaged electron density (d), radiation power fraction (e), and plasma current $I_p=185$ kA (f).

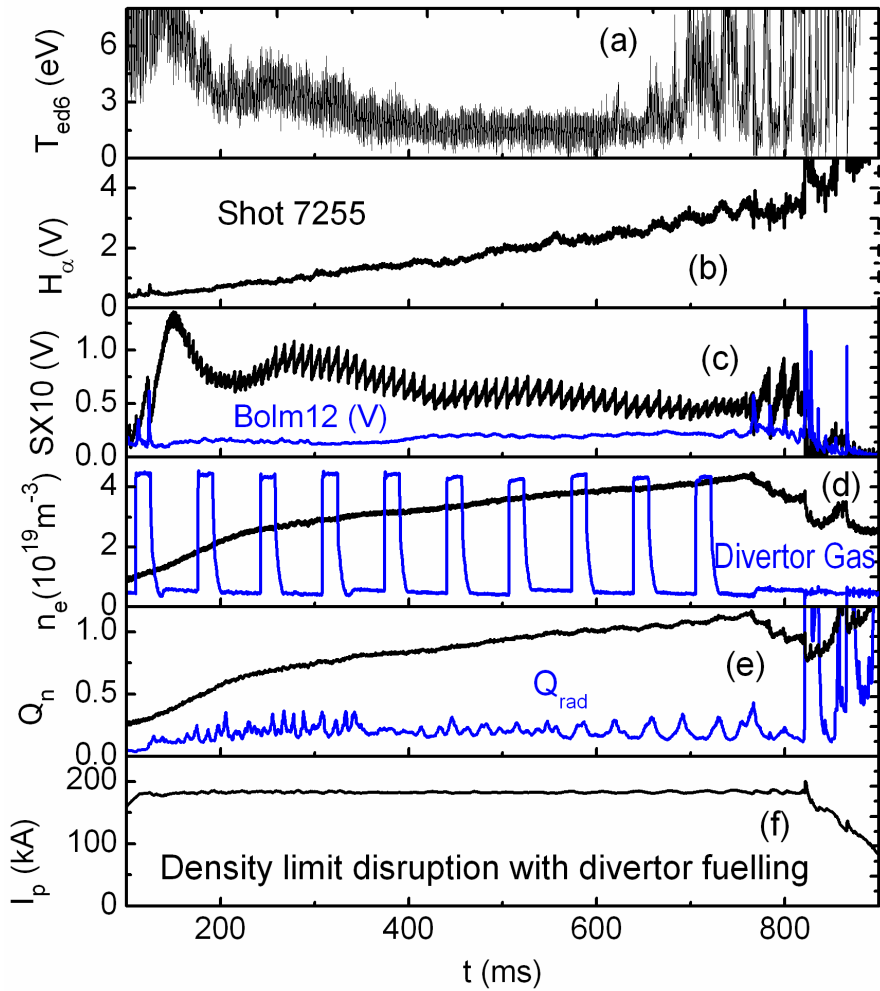


Fig.4 Parameter evolutions of a density limit discharge with divertor fuelling

The curves are, the electron temperature at outer target (a), H_α emission passing through X-point (b), central chord soft X-rays and bolometer via X-point (c), central line-averaged density and gas pulses in divertor (d), the ratio of line-averaged density with Greenwald density limit (Q_{ne}) and radiating power fraction (Q_{rad}) to Ohmic power (e), and plasma current (f).

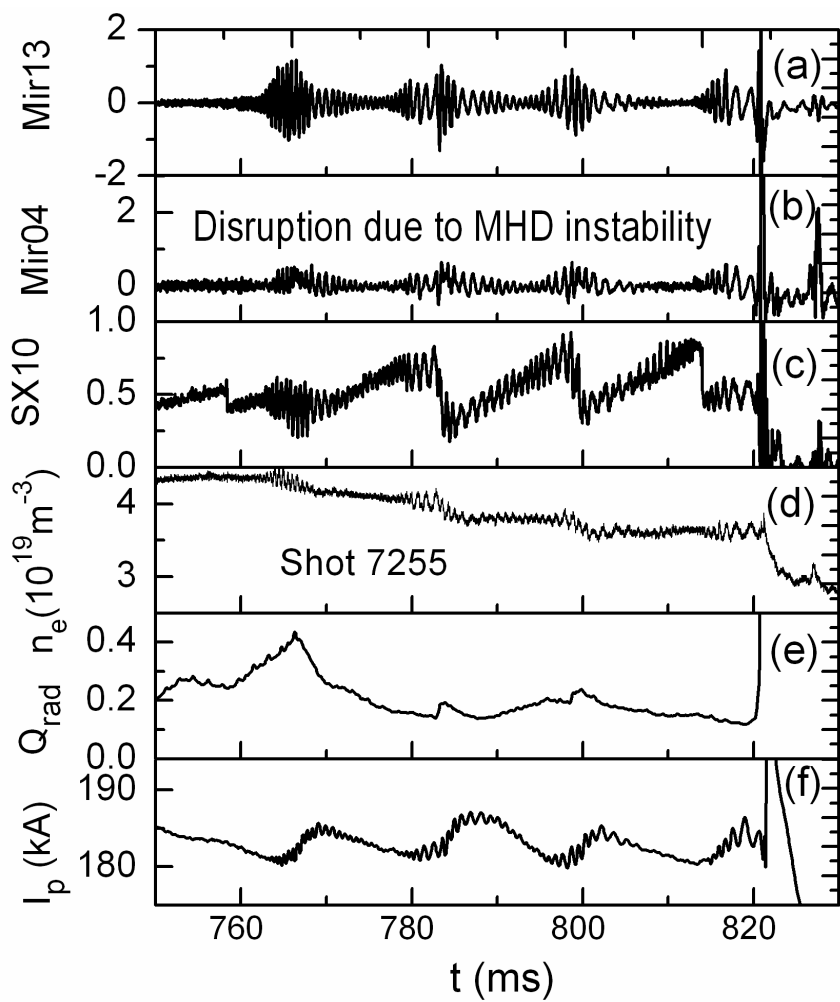


Fig.5 Density limit disruption with divertor fuelling

The parameters are the same as in Fig.3.

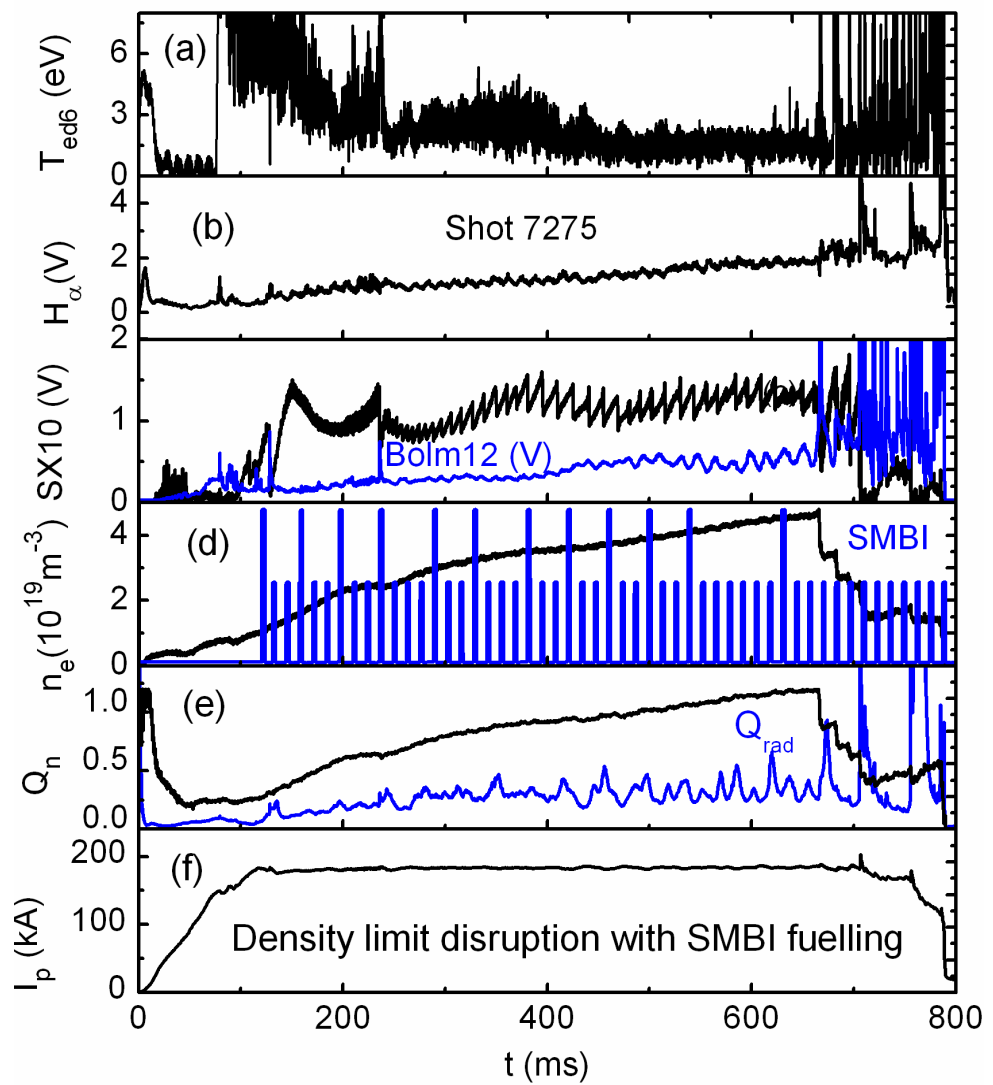


Fig.6 Parameter evolutions of a density limit discharge with SMBI fuelling

The curves are the same as in Fig.4 except SMBI pulses in Fig.6 (d).

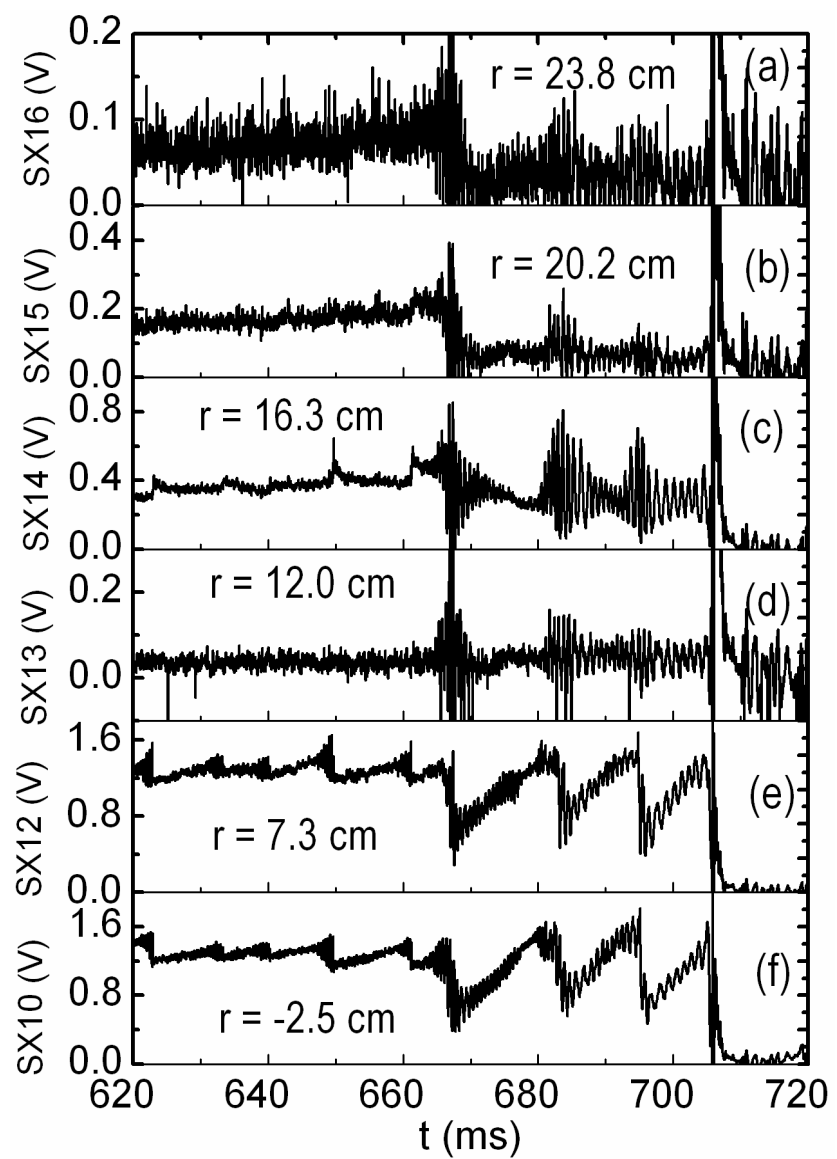


Fig.7 The SXR profile evolutions during density limit disruption

The curves of (a)-(f) are the soft X-ray intensities through the chord radii of $r = 23.8, 20.2, 16.3, 12.0, 7.3, -2.5$ cm.

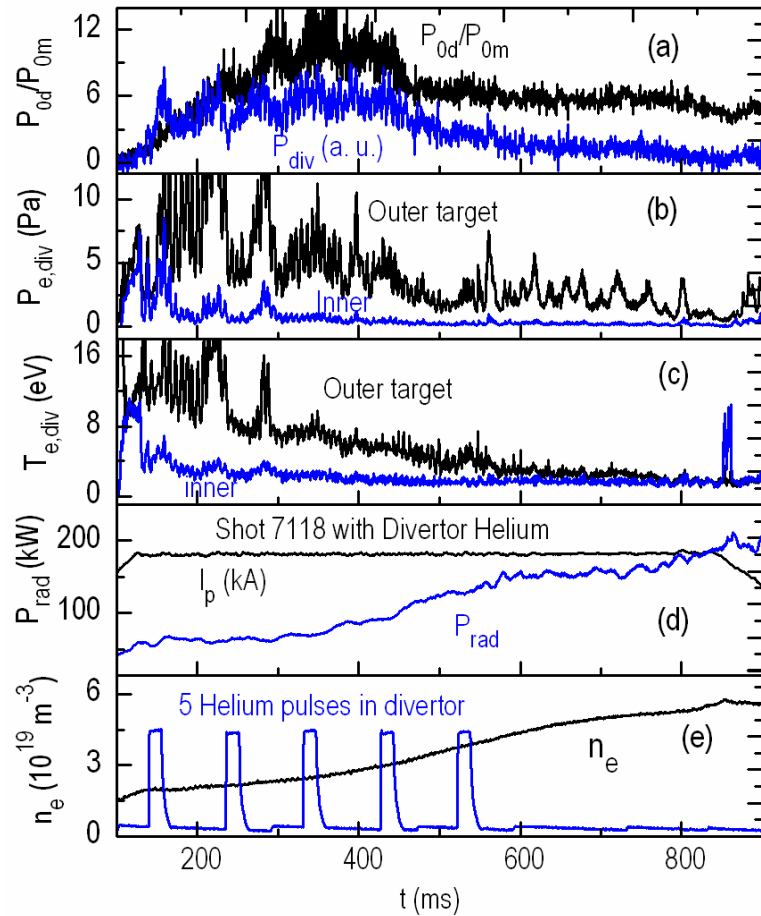


Fig.8 The completely detached plasma discharge with helium puffing in divertor

The curves are, (a) the ratio ($R_{p0}=P_{0d}/P_{0m}$) of neutral particle pressures between divertor and main chamber, radiation power in divertor (P_{div}), (b) electron pressures at inner and outer targets, (c) electron temperatures at inner and outer targets, (d) radiation power in main plasma (P_{rad}) and plasma current (I_p), (e) line-averaged electron density (n_e) and deuterium GP pulses in divertor.

Modelling of EAST with LHRF and NBI*

ZHOU Deng (周登)^{1,2}, Holger St. JOHN³

¹Institute of Plasma Physics, Chinese Academy of Sciences, Hefei, 230031, China

²Centre for Magnetic Fusion Theory, Chinese Academy of Sciences, China

³General Atomics, PO Box 85608, San Diego, California 92186-5608, USA

Abstract The lower hybrid simulation code (LSC) is integrated into transport code ONETWO to model discharges for EAST device with heating and current drive using lower hybrid wave and neutral beam injection. The profiles of current driven by lower hybrid wave and neutral beam injection are presented for a sample self-consistent pressure profile with the same shape of density and temperatures. For the H-mode discharge, a simple model is used to predict the pedestal characteristics. The temperature profiles are evolved using GLF23 transport model. A case of steady state with non-inductively driven current accounting for up to 80% is presented.

Keywords: ONETWO, LSC, EAST modeling

PACS: 52.50.Sw, 52.55.Fa, 52.55.Dy

Email : dzzhou@ipp.ac.cn

Tel: 0551-5593266

Fax:0551-5591310

*Supported by National Science Foundation of China under Grant No. 10775137.

1 Introduction

Experimental Advanced Superconducting Tokamak (EAST) is a full super-conducting tokamak, the first discharge was carried out in 2006^[1]. One of missions of EAST is to demonstrate long duration discharge (1000s) sustained completely by non-inductively driven current. The method for auxiliary heating and current driving on EAST includes lower hybrid radio frequency wave (LHRF) and ion cyclotron radio frequency wave (ICRF). The neutral beam injection (NBI) is under construction. In Fig. 1, the schematic diagram of the poloidal cross section of EAST is presented. The major parameters for EAST are given in table 1.

Although the experiment on EAST is under steady progress we still have an urgent need for the predictive modeling, simulation and data analysis for experiments. Recently, the initial stage Ohmic discharges were simulated using a 1.5D equilibrium evolution code^[2]. In the present work, we present a modeling for a H-mode steady state discharge with LHRF and NBI using ONETWO transport code.

ONETWO is a computer code developed at General Atomics for modeling most phenomena occurring in tokamak plasma on the transport time scale. It can be used for determination of transport coefficients from experimental data as well as for predictive modeling of tokamak discharges using a variety of transport models. It includes all kinds of sources and sinks for energy, particles and rotation. Independent codes for source calculation can be conveniently integrated into ONETWO. The code was recently used for ITER and DIII-D steady state simulations^[3,4].

LHRF is one of the primary heating and current driving method used on HT-7 and EAST. A reliable code for modeling LHCD is required. Recently, the Lower Hybrid Simulation code (LSC)

was successfully integrated into ONETWO. LSC was first developed for Tokamak Simulation in Princeton Plasma Physics Laboratory^[5]. It includes a ray-tracing method for power deposition and a 1-D Fokker-Planck equation solver. Heuristic power and current diffusion is optionally included^[6]. The code has been in use for HT-7 since 1996. In a recent publication, the code was used to calculate the energy of hard-X radiation in LHRF on HT-7^[7]. To test the integrated performance of LSC and ONETWO, we present a sample case of current drive using LHRF and NBI for a self-consistent pressure profile in section 2. Effective driving can be achieved by adjusting controlling parameters for this fixed profile.

In section 3, the modeling for a steady state H-mode discharged is presented. The temperature core plasma is evolved using the GLF23 transport model. Up to 80% of the total current is accounted for by non-inductive current. A summary and future plan are presented in section 4.

2 Driven current for a self-consistent profile

In this section, to test the performance of LSC in ONETWO, the current profile driven by LHRF and NBI is calculated for a self-consistent pressure profile. The profile consistency or stiffness is referred to a pressure profile given by $P(r) = p_0 / [1 + (r/a)^2]^2$, where r is the usual minor radius for a circular cross section and is proportional to the square root of toroidal flux for a shaped cross section, a is the value of r on boundary^[8-10]. The temperature and the electron density are assumed to have the same shape, with central value $T_e(0) = T_i(0) = 5 \text{ KeV}$, $n_e(0) = 5 \times 10^{19} \text{ m}^{-3}$. $Z_{\text{eff}} = 2$ is assumed to be uniform with a Carbon impurity. The calculated equilibrium configuration with a toroidal current $I = 1 \text{ MA}$ and $B_0 = 3.5 \text{ T}$ is presented in Fig. 2. Presented in Fig. 3 is the density or temperature profile, where

the horizon axis denotes $\rho = \sqrt{\phi_{\text{tor}} / \pi B_0}$.

The LHRF driven current is calculated by LSC. The Gaussian spectrum is assumed with changeable parallel refractive index n_{\parallel} and fixed width $\delta n_{\parallel} = 0.2$, the launched power is $P_{\text{LH}} = 1.5 \text{ MW}$. The profiles of driven current for a few different n_{\parallel} values are shown in Fig. 4. The total driven current changes drastically with n_{\parallel} , but the peak location changes little.

The NBI driven current is calculated using the analytical models embedded in ONETWO. The launched power is $P_{\text{NBI}} = 1.5 \text{ MW}$, the maximum energy of the beam particle is $E_{\text{max}} = 80 \text{ KeV}$, accounting for 75% of total beam particles. The beam is injected tangentially. In Fig. 5, the profiles of driven current are presented for three different beam directions.

We can see that current can be effectively driven and the profile can be adjusted by changing controlling parameters using LHRF and NBI for this sample fixed pressure profile.

3 Modeling of a steady state H-mode discharge

One of goals for EAST is demonstrate long pulse, steady state H-mode discharges. Predictive modeling works has been performed for ITER and large devices world-wide in the past, using different transport codes^[3,4,11-14]. We present a sample modeling of a steady state H-mode discharge in this section.

The pedestal can be set using some empirical models developed by different authors^[15-17]. However, complex nonlinear calculation is needed to get a self-consistent pedestal shape. In this work, we only give a simple estimate for a pedestal using the formula presented in ref. 17.

The plasma is evolved from an initial equilibrium with a fixed boundary as given in Fig 3. The total toroidal current is $I = 1.0$ MA and not changed with time. The density profile is fixed in the evolution process as shown in Fig. 6. The plasma consists of electrons, a primary ion Deuterium and a Carbon impurity, and the effective charge number $Z_{eff} = 2$ is uniform. The temperature of the core plasma evolves according to the GLF23 transport model^[18].

The injected power is $P_{LH} = 3.0$ MW and $P_{NBI} = 3.0$ MW, to ensure the total power exceeding the threshold values for H-mode requirement. The temperatures evolve to a steady state much faster than the current density (magnetic field). From Fig. 7, we find that after almost 250 ms, the temperature profiles are almost fixed with respect to time. Hence, the values of current from different channels are almost not changed after 250 ms, as indicated in Fig. 8. But the inductively driven current profile is still changed with time.

We can continue the evolution process until the a full steady state ($\partial/\partial t = 0$) is reached. However, the steady state solution can be searched quickly using the profiles at $t \approx 256$ ms as an initial guess. This is an unique feature of ONETWO.

The final solution of current profiles is presented in Fig.9. The non-inductive current, including bootstrap current, LHRF and NBI driven current, accounts for almost 80% of the total current. Fig.10 shows the initial ($t=256$ ms) and the final electric field, where the parallel electric field is defined $E_{||} = \langle E \cdot B / B_0 \rangle f_{lim} / f$, $f = BR$. The relation $\partial B_p / \partial t = \partial E_{||} / \partial \rho$ holds^[19].

4 Summary and future plan

The LSC is integrated into the transport code ONETWO for the first time to do the LHCD calculation and to carry out the transport modeling for EAST. A sample steady state H-mode modeling is performed with LH wave power 3.0 MW and NBI 3.0 MW. The temperature profiles almost evolve to steady states in 250 ms. But it takes much longer time for current to evolve. In the final state, non-inductive current (Bootstrap, NBI, LHCD) accounts for up to 80% of the total current. Although it is not a full non-inductively driven steady state, it is expected to reach a full non-inductive current drive by increasing the auxiliary power.

We are still at an early stage to do predictive numerical modeling for tokamak experiments. The present work is still very rough. In the future, we are planning to model the core and edge together using global believable transport models and do the self-consistent pedestal calculation

for H-mode modeling using a NTCC code PEDESTAL. In addition, the ion cyclotron wave needs to be included into the modeling since it is also an important auxiliary heating method on EAST.

Acknowledgements

One of the author (D. Zhou) appreciates help from L. Lao, V. Chan, M. Chu, M. Choi and D. Brennan when he visited GA. This work was partially supported by the JSPS-CAS Core-University program in the field of ‘plasma and nuclear fusion’ .

References

- 1 Wan Y X. 2006, Overview progress and future plan of EAST project, 21st IAEA FEC, Chengdu, China.
- 2 Liu Chengyue, Wu Bin, Xiao Bingjia, et al. 2008, Plasma Sci. Tech., 10: 8.
- 3 Kessel C E, Giruzzi G, Sips A C C, et al. 2007, Nucl. Fusion, 47: 1274.
- 4 Murakami M, Greenfield C M, Wade M R, et al. 2005, Nucl. Fusion, 45: 1419.
- 5 Jardin S C, Pomphrey N, DeLucia J. 1986, J. Comput. Phys., 66: 481.
- 6 Ignat D W, Valeo E J, Jardin S C. 1994, Nucl. Fusion, 34: 837.
- 7 YOUNIS J, Wan B, Chen Z, et al. 2008, Plasma Sci. Tech., 10: 529.
- 8 Dnestrovskij Yu N, Razumova K A, Donne A J H, et al. 2006, Nucl. Fusion, 46: 935.
- 9 Razumova K A, Andreev, Donne A J H, et al. 2006, Plasma Phys. Control. Fusion, 48: 1373.
- 10 Coppi B. 1980, Comments Plasma Phys. Control. Fusion, 5: 261.
- 11 Gao Q D, Budny R V, Jiao Y M, et al. 2007, Nucl. Fusion, 47: 1318.
- 12 Ju M, Kim J, KSTAR Team 2000, Nucl. Fusion, 40: 1859.
- 13 Becker G. 1994, Nucl. Fusion, 34: 507.
- 14 Basiuk V, Artaud J E, Imbeaux F, et al. 2003, Nucl. Fusion, 43: 822.
- 15 Shimomura Y, Murakami Y, Polevoi A R, et al. 2001, Plasma Phys. Control. Fusion, 43: A385.
- 16 Bateman G, Bandres M, Onjun T, et al. 2003, Phys. Plasmas, 10: 4358.
- 17 Onjun T, Bateman G, Kritz A H, et al. 2002, Phys. Plasmas, 9: 5018.
- 18 Kinsey J E, Staebler G M, Waltz R E. 2005, Phys. Plasmas, 12: 052503.
- 19 Pfeiffer W W, Davidson R H, Miller R. L., Waltz R E. 1980, ONETWO: A computer code for modeling plasma transport in tokamaks, San Diego: General Atomics Company, GA-A16178.

Table 1. Major parameters of EAST

Items	Values
B (T)	3.5~4
I (MA)	1.0~1.5
R (m)	1.7
a (m)	0.4
κ	1.5~2
δ	0.3~0.5
NBI (MW)	4.0~8.0
LHRF (MW)	3.5~8.0
ICRF (MW)	3.0~6.0

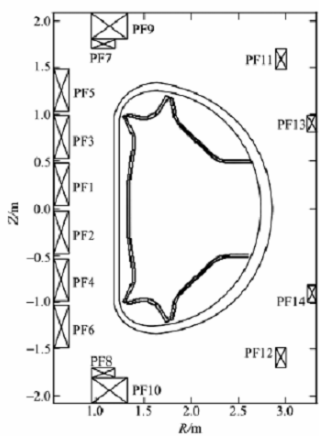


Fig.1 Schematic diagram of the poloidal cross section for EAST.

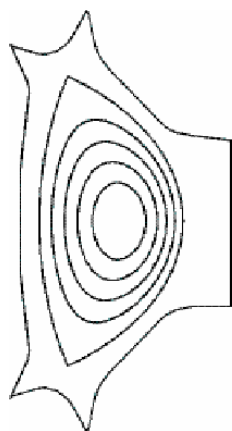


Fig.2 The equilibrium magnetic configuration for testing LHRF and NBI.

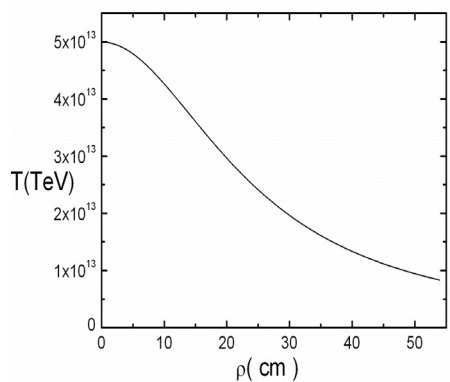


Fig.3 The self-consistent temperature profile, the density has the same shape.

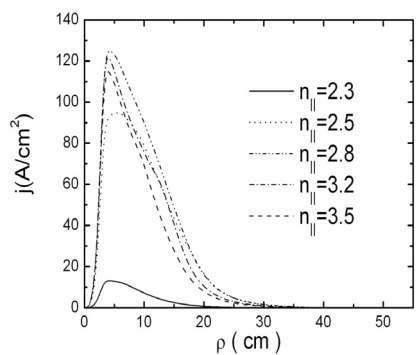


Fig.4 Current density profile driven by LHRF with a Gauss spectrum for different peak values of parallel refractive index, the width of the spectrum is 0.2.

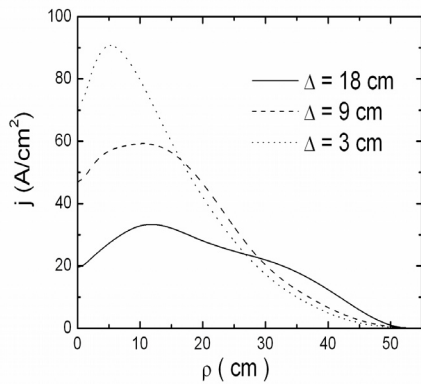


Fig.5 Current density profile driven by NBI, Δ is the distance between the magnetic axis and the beam line.

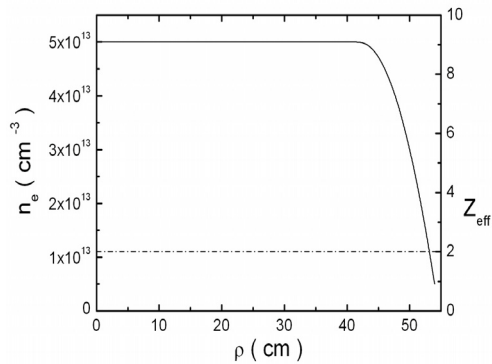


Fig.6 Density profile and effective Z fixed in the time evolution process of plasmas.

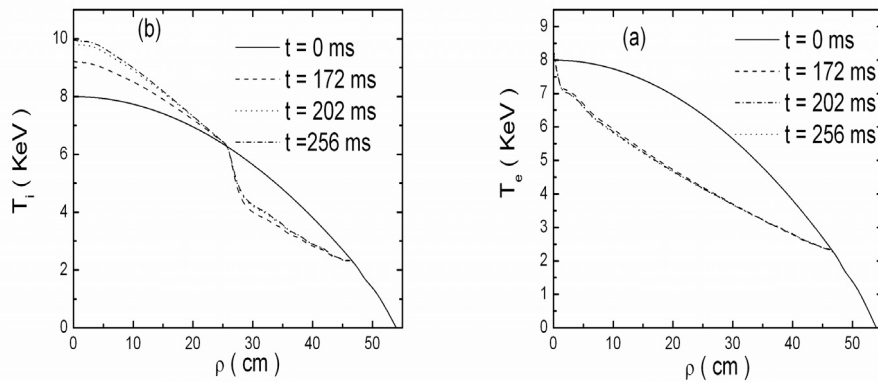


Fig.7 Time evolution process for, (a) electron and (b) ion, temperatures. Note that the lines between t=202 s and t=256 s are almost indistinguishable in (a).

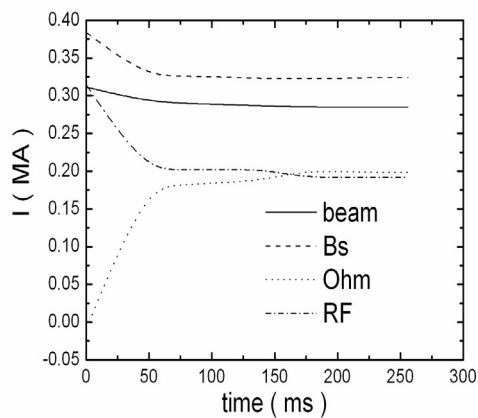


Fig.8 The time evolution process of current from different channels.

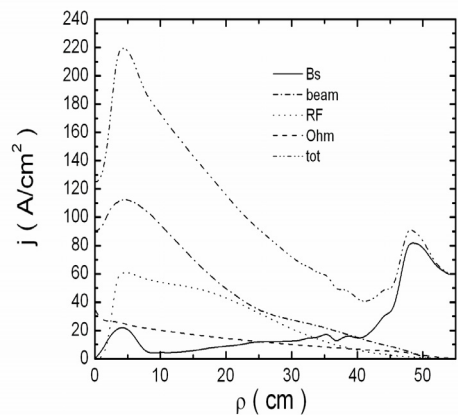


Fig.9 The final steady state current density profiles.

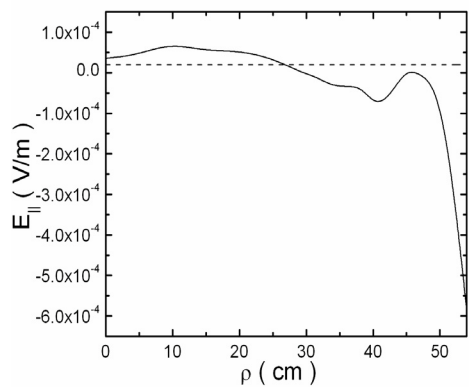


Fig.10 The initial (solid) and the final (dash) parallel electric field.

Soft x-ray tomography on HT-7 tokamak

Kaiyun Chen^{1*}, Liqun Hu¹, Yanmin Duan¹, Yue Ding², Tianpeng Ma³

¹ Institute of Plasma Physics, Chinese Academy of Sciences, Hefei 230031

² Department of Modern Physics, University of Science and Technology of China, Hefei 230026

³ Foundation Department, The North University for Ethnics, Yinchuan 750021

Abstract: The hardware of the soft x-ray imaging system on HT-7 tokamak is described. Fourier-Bessel expansion method is used to reconstruct the soft x-ray emission distribution. The simulation results show that the inversion accuracy is associated with the angular expansion limit and the hot core displacement. Besides, tomographic results of sawtooth oscillations in a typical LHCD plasma are presented.

Keywords: Tomography, sawtooth, soft x-ray

PACS: 52.35.Py; 52.70.La; 52.55.Fa

Corresponding author: K.Y. Chen

Postal address: P. O. Box 1126, Hefei, Anhui 230031, P. R. China

Tel: +86-551-5593516

Fax: +86-551-5591310

E-mail address: kychen@ipp.ac.cn

1. Introduction

The measurement of soft x-ray intensity is an important diagnostic on HT-7 tokamak. From the chord-integrated measurements, soft x-ray emission distribution on a poloidal cross section can be reconstructed. Based on the assumption that an iso-emission surface is a magnetic surface, the magnetic surface structure of the central plasma can be reconstructed. This can provide much information on the plasma structure and the evolution of the image with time is useful for studying MHD instabilities.^[1]

In this paper, the hardware and software of the soft x-ray imaging system on HT-7 tokamak will be described. The following of this paper is organized as follows. In the second section, the principal of soft x-ray tomography on HT-7 tokamak is briefly introduced. In the third section, the diagnostic set-up is shown. In the fourth section, test results of the tomography code with Kadomtsev's model are given. In the fifth section, tomographic results of sawtooth oscillations in a typical LHCD plasma are presented. In the last, the summary is given.

2. Principal of soft x-ray tomography on HT-7

The soft x-ray intensity measured by a detector can be expressed with the formula ^[1]

$$P = \left[\frac{A_{ap} A_{det} \cos \theta_{inc} \cos \theta'_{inc}}{4\pi d^2} \right] \int_{L(p,\phi)} g(r, \theta) dL \quad (1)$$

Where $g(r, \theta)$ is local soft x-ray emissivity. The quantity in the bracket is a constant and can be divided into the left side to simplify Eq. (1) with

$$f(p, \phi) = \int_{L(p,\phi)} g(r, \theta) dL \quad (2)$$

Where $f(p, \phi)$ is usually called chord ‘brightness’ with unit $\text{W} \cdot \text{m}^{-2}$, p and ϕ are the chord distance and azimuth angle of a chord $L(p, \phi)$ of a detector through the plasma. The schematic plot for the quantities r , θ , p , ϕ and $L(p, \phi)$ are shown in Fig.1. The goal of soft x-ray tomography is to extract $g(r, \theta)$ in Eq. (2) from chord-integrated measurements.

On HT-7, Fourier-Bessel expansion method is used to reconstruct soft x-ray emission distribution. In this method, local soft x-ray emissivity $g(r, \theta)$ is expanded with Fourier series in the angular direction and Bessel series in the radial direction ^[2]

$$g(r, \theta) = \sum_{m=0}^{m_{\max}} \sum_{l=0}^{l_{\max}} [a_{m,l}^c \cos m\theta + a_{m,l}^s \sin m\theta] J_m(\lambda_m^{l+1} r) \quad (3)$$

Where λ_m^{l+1} is the l th zero of the Bessel function. As a result, the chord brightness $f(p, \phi)$ can be written as

$$f(p, \phi) = \sum_{m=0}^{m_{\max}} \sum_{l=0}^{l_{\max}} \int_{L(p,\phi)} \sum_{m=0}^{m_{\max}} \sum_{l=0}^{l_{\max}} [a_{m,l}^c \cos m\theta + a_{m,l}^s \sin m\theta] J_m(\lambda_m^{l+1} r) dL \quad (4)$$

Through numerical integration along chord $L(p, \phi)$, Eq. (4) is transformed into a linear equation with unknown coefficients $a_{m,l}^c$ and $a_{m,l}^s$, and each chord-integrated signal represents such an equation. Through solving the linear equations with least-square method, the unknown coefficients $a_{m,l}^c$ and $a_{m,l}^s$ can be obtained. Consequently, local emissivity $g(r, \theta)$ is derived from Eq. (3). Usually, the radial expansion limit l_{\max} is adequate, whereas the angular expansion limit m_{\max} is restricted by the number of soft x-ray cameras. For a soft x-ray imaging system with

N cameras, m_{\max} can be N-1/2 at most, where 1/2 represents the component $\cos(N\theta)$ or $\sin(N\theta)$.

3. Diagnostic set-up

The HT-7 tokamak has major and minor radii of $R_0 = 122$ cm and $a = 27$ cm, respectively. There are five soft X-ray cameras on the machine as shown in Fig. 2. Each camera array consists of a slit and 46 channels of soft x-ray detector, which is sensitive to photon energies from 1 to 13 keV. The thickness of the beryllium filter is about 12.5 μm . For each camera, the distance from geometric center of plasma to the center of beryllium filter is 400 mm. The maximum sampling rate of this diagnostic system is 250 kHz, while their spatial resolution is changed from 0.6 to 1.5 cm. The chord-integrated soft X-ray signals are transferred to a data storage computer at the control room.

4. Test results of the tomography code

Before doing reconstructions from experimental data, the tomography code is checked with simulated emission distribution. In the simulation, the equilibrium temperature profile and density profile are derived from PHA (pulse height analyzer) temperature diagnostic and HCN density diagnostic in a typical discharge. The time evolutions of temperature and density distributions during a sawtooth crash corresponding to Kadomtsev's model are simulated with the rules introduced in ^[3, 4]. The plasma is assumed to be a pure Hydrogen or Deuterium plasma. Thus, the soft x-ray emissivity is related to electron temperature and electron density as ^[5]

$$g(r, \theta) \propto \int n_e^2 \frac{1}{\sqrt{k_B T_e}} \exp\left(-\frac{h\nu}{k_B T_e}\right) d\nu \quad (5)$$

Where n_e is electron density, T_e is electron temperature, k_B is Boltzmann's constant, h is Planck's constant and ν is the frequency of the radiation. With Eq. (2), the soft x-ray emission distribution and line-integrated signals can be simulated.

On HT-7 tokamak, for the emission structure simulated with Kadomtsev's model, it is found that the inversion results depend on the angular expansion limit m_{\max} heavily as the hot core displacement is large. Fig.3 (a) shows the virtual emission structure created with Kadomtsev's model. The hot core displacement is 0.3, where the inversion radius is 0.3 and the mixing radius is

0.42. Fig.3 (b), (c) and (d) show the inversion results with $m_{\max} = 1^{1/2}$ (two soft x-ray arrays), $m_{\max} = 2$ (three arrays) and $m_{\max} = 3$ (four arrays) respectively. We can see that $m_{\max} = 1^{1/2}$ and $m_{\max} = 2$ are not enough to describe the emission structure. As the hot core is pushed outward further, even the reconstruction with $m_{\max} = 3$ will deviate from the original emission structure obviously.

However, as the hot core displacement is relatively small, the inversion results seem satisfactory even with $m_{\max} = 1^{1/2}$ and $m_{\max} = 2$. Fig.4 shows the virtual emission structure created with Kadomtsev's model and the inversion results, where the hot core displacement is 0.2. The other parameters are the same as that in Fig.3. It is seen that with $m_{\max} = 1^{1/2}$, $m_{\max} = 2$ and $m_{\max} = 3$, all the inversion results resemble the original emission structure well. These suggest that as the hot core displacement is relatively small, the reconstructions can be done with relatively low harmonic, such as $m_{\max} = 2$. In other words, except for the later phase of a sawtooth crash corresponding to Kadomtsev's model, soft x-ray tomography can be used to do reconstructions with relatively low harmonic. With only two or three soft x-ray cameras, the early stage of sawtooth crash corresponding to Kadomtsev's model can be studied.

5. Tomographic results of a sawtooth oscillation in a typical LHCD plasma

On HT-7, sawtooth oscillation is a commonly observed phenomena in LHCD plasmas. Fig.5 (a) shows the temporal evolution of main plasma parameters in a typical sawtoothing discharge with LHCD. Fig.5 (b) shows the expanded view of soft x-ray intensities. It is seen from Fig.5 (b) that, in the middle of a sawtooth period, MHD oscillations appear, saturate and decay. In the following, this kind of oscillation will be called mid-oscillation. It is also seen from Fig.5 (b) that the sawtooth crash is preceded with precursor oscillations.

Through singular value decomposition (SVD), the perturbation components and their weight can be analyzed. Fig.6 shows SVD results of the mid-oscillations in Fig.5 (b). It is seen from this figure that $m = 1$ component takes most of the signal energy. In other words, $m = 1$ mode is the main perturbation responsible for mid-oscillation. Fig.7 shows the tomography results. It is seen

that before the mid-oscillation, the emission pattern is composed of nearly concentric circles. During the mid-oscillations, the hot core is pushed outside and a relatively flat region is formed on the opposite side of the hot core. This flat region is believed to be a magnetic island. After the mid-oscillations, poloidal symmetry is restored and the emission pattern is composed of nearly concentric circles again. We can see from Fig.5 that, mid-oscillations do not cause sawtooth crash. This indicates that $m = 1$ mode does not necessarily trigger sawtooth crash. Besides, mid-oscillation is seldom observed in ohmic-heating plasmas. This suggests that the appearance of mid-oscillation may be associated with LHCD.

Fig.8 shows the tomography results of sawtooth crash. We can see that at the beginning of the crash, the emission pattern is composed of a displaced hot core and a relatively flat region on the opposite side of the hot core. During the crash, the flat region is enlarged. After the crash, the whole central region is relatively flat. The tomography results indicate that sawtooth crash is due to the hot core displacement and the enlargement of cold flat region. In the middle of the crash, the hot core seems like a crescent to a certain degree. This may be due to the inversion error. As shown in the test results in section 4, the inversion accuracy is associated with the hot core displacement. Therefore, it is thought that in the middle of sawtooth crash, the hot core may still be round shaped.

5. Summary

Five soft x-ray cameras have been installed on HT-7 tokamak. The temporal and spatial resolution are $4 \mu s$ and $0.6-1.5$ cm respectively. Fourier-Bessel inversion method was used to reconstruct the distribution of soft x-ray emissivity. The test results of the tomography code show that the inversion accuracy is associated with the angular expansion limit and the displacement of plasma hot core. The tomography results in LHCD plasmas show that mid-oscillations are due to the behavior of $m=1$ mode and the crash pattern is composed of a displaced hot core and a relatively flat region on the opposite side of the hot core.

Acknowledgements

This work has been supported by the National Nature Science Foundation of China, No.10675124, and partially supported by JSPS-CAS Core -University Program in the field of “Plasma and Nuclear Fusion”. The corresponding author is grateful to all members of the HT-7 Team for their contribution to HT-7 experiments.

References

- [1] R.S. Granetz and P. Smeulders, Nucl. Fusion 28, (1988) 457.
- [2] Y. Nagayama, J. Appl. Phys. 62, (1987) 2702.
- [3] B. B. Kadomtsev, Sov. J. Plasma phys. 1, (1975) 389.
- [4] I. Furno, et al., Nucl. Fusion 41 (2001) 403.
- [5] M. Anton, H. Weisen, M.J. Dutch, et al., Plasma Phys. Control. Fusion 38, (1996) 1849.

Figure captions

Fig.1 Schematic plot of a measurement chord.

Fig.2 Arrangement of soft x-ray arrays on HT-7 tokamak

Fig.3 Virtual emission structure created with Kadomtsev's model and the reconstructions with different angular expansion limits. The hot core displacement is 0.3. (a) is the virtual emission structure. (b), (c) and (d) are the inversion results with $m_{\max} = 1 \frac{1}{2}$ (two arrays), $m_{\max} = 2$ (three arrays) and $m_{\max} = 3$ (four arrays) respectively.

Fig.4 Virtual emission structure created with Kadomtsev's model and the reconstructions with different angular expansion limits. The hot core displacement is 0.2. (a) is the virtual emission structure. (b), (c) and (d) are the inversion results with $m_{\max} = 1 \frac{1}{2}$ (two arrays), $m_{\max} = 2$ (three arrays) and $m_{\max} = 3$ (four arrays) respectively.

Fig.5 Temporal evolution of main plasma parameters in a typical sawtooth discharge with LHCD. (a) Temporal evolution of main plasma parameters. (b) Expanded view of soft x-ray intensities.

Fig.6 SVD results of mid-oscillations. (a) Eigenvalues corresponding to different perturbation components. The square of an eigenvalue represents the weight of the corresponding perturbation component. (b) Spatial eigen vectors of the first four perturbation components.

Fig.7 Tomography results of mid-oscillations. (a), (b) and (c) correspond to the times before, during and after mid-oscillation.

Fig.8 Tomography results of sawtooth crash. (a), (b) and (c) correspond to the beginning of the crash, during the crash and after the crash.

Figures

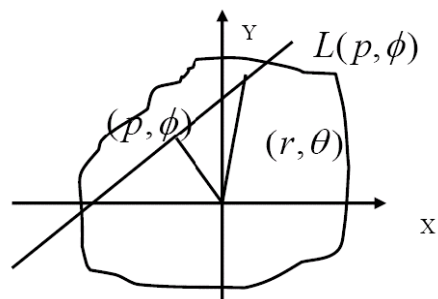


Fig.1

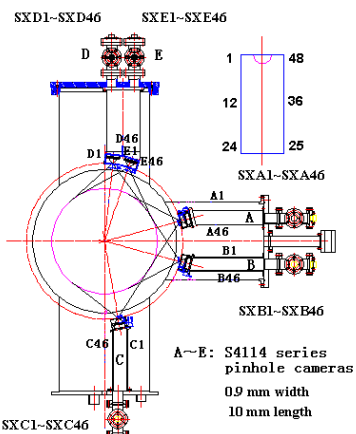


Fig. 2

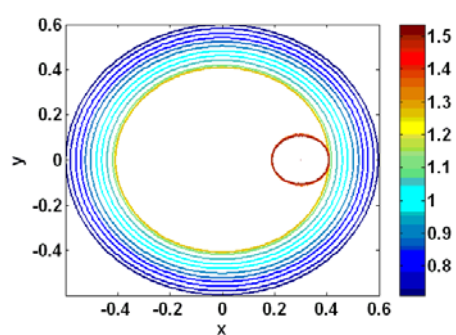


Fig. 3 (a)

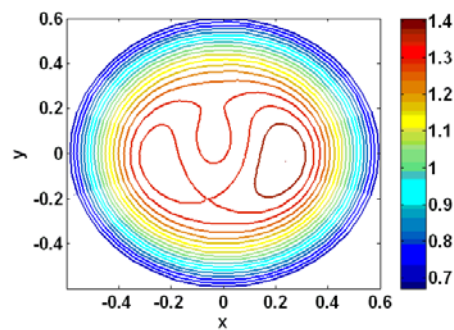


Fig. 3 (b)

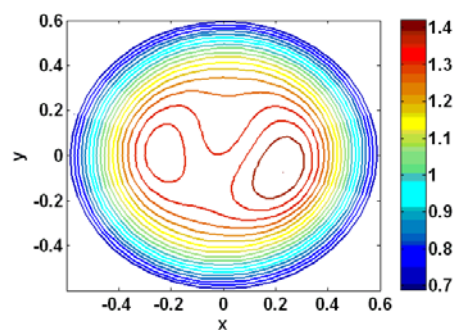


Fig. 3 (c)

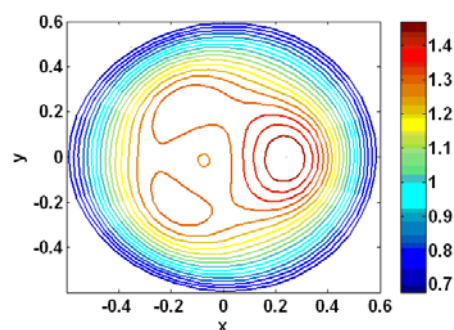


Fig. 3 (d)

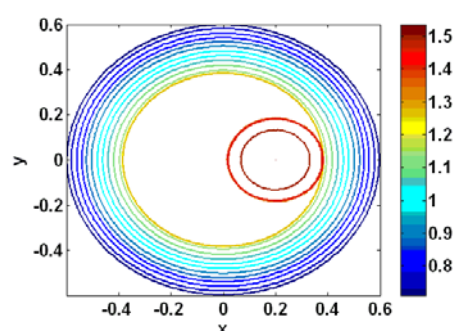


Fig. 4 (a)

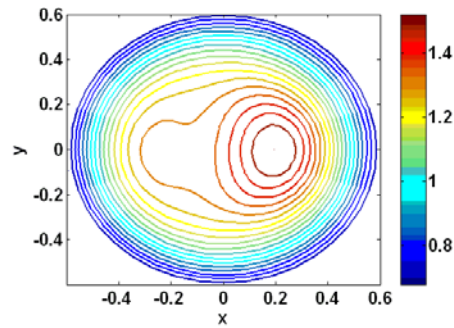


Fig. 4 (b)

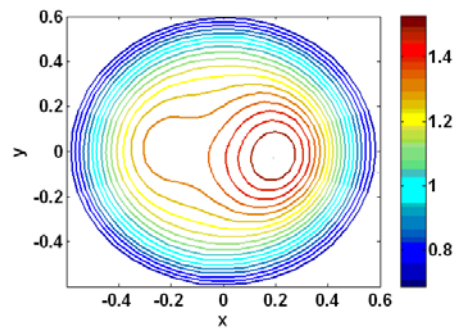


Fig. 4 (c)

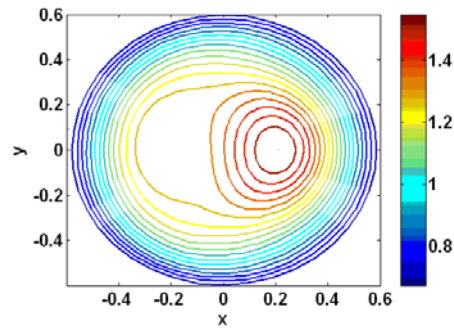


Fig. 4 (d)

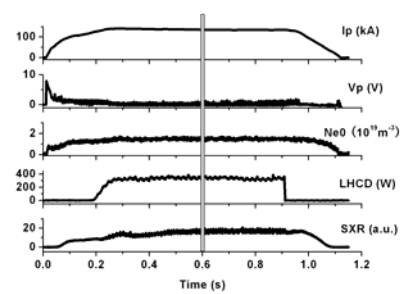


Fig. 5 (a)

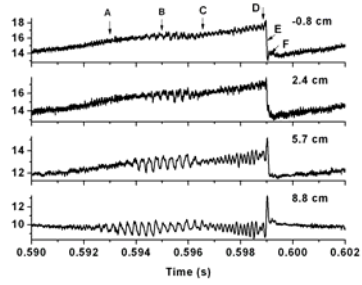


Fig.5 (b)

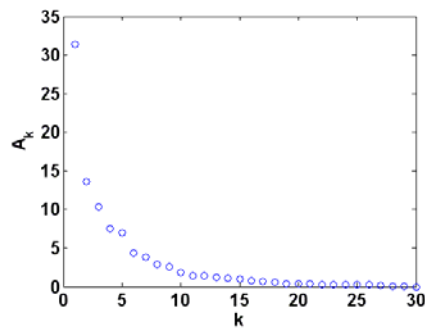


Fig.6 (a)

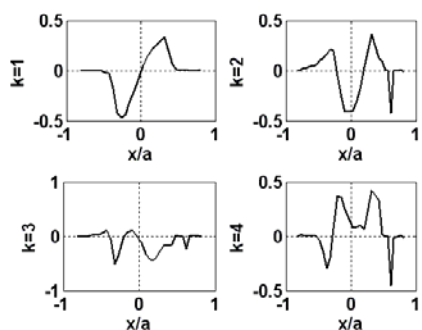


Fig.6 (b)

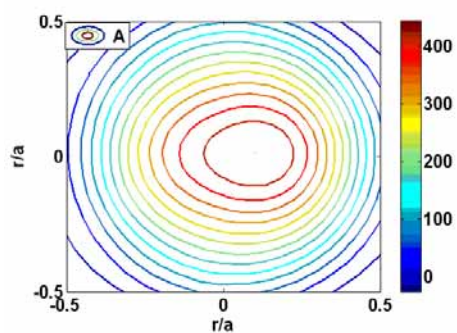


Fig.7 (a)

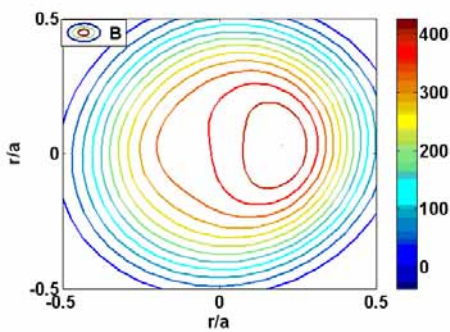


Fig.7 (b)

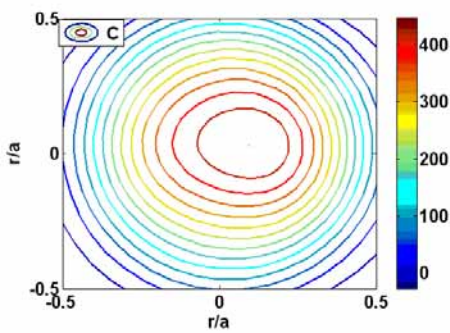


Fig.7 (c)

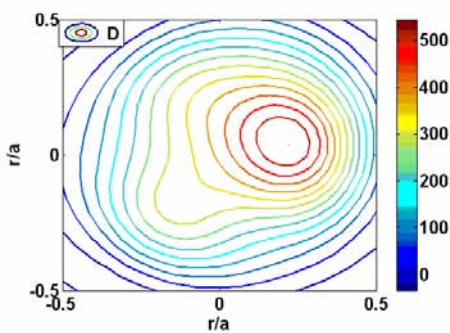


Fig.8 (a)

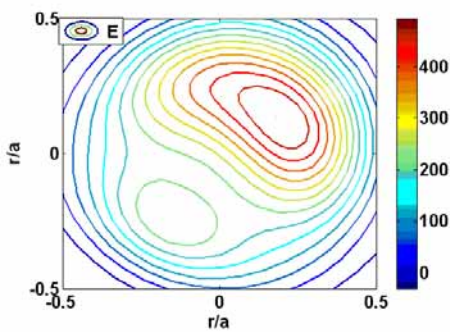


Fig.8 (b)

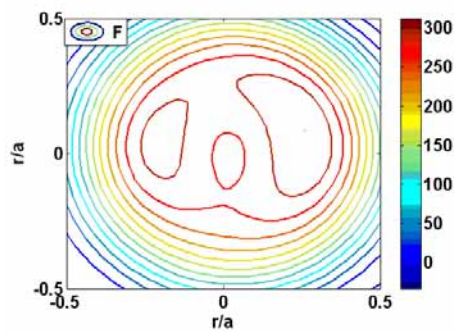


Fig.8 (c)

Evaluation of the Optical Design of Laser Thomson Scattering Diagnostics for High-Temperature EAST Tokamak and Low-Temperature MAP-II Divertor Simulator

Shinichiro KADO (門信一郎) , Filippo SCOTTI*
Xiaoqi XI¹ (席晓琦) and Junyu ZHAO¹ (赵君煜)

School of Engineering, The University of Tokyo, Bunkyo, Tokyo, 113-8656, Japan

¹Institute of Plasma Physics, Chinese Academy of Sciences (ASIPP), Hefei, China

** present address: Princeton Plasma Physics Laboratory (PPPL), Princeton, US*

The optical design of the laser Thomson scattering (LTS) system for EAST tokamak is now on-going. Based on the Visible YAG laser TVTS system developed in the MAP-II (material and plasma) steady-state linear divertor/edge plasma simulator at the University of Tokyo, the required specification and the applicability of the VIS-YAG-TVTS system was evaluated in terms of the photon number to be collected by the fiber light-guide to a spectrometer and the reciprocal linear dispersion of the spectrometer. Then, the possible design of the optical system was proposed.

1. Introduction

Laser Thomson scattering (LTS) has been regarded as a reliable electron temperature measurement, since it detects Maxwellian temperature of the velocity distribution function. LTS was developed in 1960s [1] and has been sophisticated as the laser and detector technologies improve.

Conventional system employs the ruby laser (694.3 nm) and photo-multiplier tube (PMT). The advanced types of the LTS in the fusion research can be categorized into the following 3 schemes: YAG-LTS (using high repetition rate Nd-YAG laser 1064 nm in wavelength) [2], TVTS (detecting spatial profile using Television, i.e. CCD detector for the visible wavelength) [3, 4] and LIDER (Light Detection And Ranging, making use of time-of flight to yield spatial resolution) [5]. These schemes can be combined depending on the situation.

We have been applied the TVTS using a frequency doubled visible (VIS) Nd-YAG laser aiming at the low temperature detached recombining plasmas [6]. Bright double monochromator equipped with a stray light rejection filter at the wavelength domain, called Rayleigh block, and data accumulation technique, allow us to access below 1-eV plasmas [7, 8]. The reliability of the measurement was examined for the helium recombining plasmas [9]. We have recently been succeeded in measuring the helium recombining front where the electron temperature is as low as 0.05 eV [10].

In this report, we reevaluate the optical design of the LTS for low temperature recombining plasmas in MAP-II divertor simulator in the University of Tokyo [11]. Then consider the applicability of the similar VIS-YAG-TVTS system in the EAST tokamak in hefei, China.

2. Key parameter for the optical design of the LTS system.

One of the most important parameter in evaluating the system is the photon numbers per pulse collected by the single fiber. Then we can design the number of pulses to be accumulated, the number of fibers to be bundled in a channel, and the number of channels to be binned in the CCD tip.

The photon number per pulse scattered in the detection solid angle $d\Omega$ can be evaluated, for the polarization yielding the maximum intensity and for 90 degree detection, as

$$\Delta N_{\text{photon}} = r_e^2 [I_{\text{in}} A \Delta t] n_e L d\Omega / h \nu, \quad (1)$$

with the electron classical radius,

$$r_e = \frac{e^2}{4\pi\epsilon_0 m_e c^2} = 2.82 \times 10^{-15} m, \quad (2)$$

where, n_e is the electron density in m^{-3} , I_{in} is the probe laser intensity in W/m^2 , A and L are the cross section of the beam and the interaction length in m , respectively, yielding scattering volume of AL . When the spot size of the viewing chord is smaller than A , the collection efficiency is degraded. Therefore, the ideal case demands the focusing of the laser at the center of the observing area. Δt is the pulse length of the laser. Therefore, square bracket $[]$ denotes the pulse energy in $J/pulse$.

For the solid angle $d\Omega$ much smaller than hemisphere can be interpreted using the optical parameters of the F number and magnification M (= images at fiber / at plasma) as

$$d\Omega = \frac{\pi}{4} \frac{1}{F^2 (1+1/M)^2} = \frac{\pi}{4} \frac{1}{F_{eff}^2} = \pi (NA)^2, \quad (3)$$

where F_{eff} is the effective F - number of the imaging optics: $F_{eff} = F$ for collimated input (object at the infinite distance) and $= 2F$ for 1 to 1 magnification. NA denotes the numerical aperture. Namely, brightness is proportional to the square of NA for the small detection solid angle.

Usually, $d\Omega$ is limited by the NA of the fiber. For example, 1 $J/pulse$ 532 nm laser (frequency doubled Nd:YAG Laser), $n_e = 10^{19} m^{-3}$ plasma, $L = 1$ mm and $M = 0.25$ (namely fiber 0.25 mm in core diameter) yield only about 1000 photons, which can be collected per pulse. These photons are further lost through the spectrometer and detector by one or two order of magnitude.

Maximal NA of the fiber with which photons are efficiently transmitted to the detector is limited in the F -number of the spectrometer.

Therefore, in order to increase the temporal resolution, by detecting the scattered photons using the high repetition laser and fast detectors without accumulation, increase in the fibers per channel is necessary. As a result, the spatial resolution can be degraded. In order to increase the spatial resolution, on the other hand, the number of fibers to be summed along the laser path cannot be increased. In this reason, bright spectrometer and accumulation technique are necessary. Hence, one has to determine the priority in its design considering the objective of the research, unless one can afford to introduce the large number of optical fibers covering large solid angle [12].

Another issue to be considered in TVTS is the wavelength range to be recorded in the CCD tip. In the Czerny-Turner mount spectrometer using reflection grating of g (grooves/mm), reciprocal linear dispersion (nm/mm) [13] can be described as

$$\left| \frac{d\lambda}{dx} \right| = \frac{1}{f} \left(\sqrt{\left(\frac{\cos\theta_0 \cos\epsilon}{mg \cdot 10^{-6}} \right)^2 - \left(\frac{\lambda}{2} \right)^2} + \frac{m}{|m|} \frac{\lambda}{2} \tan\theta_0 \right), \quad (4)$$

where, f is the focal length of the spectrometer in mm, m is the diffraction order. θ_0 is the geometrical angle determined by the optical mount of the spectrometer: half angle of the sum of the incident and the diffracted angles to be detected. ϵ is the tilt angle with respect to the grating normal and parallel to the groove, which causes the distortion of the slit image, sometimes referred to as "grating smile".

In the double monochromator with dispersion addition, total reciprocal linear dispersion can be expressed [14] as

$$\left(\frac{1}{\frac{d\lambda}{dx}} \right)_{total} = \left(\frac{1}{\frac{d\lambda}{dx}} \right)_{1st} + \left(\frac{1}{\frac{d\lambda}{dx}} \right)_{2nd}. \quad (5)$$

A merit in using the double monochromator lies in the fact that a physical block (wire) can be placed at the image of the first monochromator in order to reject the strong stray light at the laser wavelength. Drawbacks are on the other hand, the lower throughput of the spectrometer, stronger vignetting effect and complicity of the alignment.

2. Optical system for low-temperature MAP-II divertor simulator

The MAP-II (material and plasma) [11] divertor simulator at the university of Tokyo is a dual-chamber linear device consisting of a first chamber in the upstream (called the source chamber) and a second chamber in the downstream (called the target chamber) connected to each other by means of a drift tube having two diaphragms 50 mm in diameter. A longitudinal magnetic field of about 20 mT suppresses the radial diffusion, forming a plasma stream of approximately 50 mm in core diameter and about 2 m in length, which is terminated at the target plate at the second chamber.

The VIS-YAG-LTS system has been operating in the source chamber of the MAP-II, since around 2004 [6] and has been upgraded for the purpose of measuring helium recombining plasmas of about 0.05 eV [10].

The configuration of the system is schematically shown in Fig. 1 [6]. A frequency-doubled Nd:YAG laser beam (532 nm in wavelength, 10 Hz in repetition rate, 7 ns in pulse duration, and typically 400 mJ in energy per pulse, 8 mm in diameter) is directed to a plasma by means of a mirror located beneath the chamber. A lens with a focal length of 900 mm focuses the beam in the center of the plasma through a Brewster window and three baffle plates. An object lens with a 150-mm focal length and a diameter of 100 mm is used to image the plasma in the laser path onto the bundled fiber with a magnification of 2/3. The fiber bundle consists of the quartz optical fibers 0.1/0.125 mm in core/clad diameters and 0.2 in N_A which corresponds to the solid angle of 0.17% of the sphere. Signals from 8 fibers, corresponding to about 4 mm in plasma, are binned in the CCD tip.

Since the 1 eV electron temperature corresponds to about 1.5 nm in the Doppler half-width at 1/e maximum at 532 nm for an orthogonal viewing chord, it is difficult for commercially available narrow-band interference filters (which typically have a pass band broader than about 1 nm) to resolve the Doppler profiles as is performed in YAG-LTS. For this reason, we have assembled a double monochromator equipped with an image-intensified charge-coupled device (ICCD) detector (Hamamatsu C4078+C4742, 1344x1024 pixels). Initial system included the double monochromator, having the focal length of 135 mm and F/2.8 [6] (Fig. 1), i.e. a conventional type of the double monochromator with dispersion addition (homo-tandem type). The photons transmitted through $N_A=0.2$ (F/2.5) fibers are somewhat lost in the spectrometer.

In contrast, the present double monochromator system adopts what we call Hetero-Tandem Double Monochromator (HTDM), composed of two non-symmetric stages. Bright achromatic lenses $F/2$ ($f=200$ in the first stage and $f=100$ in the second stage) and holographic gratings 1800 grooves/mm having dimensions of $100 \times 135 \text{ mm}^2$ for the first stage and $50 \times 50 \text{ mm}^2$ for the second stage were used. The first grating produces a dispersed Thomson spectrum in the image plane, where a spatial stray-light filter, called a Rayleigh-block, is located and filters out the stray light which dominantly originates in the random reflection of the probe laser at the chamber walls and windows. The Rayleigh scattering component is expected to be negligible in the low pressure (\sim tens of mTorr) discharges.

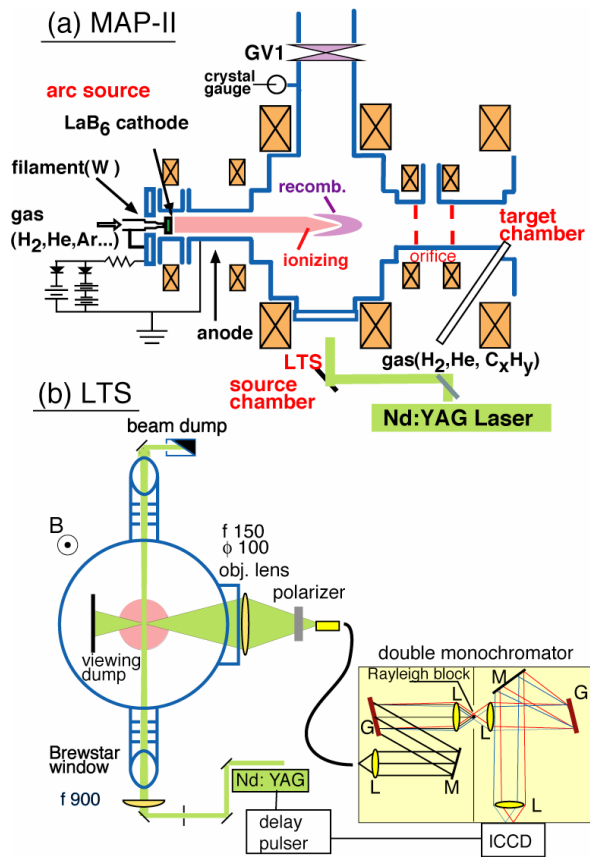


Fig.1 Schematic views of (a) MAP-II and (b) LTS system in the initial configuration [6]. The target chamber is omitted.

The reciprocal linear dispersion evaluated using Eq. (4) is 2.03 nm/mm. The Rayleigh block, the copper wire 0.2 mm in diameter, then, corresponds to the theoretical lowest measurable T_e of 0.03 eV and to the experimental one of 0.05 eV considering the safety margin in the fitting procedure.

The second grating then disperses the notch-filtered Thomson spectrum, which is imaged on the photocathode of an ICCD detector. Reciprocal linear dispersion evaluated using Eq. (4) is 4.05 nm/mm. The wavelength resolution is 0.19 nm in FWHM for a slit width of 45 μm , which is a typical setting in our T_e measurement. The total reciprocal linear dispersion obtained using Eq. (5) is 1.37 nm/mm and the highest measurable T_e is 40 eV, which is almost equal to that in the previous homo-tandem ones of 1.57 nm/mm.

3. Evaluation of the optical system for high-temperature EAST tokamak

Based on the experience in the MAP-II device, we are evaluating the optical design for the LTS on EAST (Experimental Advanced Superconducting Tokamak) device in hefei, China. Major and minor radii are 1.7 and 0.4 m, respectively. The target electron density in the EAST tokamak is typically in the same order as that of MAP-II, so that the similar scattered photon fraction can be expected. However, the electron temperature in the core region can be up to several keV and that of the edge plasma will be 50-100 eV. Therefore, we need the spectrometer that is designed to cover these temperature ranges. A planned diagnostic port for the EAST LTS system is shown in Fig. 2.

In MAP-II, number of photons collected in the single laser pulse per 8 ch fiber is about 2500 when the electron density is as high as 10^{19} cm^{-3} . In order to increase the signal to noise ratio, we usually accumulate at least 10 minutes with 10 Hz. The total input energy is then equivalent to 2400 J and 1.6×10^7 photons can be collected. In reality however, the spot size of the viewing chords are 1/10 that of the laser, so that we estimated that 10^6 photons are desirable to obtain Doppler profiles of the scattered photons. This requirement can be mitigated if one can assume the thermal equilibrium for either relativistic or non-relativistic electron velocity distribution function.

In the EAST case, on the other hand, enhancement of the signal by 3 orders of magnitude is required from the default case mentioned in Sec 2. where $M = 0.25$ as the EAST system was assumed.

We are planning to use high- NA fiber, such as 0.3 and the bright spectrometer to match $NA=0.3$, namely, F/1.6. Use of 0.6 mm core radius fiber can increase the photon number by about 2.4 due to the increase in L , and the summation of 4 fibers can be applicable to keep the spatial resolution of 10 mm.

A laser with 3 J per pulse at 532 nm and the repetition rate of 10 Hz is planned to be installed in EAST, that is 8 times higher than the MAP-II case.

In addition, we are planning to use single Czerny-Turner monochromator instead of the double monochromator with Rayleigh block, because the throughput, especially in the off-axis light is considerably higher, due to less vignetting effect.

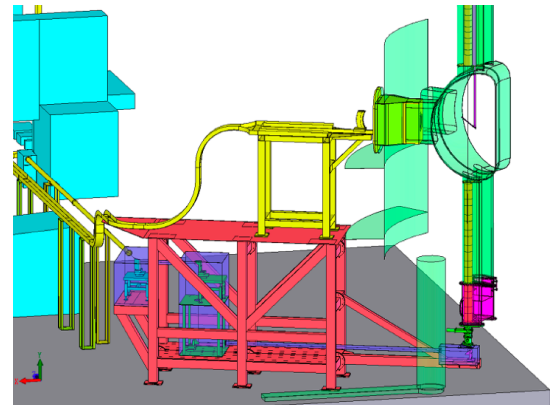


Fig. 2. Schematic view of the diagnostic port for the LTS system in EAST. The laser beam is injected from the port in the bottom. Object lens can be located at the horizontal viewing port (tentative design).

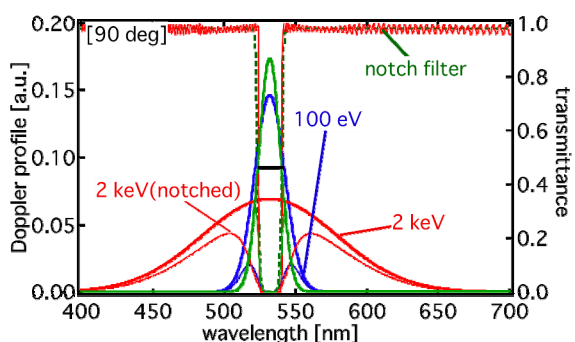


Fig. 3. Simulated scattered spectrum in the EAST LTS system together with the transmittance of the holographic notch filter.

Table 1 Candidates of the optical elements in the spectrometer in EAST LTS system.

item	f [mm]	g [gr/mm]	θ_0 [deg]	m	disp. [nm/mm]	available F/
1	100	600	20	-1	14.5	2 (achromatic)
2	105	600	20	-1	13.8	2 (camera)
3	85	650	20	-1	14.3	1.4(camera)
4	50	1200	20	-1	12.8	1.2(camera)

For the stray light rejection technique, we are planning to apply holographic notch filter having the notch band of 17 nm with respect to 532 nm. Due to this, the lower measureable temperature becomes higher up to 50 - 100 eV.

As a result, we expect that the photon number can be increased up to about 20000 per pulse. Although this number is still small, summing of multiple pulses, such as 10-20, corresponding to 1-2 seconds, or binning of the CCD pixels also in the wavelength direction can make it close to the detectable condition.

The reciprocal linear dispersion suitable to this system is about 10-15 nm/mm since 400-700 nm spectra should be measured using a detector about 20 - 30 mm in aperture, as shown in Fig. 3. Using Eq. (4), we have selected a possible combination of the optical elements shown in Table 1. In order to match $NA=0.3$ fiber, commercially available camera lenses 85 or 50 mm in focal length are recommendable in terms of the detection efficiency. We are now designing the spectrometer based on the above-mentioned requirements.

Acknowledgements

We acknowledge Bingjia Xiao in ASIPP for the help in launching and organizing this collaboration. This work was partially supported by the JSPS-CAS Core-University program in the field of 'Plasma and Nuclear Fusion'.

References

- [1] N.J. Peacock, D.C. Robinson, M.J. Forrest, P. Wilcock and V.V. Sannikov, *Nature* **224**, 448 (1968)
- [2] H. Rohr, K.-H. Steuer, G. Schramm, K. Hirsch, H. Salzmann, *Nucl. Fusion*, **22**, 1099 (1982).
- [3] N. Bretz, D. Dimock, V. Foote, D. Johnson, D. Long, and E. Tolnas, *Appl. Opt.* **17**, 192 (1978).
- [4] D. Johnson, D. Dimock, B. Grek, D. Long, D. McNeill, R. Palladino, R. Robinson and E. Tolnas, *Rev. Sci. Instrum.* **56**, 1015 (1985).
- [5] H. Salzmann, K. Hirsch, P. Nielsen, C. Gowers, Gadd, M. Gadeburg, H. Murmann and A. Schrodter, *Nucl. Fusion*, **27**, 1925 (1987).
- [6] A. Okamoto, S. Kado, S. Kajita and S. Tanaka, *Rev. Sci. Instrum.* **76** (2005) 116106.
- [7] F. Scotti, S. Kado, A. Okamoto, T. Shikama and S. Tanaka, *Plasma Fusion Res.* **1**, **54-56** (2006).
- [8] F. Scotti, S. Kado, A. Okamoto, T. Shikama, Y. Kuwahara, K. Kurihara, K-S. Chung and S. Tanaka, *Plasma Fusion Res.* **2**, S1110(2007).
- [9] S. Kado and F. Scotti, Proc. 13th International Symposium on Laser-Aided Plasma Diagnostics, Takayama, Japan, 2007. (NIFS-PROC-68, ISSN 0915-6348), General Talk 3.
- [10] F. Scotti and S. Kado, *to be published in J. Nucl. Matter.*,
- [11] S. Kado, Y. Iida, S. Kajita *et al.*, *J. Plasma Fusion Res.* **81** (2005) 810.
- [12] H. J. van der Meiden, S. K. Varshney, C. J. Barth, et. al., "10 kHz repetitive high-resolution TV Thomson scattering on TEXTOR: Design and performance(invited)", *Rev. Sci. Instrum.* **77**, 10E512 (2006). □
- [13] S. Kado, "Plasma Flow Measurements - Spectroscopic Methods -", *J. Plasma Fusion Res.* **83**, 176 (2007). [in Japanese]
- [14] F. Scotti, master thesis dissertation, the University of Tokyo (2007).

Dynamics of dust particle in SOL/Divertor plasma of HL-2A

Yukihiro Tomita, Gakushi Kawamura, Yudong Pan¹, Yan Zhou¹ and Longwen Yan¹

National Institute for Fusion Science, 322-6 Oroshi-cho, Toki 509-5292 Japan

¹ *Southwestern Institute of Physics, P.O. Box 432, Chengdu 610041, Sichuan, China*

e-mail: tomita@nifs.ac.jp

Abstract

Dynamics of a dust particle is studied in the SOL/divertor plasma of the HL-2A device with a single-null configuration. In this study the simplest model of the dust dynamics is applied: spherical shape of a dust, ion drag force due to Coulomb scattering as a dominant force, and spontaneous charging of a dust particle to the equilibrium charge. In the outer region near the plasma-facing wall the poloidal plasma flow pushes the dust particle to the divertor plates. It is clarified that the dust particle with a radius of 1 μ m from the top of the SOL/divertor region is accelerated up to around 100 m/sec to the poloidal direction at the divertor plates.

PACS: 52.30, 73.20.H, 83.50.P

1. Introduction

The presence and behavior of dust particles in fusion plasmas are one of the interesting topics as well as in the astrophysical, space, laboratory, and processing plasmas. In present fusion devices (TEXTOR-94, ASDEX-U, LHD, JT60-U etc.), the dust particles were collected after several hundred shots and analyzed their characteristics [1 - 3], where the dust radii are widely ranged between 10 nm and 100 μ m. Their components were mainly of carbon and constituents of stainless steel, which are used for divertors and most plasma-facing walls. One of the particular subjects in fusion devices is associated with absorption of radioactive tritium [4]. After operation of plasma discharges, the disposal of the radioactive dusts is one of key issues from the viewpoint of the safety.

In the HL-2A device [5] the deposition of dusts or impurities on the surface of reflection mirrors for the interferometer, which is installed high-field side on a equatorial plane, is one of the issues for sensitivity and quality of the experimental data [6]. In this study we investigate dynamics of the dust particle in the SOL/divertor plasma of the HL-2A device with the single-null configuration. Up to now the mechanism of production and growth of dust particles are not clarified. Here we analyze behavior of the produced dust particle. The density of the dust particle in fusion devices is so low that the collective effects of the dust particles are safely ignored. The background plasma in the SOL/divertor region, which is required to calculate the orbit of the dust, is given by using the B2-EIRENE code for the 500 kW power flow from the core plasma to the SOL/divertor region [7].

2. Forces on dust

The force acting on a dust particle with a radius R_d and a mass m_d is including the various forces [8 - 10]:

1) the ion drag force due to absorption,

$$\vec{F}_{iab} = \pi R_d^2 m_i n_i V_i (\vec{V}_i - \vec{v}) \left(1 + \frac{Z_d e^2}{2\pi\epsilon_0 R_d m_i V_i^2} \right), \quad (4)$$

where m_i , n_i and V_i is the mass, density and flow speed of plasma ion, respectively. The dust velocity is indicated by \vec{v} . Here a dust particle is negatively charged with the charge state of Z_d (> 0) due to the high mobility of electrons. The OML (Orbit Motion Limited) theory [11, 12] is applied to the absorption cross-section.

2) the ion drag force due to Coulomb scattering of plasma,

$$\vec{F}_{isc} = \frac{n_i Z_d^2 e^4 \ln \Lambda}{4\pi \epsilon_0^2 m_i V_i^3} (\vec{V}_i - \vec{v}), \quad (5)$$

where $\ln \Lambda$ is the Coulomb logarithm.

3) the electrostatic force,

$$\vec{F}_E = -Z_d e \vec{E}, \quad (6)$$

where \vec{E} is the electrostatic field at the dust position,

4) the Lorentz force:

$$\vec{F}_B = -Z_d e (\vec{v}_d \times \vec{B}), \quad (7)$$

where \vec{B} is the magnetic field,

5) the gravity force,

$$\vec{F}_g = m_d \vec{g}, \quad (8)$$

where \vec{g} is the gravitational acceleration.

One finds that the dominant force on the dust is the ion drag force \vec{F}_{isc} due to Coulomb scattering of plasma for the case of $n_i \sim 10^{18} m^{-3}$, $T_e \sim 100 eV$, $V_i \sim c_s \sim 10^4 m/s$, $R_d \sim 1\mu m$, $Z_d \sim 10^5$, $E \sim 10V/m$, $B \sim 1T$, where these quantities correspond to the parameters at the SOL/divertor region in HL-2A device. The other forces are much smaller than around three order of the scattering force. In this study, therefore, we consider the dust dynamics due to the ion drag force by Coulomb scattering. This drag force accelerates a dust particle to the direction of the plasma flow.

3. Dust charge and dust dynamics

Dust charge Q_d is determined by the plasma particle fluxes to the dust particle:

$$\frac{dQ_d}{dt} = I_{di} + I_{de}, \quad (9)$$

where I_{di} and I_{de} are the ion and electron absorption current to the dust, respectively. Here we neglected the thermionic current, secondary electron emission current and charging current due to impurities. According to the OML theory, the ion current to the dust is expressed for the case of the mono-energetic ion flow with the velocity V_i :

$$I_{di} = e\pi R_d^2 n_i V_i \left(1 + \frac{Z_d e^2}{4\pi \epsilon_0 R_d m_i V_i^2}\right). \quad (10)$$

On the other hand, since the thermal velocity of electrons is much faster than the electron flow velocity, the electron current I_{de} is obtained for the case of Maxwell velocity distribution:

$$I_{de} = -e\pi R_d^2 n_e \sqrt{\frac{8T_e}{\pi m_e}} \exp\left(-\frac{Z_d e^2}{4\pi \epsilon_0 R_d T_e}\right). \quad (11)$$

At the steady state, i.e. $dQ_d/dt = 0$, the charge state of the dust Z_d is given by the relation for the case of ion flow with the ion sound speed:

$$Z_d = 1.06 \times 10^{28} R_d T_e. \quad (12)$$

This relation gives the dust charge $Z_d = 1.70 \times 10^5$ for the R_d of $1\mu m$ and T_e of $100eV$. By using the relation (12), the equation of motion of the dust particle is expressed under the dominant force of the ion drag force due to Coulomb scattering:

$$\begin{aligned} \frac{d\vec{v}}{dt} &= \frac{\vec{F}_{isc}}{m_d} = \frac{n_i Z_d^2 e^4 \ln \Lambda}{4\pi \epsilon_0^2 m_i V_i^3 m_d} (\vec{V}_i - \vec{v}) \\ &= \frac{3.37 \times 10^{56} e^4 \ln \Lambda}{(4\pi)^2 \epsilon_0^2 m_i} \frac{1}{R_d \rho_d} \frac{n_i T_e^2}{V_i^3} (\vec{V}_i - \vec{v}), \end{aligned} \quad (13)$$

where ρ_d is the mass density of the dust particle. The acceleration is inversely proportional to the dust radius and the mass density, which comes from the relation of the stationary dust charge, Eq. (12).

4. Dust dynamics in HL-2A

The behavior of the dust particle in the HL-2A plasma with the single-null configuration is investigated under the background plasma from the B2-EIRENE code. The calculation mesh and the arrangement of divertor and plasma-facing wall are shown in Fig.1. The poloidal plasma flow velocity at the outer region and the private region near the boundaries of the B2-EIRENE mesh is shown in Fig.2 (A) and (B) for the 500 kW power input from the core region to SOL, where the distance is calculated from the surface of the inner to outer divertor plates along the poloidal direction. The flow speed gets to the few km/s. The stagnations of the poloidal flow are located at the top of the outer region and the private region. The dust particles produced on the wall move to the divertor plate along the poloidal direction due to the strong poloidal plasma flow. The time behavior of the carbon dust velocity with the radius of 1 μm to the poloidal direction at the high-field side (from c to a by way of b , see Fig.1) and the low-field side (from c to e by way of d , see Fig.1) is shown in Fig. 3 (A) and (B), respectively, where the initial speed is zero. The initial straight increase of the velocity comes from the roughness of the calculation mesh. At the high-field side the carbon dust ($\rho_d = 2 \text{ g/cc}$) is accelerate to 90 m/sec during 30 msec. On the other hand at the low-field side the dust speed to the poloidal direction becomes 120 m/sec for 10 msec, which comes from the dependence of the plasma quantities. The heavier ion ($\rho_d = 7.9 \text{ g/cc}$) dust is less acceleration because of its heavy mass: 75 m/sec during 35 msec and 80 m/sec during 15 msec at the high- and low- field side, respectively.

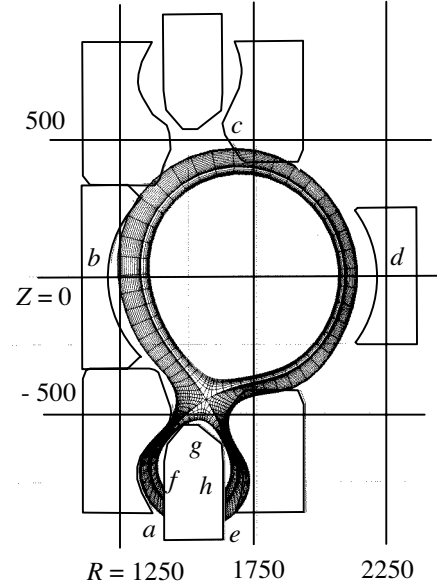


Fig.1 The calculation mesh for the B2-EIRENE code and the arrangement of divertor and plasma-facing wall in HL-2A device. The indices a - h indicate the positions for the spatial profiles in Fig.2.

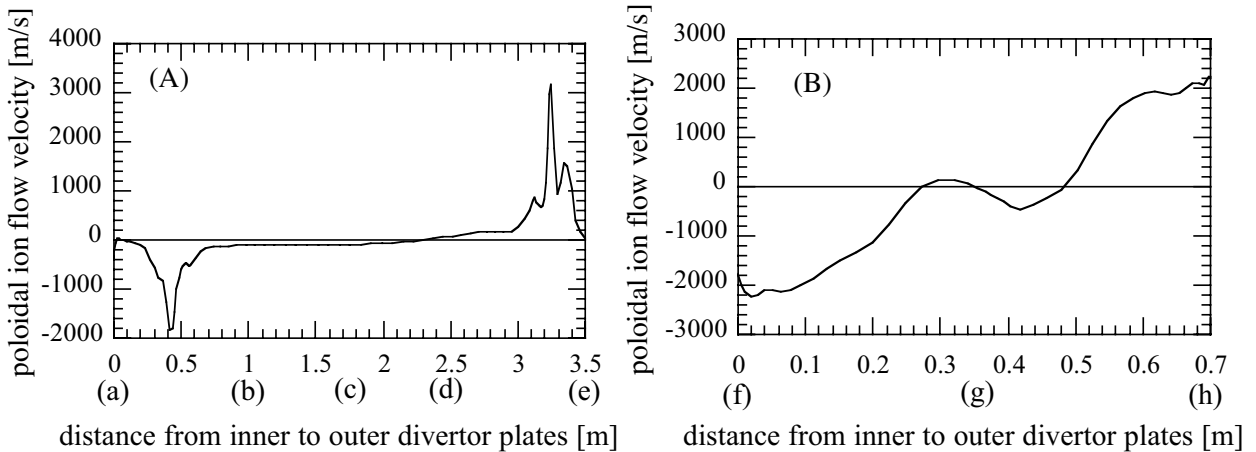


Fig.2 poloidal ion flow velocity at the outer region (A) and the private region (B), where the distance is calculated from the surface of the inner to outer divertor plates along the poloidal direction, see Fig.1.

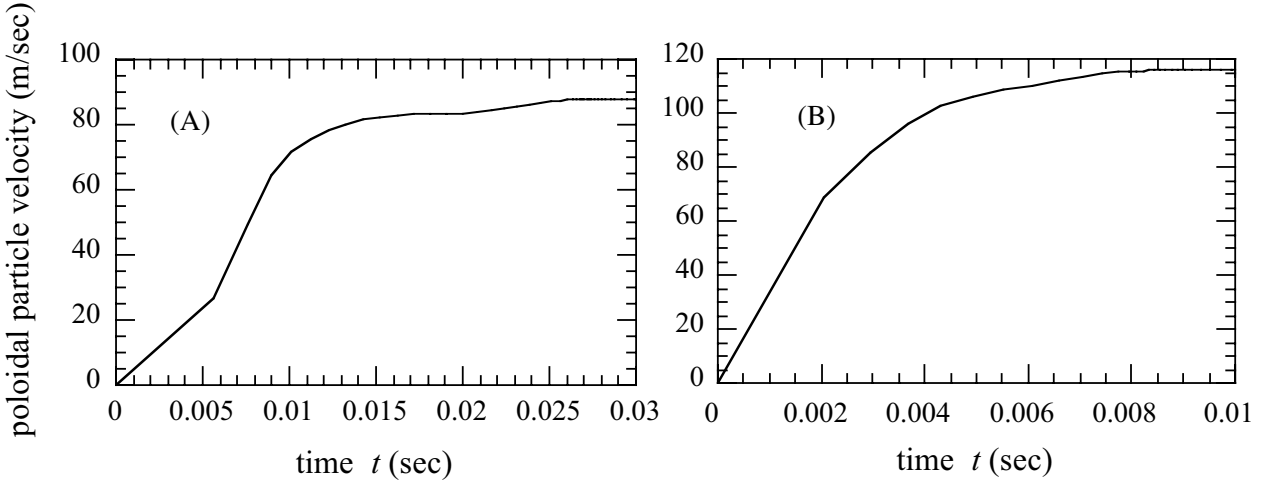


Fig.3 Time behavior of poloidal velocity of carbon dust particle along the poloidal direction at high-field side (A) and low-field side (B).

5. Conclusion

The dust behavior in the SOL/divertor region of the HL-2A plasma with the single-null configuration was investigated. The dominant force on the dust is the ion drag force due to the Coulomb scattering, which accelerates the dust to the direction of the plasma flow. In the outer region near the plasma-facing wall the poloidal plasma flow pushes the dust particle to the divertor plate. It is clarified that the dust particle, which starts from the top of the SOL/divertor region, is accelerated to around 100 m/sec to the poloidal direction. In order to investigate the deposition of the dust particle on the reflection mirrors more detailed analysis is required including time behavior of the dust charge and the plasma flow across the magnetic field lines. Furthermore in order to analyze the dust behavior in front of the plasma-facing wall the configuration of plasma and electrostatic field between the outermost boundary of the SOL/divertor region and the plasma-facing wall should be analyzed self-consistently.

Acknowledgements

This work is partly supported by the JSPS-CAS Core-University Program in the field of Plasma and Nuclear Fusion, a Grant-in-Aid for scientific research from Ministry of Education, Science and Culture of Japan (No. 19055005) and the program of the Formation of the International Joint Research Base Network in the National Institute for Fusion Science.

References

- [1] J. Winter, Plasma Phys. Control. Fusion, **40** (1998) 1201.
- [2] A. Sagara, S. Masuzaki, T. Morisaki *et al.*, J. Nucl. Mater. **313-316** (2003) 1.
- [3] J. Sharpe, *et al.*, J. Nucl. Mater., **313-316** (2003) 455.
- [4] J. Winter, Plasma Phys. Control. Fusion, **46** (2004) B583.
- [5] Y. Liu *et al.*, Nuclear Fusion, **44** (2004) 372.
- [6] Y. Zhou, *et al.*, Fusion Engineering and Design, **81** (2006) 2823.
- [7] Y. D. Pan and R. Schneider, J. Nucl. Mater. **363-365** (2007) 407.
- [8] S. Krasheninnikov, Y. Tomita, R. Smirnov, and R. Janev, Phys. Plasma, **11** (2004) 3141.
- [9] R. D. Smirnov, *et al.*, Plasma Phys. Control. Fusion, **49** (2007) 347.
- [10] Y. Tomita, R.D. Smirnov, T. Takizuka, D. Tskhakaya, Contrib. Plasma Phys., **48** (2008) 285.
- [11] H. Mott-Smith and I. Langmuir, Phys. Rev. **28** (1926) 727.
- [12] J. E. Allen, Phisica Scripta **45** (1992) 497.

Analysis on EAST LHCD operation space by using simple Core-SOL-Divertor model

R. Hiwatari, A. Hatayama¹⁾, S.Zhu²⁾, and Y. Tomita³⁾

Central Research Institute of Electric Power Industry, Tokyo, JAPAN

¹⁾*Faculty of Science and Technology, Keio University, Yokohama, JAPAN*

²⁾*Institute of Plasma Physics, Chinese Academy of Sciences, Hefei, P.R.China*

³⁾*National Institute for Fusion Science, Toki, JAPAN*

E-mail: hiwatari@criepi.denken.or.jp

Abstract

A simple Core-SOL-Divertor model (CSD model) has been developed to investigate qualitatively the overall features of the operational space for the integrated core and edge plasma. In the CSD model, the core plasma model of ITER physics guidelines and the two-point SOL-divertor model are applied. This CSD model is validated by the two dimensional divertor transport code (B2-EIRINE) and by the JT-60U divertor recycling database, and this model is applicable to the low- and high-recycling state of the divertor plasma. The CSD model is applied to the study of the EAST operational space with lower hybrid current drive experiments under various kinds of trade-off for the basic plasma parameters, and the relationship between the operational space and the plasma discharge duration is also discussed.

Keywords: Core transport, SOL-Divertor transport, operation space, EAST

1. Introduction

Consistency between the edge plasma operation and the core plasma operation is an important issue for the design of ITER and the future fusion power plant. In case of the ITER divertor predictive

modeling, the fitting scaling laws for divertor plasma property are built with a two dimensional (2D) divertor transport code, and these are used as boundary conditions for the core plasma analysis[1]. Prior to such detailed and massive calculations by multi-dimensional transport codes, it is useful to understand qualitatively the overall features of plasma operational space including the requirements for the SOL and divertor plasma. For this purpose, we are developing a simple Core-SOL-Divertor model (CSD model)[2]. In the present paper, we extend the core plasma model in which the hybrid operation can be taken into account, and apply this CSD model to investigate the relationship between the plasma discharge duration and the plasma operational space of low hybrid current drive (LHCD) experiments for EAST[3].

2. Simple Core-SOL-Divertor Model

2.1. Core plasma model

In the present paper, the 0D plasma model based on ITER physics guidelines is applied to the core plasma transport. This model has been widely used in the ITER design and other reactor designs, when one roughly estimates the operational region for plasma parameters of a tokamak reactor. The averaged power and particle balance equations (units are $[MW/m^3]$ and $[i/m^3]$, respectively) are as follows[4]:

$$\begin{aligned}\frac{dW_p}{dt} &= -\frac{W_p}{\tau_E} + P_\alpha + P_{OH} + P_{aux} - P_{Brad} - P_{sync}, \\ \frac{dn_j}{dt} &= -\frac{n_j}{\tau_p} + S_j, \quad (j = e, He)\end{aligned}$$

where W_p is plasma thermal stored energy, and P_α , P_{OH} , P_{aux} , P_{Brad} and P_{sync} are the total powers of alpha heating, ohmic heating, auxiliary heating, bremsstrahlung loss and synchrotron radiation loss. The scaling law of the L-mode energy confinement time $\tau_E^{ITER89L}$ is applied to the energy confinement time

$$\tau_E = f_H \tau_E^{ITER89L}, \text{ where } f_H \text{ is the confinement improvement factor for H-mode.}$$

The particle confinement time τ_{pj} is defined by $\tau_{pj} = C_{pj} \tau_E$, where C_{pj} is the correction factor for each species(electron, and helium). In the present paper, $C_{pj} = 1.0$ is assumed. The fuel ion density is obtained by the charge neutrality condition. The L-H transition condition is installed by the same fashion as in ref.[5] in order to examine

the consistency between H-mode and SOL conditions. We apply the experimental scaling law

$P_{thr} = 2.67 M^{-1} B_t^{0.92} n_{20}^{0.77} R^{1.23} a^{0.76}$ to the threshold power for H-mode, where M , B_t , n_{20} , R , and a are ion mass number, toroidal magnetic field, averaged electron density, major radius, and minor radius, respectively[6].

2.2. SOL-divertor plasma model

The two-point model under steady state conditions can be applied with a time dependent core transport model, because the time scale of core plasma transport is much longer than that of SOL-divertor plasma. Basic equations of the usual two-point model are as follows[7]:

$$(1 - f_{mom}^{div}) n_s T_s = (1 + M_d^2) n_d T_d, \quad (1)$$

$$\frac{7}{2} (1 - f_{imp}) L_s q_\perp = n_d M_d C_s (T_d) \Delta [\varepsilon + (\gamma + M_d^2) T_d], \quad (2)$$

$$\Delta = \frac{5}{2} \chi_\perp \frac{n_s T_s}{q_\perp}, \quad (3)$$

$$L_d^2 q_\perp = \frac{4\kappa_0 \Delta}{49} T_s^{\gamma/2} \left[1 - \left(\frac{T_d}{T_s} \right)^{\gamma/2} \right], \quad (4)$$

where n and T are density and temperature. The subscript “s” and “d” express the upstream SOL and divertor region, respectively. The heat flux from the core plasma, temperature decay length, and Mach number at the divertor plate are defined by q_\perp , Δ , and M_d , respectively. The coefficients f_{mom}^{div} and f_{imp} are the fraction of momentum loss and impurity radiation loss. The coefficient $\gamma (\approx 7.0)$ is the sheath energy transmission coefficient, and the heat load $\varepsilon (\approx 21.8 \text{ eV})$ on the plate comes from the recombination and radiation process[8].

2.2. Particle balance to determine the upstream SOL density

In order to integrate the core and edge plasma model, the upstream SOL density n_s should be given in a self-consistent manner both for the core plasma and for the edge plasma. For this purpose, the particle balance equation in the SOL and divertor regions is solved in the CSD model. It is assumed that all neutral particles to originate at the divertor plate at the rate proportional to the total particle flux to the divertor plate. Consequently, total neutral source rate at the edge region N_n including gas puff term N_{puff} is as follows:

$$N_n = C_n \frac{1}{2} \left(1 - \frac{1}{e^2} \right) n_d M_d C_s 2\pi R \Delta_n \sin(\psi) + N_{\text{puff}}, \quad (5)$$

where Δ_n is the density decay length. We assume that $\Delta_n = 2\Delta$ ψ is the angle of the magnetic field to the divertor plate. The term $(1/2)(1 - 1/e^2)$ comes from the integration of the radial direction (from the separatrix to the density decay length Δ_n) on the divertor plate. The coefficient C_n is a calibration factor and $C_n = 0.5$ is assumed (This value is derived from the following comparison with experimental database[9]). By using the simple neutral model and the particle flux across the separatrix, Γ_{core} , from the 0-D core plasma calculation, the particle balance equation for the SOL-divertor region becomes

$$\Gamma_{\text{core}} S_{\text{core}} + N_n^{\text{sol}} + N_n^{\text{div}} = \frac{1}{2} \left(1 - \frac{1}{e^2} \right) n_d M_d C_s 2\pi R \Delta_n \sin(\psi) \quad (6)$$

where $N_n^{\text{div}} = f_{\text{ion}}^{\text{div}} N_n$ and $N_n^{\text{sol}} = f_{\text{ion}}^{\text{sol}} (1 - f_{\text{ion}}^{\text{div}}) N_n$. $f_{\text{ion}}^{\text{div}}$ and $f_{\text{ion}}^{\text{sol}}$ are the ionization fraction in the divertor and the SOL region, respectively. S_{core} is the core plasma surface normal to the particle flux. The ionization fraction in the divertor region is modeled by[10]

$$f_{\text{ion}}^{\text{div}} = 1 - \exp \left(- \frac{L_d \sin(\psi)}{\lambda_{\text{ion}}^{\text{div}}} \right) \quad (7)$$

where $\lambda_{\text{ion}}^{\text{div}} = v_n / (n_d \langle \sigma v \rangle_{\text{ion}})$ is defined by the ionization cross section $\langle \sigma v \rangle_{\text{ion}}$, which is the strong function of T_d , and the neutral velocity $v_n = \sqrt{T_n/m}$. In the present paper, the neutral temperature of $T_n = T_d$ is assumed. The ionization fraction in the SOL region is defined by

$$f_{\text{ion}}^{\text{sol}} = \frac{A_{\text{sol}}}{A_{\text{core}} + A_{\text{sol}} + A_{\text{pump}}} \quad (8)$$

where A_{core} , A_{sol} and A_{pump} are the effective areas for the core region, the SOL region, and the pumping effect from the divertor region, respectively. In the present paper, the effective areas of A_{core} and A_{sol} are assumed to be their each cross section area on the plasma midplane, i.e., $A_{\text{core}} = 2\pi R \cdot a$ and $A_{\text{sol}} = 2\pi R \cdot \Delta_n$. The effective area of A_{pump} is defined by $A_{\text{pump}} = C_{\text{pump}} / (v_n / 4)$, where C_{pump} is the speed of the pumping system[11], but pumping effect is not considered in the present paper($C_{\text{pump}} = 0.0$). To check the validity of this CSD model, comparison with the edge transport code (B2-EIRENE) has been carried out. We focused on the JT-60U L-mode discharge in the high recycling state[12]. The parameter dependence on the total particle flux across the separatrix can be clearly reproduced[2]. Furthermore, comparison with JT-60U divertor recycling database[9] has been also carried out. In case of the calibration factor $C_n = 0.5$, the result from CSD model is consistent with the database and this calibration factor is applied in the present paper.

3. EAST operation space by low hybrid current drive

3.1. Main trade-off on the operation space

In the initial phase of the EAST plan, current drive experiments are planned to be carried out by LHCD[3]. Low density operation is preferable for good current drive efficiency. On the other hand, such operation is disadvantageous to the divertor performance, because it generally results in high heat load on the divertor plates. As for the steady state experiment with high performance plasma such as H-mode, reduction of the heat load onto the divertor plate is a critical issue. Considering discussions above, we take into account the following trade-off, or constraints, i.e., 1) plasma discharge duration 2) available LHCD power, 3) allowable heat load to the divertor plates, 4) available heating power for sustaining the quasi-steady state power balance in the core and also 5) threshold power for L-H transition.

The total plasma current is defined by

$$I_p = I_{OH} + I_{BS} + I_{LHCD} \quad (9)$$

where I_{OH} , I_{BS} , and I_{LHCD} (the unit is MA) are the ohmic current, the bootstrap current and the driven current by the LHCD system, respectively. The poloidal coil system of EAST has 10 VS flux supply, which corresponds to 10 sec plasma operation with 1.0 MA plasma current. The relationship between the ohmic current I_{OH} and the plasma operation duration t_{op} is roughly defined by $t_{op} = 10/I_{OH}$. The bootstrap current is estimated from the following definition[13]:

$$I_{BS} = C_{BS1} \varepsilon^{0.5} \beta_p I_p, \quad (10)$$

where ε and β_p are the inverse aspect ratio and the poloidal beta value. The coefficient of C_{BS1} in eq.(10) is defined by $C_{BS1} = 1.32 - 0.235(q_{95}/q_0) + 0.0185(q_{95}/q_0)^2$, where q_{95} and q_0 are the safety factor on 95% flux surface and on the magnetic axis, respectively. The power required for LHCD is estimated by the following model[14]:

$$P_{LHCD} = \frac{R \ln \Lambda I_{LHCD}}{0.122(j^*/p^*)} \frac{n_{20}}{T} \quad (10)$$

where $(j^*/p^*) = 10$ is assumed in the present paper, and the available LHCD power is 3.5 MW for the EAST[3].

Based on the particle and power balance of the core plasma[2,4], the total particle flux Φ_p and the total heat flux Q_{in} across the separatrix are $\Phi_p = (n_{20}V_p)/(C_p \tau_E)$ and $Q_{in} = (0.048n_{20}TV_p)/\tau_E$,

respectively (V_p is the plasma volume). From these quantities and the definition of the energy confinement time, the temperature and the density of the core plasma are written as $T = C_T Q_{in}/\Phi_p$ and $n_{20} = C_d \Phi_p^{10/9} / Q_{in}^{5/9}$, respectively (where C_T and C_d are functions of core plasma parameters). With these equations, we express the following trade-off, or constraints as functions of (Q_{in}, Φ_p) , and discuss the plasma operation space on (Q_{in}, Φ_p) .

Then, Eq. (9) is written as

$$P_{LHCD} = \frac{R \ln \Lambda}{0.122(j^*/p^*)} C_n \Phi_p^{19/9} C_T^{-1} Q_{in}^{-14/9} (I_p - C_{BS2} \Phi_p^{1/9} Q_{in}^{49} I_p - I_{OH}) \leq 3.5 . \quad (12)$$

where $C_{BS2} = 4C_{BS1} \epsilon^{0.5} C_n C_T (1 + n_i/n_e) (1 + \kappa^2 (1 + 2\delta^2 - 1.2\delta^3)/2\kappa)^{1/2} B_p^{-2}$. In addition, the total heating power for the EAST is set to be 7.5 MW[3], then the following relationship has to be considered,

$$P_{LHCD} \leq Q_{in} \leq 7.5 . \quad (13)$$

The left inequality in Eq.(11) is rewritten as

$$Q_{in}^{23/9} \geq \frac{R \ln \Lambda I_p}{0.122(j^*/p^*)} \frac{C_n}{C_T} \Phi_p^{19/9} \quad (14)$$

The scaling law of the threshold power for the LH transition can be also written as the function of Φ_p

and Q_{in} ,

$$Q_{in} \geq P_{thr} = 2.75 B_t^{0.96} R^{1.23} a^{0.76} M_i^{-1} C_n^{0.77} \left(\frac{\Phi_p^{7.7}}{Q_{in}^{3.85}} \right)^{1/9} \quad (15)$$

where M_i is the average ion mass (amu). The heat flux q_{div} to the divertor plates is limited to the maximum allowable heat flux q_{max} from the engineering viewpoint. This condition is expressed as

$$q_{div} = [\epsilon + (\gamma + M_d^2) T_d] n_d M_d C_s \sin(\psi) \sin(\theta) \leq q_{max} \quad (16)$$

where θ denotes the inclination angle of the divertor plate to the magnetic lines force in the poloidal plane. Eq.(14) can be also expressed by Φ_p and Q_{in} defined above. The q_{max} is taken to be 3.5MW/m^2 , which corresponds to the averaged value estimated in ref.[3]. Finally, we obtain the four inequalities, i.e, Eqs.(12), (14), (15) and (16), for the trade-off relationships of LHCD experiments.

3.2. LHCD operational space

The main parameters of EAST are summarized in Table 1[3]. With these parameters, the possible operation space in the (Q_{in}, Φ_p) space is explored. Figures 1 show the operational spaces depending on the fraction of the ohmic current to the total plasma current $f_{ohm} = I_{ohm}/I_p$. In this exploration, the gas puffing of $N_{puff} = 1.0 \times 10^{21} \text{ s}^{-1}$ (which corresponds to about 5% of total neutral source rate N_n) in the divertor region and the fraction of impurity radiation $f_{imp} = 0.3$ are assumed. The operational space is painted, and each boundary is the operation condition as mentioned in the previous subsection. Figure 1(a) corresponds to $f_{ohm} = 0.0$, namely, fully non-inductive operation, and the bootstrap current fraction f_{BS} is estimated at $f_{BS} \leq 0.25$ here. This figure indicates that the allowable heat flux to the divertor plate is a key parameter to extend the possible operation space. The upper boundary of Q_{in} is limited by $q_{div} \leq 3.5(\text{MW/m}^2)$. The boundary of $q_{div} \leq 3.5(\text{MW/m}^2)$ for $Q_{in} \leq 6.0(\text{MW})$ region implies a decrease of q_{div} by the transition from low to high recycling state. The upper boundary of the particle flux Φ_p is dominated by the power balance requirement.

The dependence of the operational space on the fraction of the ohmic current to the total plasma current f_{ohm} is investigated here. In this series of investigation, the remaining parameters except the key parameter in the following methods are kept at the same values as those in Figure 4(a). Figure 4(b) shows the operational space for the hybrid operation case of $f_{ohm} = 0.3$ (which roughly corresponds to the plasma

operation duration $t_{op} = 33$ sec). The upper boundaries of the LHCD current drive and the power balance requirement move to higher particle flux region, which corresponds to the high density region. When the fraction of the ohmic current to the total plasma current increases up to $f_{ohm} = 0.5$ (which roughly corresponds to the plasma operation duration $t_{op} = 20$ sec), the boundaries of the LHCD current drive and the power balance requirement move to higher particle flux region and the boundary of the LH transition condition limits the upper operational space in the low heating region of $Q_{in} \leq 3.0$ MW. In the future, comparison with these results and the two dimensional divertor transport code B2-EIRINE will be carried out, and the high recycling or detachment operation point for the LHCD H-mode operation will be assessed.

4. Summary

The CSD model has been developed to investigate overall and integrated features of core and edge plasma in tokamaks, and applied to the analysis of the EAST operational space. Various kinds of trade-off have been taken account into in the analysis. The basic features of possible operation space and its dependence on the fraction of the ohmic current to the total plasma current f_{ohm} have been made clear for the LHCD operation. Based on these results, comparison with these results and the two dimensional divertor transport code B2-EIRINE will be carried out, and the high recycling or detachment operation point for the LHCD H-mode operation will be assessed.

Acknowledgement

This work was partly supported by JSPS-CAS Core-University Program in the field of Plasma and Nuclear Fusion.

Reference

- [1] A. S. Kukushkin, *et al*, IAEA-CN77/CT/P-07, *Proc. 19th IAEA Fusion Energy Conf. (Lyon, France, 2002)*, G. W. Pacher, *et al.*, *Nucl. Fusion* **43** (2003) 188.
- [2] R. Hiwatari, *et al*, *J. Nucl. Matt.* **337-339**(2005)386-390.
- [3] S.Zhu, *Contrib. Plasma Phys.* **40**(2000)322.
- [4] N. Uckan and ITER Physics Group 1990 ITER Physics Design Guidelines:1989 *ITER Documentation Series No.10*
- [5] T. Yamamoto, *et al.*, *Fusion Eng. Des.* **39-40**(1998)143.
- [6] ITER Physics Expert Groups on Confinement and Transport and Confinement Modeling and Database, ITER Physics Basis Editors, *Nucl. Fusion* **39**(1999)2175.
- [7] K.Borrass, *Nucl. Fusion* **31**(1991)1035.
- [8] S.Takamura, *J. Plasma Fusion Res.* **72**(1996)866 (in Japanese).
- [9] T.Takizuka, *et al.*, “Development of Database for the Divertor Recycling in JT-60U and Its Analysis” *JAERI-Research* 2003-010 (2003) (in Japanese)
- [10] N.Hayashi, *et al.*, *J. Phys. Soc. Japan* **66**(1997)3815.
- [11] M. Sugihara, *et al.*, *J. Nucl. Mater.* **241-243**(1997)299-304.
- [12] A. Hatayama, *et al.*, *Nucl. Fusion* **40**(2000)2009, *J. Nucl. Mater.* **290-293**(2001)407.
- [13] Cordey. J. G. *et al.*, *Plasma Phys. And Cont. Fusion* **30**(1988)1625
- [14] S.Takamura, Purazuma Kanetsu Kisoron, Nagoya Daigaku Shuppankai (1986) (in Japanese).

Table 1. Main plasma parameters of EAST[3].

	EAST
R/a (m)	1.97/0.5
κ_{95}/δ_{95} (-)	1.6/0.8
B_t (T)	3.5
I_p (MA)	1
P_{LHCD}/P_{aux} (MW)	3.5/7.5
L_s/L_d (m)	31/4.3

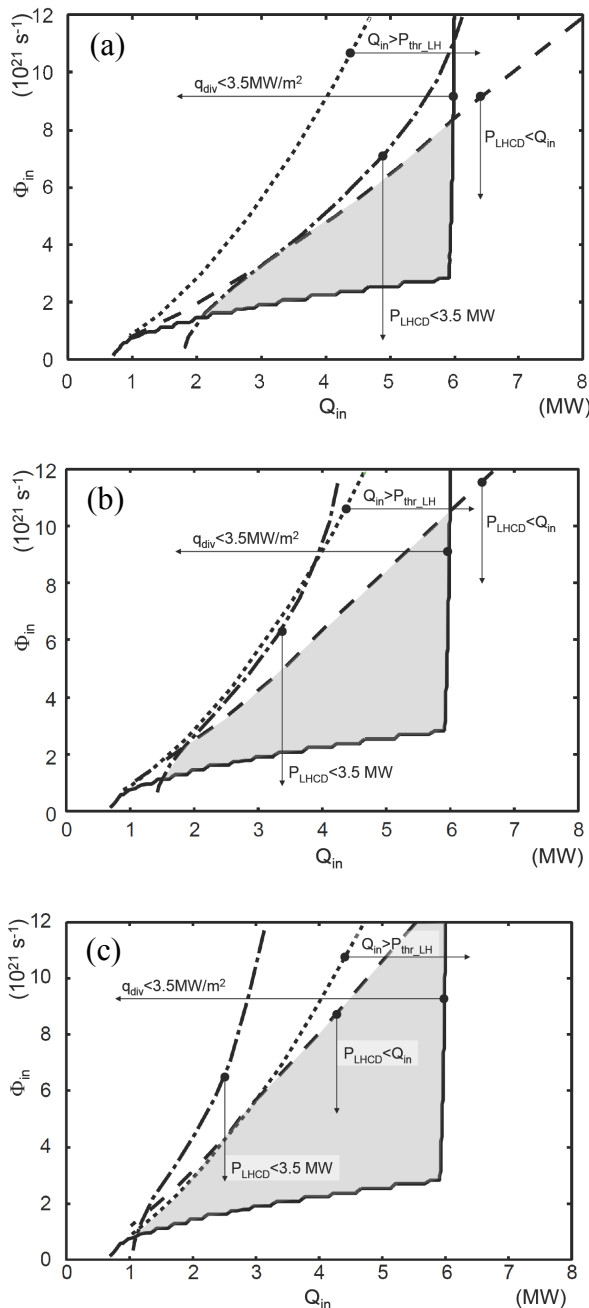


Fig.1 Operational space of LHCD operation and dependence on the fraction of ohmic current fraction f_{ohm} , (a) $f_{\text{ohm}}=0\%$, (b) $f_{\text{ohm}}=30\%$, and (c) $f_{\text{ohm}}=50\%$,

Two dimensional density fluctuation measurements during the non-inductive current ramp-up phase in the compact plasma wall interaction experimental device CPD

H Zushi¹⁾, T Ryoukai²⁾, K Kikukawa²⁾, T Morisaki³⁾, R Bhattacharyay²⁾, T Yoshinaga^{1,3)}, K Hanada¹⁾, T Sakimura²⁾, H Idei¹⁾, K Dono²⁾, N Nishino⁴⁾, H Honma²⁾, S Tashima²⁾, T Mutoh³⁾, S Kubo³⁾, K Nagasaki⁵⁾, M Sakamoto¹⁾, Y Nakashima⁶⁾, Y Higashizono¹⁾, K N Sato¹⁾, K Nakamura¹⁾, M Hasegawa¹⁾, S Kawasaki¹⁾, H Nakashima¹⁾ and A Higashijima¹⁾

¹⁾ RIAM, Kyushu University, Kasuga, Fukuoka, Japan, 816-8580, ²⁾ IGSES, Kyushu University, Kasuga, Fukuoka, Japan, 816-8580, ³⁾ National Institute for Fusion Science, ⁴⁾ Hiroshima University, ⁵⁾ Kyoto University, ⁶⁾ University of Tsukuba,

zushi@triam.kyushu-u.ac.jp

Abstract The two dimensional structure of density fluctuations is examined during the current jump phase indicating a change from the open magnetic fields to the closed ones. During the smooth current ramp-up phase the 2D contour of LiI shows vertically alignment, consistent with the magnetic surfaces. At the inflection point in I_p ramp-up the profile becomes flat and then suddenly a steep gradient and higher intensity regime are formed. According to these changes in the profiles, it is found that within ± 1 ms around the burst of LiI a low frequency coherent wave with a long wavelength rapidly grows. The relations with other signals (magnetic flux and microwave stray power) are discussed.

1. Introduction

Since the inner space of the device is limited physically, one of the important issues for spherical tokamak is to ramp-up plasma current by non-inductive methods. Most popular one is a method with electron cyclotron waves ECW [1-4]. In this method a small vertical field B_z with a positive curvature was superimposed to a toroidal field B_t which corresponded to the cyclotron resonance. The role of B_z on the equilibrium of the plasma in the open magnetic field has been studied and an optimum B_z has been derived by balancing the enhanced end loss along the magnetic field lines intersecting the chamber and reduced $E \times B$ loss by compensating the vertical electric field E induced by the toroidal drift [5, 6]. Density and potential fluctuations [7-9] have been also affected by this B_z , however, no systematic study has been done from the view point of the current ramp-up. In the spherical tokamak device CPD (Compact Plasma wall interaction experimental Device), the non-inductive current drive experiments have been performed using electron cyclotron waves at 8.2 GHz [10, 11] and the characteristics of the density fluctuations during the ramp-up phase have been studied, at least a change in characteristics of the fluctuations near the “current jump” will be presented in this report.

This paper is organized as follows. In section 2, descriptions of CPD device and fluctuation measurement with the sheet lithium beam are given. In section 3, characteristics of fluctuations will be present at the current jump phase. Finally we will conclude the experiments in section 4.

2. Experimental Arrangement

CPD is a spherical tokamak device whose diameter as well as height is ~ 1.2 m [10, 11]. The diameter of the cover of the center stack is 0.27 m. The $B_t = 0.25$ T at R_0 of 0.16 to 0.2 m. $B_z \sim 50$ G at $R = 0.2$ m with the decay index of ~ 0.046 is added by three sets of poloidal field (PF) coils. A set of 8.2 GHz klystrons (8×25 kW, CW) is used for ECH. Linearly polarized microwaves (both Ordinary and eXtraordinary modes) are injected from the low field side. A set of flux loops (45), wounded inside the chamber, is used to reconstruct the last closed flux surface [12]. A thermal Li sheet beam is injected from the bottom of the chamber and the 2D images (300×600 mm) of LiI (670.8 nm) intensity for 1 ms are taken at every 40 ms and spatial resolution is 1 mm^2 . They can be converted to the density profile [13]. Two dimensional profile of $n_e(r, z)$ is obtained by interpolation of data along the sheet Li beam paths [14-16]. In addition, the fluctuation measurement is performed by a LBFS system consists of 50 spatial points, connected to photomultiplier tubes via a fiber bundle (10×10) [17]. Fluctuations of LiI intensity are proportional to the local density fluctuations, $\tilde{n}_e/n_e = \tilde{I}_{Li}/I_{Li}$. The viewed area is $50 \text{ mm} \times 25 \text{ mm}$ within the 2D CCD image in an R-Z plane. The radial resolution of each fiber is $\sim 5 \text{ mm}$. Sampling frequency of analog to digital convertor is 300 kHz. The flat frequency band of the amplifier extends to 500 kHz. LBFS

measures local and long wavelength ($k_{\perp}\rho_s < 1$) density fluctuations, where k_{\perp} and ρ_s are wave number perpendicular to the magnetic field and the ion Larmor radius evaluated at T_e , respectively. Cross correlation and cross power spectrum between each 50 signals are analyzed by fast Fourier transform technique. The line averaged density is measured along the vertical chord at $R=0.3$ m by an interferometer at 140 GHz. The scattered stray microwave components reflected at a cutoff layer or from the chamber are monitored by diode detectors at three different locations around the torus. The sampling frequency is 1MHz. Both O and X-waves reflected from the cutoff layer are also measured with a reflectometer located above the mid plane by 0.2 m at the 160° from the RF injection port. T_e is measured by a scanning Langmuir probe in the shadow of the poloidal limiter. A set of two probes separated by an insulator is used to monitor the floating potentials and the existence of the energetic electrons [12]. Typical plasma discharge is shown in Fig.1. In these experiments RF power is ramped up. The small RF power (~ 1 kW) was applied at $t=0.1$ s and both B_t and B_z were raised. At ~ 0.16 s R_{res} appeared inside the chamber and slab plasma was formed at $R \sim R_{\text{res}}$ until $t=0.2$ s, as shown in Fig. 2 (b). Smooth signal of stray power before the plasma formation started to fluctuate at 0.16 s. Since at $t=0.2$ s both B_t and B_z reached to steady values, RF power was ramp-up at a rate of 1 MW/s. Then I_p was driven with increasing P_{rf} . However, at ~ 0.22 s it suddenly jumped up from 0.7 kA to ~ 2 kA within a few ms. Although P_{rf} continued to raise, I_p was remained ~ 1.6 kA. At the current jump bursts were recorded on several signals; LiI intensity (b) and flux loop signal (c), stray power and H_{α} viewing CS, (not shown).

3. Characteristics of Density Fluctuations during Current Ramp-up phase

The waveform of plasma parameters are shown in the expanded time scale in Fig. 2. The time derivative of I_p changes at ~ 0.218 s, which corresponds to generation of the loop voltage of ~ -10 mV. As I_p grows, negative V_{loop} increases further and reaches to ~ -30 mV at ~ 0.2195 s, suggesting that a return current flows near the CS. After that it reduces to ~ -5 mV within 0.5 ms. This phase lasts for 1 ms and V_{loop} also shows large amplitude of fluctuation. The burst of LiI occurs at 0.212 s and quickly decays within 1 ms. Hereafter several negative spikes are seen on V_{loop} , indicating instabilities

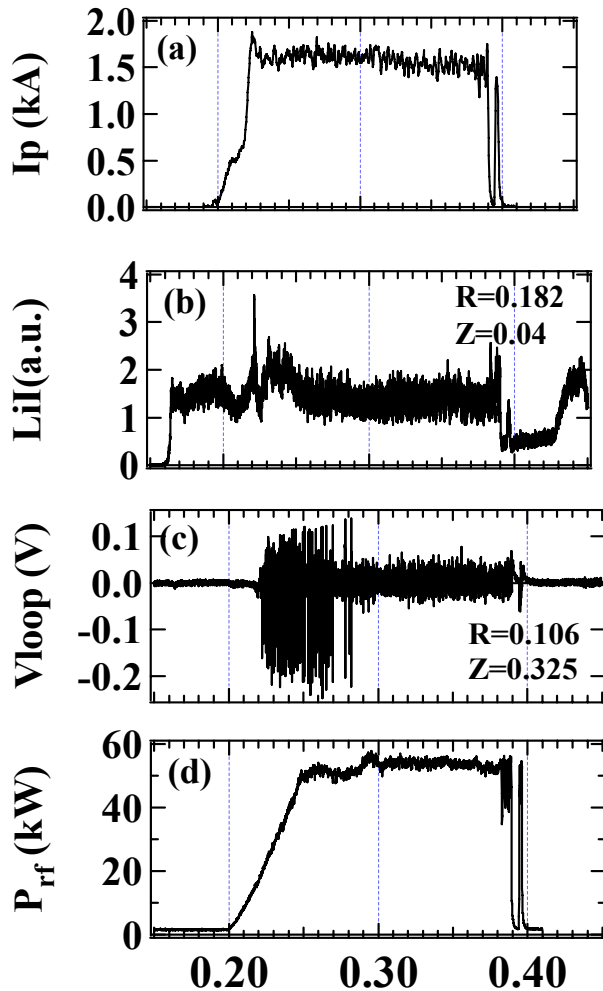


Fig.1 Waveform of plasma parameters in typical discharge(508279); (a) I_p , (b) V_{loop} , (c) LiI at $R < R_{\text{res}}$ and (d) stray power. At $t \sim 0.22$ s “current jump” occurs. Before $t=0.2$ s low power RF is injected to produce a slab plasma.

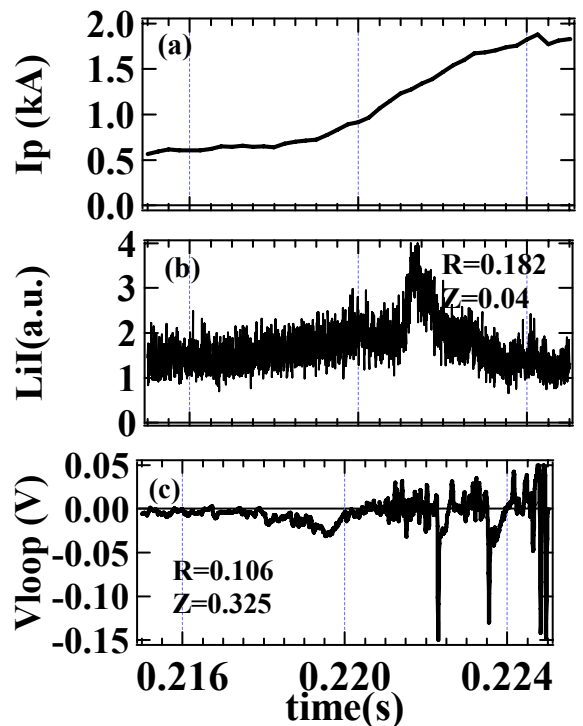


Fig. 2 (a) I_p , (b) LiI , and (c) V_{loop}

preventing from further rise of I_p .

Since LiI measured by LBFS is proportional to the local value of n_e and injected lithium density, the contour of LiI represents the contour of $n_e(R, Z)$ if complicated Li beam attenuation within 25 mm along the Z direction can be ignored. Thus rapid evolution of $n_e(R, Z)$ is deduced. Figure 3 shows the time sliced contour of LiI(R, Z) integrated over 0.1 ms during the current jump phase. Figure 3 (a) – (c) are characterized by the vertically aligned contour in the left region and slightly inclined lines in the right region. This aspect is similar to the magnetic flux contour [11, 12]. The density gradient is deduced to be positive in this area. R_{res} locates at the middle of the figure. It is worth noting that density flattening occurs at Fig. 3(d) ($t=0.2209-0.221s$). When LiI grows rapidly, the contour tends to be modified from the top-right portion (Fig.3 (e)), and then strong gradient is formed along the R direction (Fig.3 (f)). This phase corresponds to the peak of the burst. As the intensity starts to decay, higher intensity portion moves from the right to left, and finally the contour of the intensity aligns along the R direction and the density gradient is formed vertically (minor radius direction), as shown in Fig. 3 (h)-(i). As it is well known that magnetic surfaces inside the last closed surfaces are difficult to be determined only by flux loop signals, the LBFS system offers some information of the dynamic process of

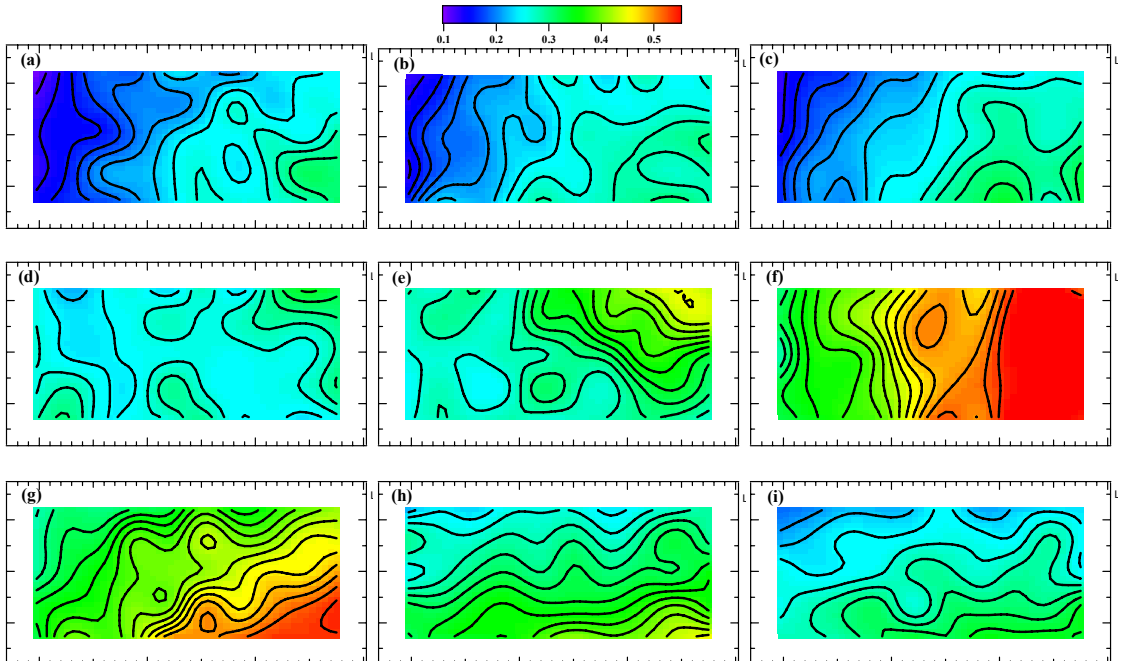


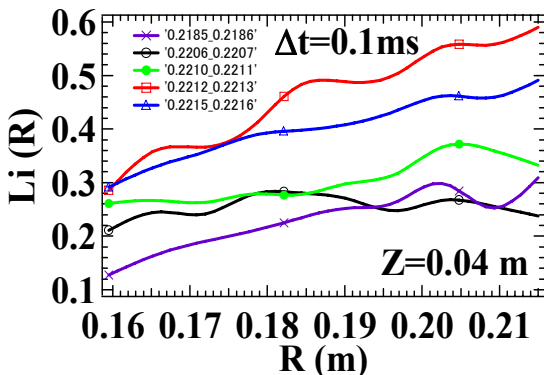
Fig. 3 Time sliced LiI contours at $t= 0.218s$ (a), $0.219s$ (b), $0.2195s$ (c), $0.2209s$ (d), $0.221s$ (e), $0.2212s$ (f), $0.2215s$ (g), $0.2218s$ (h), and $0.222 s$ (i). Averaging time is 0.1 ms. Color chart indicates the intensity of LiI. The viewing area is $R=159-215$ mm and $Z=27-52$ mm.

the current jump. Figure 4 shows the Li intensity profiles at $Z=0.04$ m corresponding to Fig.3. At $t\sim 0.2206$ s

(around Fig.3 (c)) an initial steep profile ($t=0.185$ s) becomes reduced and then it becomes very steep within 0.5 ms.

The fluctuations of the LiI are also analyzed during this phase. Since sampling time is 3.3 μ s, a time window of 2 ms and 1024 points are chosen to obtain the ensemble averaged spectrum. The results are shown in Fig. 5. Square coherency at $f= 1.17$ kHz are shown at several times. Figure 5 (a)-(c) ($t= 0.212s - 0.218s \pm 1$ ms) shows short wavelength modes or no clear correlation with respect to the density profiles (Fig. 3 (a)-(c)). During $t= 0.219-0.222$ s this mode becomes highly coherent and dominates the whole region. The correlation length becomes at least > 50 mm. After the

Fig.4 Li(R) at $Z=0.04$ m from $t=0.2185$ s to 0.2215 s.



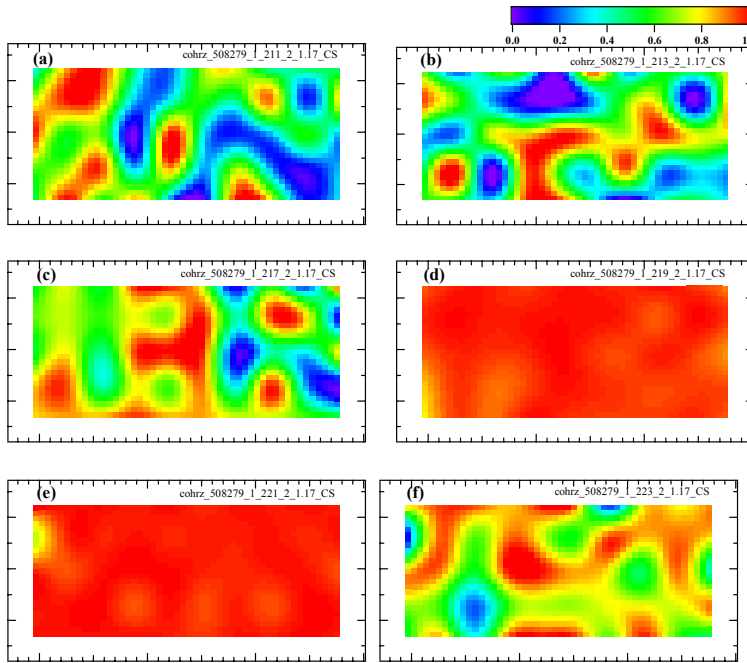


Fig. 5 Spatial contour of γ^2 at 0.212s, 0.214s, 0.218s, 0.220s, 0.222s, 0.224s from top-left to right-bottom during the current jump. Time window is ± 1 ms. The viewing area is $R=159 - 215$ mm and $Z=27 - 52$ mm.

contour of LiI shows a change from vertical alignment to the horizontal one within ± 1 ms around the burst of LiI. The fluctuations at ~ 1 kHz are found to grow rapidly and its correlation length becomes at least more than 50 mm at the current jump.

Acknowledgments

This work is performed with the support and under the auspices of the NIFS Collaboration Research Program (NIFS07KOAR009, NIFS05KUTR012). This work was also partially supported by the JSPS-CAS Core-University program in the field of 'Plasma and Nuclear Fusion'.

References

- [1] Forrest C B, et al., 1992 PRL **68** 3559.
- [2] Forrest C B, et al., 1994 Phys. Plasmas **1** 1568.
- [3] Maekawa T, et al., 2005 NF **45** 1439.
- [4] Yoshinaga T, et al., 2006 PRL **96** 125005.
- [5] Nakao S, et al., 1983 Physics Letters **96A** 405
- [6] Muller S H, et al., 2004 Phys. Rev. Lett. **93** 165003
- [7] Lemoine N, Gresillon D 2005 Phys. Plasma **12** 092301
- [8] Sharma P K, et al., 1997 PPCF **39** 1669.
- [9] Sharma P K, et al., 1995 PPCF **37** 1003.
- [10] Yoshinaga T, et al., 2008 22nd IAEA FEC EX/W
- [11] Yoshinaga T, et al., 14th Int. Congress on Plasma Phys., Fukuoka (2008)
- [12] Yoshinaga T, et al., 2007 NF **47** 210
- [13] Huber A, Samm U, Schweer B, and Mertens Ph, 2005 PPCF **47**, 409
- [14] Zushi H, et al., 2007 J. Nucl. Mater. **363**, 1429 ()
- [15] Bhattacharyay R, et al., 2008 POP **15**, 022504 ()
- [16] Kikukawa T, et al., 2008 J. PFR **3**, 010 ()

closed flux surfaces are established this mode disappears or spatial structure becomes similar to those in the open field configuration. By comparison with the magnetic fluctuations on flux loop signals, this low frequency mode correlates each other and may play an important role to trigger the magnetic reconnection.

5. Conclusion

The 2 D structure of density fluctuations has been measured with LBFS in initial annulus rf plasma which has been produced by ECR at small power. The equi-intensity contour is observed to be aligned along the vertical direction and coherent waves are found to be excited in the low frequency range (1-10 kHz). It should be noted that the vertical field, which is pre-required for ramp-up plasma current, stabilizes these coherent waves. The relative amplitude is reduced by a factor of 2 and the correlation length is reduced < 5 mm. With increasing RF power the plasma expands towards LFS and driven current increases. The 2D

[17] Ryoukai T, et al., 14th Int. Congress on Plasma Phys., Fukuoka (2008)

Recent Progress of the HL-2A Laser Interferometer

Y.Zhou Z.C. Deng J. Yi Y. G. Li L.C.Li L.Zheng
K.J.Zhao Q.W.Yang X. T. Ding

Southwestern Institute of Physics, Chengdu, 610041, China

Abstract

A new multi-channel FIR laser interferometer has been constructed and applied on HL-2A. The unique feature of this real-time heterodyne interferometer is the combination of high power radiation source(300mW), high response room temperature detector(noise temperature of <6000K) and good space resolution(7cm). Optimization of various parameters for maximum laser output power is discussed. Zero crossings of the signals are counted with FPGA digital circuitry yielding fringe resolution of 1/100. The new measured results including density fluctuations is also present.

Keywords: FIR interferometer, measurement, density fluctuation

PACS: 52.35.-g, 52.55.Fa, 52.55.Dy

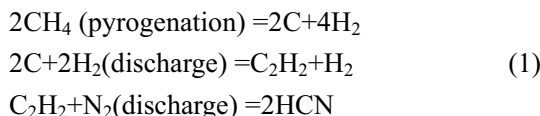
1 Introduction

The electron density is a fundamental parameter to be measured in tokamak plasma. Interferometers operating in the wavelength region of infrared or far infrared have been regarded as a basic diagnostic tool for the measurement of plasma electron density in tokamak¹⁻⁵. Though interferometer technique has been developed for many years, there are many problems to be resolved such as how to increase measurement precision and reliability, estimation of the lifetime and performance of the in-vessel optical element, etc.

On HL-2A tokamak($R=1.64\text{m}$, $a=0.4\text{m}$, $I_p=480\text{kA}$), the maximum electron density is about 10^{20} m^{-3} . Considering of the mechanical stability of the interferometer, the beam refraction caused by the plasma density gradient, HCN laser at $337\mu\text{m}$ is used for diagnosis density on HL-2A. In this paper the new multi-channel interferometer implementation with various improvements is described in detail. Some new experimental results of the interferometer are also presented.

2 HCN laser work parameter optimization

As we know, good signal with higher signal-to-noise ratio can be obtained by high power optical resource in an interferometer. Generation of HCN laser out put power depends on geometry and work parameters. According to the Belland scaling law⁶, the HCN laser tube is designed with inner diameter of 68 mm, discharge length of 5.6 m and straightness accuracy of 0.5‰ per meter⁷ respectively. The laser cavity is formed with two flat reflectors, one being gilded glass mirror, and the other being inductive nickel mesh. The HCN laser work principle is described from the following chemistry equations.



A mixed gas of CH_4 , N_2 and He ($\text{N}_2:\text{CH}_4:\text{He}=8.8\%:22.8\%:68.4\%$) is used to obtain the laser oscillation. Meanwhile extra He is added to stabilize the discharge. Because mixed gas is consumed during discharge, work gas should be puffed into the laser tube continuously. Two flow meters measure and control gas flow rates of mixed gas and He.

Figure1 shows typical output characteristics for the rate of the gas mixture under different mesh parameters. The laser output power depends strongly on gas flow rates and laser output

couple coefficient. The output power increase by the increasing of the mixture gas flow rate and saturates when the flow rate at the optimal value. This optimal value is different from different mesh parameter. In our experiment, the optimal output power is obtained by 400lpi (lines per inch) mesh, corresponding laser output couple coefficient is 14%.

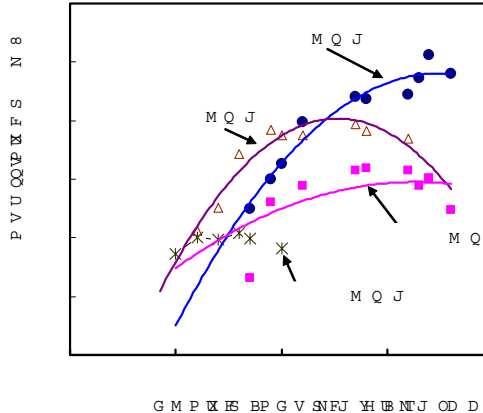


Fig.1 laser output power as a function of flow rate of mixed gas.

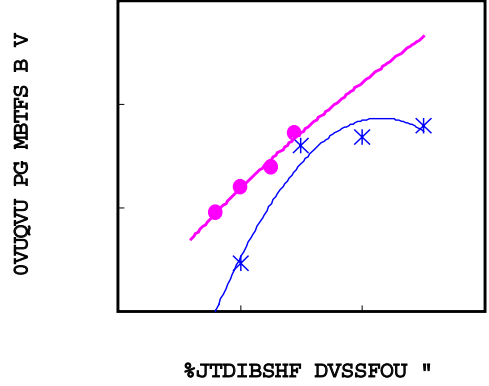


Fig.2 laser output power vs. discharge current by used LaB₆(dot) and Ta(star).

In order to ensure a stable glow discharge, hot cathodes of LaB₆ and Ta are used for our laser system. Fig.2 shows the experiment result compared two kinds of cathodes. As LaB₆ has high electron emission capability, the output power with LaB₆ is higher than power with Ta under the same discharge current. LaB₆ is poisoned by metal easily, a graphite coat is used to support the cathode. Glow discharge makes the graphite material deposited on the laser tube and discharge become unstable. So in order to control discharge stable for long time (8h/day), Ta cathode is used for higher current discharge. Up to now, the output power of the laser is over 300mW with discharge current of 1.5A and voltage of 6.7kV.

3 Detectors

We employ room temperature deuterated L-lanine doped triglycine sulfate (DLATGS) detectors (Selex Sensors and Airborne System Infrared Ltd, type P5243) for both the reference and probe signals. These detectors give a response (responsivity $\sim 400\text{mV/mW}$, noise equivalent power (NEP) $\sim 6 \times 10^{-10} \text{ W}/\sqrt{\text{Hz}}$) at 337 μm when beat signal frequency is 10 kHz. As optical beam adjustment error and transmission loss, sometimes the signal-to-noise rate of ch8 is low with DLATGS. So another new high response room temperature waveguide detector (Shottky Diode Detector, noise temperature $< 6000\text{k}$, video responsivity $\sim 400\text{mV/mW}$) has been applied. In this new kind of Shottky detector, a circular feed horn waveguide is as an antenna to replace the usual corner cube, and a DC-bias applies for the diode to achieve the lowest conversion loss. The optical beam receiving efficiency is improved. Fig.3 shows the new detector configuration and work sketch map. Compared result of ch8 beat signal by DLATGS and waveguide detector confirms that with new Shottky detector the signal becomes very clear and the SNR has been improved about 2-4 times.

4 Data acquisition and processing system

Usually a multi-channel phase comparator can be applied to realize density real-time measurement. The signal from detector is transmitted to a pre-amplifier and a band pass filter with

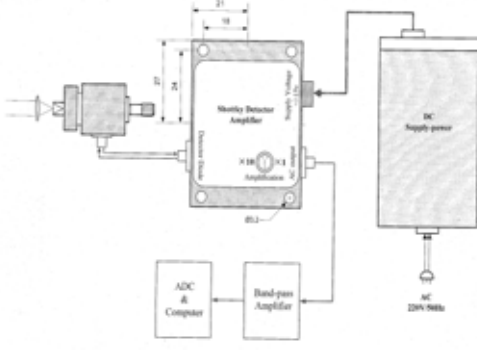


Fig.3 New Shottky detector with circular feed waveguide system.

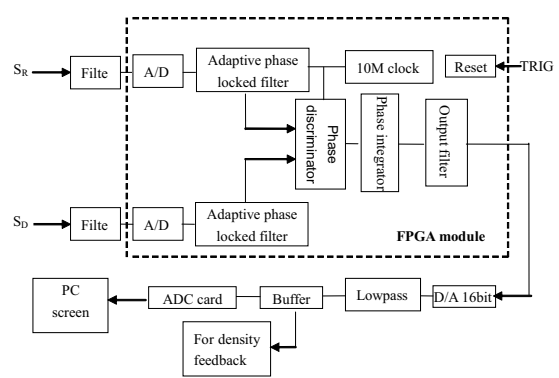


Fig.4. Flow diagram of data acquisition system by FPGA module.

bandwidth of 30%-40% center frequency. At the present experiment, the signal frequency is 10 kHz, and the bandwidth of amplifier is $10 \text{ kHz} \pm 2 \text{ kHz}$. Two different phase compared methods are employed in our experiment. One is software comparator: the waveform of beat signals from both reference beam and probe beam will be recorded by ADC collection card DAQ2010 and memorized in a computer. The zero crossing position of waveform is located and the phase shift between reference and probe signal is accounted by software. The other one is real-time digital signal processor by FPGA technique. Combined with the advantage of software and hardware phase comparator, the FPGA technique is characterized by high reliability, easy modification and low cost. Fig.4 is the flow diagram of data acquisition system by FPGA. 10 Mega Hz clock and 16 bit A/D and D/A conversion are applied, the phase comparator has an ability to make phase resolution up to $0.1\mu\text{s}$. At present the grating modulation frequency is 10 kHz, so the phase resolution is 1/100 fringe. The delay time of real time phase compared is about 0.2ms. This density signal is satisfied for density feedback control.

5 Experimental results

In order to study density fluctuation in core plasma, Density fluctuations have been first measured in the core region of HL-2A tokamak plasma using a newly developed multi-channel FIR interferometer system. Fig.5 shows the typical line density fluctuation from phase comparator by FPGA technique. The low-frequency oscillations with period roughly 1ms are presented at all the chords signals. A phase delay within each channel location is revealed from line fig.5 (d) ($r=3.5\text{cm}$) to line fig.5 (e) ($r=24.5\text{cm}$). We observe a minimum line density fluctuation appeared in the plasma center (the magnetic axis), and a π -phase change observed on the chord of $r=24.5\text{cm}$ (0.61a). By computing the delay phase between two adjoining chords, one can estimate the mode poloidal rotation speed which is about 1100m/s, and the direction of rotation is in the electron diamagnetic direction.

Using the FFT technique, the frequency power spectrum, averaged over 100ms, for typical chord-averaged data is analyzed. Correlation between different FIR chords (see Fig.6) demonstrate that these fluctuations are highly coherent and in phase across the entire plasma column. By correlating individual interferometer chord with individual poloidal harmonics, which obtained

from a magnetic pick-up coil array, we can extract the density fluctuation associated with the $m=2$ magnetic tearing modes.

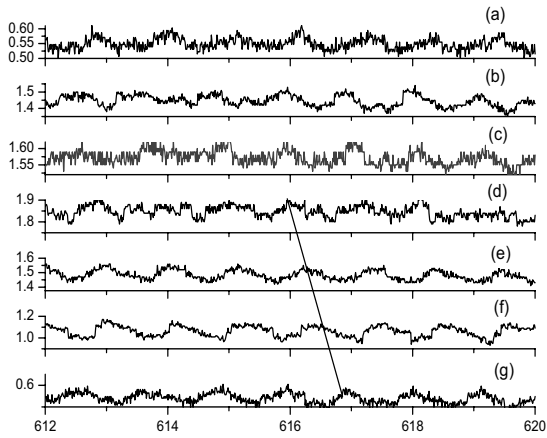


Fig.5 Density fluctuation during MHD oscillation. The line connects maxima showing a time delay from chord to chord.

Acknowledgements

The authors wish to acknowledge and express their appreciation for the contribution of HL-2A team, Dr. K. Kawahata, Dr. W.X.Ding and Dr. X.Gao. This work was supported by the National Natural Science Foundation of China (Grant No.10575030, 10675043), and supported partially by the JSPS-CAS Core University Program in the field of 'Plasma and Nuclear Fusion'.

References

- 1 D.Veron, Infrared and Millimeter Wave (Vol.2, Edited by K.J.Button, Academic Press, New York, 1979)
- 2 D.K.Mansfield,H.K.Park,L.C.Johnson,H.M.Anderson,R.Chouinard,V.S.Foote,C.H.Ma.and B.J.Clifton, Appl. Opt.26,4469-4474(1987)
- 3 Kazuo Kawahata,Kiichiro Haba and Junji Fujita,Rev.Sci.Instrum,60(12)3734(1989)
- 4 K.Kawahata,*et al.*, Rev.Sci.Instrum.75,3508 (2004)
- 5 D.L.Brower,W.X.Ding, S.D.Terry,*et al.*, Rev.Sci.Instrum, 74(3)1534(2003)
- 6 P.Belland, D.Veron and I.B.Whitbourn, J.Phys.D8, 2113(1975)
- 7 Y.Zhou, Z C Deng, Z T Liu, J Yi, Y W Tang, B Y Gao, C L Tian, Y G Li and X T Ding , Rev. Sci. Instrum78,11, 3503(2007)

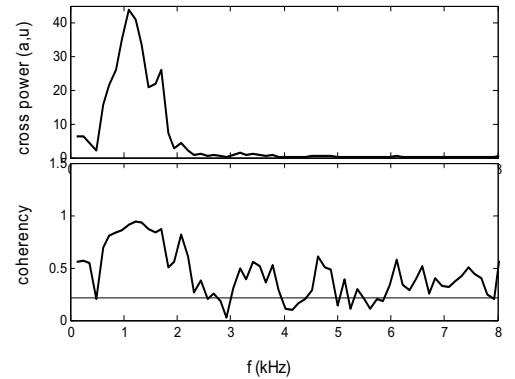


Fig.6 Power spectra and coherency curves for Fig.5 chords($r=17.5\text{cm}$ and 24.5cm).The spectrum is peaked strongly at $f=1.09\text{ kHz}$, corresponding the magnetic probe signal at the same frequency.

Plasma boundary position measurements using frequency sweep microwave reflectometer in LHD

T. Tokuzawa, K. Kawahata, K. Tanaka, Y. Ito, and LHD Experimental Group

National Institute for Fusion Science, Toki 509-5292, Japan

LING Bili

Institute of Plasma Physics, Chinese Academy of Sciences, China

Abstract

In order to measure the plasma boundary position in the high-temperature plasma, the broadband frequency tunable microwave reflectometer system, which has the ability of fast and stable sweeping operation, is applied in the Large Helical Device. When the microwave launches with the extraordinary polarization from the low field side of the magnetic field strength and its frequency is swept from low to high, the microwave of minimum right-hand cut-off frequency is started to reflect at the plasma edge. We can estimate the plasma boundary to measure the change of the reflected power from the cut-off layer. In the plasma experiment, the reflect signal increases according to the sweeping frequency and the information of the plasma edge position can be obtained.

I. INTRODUCTION

The information of the plasma boundary is important for deciding the plasma size and also controlling the plasma position in the magnetized confinement plasma. For this study, the magnetic probe array is installed to the vacuum vessel in several devices. In general, the direct measurement can give more precise information. For example, a fast-scanning Langmuir probe has been utilized the edge plasma measurement in the Large Helical Device (LHD) [1]. However, an electrostatic probe cannot be always put into the high-temperature plasma deeply. Microwave reflectometer has a potential of localized measurement by using the cut-off effect in the plasma core region without any affection.

When the extraordinary wave launches to the plasma from the low field side of the magnetic field strength, the wave is reflected back from the right-hand cut-off layer or left-hand cut-off layer. The right-hand and left-hand cut-off frequencies are described by,

$$f_{right-hand} = \frac{f_{ce}}{2} + \sqrt{f_{pe}^2 + \left(\frac{f_{ce}}{2}\right)^2}, \quad f_{left-hand} = -\frac{f_{ce}}{2} + \sqrt{f_{pe}^2 + \left(\frac{f_{ce}}{2}\right)^2} \quad (1)$$

Here, f_{ce} is the electron cyclotron frequency and f_{pe} is the electron plasma frequency. The radial profile of magnetic field strength decreases according to the major radius in the most of the magnetic plasma confinement device. When the plasma is produced and also the right-hand cut-off layer exists, the microwave with the corresponding frequency is reflected back. In the previous study, the minimum electron density, which the cut-off phenomena is occurred, is defined $1 \times 10^{16} \text{ m}^{-3}$ [2]. In this paper, we use the term “plasma boundary” which is defined as this minimum density layer.

When the launching microwave frequency is lower than the minimum right-hand cut-off frequency or higher than the maximum right-hand cut-off frequency, the launching wave penetrates through the plasma. Figure 1 shows the schematic drawing of the plasma boundary measurement method. The frequency of launching wave sweeps from low to high and the reflected power increases during the cut-off layer exists in the plasma. The frequency component, which the cut-off signal appears at first, is reflected back at the plasma edge and its frequency is quite equal to the electron cyclotron frequency at the position. Usually, we know the radial profile of magnetic field strength by the other diagnostics such as MSE. Therefore, we can get the information about the plasma edge position. In this paper, we describe the frequency sweep microwave reflectometer system in Sec. 2, and present the experimental results in Sec. 3, and show some applications of this measurement in Sec.4, and then we summarize the present results in Sec. 5.

II. EXPERIMENTAL APPARATUS

The schematic of frequency sweep microwave reflectometer system is shown in Fig. 2. A voltage controlled oscillator (VCO), which can sweep the frequency range with 11 - 18.5 GHz and its sweep time can be lower than 10 μ s, is used as a source. The output frequency of VCO is increased linearly by the external controlled signal which is generated by the arbitrary wave generator. The output frequency is changed followed by an active doubler to bring the launching frequency up to 22 - 37 GHz (ka-band). The microwaves launch from the outboard side along inverse the major radius direction on equatorial plane. The polarization of launching wave is set on the

extraordinary mode (X-mode) and the right-hand cut-off layer is used as the reflected surface. The reflected wave is received and mixed with a fixed frequency wave of local oscillator and intermediate frequency (IF) signal is amplified and detected. Then the output signal is led to the data acquisition system. In the edge position measurements of this paper, the fast sampling digital oscilloscope is used for the data acquisition.

III. EXPERIMENTAL RESULTS

Here, we show a preliminary experimental result of this frequency sweeping system for the plasma boundary measurement in the LHD plasma. The experiment is carried out the magnetic axis position is 3.60 m, the axial magnetic field strength is 2.0 T, the averaged electron density is under $0.4 \times 10^{19} \text{ m}^{-3}$, and three tangential neutral beams are injected with constant power. The radial profile of the right-hand cut-off frequency and the electron cyclotron frequency are shown in Fig. 3(a). In this figure the right-hand cut-off frequency is calculated using the assumed electron density profile which is the flat profile. Figure 3(b) shows the cross section of the magnetic surface, the ergodic layer, and also the divertor legs in this plasma experimental condition. When the plasma condition is mostly steady during 20 ms, the source frequency is swept from 22 to 37 GHz linearly. Figure 4(b) shows detector output signal of the frequency sweeping reflectometer. The amplitude increases, when the frequency ramps up and the corresponding cut-off layer exists in the plasma. This critical frequency is around 26.5 GHz and the corresponding radial position is $R \sim 4.9 \text{ m}$ where is just at the X-point.

IV. APPLICATION TO BOUNDARY POSITION SENSOR

For the routinely plasma boundary measurements, the frequency sweeping microwave reflectometer system should be added for a direct reading. There are two types of analyzing technique. One is used the amplitude variation of reflected signal (type 1) and another is used the beat frequency variation (type 2). Figure 5 shows the schematic diagram of type 1 system. In this case, the detector output signal is directly related with the power of reflected microwave. When the amplitude voltage crosses over the threshold value, we know the cut-off start frequency, that is, the plasma boundary position shown as Fig. 6. However, the plasma shape or the plasma perturbation may affect the amplitude of the reflected wave and lead the error of the measurement. On the other hand, the beat frequency of the reflected wave is related with the distance between the reflected surface and antenna. When we measure the frequency variation of the reflected wave, it can be distinguish where the wave is reflected from the opposite wall or the plasma. Figure 7 shows the schematic diagram of type 2 system. The output of frequency-voltage converter (fV) is changed with the variation of reflected position shown as Fig. 8. When the fV output decreases cross the threshold voltage, we know the reflected position moves close to the antenna and then the information of the plasma boundary position can be obtained.

IV. SUMMARY

Frequency sweeping microwave reflectometer system has been installed in the

LHD and performed the plasma boundary position measurement. System utilizes a VCO as a source for the wide range frequency sweep operation and simply heterodyne IF detection is carried out. In the LHD plasma experiment, the launching frequency is swept from low to high and it can be observed the reflected signal from the plasma edge region. The plasma edge position can be estimated at just the X-point in this experimental configuration. This system will apply the position sensor to inform the plasma edge. If some antenna can be installed in the poloidal direction in the vacuum vessel, we will get the information of plasma movement and transformation by correlation analysis in future.

Acknowledgement

This work was partially supported by a Grant-in-Aid for Scientific Research on Priority Areas (Nos.18035015 and 20026010) and a Grant-in-Aid for Young Scientists (A) (No. 18686075) from the Ministry of Education, Culture, Sports, Science and Technology Japan and also a budgetary Grant-in-Aid No. NIFS08ULHH508 of National Institute for Fusion Science. This research is also supported by the JSPS-CAS Core-University Program in the field of “Plasma and Nuclear Fusion”.

References

- [1] S. Masuzaki, T. Morisaki, N. Oyabu *et al.*, Nucl. Fusion **42**, 750 (2002).
- [2] T. Tokuzawa, K. Kawahata, K. Tanaka *et al.*, Rev. Sci. Instrum. **74**, 3, 1506 (2003).

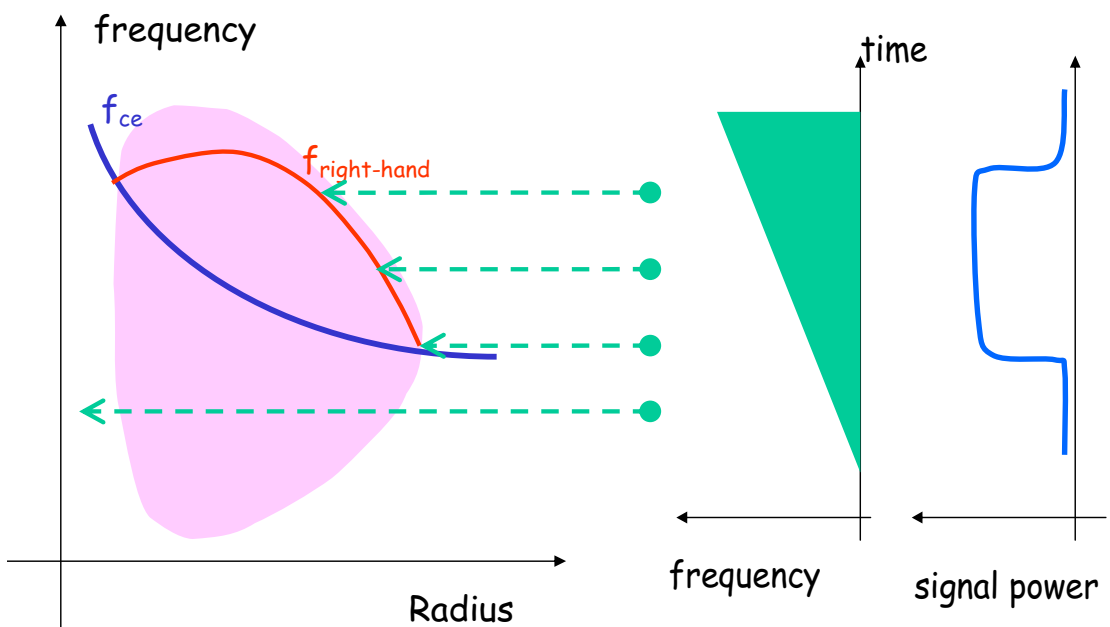


Figure 1 Schematic concepts of the plasma boundary measurement method. When the launching frequency is sweeping, the reflectometer signal power increases during the corresponding cut-off layer exist in the plasma.

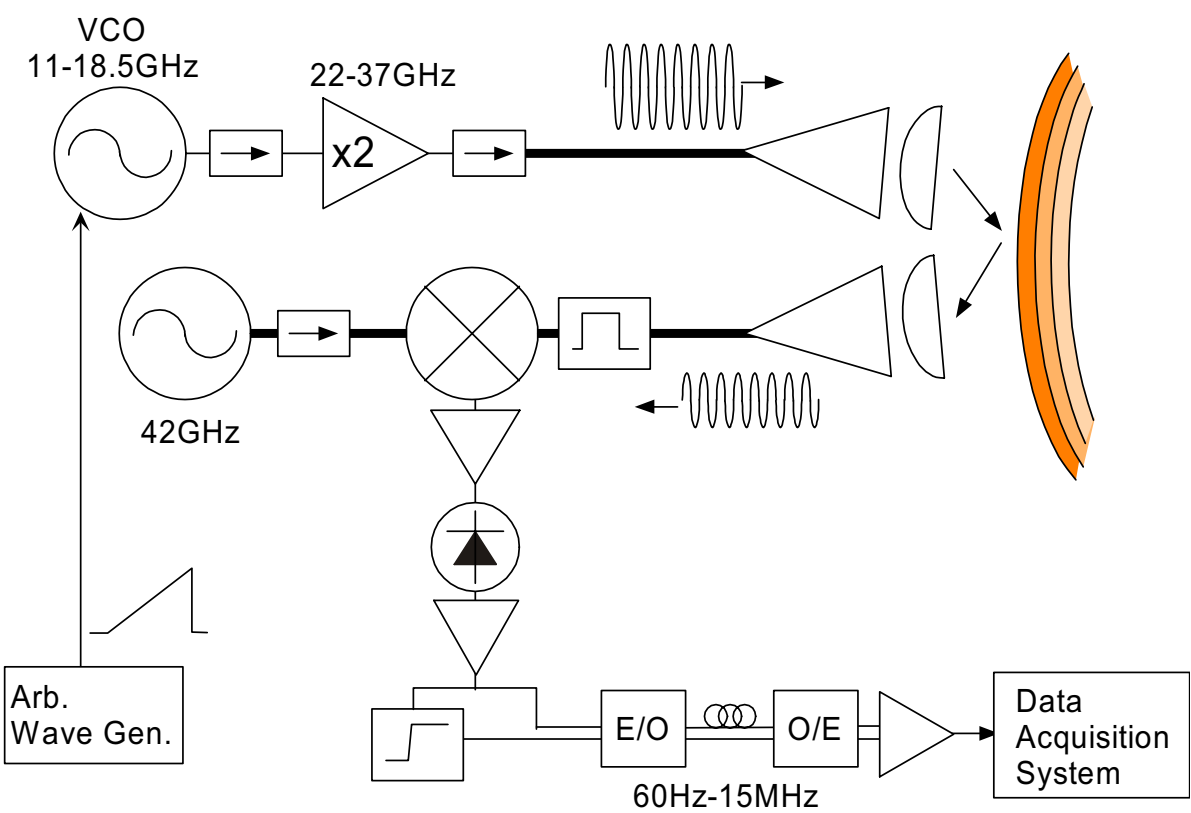


Figure 2 Schematic view of the frequency sweep microwave reflectometer system.

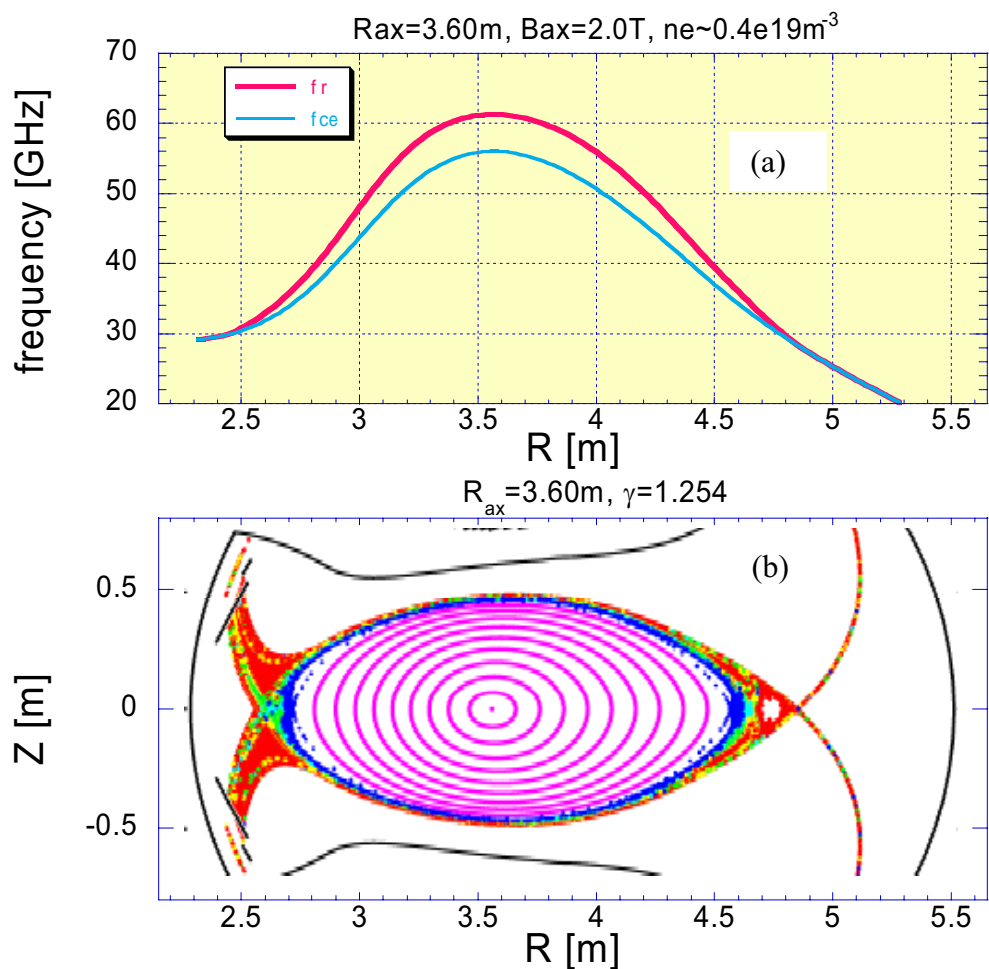


Figure 3 (a) Radial profile of the right-hand cut-off frequency (red) and electron cyclotron frequency (blue). (b) Cross section of the magnetic surface, ergodic layer, and divertor legs.

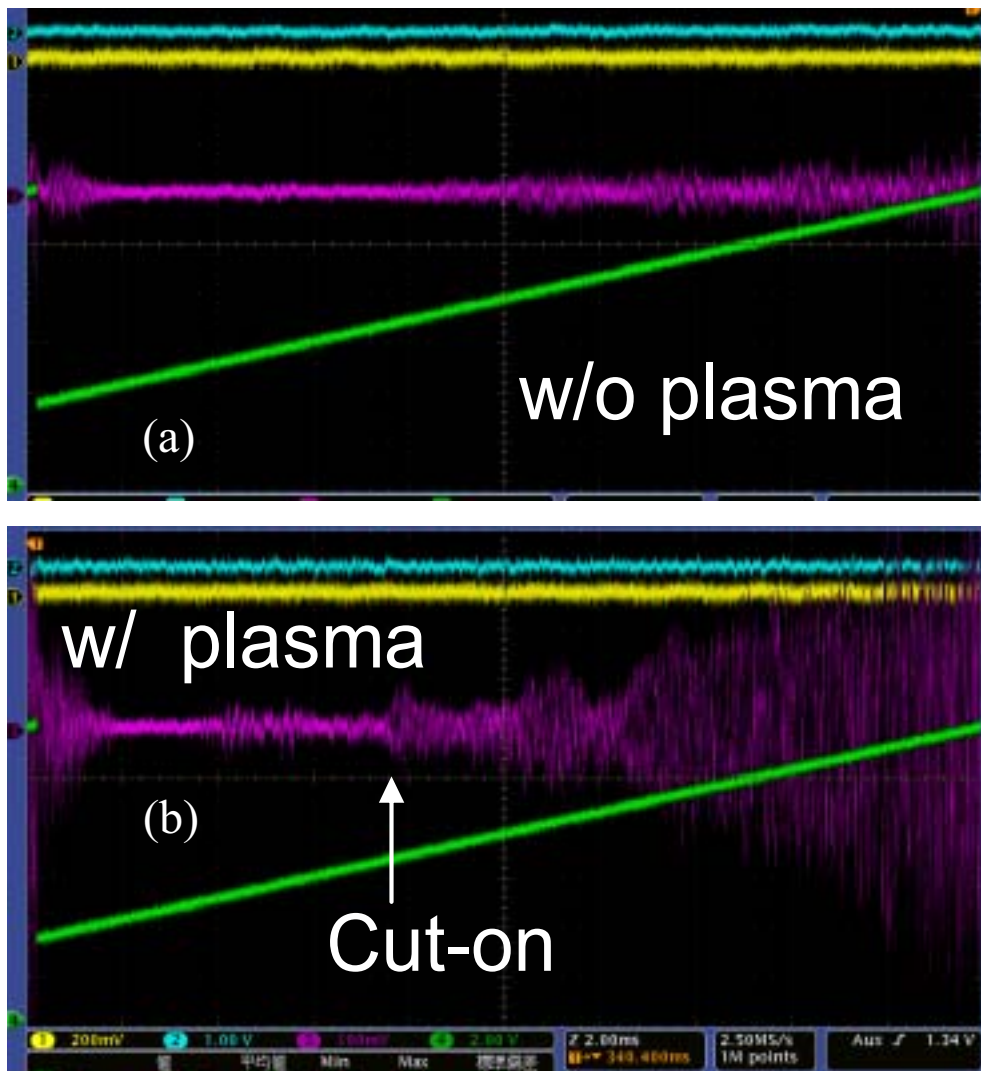


Figure 4 Detector output signal (purple line) of frequency sweeping reflectometer (a) without plasma case, and (b) with plasma discharge case. Green line means the frequency sweeps from low to high. After “Cut-on”, the reflectometer signal increases. Here, just before “Cut-on”, the signal is slightly perturbed with low frequency and it is a noise.

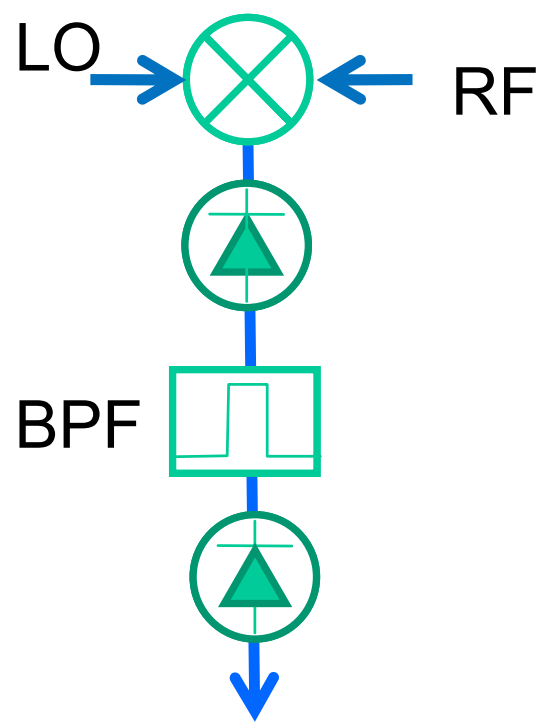


Figure 5 Schematic Diagram of type 1 of plasma boundary measurement system. This system uses the amplitude variation of reflected signal.

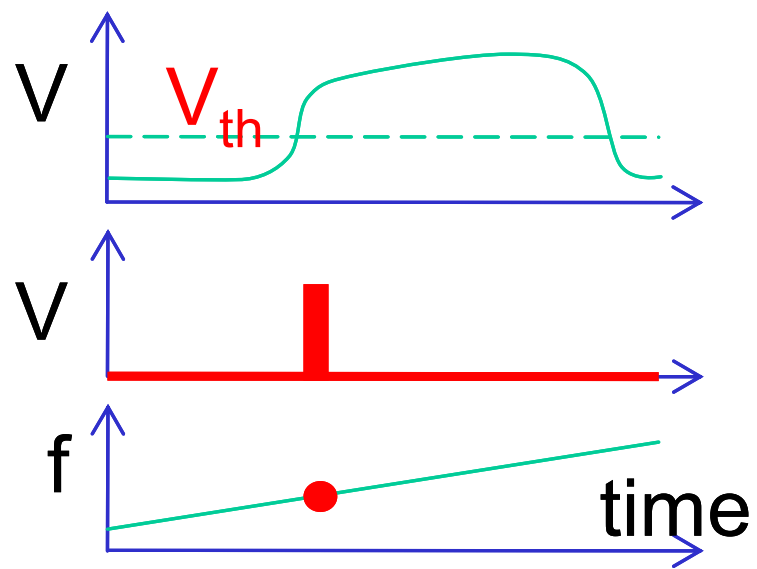


Figure 6 Schematic drawing of the output signal. Temporal behavior of detector output signal (top). When the output signal increases and crosses over the threshold voltage, the timing signal is outputted.

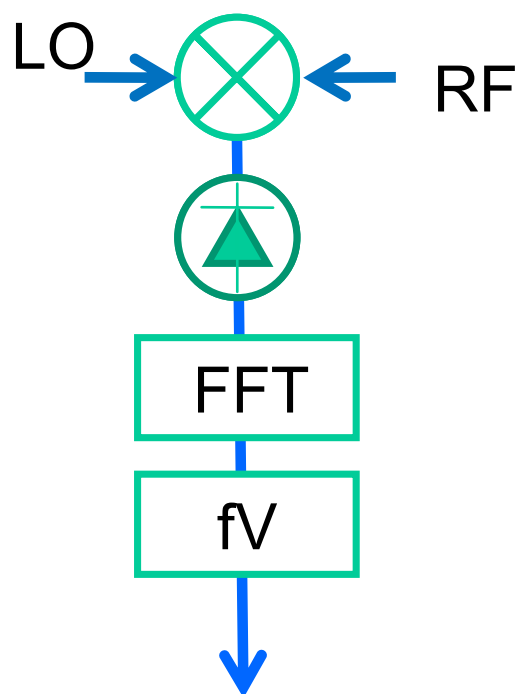


Figure 7 Schematic Diagram of type 2 of plasma boundary measurement system. This system uses the frequency variation of reflected signal.

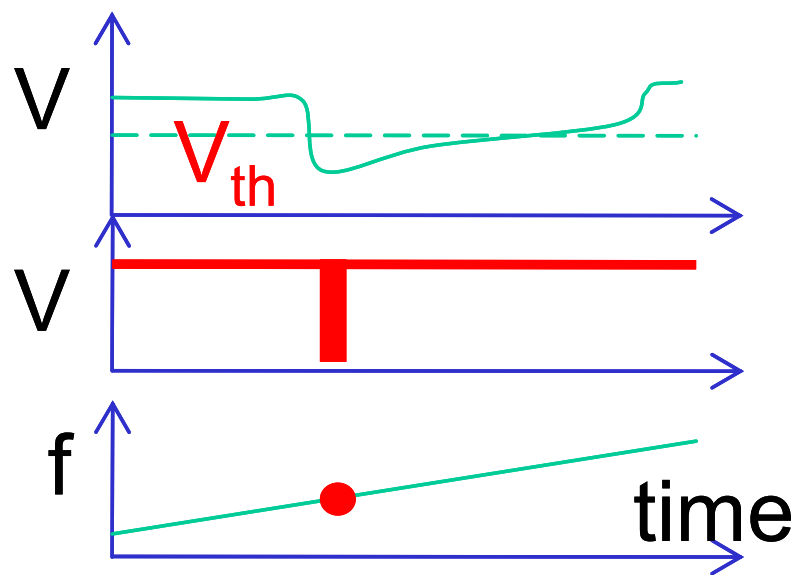


Figure 8 Schematic drawing of the output signal. Temporal behavior of frequency-voltage converter (fV) output signal (top). When the output signal decreases and crosses the threshold voltage, the timing signal is outputted.

Experimental progress on the EAST superconductor tokamak

L.Q.Hu for EAST team

Institute of Plasma Physics, Chinese Academy of Sciences
PO Box 1126, Hefei, Anhui 230031, People's Republic of China

EAST as a full superconducting tokamak is aimed for long pulse (60-1000s) high performance operation, which requires specific in-vessel structures and PFCs. It should be capable to handle the particle and heat fluxes through the plasma boundary to the wall in a variety of operation scenarios under steady-state condition, as well as to protect vacuum vessel and other components such as magnetic sensors, internal cryo-pump etc from direct plasma interaction. The geometry is designed as top-bottom symmetry to accommodate both double null or single null divertor configuration. The in-vessel structure is a complicated integration of multi-systems, including the fully actively water cooled PFCs and their supporting structures, a full set of magnetic inductive sensors for machine operation and plasma control, the divertor cryopump, the actively water cooled internal coils for vertical stabilization control, divertor probe arrays, baking system and thermal coupler etc. In the first stage of the machine operation, total heating and current drive power will be about 8~10MW. But peak heat flux will not be more than 3.6MW/m^2 on the divertor plates from the B2-Eirene simulation based on typical EAST operation scenario. All plasma facing surface are one kind of multi-element doped graphite materials. Two gaps between inner, outer target and dome were provided with total $180\text{m}^3/\text{s}$ gas conductance for particle and impurity exhaust by cryopump. The passive stabilizer is placed on the outer radius of the plasma above and below midplane. The 4 DC glow discharge anodes and 2 RF conditioning antenna were also installed for wall conditioning. The thermal couplers are embed in the graphite titles of the liner, limiter and diverter plates for machine operation and wall conditioning. Two movable molybdenum limiters have been installed, which allow radial movement from 2.26m to 2.42m.

More than twenty diagnostics were employed for machine operation, plasma control and physics analysis, including magnetic measurement, Langmuir probe and mach probe, laser interferometer for line integrated density and density feedback control, visible CCD camera. Those diagnostics presently can provide measurements of electron/ion temperatures, surface temperature of the liner or diverter plates, radiation power, and information of soft-X ray, visible to near UV radiation of impurities, $\text{H}\alpha$ radiation etc. Hard-X ray and neutron flux measurements are also available for LHCD experiments and monitoring runaway electrons. Plasma discharges are controlled by a plasma control system (PCS) built in collaboration with GA, which is similar to the PCS of DIII-D, but with new EAST features such as the coil current ramping rate limitations due to the eddy current heating on the

superconducting cables, IC power supply command algorithms, etc. The RF systems at ICRF with 1.5MW, 30~110MHZ and at LHF with 2MW, 2.45GHz are available for heating and current drive experiments as well as wall conditioning and discharge pre-ionization.

EAST has new features compared to conventional tokamak and also those tokamaks only with the toroidal superconducting coils. These issues, particularly, the limitation of current ramping rate in PF coils, relative weak coupling between plasma and PF coils, PF field penetration through the vacuum vessel and thermal shielding into the plasma etc affecting the machine operation have been discussed elsewhere. The graphite wall with the vacuum chamber was baked up to nearly 300°C and 200°C continuously for about 10 days before the plasma discharges. However burn through mainly caused by out-gassing from the graphite tiles caused difficulty for the further current ramping up after break down. To achieve reliable break down and plasma current ramping up, the machine was boronized by RF discharge, which was used as routine wall conditioning in HT-7. The working gas was hydrogen in 2007 and then switched to deuterium in recently campaign. The experiments have firstly performed using pre-programming shape control (elongation and divertor) and feedback control for plasma position and current with the (copper) internal control coils (ICs) for vertical stabilization. The principal goal of this experiment was achieved with the appearance of stably controlled diverted plasmas with sufficient elongations and triangularities. The full equilibrium reconstruction both by EFIT (GA) and IPPEQ (ASIPP) identified the following configurations: double null configuration with $\kappa=1.9$ and $\delta=0.50$; top or bottom single null configurations with $\kappa=1.7$ and $\delta=0.64$, which almost covers all designed configuration in EAST. The discharges with plasma current ranged from 0.2~0.6MA, toroidal magnetic field from 2~3T show the confinement consistent with Neo-Alcator scaling for ohmic plasmas. Experiments provide the basis for algorithm development and optimization of real time control of plasma shape. The full reconstruction of the equilibrium has been performed by using EFIT code routinely between shots. This kind of reconstruction was made to be real-time (RTEFIT) and sufficiently fast for the real-time shape control in DIII-D by using a fast loop and a slow loop calculations on separate CPUs. While RTEFIT has been done at a control cycle, the control reference points was determined at first. Under the collaboration with DIII-D, EAST also adapted DIII-D plasma control software system. RTEFIT/ISOFLUX was primarily realized on EAST in 2008 summer campaign. The RF powers were applied in several aspects. The LHW was used for current drive both in sustaining plasma discharges and assisting the plasma start-up. The ICRF was mainly applied for pre-ionization for reliable plasma start-up and wall conditioning. Most of these experiments were performed by pre-programming control of plasma shape and feedback control of RZIp. The plasma shape and position were optimized to maximize the wave coupling into the plasma. Nearly 0.8MW LHW has been successfully delivered, from what about 0.65MW power has been coupled into the plasma. This power can almost sustain a fully non-inductive plasma discharge at $I_p=250\text{kA}$ and line averaged density of $\sim 1.5\times 10^{19}\text{m}^{-3}$. The current driving efficiency estimated from power scanning under this

condition is about $0.8 \times 10^{19} \text{ Am}^{-2}\text{W}^{-1}$. It is double higher than the LHCD efficiency obtained in HT-7, but smaller than that in tore-supra mainly due to the lower volume averaged electron temperature in present experiments. The plasma discharges can be sustained over 20 seconds in such operation scenarios, which were mainly limited by unstable coupling due to pre-programming shape control and the power supply stability of klystrons inside the LHCD system.

The primary achievements, particularly, the experiences from last two years provide us confidence that the highly shaped plasma with relevant performance could be sustained by RF powers for long duration, although significant improvements are needed for reliable machine operation and effective experiments. Except that a 2MW lower hybrid current drive system at 2.45GHz and a 1.5MW ICRF system at 30-110MHz are in operation presently, a new 4.5MW ICRF system at 25-70MHz will be available in 2009. The present LHCD system is planed to be upgraded to 4MW, where existing klystron of 100kW will be replaced by new klystron of 200kW. Capability of corresponding power supplies and water cooling etc will be expanded within next 2 years. The total heating and current drive power will be 10MW before end of 2010. This power is much higher than the H-mode threshold, which is about 4MW for standard EAST operation scenario at 1MA plasma current and toroidal field strength of 3.5T. The flexibilities of heating scenarios and current drive in controlling current density profile provide the possibilities to operate EAST in high performance regime with edge and/or internal transport barrier. A new proposal for a 4MW LHCD system at 4.6GHz and a 2~4MW neutral beam injection system at 50~80keV will be funded for next 4 years.

In the next two years, diagnostics on EAST will provide measurements of all key profiles, which include Thomson scattering for density and electron temperature, charge exchange recombination spectroscopy based on a diagnostic beam for ion temperature and rotation, bolometry for radiation power, X-ray crystal spectroscopy for ion/electron temperature, multi-channel ECE or 2D ECE image for electron temperature and fluctuation, visible bremsstrahlung for effective charge number, multi-channel DCN laser interferometer for density, HX-ray arrays for LHCD, neutral particle analyzer (NPA) for energetic particles, optical and spectroscopic diagnostics for impurity, etc. Some of them will be built via international collaboration. These diagnostics should be sufficient to describe the basic plasma performance and for integrated modeling and data analysis.

Acknowledgments

All contents in this summary report come from overview report OV_3-4 of Professor Baonian Wan in 22nd IAEA Fusion Energy Conference, 13-18 October 2008, Geneva, Switzerland. Herein, the author Dr. Liqun HU wants express his special thanks to Prof. Baonian Wan for his permission to copy contents of his overview report to produce this report. The author would like to be very grateful to all members of EAST team, and to all attendee from other domestic and international facilities for their contribution to significant progress of the EAST experiment. This work was partially supported by the JSPS-CAS Core-University program in the field of 'Plasma and Nuclear Fusion'.

Data Processing of Divertor Probes on EAST *

WANG Jun(王俊), CHANG Jiafeng(常加峰), XU Guosheng(徐国盛), ZHANG Wei(张炜),
MING Tingfeng(明廷凤), DING Siye(丁斯晔), HU Liqun(胡立群), GAO Xiang(高翔)

Institute of Plasma Physics, Chinese Academy of Sciences, Hefei, 230031, China

E-mail: jwang@ipp.ac.cn

Abstract The divertor hydrogen plasma has been achieved in EAST with stainless steel as a wall and plasma facing components (PFCs) during the second experimental campaign; data processing results of the tilting triple probes for measuring edge plasma parameters have been successfully obtained. EAST for isoflux control, a full graphite wall and PFCs has carried out diverted deuterium plasma discharges with double null configuration during the third campaign. Ohmic deuterium plasma properties, such as electron temperature, density, particle flux and power flux at the upper divertor targets, have also been successfully achieved by data processing results of the domed triple probes.

Keywords: divertor probes, edge plasma parameters, strike points, fully superconducting tokamak

PACS: 52.55.Fa, 52.70.Nc

EAST is a fully superconducting tokamak, the use of full superconducting poloidal field coils on EAST is the first trial in the world for ITER. Divertor hydrogen plasmas for full stainless steel wall were achieved during the second experimental campaign in January 2007^[1,2]. A water-cooling graphite wall and PFCs for the third experimental campaign were made in 2008; EAST has carried out diverted deuterium plasma discharges with double null configuration, which was verified by the fitting codes of online EFIT (GA), offline EFIT and IPPEQ (ASIPP).

Power deposition and wall erosion are of paramount interest in the development of next-step burning plasma experiments, such as ITER. The power which is not radiated either in the main or divertor plasmas is deposited onto the divertor plates, excessive heating of divertor plates, resulting in melting and evaporation, can severely reduce discharge performance^[3]. The wall erosion associated with the large incident ion fluxes may seriously limit the lifetime of the divertor target, particularly, during edge localized modes (ELMs) and disruptions. Derived data from Langmuir probe array^[4,5], the flux densities of power and particle at divertor plates facilitate understanding power deposition and wall erosion.

Electrostatic Langmuir probe diagnostics is an essential tool for measuring the fluxes of power and particles at divertor target plates in magnetic confinement fusion devices. Langmuir probes can be designed in different types, such as flush mounted probes^[6], tilting probes^[1], domed probes^[5,7]. The probes may be combined into triple probes^[4]. Because of both high spatiotemporal resolutions^[8] and the ability of fast simultaneous measurement of edge plasma parameters, triple probes are chosen for EAST.

20 tilting triple probes were installed in the lower both inboard and outboard divertor plates of EAST with a stainless steel wall during the August 2006. The probes were successfully used for determining edge

* Supported by the National Natural Science Foundation of China under Grant No 10605028, and the President Foundation of Hefei Institutes of Physical Science, Chinese Academy of Sciences. This work was partially supported by the JSPS-CAS Core-University program in the field of 'Plasma and Nuclear Fusion'.

hydrogen plasma parameters at divertor targets during the second experimental campaign^[11]. Typical ohmic hydrogen plasma discharge with near double null divertor configuration for strike point sweeps, shot 3743, has been analyzed. Plasma current is approximately 200kA, toroidal magnetic field is 2T, and pulse duration is about 3.4s including discharge plateau time 2.2s. The inner strike point sweeps from 2.4s to 3.3s by the fitting codes of IPPEQ (ASIPP). Data processing results have been obtained by combining the equations^[11] and raw data from the tilting triple probes: electron temperature, density, and fluxes of particles and power at the inner divertor target plates are 35-56 eV, $0.7-1.5 \times 10^{18} m^{-3}$, $0.7-1.7 \times 10^{22} m^{-2}s^{-1}$, and $0.5-1.4 MWm^{-2}$ at strike points, respectively. The average fluxes of power and particles are about $0.9 MWm^{-2}$ and $1.2 \times 10^{22} m^{-2}s^{-1}$, respectively. The real-time measurement results of the edge plasma parameters at strike points from shot 3743 are given in Fig. 1. The feature for high electron temperature and low electron density is a typical sheath-limited divertor regime. The strike points by the fitting codes of IPPEQ coincide with measured edge plasma parameters at strike points.

Acquisition of diverted plasmas with isoflux control for a full graphite wall and PFCs was one of the principal goals for the third experimental campaign. The divertor triple probes on EAST were used for determining edge divertor plasma properties. 74 domed triple probes were installed not only in the lower, both inboard and outboard, divertor plates including inside the dome, but also in the upper divertor plates in April 2008. Fig.2 shows the poloidal layout of divertor triple probes. The design of domed probes allows for the projected area of the probes to be relatively insensitive to the magnetic field angle in the divertor region. The design of the probe is shown in Fig.3. The tip of the probe is cylindrical, 0.8cm in diameter. The domed tip of the probe entirely protruded 1.5mm from the graphite target plate. The effective collection area of the probe is $8.2 mm^2$ using the strong field model^[7]. The typical spacing between groups of triple probes is poloidally 2 cm for inboard target plate and poloidally 1 cm for outboard target plate of both upper and lower divertor. One of the triple probes provides the floating potential while the other two probes are applied with a 200V bias. The domed triple probes have been successfully used for determining edge plasma parameters, such as electron temperature, density, particle flux and power flux in the upper divertor targets during the third experimental campaign.

The experiments were performed isoflux control after shaping in order to avoid strong plasma-wall interaction and damage of the in-vessel graphite components. Recently achieved typical parameters for a full graphite wall and PFCs are as follows: plasma current, $I_p = 0.2-0.6$ MA; toroidal magnetic field, $B_t = 2-3$ T; major radius, $R = 1.9$ m; minor radius, $a = 0.45$ m. The longest discharge duration exceeded 20 seconds at a plasma current of 0.25 MA. Most of the data correspond to divertor discharges with 2-2.5 T of toroidal magnetic field and 0.25-0.5MA of the plasma current.

The electron temperature in the divertor plates T_e (in eV) can be given^[4] as

$$T_e = (V_+ - V_f) / \ln 2 \quad (1)$$

where V_+ is positively biased potential and V_f is floating potential.

Particle flux, Γ_i , is^[9]

$$\Gamma_i = n_i \left(\frac{2T_e}{m_i} \right)^{1/2} \frac{\exp(\eta_s)}{\pi \eta_s^{1/2}} \quad (2)$$

where n_i and m_i are electron density at the target plate and ion mass respectively, here is $\eta_s = 0.854$.

So n_t is given by

$$n_t = \frac{\pi I_{is}(\eta_s)^{1/2} \exp(-\eta_s)}{e A_{eff} (2T_t/m_i)^{1/2}} \quad (3)$$

where I_{is} is ion saturation current, e and A_{eff} are electron charge and effective collection area of the probe respectively.

Power flux, P , is given by [10,11]

$$P = \Gamma_t (\gamma T_t + \varepsilon_{pot}) \quad (4)$$

where $c_{st} = (2T_t/m_i)^{1/2}$ and ε_{pot} are ion acoustic speed at the target plate and the potential energy ($\varepsilon_{pot} \approx 16 eV$), γ is the sheath transmission factor.

$$\gamma = 2 \frac{T_i}{T_e} + \frac{2}{1 - \delta_e} + \frac{1}{2} \ln \left(\frac{(1 - \delta_e)^2 m_i/m_e}{2\pi(1 + T_i/T_e)} \right) \quad (5)$$

where δ_e is the electron secondary electron emission coefficient. Substituting $T_i = T_e$, $\delta_e = 0$ and assuming a pure deuterium plasma, we arrive at $\gamma \approx 6.84$.

The fluxes of particles and power to the surface obey a $\sin(\theta)$ law, [4,11] the particle flux (Γ_t) and the power flux (P_t) at target plate can be achieved using the strong field model as follows.

$$\Gamma_t = \Gamma_i \sin(\theta) \quad (6)$$

$$P_t = P \sin(\theta) \quad (7)$$

where θ is the grazing angle between the surface and the incident magnetic field.

Typical ohmic deuterium plasma with near-double null divertor configuration, shot 8868, has been analyzed in detail. The plasma current is approximately 0.3 MA, the toroidal magnetic field is 2 T and the pulse duration is 3.9 s including a discharge plateau time 2.8 s. In shot 8868, the control for plasma current, positions and programmed shaping is used for up to 2.0 s, and then it is put into operation from partial isoflux control at 2.0 s to full isoflux control at 2.7 s. The inner strike point for upper divertor sweeps from probe UI15 at 2.6 s to probe UI11 at 2.8 s, then from probe UI11 to UI15 at 3.0s. The temporal evolution of the divertor plasma parameters measured for shot 8868 is shown in Fig.4. The data from all the probes at a rate of 10 kHz can be acquired simultaneously. By using such data of positively biased potential, floating potential, ion saturation current and equations (1), (3), (6) and (7) combining equations (2) and (4), the data processing results of the edge plasma parameters at inner strike points from pulse no. 8868 have been obtained, shown in Fig.5. Electron temperature, density, and fluxes of particles and power at the upper/inner divertor target plates are 23-46 eV, $1.1-4.9 \times 10^{18} m^{-3}$, $1.6-6.0 \times 10^{21} m^{-2}s^{-1}$, and $0.06-0.27 MWm^{-2}$ at strike points, respectively. The average fluxes of power and particles are about $0.16 MWm^{-2}$ and $3.7 \times 10^{21} m^{-2}s^{-1}$, respectively. Low electron temperature, fluxes of power and particles, and high electron

density at inner divertor targets for shot 8868 compared with shot 3743. Because of a full graphite wall, PFCs and isoflux control, divertor plasmas at inner targets are of good feature.

Acknowledgement

This work was partially supported by the JSPS-CAS Core-University program in the field of 'Plasma and Nuclear Fusion'. The authors are very grateful for the help of Professor Baonian Wan.

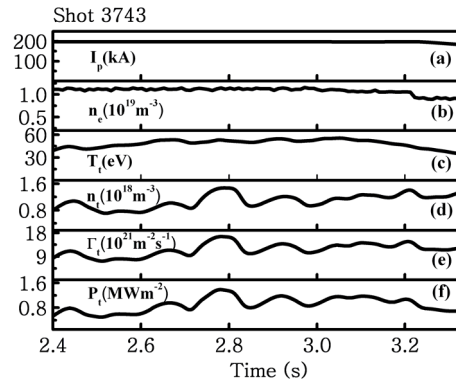


Fig.1 Evolution of the measured plasma current, line-average density and edge plasma parameters of inner divertor target plates at strike points: (a) plasma current, (b) line-average density, (c) electron temperature, (d) electron density, (e) particle flux and (f) power flux

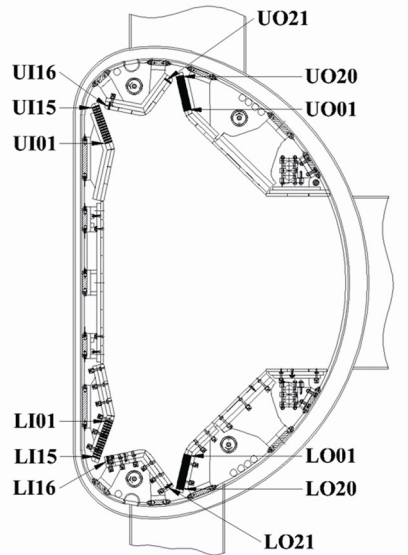


Fig.2 Poloidal layout of divertor probes

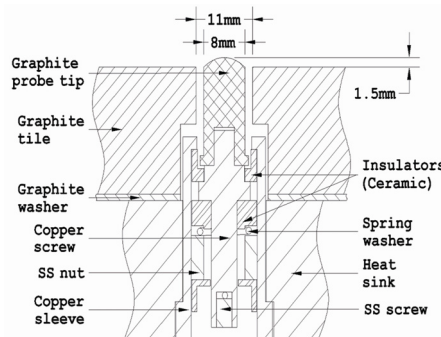


Fig.3 Cross section of divertor probe assembly

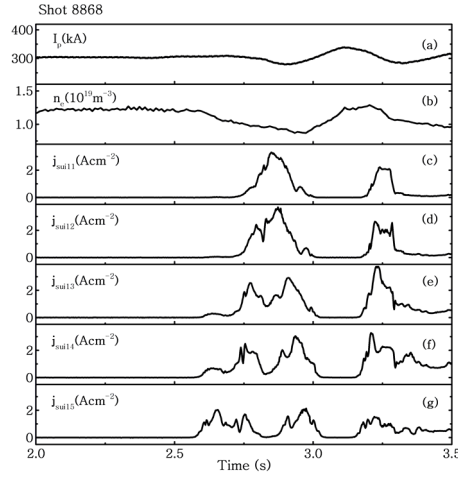


Fig.4 Evolution of the measured main plasma and upper divertor plasma parameters, where the following are plotted from top to bottom: (a) plasma current, (b) line-average density, (c)-(g) ion saturation current density of inboard divertor probes from probe UI11 to UI15

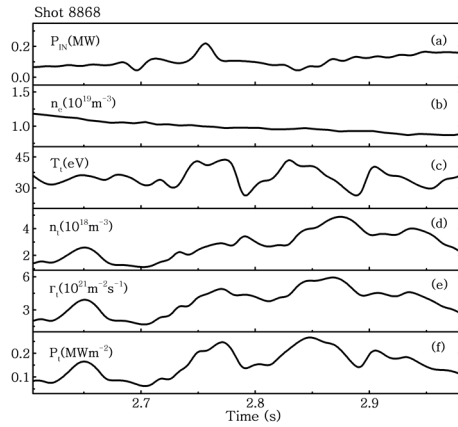


Fig.5 Evolution of the measured ohmic power, line-average density and edge plasma parameters of inner target plates in the upper divertor at strike points: (a) ohmic power, (b) line-average density, (c) electron temperature, (d) electron density, (e) particle flux and (f) power flux

References

- [1] Wang Jun et al, 2008, Phys. Scr., 78: 035501
- [2] Wan Baonian et al, 2007, Plasma Sci. Technol., 9: 125
- [3] Ulrickson M, J. 1990, Nucl. Mater. 176-177: 44
- [4] Matthews G F, 1994, Plasma Phys. Control. Fusion, 36: 1595
- [5] Kallenbach A et al, 2008, Nucl. Fusion 48: 085008
- [6] Gunn J P et al, 1997, Rev. Sci. Instrum., 68: 404
- [7] Buchenauer D et al, 1990, Rev. Sci. Instrum. 61: 2873
- [8] Yan Longwen et al, 2006, Rev. Sci. Instrum., 77: 113501
- [9] Hutchinson L H 2002 Principles of Plasma Diagnostics(2nd edition), Cambridge: Cambridge Univ. Press, p.77,79
- [10] Wesson J, 2003, Tokamaks (3rd edition), Oxford: Oxford University Press, p.546
- [11] Pitcher C S and Stangeby P C, 1997, Plasma Phys. Control. Fusion 39: 779

Soft x-ray PHA diagnostic for the electron temperature measurement on EAST

Ping Xu, Shiyao Lin, Liqun Hu, and the EAST Group

Institute of Plasma Physics, Chinese Academy of Sciences

Abstract: Two soft x-ray Pulse Height Analysis(PHA) systems, based on silicon drift detector(SDD), has been established on the EAST tokamak to measure spectrum of soft x-ray emission, one system consisting of 5 single SDDs is installed on EAST horizontal port A , the other system including one 10-channel SDD linear array on the horizontal port C. At photon energy of 5.9 keV, the energy resolution of 150-180 eV is achieved for the SDD with Peltier cooling, the SDD can maintain a good energy resolution even if the count rates up to 100 kHz. The MCA(Multi-Channel Analyzer) system which is the electronic part of PHA system has been modularized and linked to PC through LAN, the time-resolution and the whole collecting time can be conveniently adjusted by certain detecting software, therefore these PHA systems can be applied in the steady-state long pulse discharges of several minutes. By analyzing the soft x-ray spectra obtained from these PHA systems, the profiles of electron temperature can be readily derived with spatial resolution 7cm. In this paper, soft x-ray PHA systems on EAST are introduced, some experimental results of electron temperature of EAST typical discharge obtained from the soft x-ray PHA diagnostic is presented.

Key words: EAST, Pulse Height Analysis(PHA), Silicon Drift Detector(SDD), electron temperature

1 Introduction

In many magnetic fusion devices, soft x-ray PHA diagnostic has been routinely used to measure the spectrum of soft x-ray emission, and then obtain the electron temperature of plasma and the content of some heavy impurities[1-6]. In order to obtain high spatial resolution profiles of electron temperature and concentration of some heavy impurities, a compact detector is the Silicon Drift Detector (SDD)[7-9] with high energy resolution and high count rates, which has high detecting efficiency in the photon energy range of 1~20keV, has been applied to the soft x-ray PHA systems on EAST. Its working temperature is about -10 °C cooled by single-stage Peltier element which makes the SDD very compact. The energy resolution of SDD can achieve 150-180eV at 5.9 keV with Peltier cooling. It can be operated at high count rates of 100 kHz without significant signal distortion due to pile-up. SDD is very suitable for spatial multi-channel PHA measurements on tokamak due to the above advantages. In this paper, Soft x-ray PHA systems on EAST and some experimental results from this diagnostic are introduced. In Section 2, soft x-ray PHA systems on EAST are described, some typical experimental results are presented in Section 3, Section 4 gives the summary.

2 Soft x-ray PHA diagnostic systems

EAST is a full superconducting tokamak with major radius $R=1.75m$ and minor radius $r=0.4m$ [10], its objective is to study physical issues of the advanced steady-state operation modes

and establish technology basis of full superconducting tokamaks for future reactors[10]. Many diagnostic systems[11] have been established on EAST in order to get the information of some basic plasma parameters, such as plasma current, electron density, electron temperature. Two soft x-ray Pulse Height Analysis(PHA) systems, based on Silicon Drift Setector(SDD), has been established on the EAST to measure spectrum of soft x-ray emission, one system which consists of 5 single SDDs is installed on EAST horizontal port A, the other system including one 10-channel SDD linear array is mounted on the horizontal port C. All the SDD detectors of the two systems are moved from HT-7 tokamak.

The spatial arrangement of PHA system on EAST horizontal port A and the setup of sight lines are showed in Fig.1. The isolated SDD includes SDD crystal, 8mm Be foils, preamplifier, shaping amplifier, internal power supplies and active temperature control, all these integrated into a solid metal housing. The measuring range is 0~+46.5cm with a spatial resolution about 11.5cm. In order to receive the flux of soft X-ray at an appropriate level under varied discharge conditions, feedthroughs are used to adjust the size of exchangeable pinholes and the thickness of exchangeable Be foils. The system consists of a group of exchangeable Be foils(100 μ m, 200 μ m, 400 μ m) and a group of exchangeable pinholes(0.3mm, 0.5mm, 0.7mm, 1mm). The Be foils units and the pinholes units are set on sector metal plane respectively.

Fig.2 shows the spatial arrangement of PHA system on horizontal port C and the cutaway view of the system. The SDD array views the plasma from $r=-14$ cm to $r=+49$ cm and spatial resolution is about 7 cm. Each element of 10-channel SDD linear array is separated by a center-to-center distance of 8.5 mm. Feedthroughs are also used to change the size of the exchangeable pinholes (0.4 mm, 0.6 mm, 1.2 mm, and 2 mm) and the thickness of the exchangeable Be foils. One group of exchangeable Be foils with four Be foils (50 mm, 100 mm, 200 mm, and 400 mm) is placed near the pinholes and foils all lines of sight. Near the detectors four sets Be foils that can be adjusted independently is arranged. The valves in above two systems(as seen in Fig.1 and Fig.2) serves to isolate the torus vacuum system from the diagnostic vacuum system as necessary. All the SDDs in the soft x-ray PHA diagnostic are insulated from the torus potential by the thick fluoro rubber gasket and Teflon insulator.

The thickness and sensitive area of each SDD element is 280 mm and 5 mm² respectively. Each element has an 8 mm Be foil in the entrance. In soft x-ray range SDD detector with an 8 mm Be foils has high detecting efficiency[6]. To reduce the dark current, the SDD detector is cooled down to about -10 °C using single-stage Peltier element. The energy resolution of the SDD is about 153 eV at 5.9 keV with 0.5 μ s shaping time[5]. The SDD can measure x-ray phonons at count rates of about 100kHz without considerable pile-up effect, while maintaining a good energy resolution. The MCA(Multi-Channel Analyzer) system which is the electronic part of PHA system has been modularized and linked to PC through LAN(Loacal Area Network), the time-resolution and the whole collecting time can be conveniently adjusted by certain detecting software, therefore these PHA systems can be applied in the steady-state long pulse discharges of several minutes on EAST.

3 Some experimental results

PHA system on port A was applied on EAST during the last three discharge campaigns of EAST, but the data from this system is not good owing to many reasons. PHA system on port C was established and performed very well in the last EAST campaign, so all the data showing in this paper are from this SDD linear system.

A typical waveform of auxiliary heating discharge(limiter configuration) is shown in Fig. 3. The plasma current was 250 kA, the toroidal magnetic strength was 2T. The lower hybrid waves (LHW) about 750kW power was injected during the time from 1.4 to 3.3 s. As seen in Fig. 3, the central electron temperature considerably increased during the injection of Lower Hybrid Wave. The raw soft x-ray spectra of shot 8460 during the time from 2.7 to 2.8 s derived from nine line sights are shown in Fig. 4. The electron temperature profile of shot 8460 during the time from 2.7 to 2.8 s obtained from above nine line sights is showed in Fig. 5. In this figure, Te profiles under OH heating and auxiliary heating conditions with varied lower hybrid wave power are also showed, all the shots showing in this figure are limiter configuration discharges, and these shots have the same toroidal magenetic strength($B_t=2T$), plasma current($I_p=250kA$), electron density($N_{eL}=1.5$). During the LHW heating phase, the time interval is 100ms and choosed in flattop phase. From this figure, it can be clearly seen that Te in half plasma minor radius increased considerably during wave-heating phase, and Te profiles become more and more steep when more and more LHW power injected compare with the ohmic discharge, when higher power LHW was injected, about 750kW, electron temperature was increased by about 650eV. The error bars in Fig. 5 represent the statistic errors in fitting procedure of the raw spectrum.

4 Conclusion and future prospects

The use of SDD has allowed to arrange spatial multi-channel configurations for soft x-ray PHA diagnostic in tokamak. The soft x-ray pulse height analysis (PHA) diagnostic based on Silicon Drift Detector(SDD), has been established on EAST tokamak for the electron temperature measurement. Time-resolved radial profiles of electron temperature can be obtained with this diagnostic. This diagnostic has demonstrated itself to be a very useful diagnostic tool. High energy-resolution of SDD make it suitable for the investigation of heavy impurities. In the next plan, further optimize this diagnostic system and make this diagnostic become a real-time measurement tool, investigate heavy impurities, and estimate the Zeff value are our target.

Acknowledgments

This work was supported by the National Nature Science Foundation of China under Contract Nos. 10775041, 10675124 and youth science funds, Chinese Academy of Sciences. The work was partially supported by JSPS-CAS Core -University Program in the field of “Plasma and Nuclear Fusion” as well. The corresponding author is grateful to all members of the EAST Team for their contribution to EAST experiments.

References

- [1] S.von Goeler, W.Stodiek, H.Eubank, H.Fishman, S.Grebenshchikov, and E.Hinnov, Nucl.Fusion 15, (1975) 301.
- [2] D.Pasini,R.D.Gill,J.Holm, and E.vander Goot Rev.Sci.Instrum.59 (1988) 693.
- [3] E.H.Silver, M.Bitter, K.Brau,D.Eames, A.Greenberger, K.W.Hill, D.M.Meade, W.Roney, N.R.Sauthoff, and S.von Goeler, Rev.Sci.Instrum.,53 (1982) 1198.
- [4] Muto S and Morita S, Rev.Sci.Instrum., 72(2001)1206.
- [5] Z.Y.Chen, et al, A compact soft X-ray PHA in the HT-7 tokamak.Nuclear Instruments and Methods in Physics Research A, 527(2004)604-608.
- [6] Yuejiang Shi, et al, Soft x-ray pulse height analyzer in the HT-7 tokamak, Rev. Sci. Instru. 75(2004)4930-4933.
- [7] L. Struder, N. Meidinger, D. Stotter, J. Kemmer, P. Lechner, P. Leutenegger, H. Soltau, F.

- Eggert, M. Rohde, and T. Schulein, *Microsc. Microanal.* **4**, 622 (1999).
- [8] L. Struder, H. Brauninger, U. Briel, R. Hartmann, G. Hartner, D. Hauff, N. Krause, B. Maier, N. Meidinger, E. Pfeffermann, M. Popp, C. Reppin, R. Richter, D. Stotter, J. Trumper, and U. Weber, *Rev. Sci. Instrum.* **68**, 4271 (1997).
- [9] A. Longoni, C. Fiorini, P. Leutenegger, S. Sciuti, G. Fronterotta, L. Struder, and P. Lechner, *Nucl. Instrum. Methods Phys. Res. A* **409**, 407 (1998).
- [10] Wu Songtao, EAST Structure, Internal Report of Institute of Plasma Physics, Chinese Academy of Sciences, 2007.
- [11] Gao Xiang, Overview of Diagnostic System in the EAST Tokamak, 12th Conference on HIGH TEMPERATURE PLASMA DIAGNOSTICS, Zvenigorod, Moscow region, Russia, June 3-9, 2007.

Figure Caption

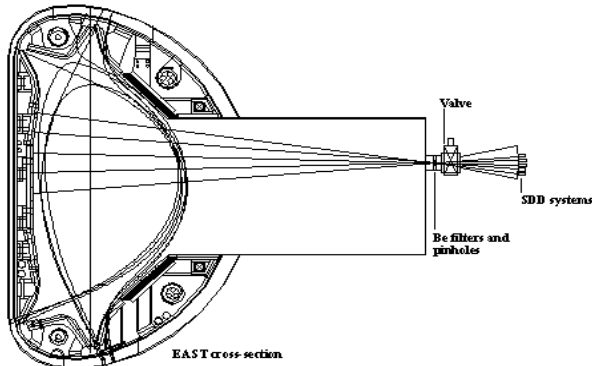


Fig.1 Spatial arrangement of soft x-ray PHA systems on EAST horizontal port A.

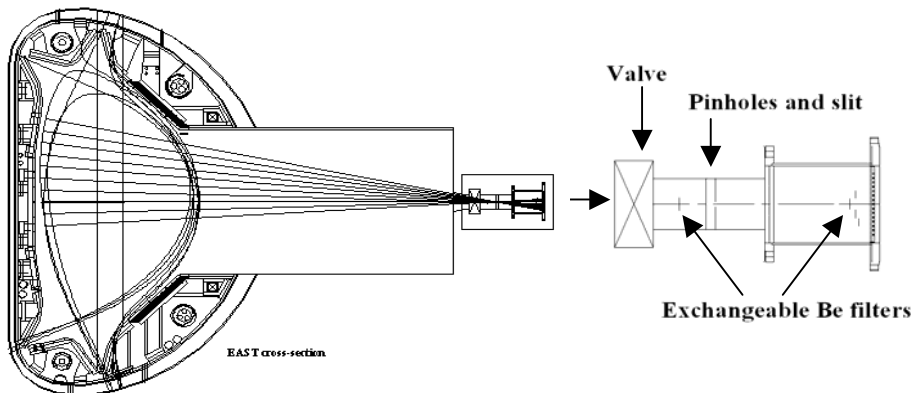


Fig.2 Spatial arrangement of soft x-ray PHA systems on EAST horizontal port C.

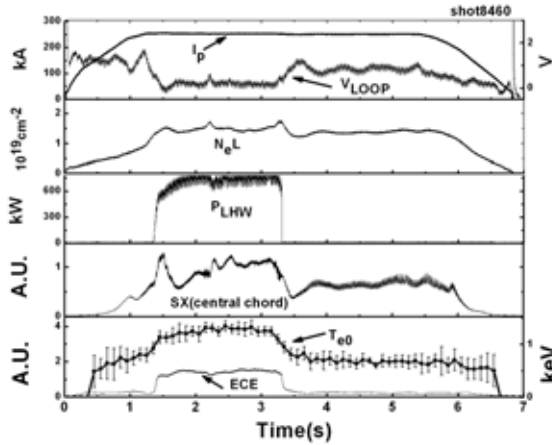


Fig.3 The waveform of shot 8460 with LHW heating. I_p is plasma current, V_{LOOP} is loop voltage, N_eL is the central chord integral electron density, P_{LHW} is the power of lower hybrid wave, SX is central chord intensity of soft x-ray emission, T_{e0} is the central chord averaged electron temperature derived from soft x-ray PHA diagnostic with 100 ms time-resolution, ECE is the electron cyclotron emission.

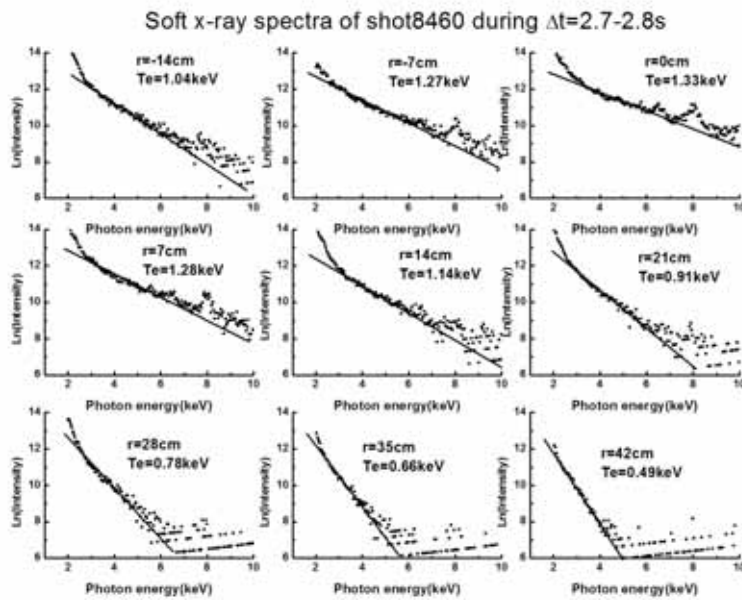


Fig.4 The raw soft x-ray spectra of shot 8460 during the time from 2.7 to 2.8 s.

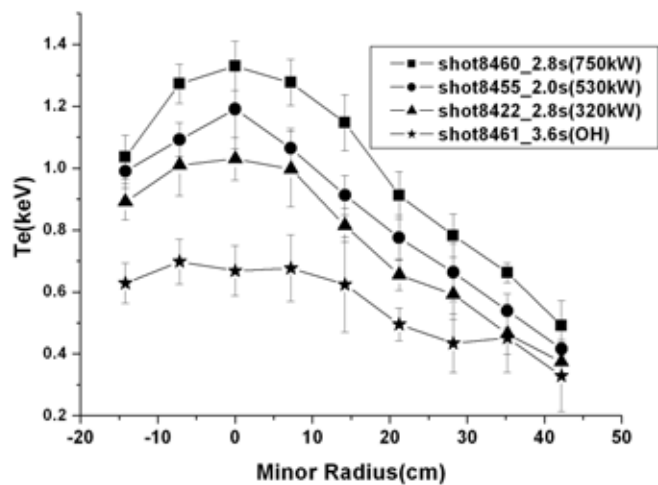


Fig.5 The profiles of electron temperature under OH heating and auxiliary heating(LHW) conditions with varied lower hybrid wave power.

Development of a heavy ion beam probe for measuring electrostatic potential profile and its fluctuation in LHD

Takeshi IDO, Akihiro SHIMIZU, Masaki NISHIURA, Haruhisa NAKANO, Shinji KATO, Shinsuke OHSHIMA, Yasuo YOSHIMURA, Shin KUBO, Takashi SHIMOZUMA, Hiroe IGAMI, Hiromi TAKAHASHI, Kazuo TOI, Fumitake WATANABE, Kazumichi NARIHARA, Ichiro YAMADA, and the LHD experimental group

National Institute for Fusion Science, Oroshi-cho, Toki-shi, Gifu 509-5292, Japan

PACS : 52.70.-m, 52.35.Bj, 52.35.Fp

Keyword : electrostatic potential measurement, HIBP , GAM, RSAE

Abstract

A heavy ion beam probe (HIBP) using a 3-MV tandem accelerator has been installed on Large Helical Device (LHD). Electrostatic potential can be measured in core plasma under the toroidal magnetic field strength of up to 3 T. By using the HIBP, a transition of potential profile from electron-root to ion-root is observed in core plasmas during ramp-up of the electron density. Potential fluctuations are also measured during controlling the magnetic shear by electron cyclotron current drive (ECCD), and two kind of characteristic fluctuations are observed in plasmas with the reversed magnetic shear. One is Reversed-Shear-induced Alfvén Eigenmode(RSAE) and the other is Geodesic Acoustic Mode(GAM), probably.

1. Introduction

Radial electric field (E_r) is a key parameter to determine transport phenomena in magnetically confined plasmas. In helical systems, for example, Core electron-root confinement (CERC)¹ is obtained by using electron cyclotron heating (ECH)²⁻⁷, and the improved confinement is considered to be related to the transition of E_r predicted by neoclassical theory. Thus, understanding of the behaviors of E_r is essential to study transport phenomena in plasmas. In Large Helical Device (LHD), a heavy ion beam probe (HIBP)⁸ has been developed to measure the electrostatic potential in core region⁹⁻¹². The HIBP also has possibility to measure the potential and density fluctuations, simultaneously. Therefore, it is a suitable tool for clarifying the role of E_r in transport phenomena.

In this paper, the present status of the HIBP on LHD (LHD-HIBP) is described and representative experimental results are shown. In section 2, the LHD-HIBP system is described schematically. In section 3, potential profiles during the ramp-up of the electron density are shown. In section 4, observations of potential fluctuations in plasmas with reversed magnetic shear are presented.

2. LHD-HIBP

A schematic view of the LHD-HIBP system is shown in Fig.1. For the LHD-HIBP, singly charged gold ions(Au^+) are injected into a plasma as a primary beam, and doubly charged ions (Au^{2+}) ionized by collision with the plasma are detected(referred to as the secondary beam). In order to extract the secondary beam from LHD under the toroidal magnetic field of 3 T, the primary beam with the energy of up to 6 MeV is required. In previous HIBPs, single-end accelerators have been used, but a tandem accelerator is used in LHD-HIBP so as to reduce the acceleration voltage. Thus, the required acceleration voltage to obtain the singly charged positive ion with energy of up to 6 MeV is reduced to 3 MV. On the other hand, tandem accelerators require negative ions as the initial particles. Hence, negative ion sources have been developed since early stage of the development of the LHD-HIBP^{13 - 15}. At present, the output current of the negative ion source is about 15 μA under the steady state operation. Since the conversion efficiency from Au^- to Au^+ in the gas cell of the accelerator is $\leq 20\%$, the primary beam current of a few microamperes can be extracted from the accelerator.

Because the tandem accelerator installed far from the torus of LHD to avoid the influence of the stray field of LHD in the accelerator and to maintain the accelerator easily, the length of the beam transport line becomes about 20 meters. The beam line for the injection consists of electrostatic quadrupole lenses to adjust the focus of the beam,

electrostatic deflectors to bend the beam line, and steering electrodes to compensate the deflection of the beam trajectory due to the stray magnetic field¹². The transport efficiency is 30 % at least, and the primary beam current of about 1 microampere can be injected into plasma.

The secondary beam is extracted from a horizontal port and its energy is analyzed by using a tandem energy analyzer¹⁶.

The measurement position is determined by the combination of magnetic field strength, beam energy, and injection angles. At present, the observable region ranges from ρ of -0.2 to ρ of 0.7, where ρ is the normalized minor radius and the positive (negative) sign means the upper-side (lower-side) of the equatorial plane. The spatial resolution is determined from the size and divergence of the probing beam and the slit height of the energy analyzer. It is estimated to be a few cm¹⁷.

3. Potential profile measurement during ramp-up of the electron density

In helical systems, neoclassical theory can estimate E_r through the ambipolarity condition of particle fluxes. As reference 1 indicates, for example, neoclassical theory predicts E_r tends to be positive in plasmas where electron temperature(T_e) is higher

than ion temperature(T_i), and the solution of ambipolarity condition is referred to as electron-root. On the other hands, E_r is predicted to be negative when $T_e \sim T_i$ and the electrons are in the $1/v$ regime. The solution is referred to as ion-root. In order to test such prediction based on the neoclassical theory, the electrostatic potential profiles are measured by using the HIBP.

In the experiments, the electron density is varied from 0.1 to $0.5 \times 10^{19} \text{ (m}^{-3}\text{)}$ to change the temperature and density. The magnetic field strength (B_t) is 1.5 T, the major radius of the magnetic axis(R_{ax}) is 3.75 m in the vacuum configuration. The timing of ECH and NBI is shown in Fig.2(a) and the power of ECH is 0.4 MW and 8 MW. The temporal evolution of the line averaged electron density is shown in Fig.2(b), where an impurity pellet is injected in edge region at 1.6 sec. The working gas is hydrogen. The energy of the probing beam of the HIBP is 1.376 MeV. The beam is reciprocated at a frequency of 10 Hz, so a potential profile is measured every 50 ms.

The electron temperature profiles are shown in Fig.2(c). During ECH, the T_e profile has a hump in the central region and the central T_e reaches about 2.5 keV, though the error is large because of the low electron density. The hump in T_e profile disappears after the ECH, and the central temperature becomes about 1 keV during NBI.

Figure 2(d) shows the observed potential profiles. While T_e is high and electron density(n_e) is

low during ECH, the electrostatic potential profile has negative gradient and E_r is positive. As n_e increases, the potential decreases and its gradient changes from negative to positive inside $\rho \sim 0.4$, that indicates E_r changes from positive to negative. According to neoclassical theory, E_r will be electron-root (positive) in the case the electron temperature is higher than the ion temperature (T_i), and E_r tends to be negative when T_e becomes close to T_i after ECH. Thus, transition from electron-root ($E_r > 0$) to ion-root ($E_r < 0$) will occur. Therefore, the observed temporal behaviors of the potential profiles can be explained by using neoclassical theory qualitatively.

4. Potential fluctuation measurement

One of the advantages of HIBPs is the measurement with the high temporal resolution ($\sim 1\text{MHz}$). In the case of LHD-HIBP, however, the attenuation of the probing beam in plasmas is severe, and the fluctuation measurement is not easy because of the poor signal to noise ratio. Nevertheless, since the attenuation strongly depends on the plasma density, potential fluctuation with the amplitude of about 50 V or more can be observed in core region of the plasma as long as the line averaged density is lower than $0.5 \times 10^{19} (\text{m}^{-3})$, at present. One of results of potential fluctuation measurement is shown below.

In LHD, a method to control the rotational transform actively by electron cyclotron

current drive (ECCD) has been developed¹⁸⁻²⁰. Characteristic behaviors of potential fluctuations are observed in core plasmas by using the HIBP during ECCD¹⁷.

The experiments have been performed under B_t of 1.5 T and R_{ax} of 3.75 m, and the working gas is hydrogen. The plasma is produced and sustained by tangential NBI from 0.4 s to 2.4 s, and Co- and Counter- NBI are balanced to minimize the beam-driven plasma current. Electron cyclotron current drive (ECCD) is superposed from 1.0 to 1.6 s. The line integrated electron density is $0.1 \times 10^{19} \text{ (m}^{-3}\text{)}$ and constant, and the central electron temperature is 4.0 and 1.0 keV with and without ECCD, respectively. Reference 20 shows that ECCD in the co-direction near the magnetic axis increases the rotational transform and the rotational transform (safety factor) profile comes to have a local minim (maximum) at around $\rho \sim 0.5$.

Figure 3(b) shows the temporal evolution of the frequency spectrum of the potential fluctuation. Note the Fig.3(b) includes the spatial structure as well as the temporal evolution because the measurement position of the HIBP is reciprocated from $\rho \sim 0.1$ to $\rho \sim 0.4$ at a frequency of 10 Hz as shown in Fig.3 (a). During the superposition of ECCD (1.3 – 1.9 s.), some modes are observed in the frequency range of 40 – 120 kHz and their frequencies change gradually with the time constant of a few hundred milliseconds, though T_e and n_e are constant. They are also observed by magnetic probes as shown in

Fig.3(c). The time constant of the frequency shift seems to reflect the change in the rotational transform profile, and the observed fluctuations are inferred to be Reversed-Shear-induced Alfvén Eigenmodes (RSAEs)²¹⁻²³, which is observed in plasmas with the reversed magnetic shear induced by using neutral beam current drive (NBCD)^{24, 25}.

In addition to that, another coherent mode with the constant frequency of 32 kHz during ECCD and 19 kHz just after ECCD is observed. The frequency spectra of the potential fluctuation and normalized intensity fluctuation of the HIBP in a plasma with the reversed magnetic shear, are shown in Fig.2(d) and (e). The latter fluctuation reflects the normalized density fluctuation. The coherent mode is observed in the density fluctuation as well as the potential fluctuation. The frequency does not depend on the rotational transform but depends on T_e as shown in Fig. 4. Since the frequency seems to depend on $\sqrt{T_e}$, a candidate of the mode is Geodesic-Acoustic-Mode (GAM)^{26,27}, which is excited as a low frequency RSEA including the compressibility²⁸.

The spatial distribution of the modes can be measured by using the HIBP during the sweep of the probing beam. Reference 17 shows that the mode is excited near the magnetic axis where the rotational transform(safety factor) is low(high). Theoretical studies^{29, 30} indicate that the GAM in helical plasmas tends to exist in the core region

where the rotational transform is small and the damping of the GAM oscillation is mitigated. Judging from the temperature dependence of the frequency and the spatial structure, the observed low frequency mode is probably GAM.

5. Summary

An HIBP using a 3-MV tandem accelerator has been installed on LHD. Potential profiles can be measured in core region by use of the HIBP.

The transition of E_r from positive to negative is observed during ramp-up of the electron density, and the behavior can be explained by neoclassical theory qualitatively.

Potential fluctuations are measured in low density plasmas. Two kind of characteristic fluctuations are observed in plasmas with the reversed magnetic shear produced by ECCD. One of the fluctuations has constant frequency during the evolution of the rotational transform profile, and the frequency depends on the electron temperature, and the mode is probably GAM. The frequencies of the others vary gradually as the rotational transform is reversed, and the modes are probably RSAE.

Acknowledgement

We appreciate Honorary Professor Y. Hamada, Drs. A. Nishizawa, A. Fujisawa, H. Iguchi of NIFS for valuable advices and discussion. We also appreciate Honorary Professor T. Watari and Dr. S. Satake of NIFS for discussion about GAMs.

This work was supported by MEXT Japan under Grant-in-Aid for Young Scientists (Nos. 16760674 and 18760640), the JSPS-CAS Core-University program in the field of 'Plasma and Nuclear Fusion', and NIFS/NINS under the project of Formation of International Network for Scientific Collaborations and NIFS07ULBB505.

Reference

- 1 Yokoyama M, et al. 2007, Nucl. Fusion, 47:1213
- 2 Fujisawa A, et al. 1999, Phys. Rev. Lett., 82:2669
- 3 Maasberg A, et al., 2000, Phys. Plasmas, 7:295.
- 4 Shimozuma T, et al., 2003, Plasma Phys. Control. Fusion 45:1183
- 5 Takeiri Y, et al., 2003, Phys. Plasmas, 10:1788
- 6 Ida K, et al., 2003, Phys. Rev. Lett., 91:085003
- 7 Estrada T, et al., 2004 Plasma Phys. Control. Fusion, 46:277
- 8 Hickok R L, 1967, Rev. Sci. Instrum., 38:142.
- 9 Fujisawa A, et al., 1994, IEEE Trans. Plasma Sci., 22:395
- 10 T. Ido *et al.*, 2006, Rev. Sci. Instrum., 77:10F523.
- 11 A. Shimizu *et al.*, 2007, Plasma Fusion Res., 2:S1098
- 12 Ido T *et al.*, 2008, Plasma and Fusion Res., 3:031
- 13 Sasao M, *et al.*, 1992, Rev. Sci. Instrum. 63:2726
- 14 Taniike A, *et al.*, 1994, IEEE Trans. Plasma Sci., 22:430
- 15 Nishiura M, *et al.*, 2006, Rev. Sci. Instrum., 77:03A537
- 16 Hamada Y, et al., 1997, Rev. Sci. Instrum., 68:2020
- 17 Ido T, et al., 2008, Rev. Sci. Instrum., 79:10F318
- 18 Shimozuma T, et al., 2006, Fusion Science and Technology 50:403

- 19 Notake T, et al., 2008, Plasma and Fusion Research 3:S1077
- 20 Kubo S, et al., 2008, “Profile control by local ECRH in LHD”, 22nd IAEA Fusion Energy Conference, Geneve (http://www-pub.iaea.org/MTCD/Meetings/FEC2008/ex_p6-14.pdf)
- 21 Kimura H, et al., 1998, Nucl. Fusion, 38:1303
- 22 Sharapov S, et al., 2001, Phys. Lett. A 289:127
- 23 Fukuyama A, 2002, “Kinetic Global Analysis of Alfvén Eigenmodes in Toroidal Plasmas”, 19th IAEA Fusion Energy Conference, Lyon, France
- 24 Toi K, et al. 2007, “Observation of Alfvén Eigenmodes with Frequency Sweeping in a LHD Plasma with Large Counter Beam-Driven Current”, 10th IAEA Technical Meeting on Energetic Particles in Magnetic Confinement Systems, Kloster Seeon.
- 25 Toi K, et al., 2008, “Alfvén Eigenmodes and Geodesic Acoustic Modes Driven by Energetic Ions in an LHD Plasma with Non-monotonic Rotational Transform Profile”, 22nd IAEA Fusion Energy Conference, Geneve, (http://www-pub.iaea.org/MTCD/Meetings/FEC2008/ex_p8-4.pdf)
- 26 Winsor N, Johnson J L, Dawson J M, 1968, Phys. Fluids, 11:2448
- 27 Diamond P H, Itoh S-I, Itoh K, Hahm T S, 2005, Plasma Phys 47:R35
- 28 Breizman B N, Pekker MS, Sharapov S E, JET EFDA contributors, 2005, Phys. Plasma, 12: 112506.
- 29 Watari T, et al., 2005, Phys. Plasma, 12:062304
- 30 Satake S, Okamoto M, Nakajima N, Sugama H, Yokoyama M, Beidler C D, 2005, Nucl. Fusion 45:1362

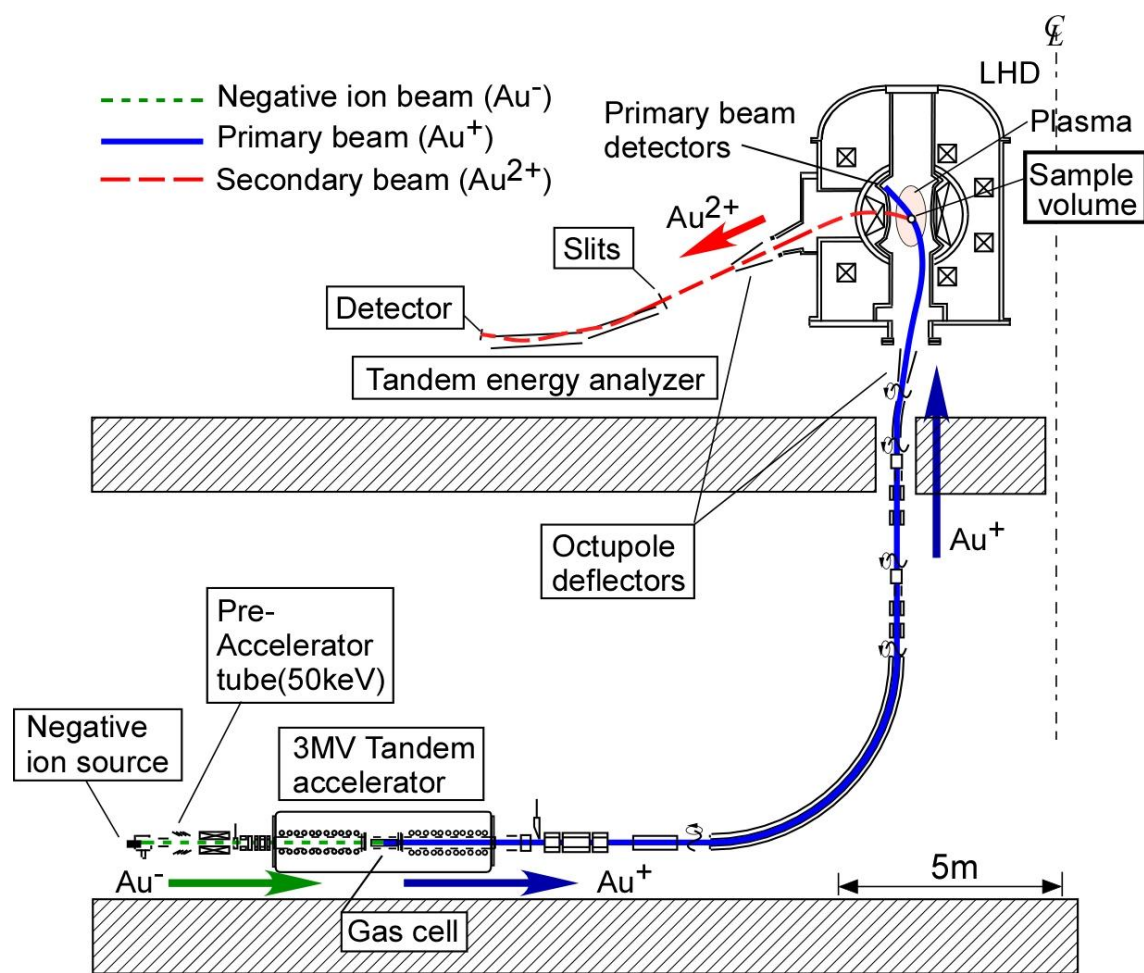


Fig.1 Schematic view of LHD-HIBP system.

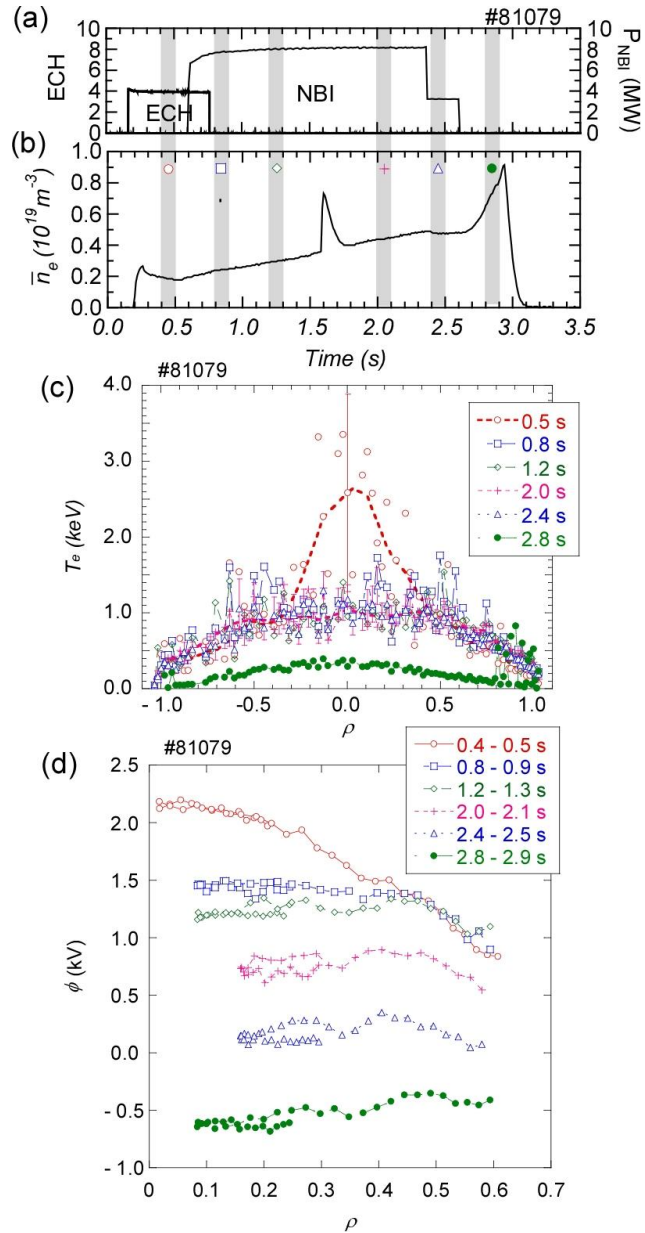


Fig.2 (a) Timing of ECH and NBI. (b) Line averaged electron density. (c) Electron temperature profiles. (d) Potential profiles. The profiles are measured in hatched period in (b).

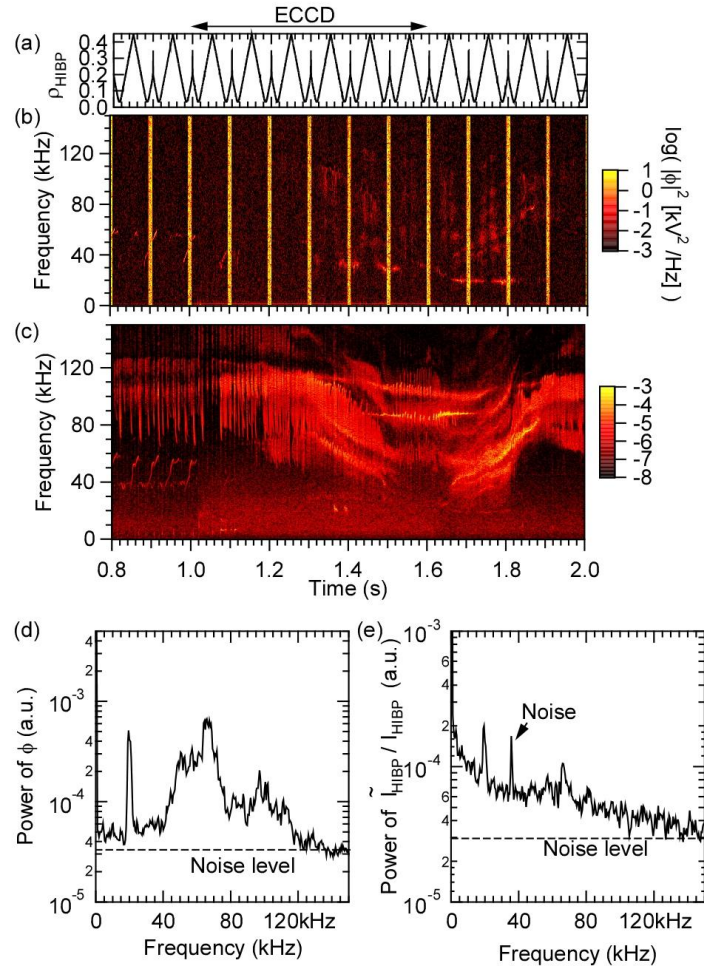


Fig.3 (a) Normalized minor radius of measurement position of the HIBP. (b) Temporal evolution of the electrostatic potential fluctuation. Note that the measurement position moves as shown in figure (a). (c) Temporal evolution of the magnetic fluctuation. ECCD is applied from 1.0 to 1.6 sec in the co-direction. (d) and (e) Frequency spectra of potential fluctuation and normalized intensity fluctuation of the HIBP, which reflects the normalized density fluctuation, just after ECCD. The measurement position is at $\rho \sim 0.15$.

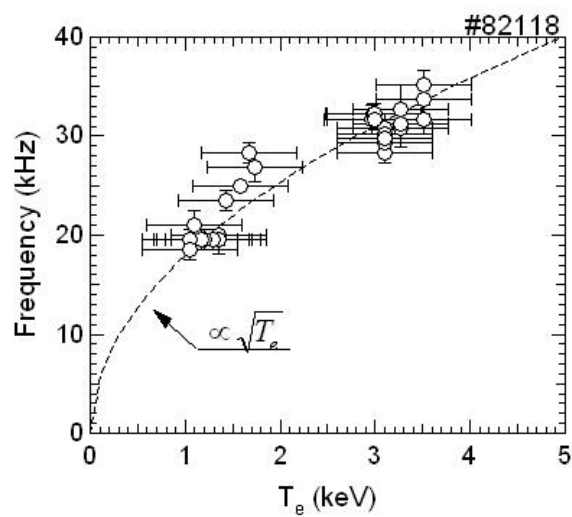


Fig.4 Temperature dependence of the frequency of the GAM-like mode.

Recent Progress in Heliotron J Experiments for Exploration of the Helical-Axis Heliotron Concept

T. Mizuuchi, S. Kobayashi, H. Okada, K. Nagasaki, S. Yamamoto, G. Motojima¹, S. Watanabe²,
K. Mukai², K. Hosaka², Y. Kowada², S. Mihara², H. Lee², Y. Takabatake², A. Matsuyama²,
Y. Nakamura², K. Hanatani, Y. Suzuki¹, S. Konoshima, K. Kondo² and F. Sano

Institute of Advanced Energy, Kyoto University, Gokasho, Uji 611-0011, Japan

¹National Institute for Fusion Science, 322-6 Oroshi-cho, Toki 509-5292, Japan

²Graduate School of Energy Science, Kyoto University, Gokasho, Uji, 611-0011, Japan

(Proceedings for JSPS-CAS Core University Program Seminar (Lijiang, Nov. 4-7, 2008))

Heliotron J is a flexible concept exploration facility for the helical-axis heliotron concept, where the bumpiness (ε_b) is introduced as the third measure to control the neoclassical transport in addition to the helicity and toroidicity. The effects of ε_b -control on the plasma performance are investigated in Heliotron J from the viewpoints of the fast ion confinement, global energy confinement. The effect of the bumpiness on the global energy confinement for NBI-only and ECH-only plasma has been investigated for the selected three different ε_b configurations. A favorable energy confinement was obtained in the high- ε_b configurations for NBI-only plasma, which could be attributed to the improvements in the energetic ion confinement in the high- ε_b configuration. For ECH-only plasma, however, the medium- ε_b configuration shows the longest global energy confinement time.

1. Introduction

The advanced helical concepts try to reduce the ripple-loss through recovering the symmetry of the confinement field (quasi-symmetry concept) or tailoring the Fourier harmonics of the confinement field, B_{mn} , in the Boozer coordinates (quasi-omnigeneous concept). The helical-axis heliotron [1] concept is developed by introducing an idea based on the latter line to a device having a pitch-modulated helical coil set for realization of the confinement field. The Heliotron J device with an $L/M = 1/4$ helical coil [2, 3] is a concept exploration facility for this concept. Here, the bumpiness ($\varepsilon_b = B_{04}/B_{00}$) is introduced as the third measure to control the neoclassical transport [4] in addition to the other major field harmonics, helicity ($\varepsilon_h = B_{14}/B_{00}$) and toroidicity ($\varepsilon_t = B_{10}/B_{00}$).

The configuration control studies are essential parts of the Heliotron J experiment since one of the major objectives of the Heliotron J project is to extend the understanding of the related roles of configuration parameters (the rotational transform (ι), the field harmonics, magnetic well, magnetic shear, etc.) in transport reduction, MHD activity control and/or non-inductive toroidal current control in the omnigeneous optimization scenario.

As for the effects of the rotational transform control, the ECH, NBI and their combination heating experiments in Heliotron J have revealed the existence of windows in the vacuum edge rotational transform $\iota(a)_{vac}$ for the transition to the high quality “H-mode like” discharge mode [5]. Here, $\iota(a)_{vac}$ is used just as a label of the field configuration since $\iota(r)$ can be easily modified by the plasma pressure and/or current in a low-shear device. The modification of the edge field topology and divertor plasma distribution caused by non-inductive current has been observed in Heliotron J [6]. Moreover recent NBI-only plasma experiments suggest the causal relation between the onset of the transition to an improved confinement mode and $\iota(r)$ modification due to the plasma current [7, 8]. Since it has been observed that the bootstrap current and ECCD current are affected by the bumpiness tailoring [9, 10, 11], more detailed study of bumpiness effects on the non-inductive current formation is necessary from a viewpoint of configuration control. On the other hand, the ε_b -control experiments indicated that the fast ion confinement produced by NBI or ICRF heating is better in higher ε_b configuration [12, 13, 14, 15], which is qualitatively consistent with the expectation from the drift optimization viewpoint. As for the ε_b -effects on the bulk plasma performance, however, we have observed different dependence between NBI- and ECH-only plasmas [16]. It is necessary to make it clear the role of the bumpiness control in the anomalous and neoclassical transport, and, therefore, in the confinement improvement.

This paper reviews recent configuration studies in Heliotron J, especially focusing on the bumpiness control effects on the global energy confinement.

2. Experimental setup

The details of the Heliotron J device ($\langle R_0 \rangle = 1.2$ m, $B_0 \leq 1.5$ T) is described in [2, 3]. A top view of the plasma ring has a square shape with four “straight” and “corner” sections as shown in Fig. 1, where the toroidal shape of the $\rho = 0.9$

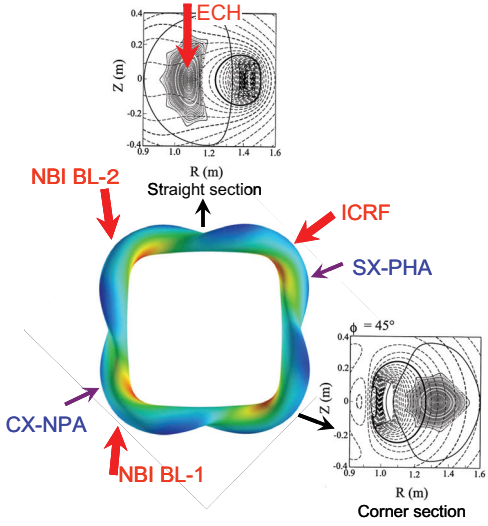


Fig. 1 Top view of the magnetic-surface shape (at $\rho = 0.9$) for the standard configuration. The nested magnetic surfaces and the mod-B surfaces at two poloidal sections (straight and corner sections) are also illustrated.

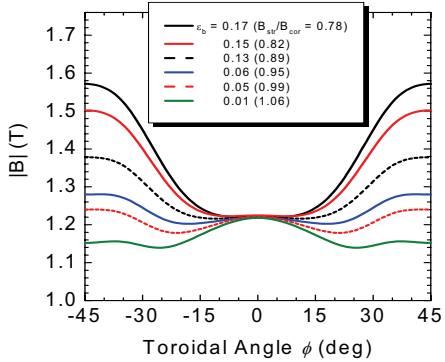


Fig. 2 The field strength along the magnetic axis for several bumpiness configurations [11].

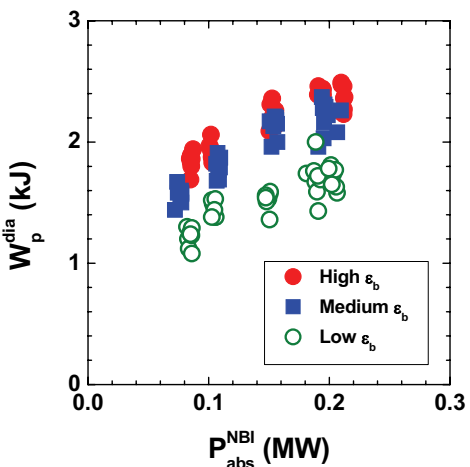


Fig. 3 Stored energy obtained in high-, medium- and low- ϵ_b configurations as a function of absorbed beam power for NBI-only plasmas [16].

magnetic-surface for the standard configuration of Heliotron J is illustrated. The color index indicates the strength of the confinement field $|B|$. At the corner section, where $|B|$ decreases along the major radius like that in tokamaks, while at the straight section, it is designed to make a weak saddle-type field gradient.

The field configuration is controlled by using the five sets of the external coils, the helical (+ vertical) coil (HV), two individual sets of the toroidal coils (TA and TB) and two sets of the vertical field coils (AV and IV). The bumpiness is mainly controlled by changing the current ratio of TA and TB coils, I_{TA} and I_{TB} , respectively. Trimming of the vertical field can make it possible to control ϵ_b within tolerable deformations of ϵ_h and ϵ_t , $\iota(a)_{vac}$, the plasma volume and the averaged major radius.

The initial plasma is produced by using the second harmonic X-mode ECH (70 GHz, < 0.45 MW) launched from a top port located at one of the straight sections. The hydrogen neutral beam (< 30 keV, < 0.7 MW/beam-line) is injected using two tangential beam-lines facing each other (BL-1 and BL-2). Selecting one of the two beam-lines or changing the direction of the confinement field, Co- or CTR-injection is performed. ICRF heating is performed by using two sets of loop antenna installed on the low-field side at a corner section of the torus ($f_{ICRF} \sim 19$ -23 MHz, $P_{inj} < 0.4$ MW/antenna). The locations of heating equipments are also shown in Fig. 1.

3. Bumpiness control experiments

To examine the bumpiness control effects on the plasma performance, we have selected three configurations with $\epsilon_b = 0.15$ (high ϵ_b), 0.06 (medium ϵ_b) and 0.01 (low ϵ_b) at $\rho = 2/3$ [17]. Here, the magnetic axis position at the ECH launching section, the plasma volume (~ 0.7 m 3), the edge rotational transform ($\iota(a)_{vac} \cong 0.56$) are kept almost constant. The standard configuration of Heliotron J corresponds to the medium- ϵ_b case. Figure 2 shows the variation of the magnetic field strength along the magnetic axis for several ϵ_b configurations as a function of the toroidal angle, where the field strength at the straight section ($\phi = 0^\circ$) is set constant to keep the ECH resonance condition. The DCOM [18] calculation indicates that the numerical sequence of the “effective helical ripple” ϵ_{eff} [19] for the three configurations is not the same as that of ϵ_b , i.e., ϵ_{eff} ’s at $\rho = 2/3$ for the low-, medium- and high- ϵ_b configurations are 0.26 , 0.13 and 0.22 , respectively [17].

3.1. Bumpiness effects on the global energy confinement in NBI-only plasma [16, 20]

Figure 3 shows the plasma stored energy measured with a diamagnetic coil system, W_p^{dia} , as a function of the absorbed NB power (P_{abs}^{NBI}) for the high-, medium- and low- ϵ_b configurations. Here, the H 0 -beam is injected tangentially into deuterium plasma after the plasma initiation by a short pulse of ECH. To compare the data for non-transition plasmas even in higher input power condition, NB is injected to the CTR-direction, where no transition phenomena have been observed so far [7, 8]. These data were obtained at a fixed

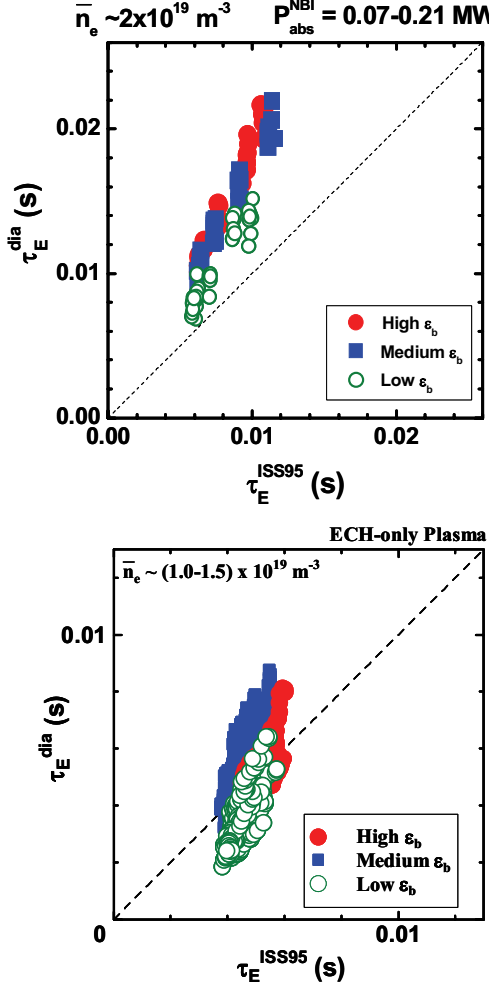


Fig.5 Comparison between τ_E^{dia} and τ_E^{ISS95} for (a) NBI-only plasmas [16] and (b) ECH-only plasma.

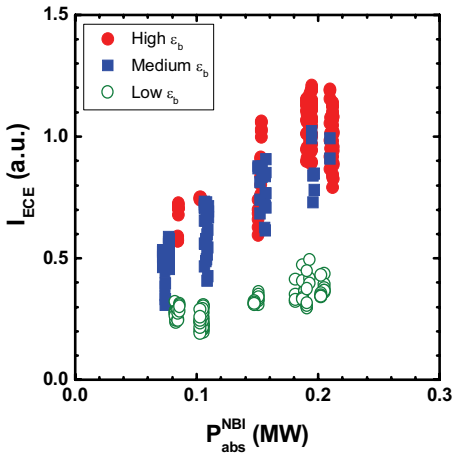


Fig.6 ECE intensity as a function of $P_{\text{abs}}^{\text{NBI}}$ in high-, medium- and low- ϵ_b configurations [16].

the latter possibility, we have found in the previous experiments that the characteristic decay time of the high energy CX flux after turning-off of NBI became longer as increasing bumpiness [12]. Since the heating source is only the fast ions in NBI-only plasmas, the improved confinement of the energetic ions would contribute to increase the plasma temperature. Therefore, it is considered that the improved confinement of the energetic ions would increase the plasma temperature and

density condition of $\bar{n}_e \approx 2 \times 10^{19} \text{ m}^{-3}$. The beam absorption profile is evaluated by FIT [21] and the orbit-loss fractions in the high-, medium- and low- ϵ_b cases are 25%, 26% and 29%, respectively. As shown in the figure, W_p^{dia} in the high- and medium- ϵ_b configurations is clearly high compared to that in the low- ϵ_b case. The difference between the high- and medium- ϵ_b is not so clear but W_p^{dia} in the high- ϵ_b configuration seems higher than that in the medium- ϵ_b one. To take into account the differences in $\langle R \rangle$, $\langle a_p \rangle$ and $|B|$ for these configurations, the comparison of the experimentally evaluated global energy confinement time (τ_E^{dia}) with the International Stellarator Scaling (τ_E^{ISS95}) is plotted in Fig. 5(a), assuming the similar dependence of τ_E on $\langle R \rangle$, $\langle a_p \rangle$ and $|B|$ for Heliotron J NBI plasmas as that in the International Stellarator Scaling. Also from this comparison, it is found that the data for the high- and medium- ϵ_b configurations are better than those for the low- ϵ_b case.

Since the data plotted in Fig. 5(a) are obtained at the same \bar{n}_e condition, the difference in W_p^{dia} (or τ_E^{dia}) should be attributed to the difference in temperature. Actually, the bulk ion (D^+) temperature, which is evaluated with a CX-NPA, increases as increase of ϵ_b ; the ion temperature at $P_{\text{abs}}^{\text{NBI}} \approx 200 \text{ kW}$ in the high-, medium- and low- ϵ_b cases were 0.23, 0.20 and 0.18 keV, respectively. Moreover, the signal intensity of the electron cyclotron emission (I_{ECE}) from the core region also indicates the higher electron temperature in higher ϵ_b case as shown in Fig. 6. As increasing $P_{\text{abs}}^{\text{NBI}}$, I_{ECE} 's in high- and medium- ϵ_b cases are increased, while the dependence of I_{ECE} on $P_{\text{abs}}^{\text{NBI}}$ is weaker in the low ϵ_b configuration.

The similar comparison of τ_E^{dia} for ECH-only plasmas is plotted as Fig. 5(b) for reference. For ECH-only plasmas, only the data of $\bar{n}_e \approx (1.0-1.5) \times 10^{19} \text{ m}^{-3}$ are plotted from the previous ECH plasma database [17, 22] to exclude the H-mode data. The lower density ($\bar{n}_e < 1.0 \times 10^{19} \text{ m}^{-3}$) data are also excluded. The data for ECH-only plasmas show that the best performance seems to be in the medium- ϵ_b case, which has the lowest ϵ_{eff} in the examined three configurations, and the difference between the high- and low- ϵ_b cases is not so clear, at least in this density range. Although the effect of the effective helical ripple has been discussed to explain the observation, more detailed studies are necessary to reach a conclusive answer.

To understand the observed difference in the ϵ_b -dependence of τ_E^{dia} (or W_p^{dia}) between NBI- and ECH-only plasmas, we should consider two possibilities besides the density dependence; one is the difference in the ϵ_b -dependence of the transport and the other is that in the “effective” heating efficiency. Since a different heating method might cause a different radial electric field structure in the plasma, the difference of the transport should be discussed taking into account the effect of the radial electric field. As for

raise the plasma performance in the high- ϵ_b configuration. In the low- ϵ_b configuration, on the other hand, the less heating due to the poor confinement of the energetic ions might enhance the degradation in the plasma performance between these configurations.

4. Summary

The recent configuration study in Heliotron J is reviewed, especially focusing on the bumpiness control effects on the global energy confinement.

The effect of the bumpiness on the global energy confinement for NBI-only plasmas and ECH-only plasma has been investigated. For NBI-only plasma, a favorable energy confinement was obtained not only in the medium bumpiness configuration, which shows better global energy confinement for ECH-only plasma than the high- or low- ϵ_b configuration, but also in the high bumpiness configurations. It is considered that the improved confinement of the energetic ions increases the plasma temperature and raises the plasma performance in the high- ϵ_b configuration.

In Fig. 5, we assume the similar parameter dependence for Heliotron J plasma as that in the International Stellarator Scaling. However, the actual parameter dependence for Heliotron J plasma is still an open question, including the effects of the heating scenario. More detailed studies are under progress.

Acknowledgement

The authors are grateful to the Heliotron J supporting group for their excellent arrangement of the experiments. This work is performed with the support and under the auspices of the Collaboration Program of the Laboratory for Complex Energy Processes, IAE, Kyoto University, the NIFS Collaborative Research Program (NIFS04KUHL001, et al.), the Formation of International Network for Scientific Collaborations, the Grant-in-Aid for Sci. Research as well as the JSPS-CAS Core-University program in the field of “Plasma and Nuclear Fusion”.

References

- [1] M. Wakatani, et al., Nucl. Fusion **40**, 569 (2000).
- [2] F. Sano, et al., J. Plasma Fusion Res. SERIES 3, 26 (2000).
- [3] T. Obiki, et al., Nucl. Fusion **41**, 833 (2001).
- [4] M. Yokoyama, et al., Nucl. Fusion **40**, 261 (2000).
- [5] F. Sano, et al., Nucl. Fusion **45**, 1557 (2005).
- [6] T. Mizuuchi, et al., Nucl. Fusion **47**, 395 (2007).
- [7] S. Kobayashi, et al., in 11th IAEA TM on H-mode Phys. Trans. Barriers (Tsukuba, 2007).
- [8] T. Mizuuchi, et al., Joint Conf. “17th Int. Toki Conf. on Phys. Flows & Turbulence in Plasmas” and “16th Int. Stellarator/Heliotron Workshop” (Toki, 2007) O-02.
- [9] G. Motojima, et al., Fusion Sci. Tech., **51**, 122 (2007).
- [10] G. Motojima, et al., Nucl. Fusion **47**, 1045 (2007).
- [11] K. Nagasaki, et al., in FEC2008 (Geneva, 2008), IAEA-CN-165/EX/P6-15.
- [12] S. Kobayashi, et al., IAEA-CN-116/EX/P4-41 (2004)..
- [13] H. Okada, et al., Fusion Sci. Tech.. **50**, 287 (2006).
- [14] H. Okada, et al., Nucl. Fusion **47**, 1346 (2007).
- [15] H. Okada, et al., in FEC2008 (Geneva, 2008), IAEA-CN-165/EX/P6-28.
- [16] S. Kobayashi, et al., in FEC2008 (Geneva, 2008), IAEA-CN-165/EX/P5-13.
- [17] T. Mizuuchi, et al., Fusion Sci. Tech. **50**, 352 (2006).
- [18] A. Wakasa, et al., J. Plasma Fusion Res. **4**, 408 (2001).
- [19] V. V. Nemov, et al., Phys. Plasmas **6**, 4622 (1999).
- [20] S. Kobayashi, et al., in 2nd Joint Meeting of US-Japan Workshop and Kyoto Univ. the 21st COE Sympo. "New approach in Plasma Confinement Exp. in Helical Systems", (Auburn, USA, 2006).
- [21] S. Murakami, et al., Trans. Fusion Tech. **27**, 259 (1995).
- [22] F. Sano, et al., IAEA-CN-149/EX/5-5Ra (2006).

Ion Cyclotron Resonance Heating System on EAST

WANG Lei and ZHAO Yanping

Institute of Plasma Physics, China Academy of Science, Hefei 230031, China

Abstract The Ion Cyclotron Resonance Heating (ICRH) system which can provide no less than 10MW radio frequency (RF) heating power (frequency range from 25MHz to 100MHz) is being set up for the experimental advanced superconducting tokomak (EAST) in the institute of plasma physics. System includes High-power and wide-frequency radio amplifier, liquid phase shifter and resonant double loop (RDL) antenna. Now one ICRH system unit whose ultimate output is 2.5MW has been set up and employed for RF heating experiment and maximum of the injected RF power reached to 200kW in 2008 EAST tokomak experiment. The results of ICRH heating are satisfying.

Key words Ion Cyclotron Resonance Heating; radio amplifier; liquid phase shifter; antenna

1 Introduction

Ion cyclotron resonance heating is an important method of heating plasma by using RF wave (frequency range from 10MHz to 200MHz) in Tokomak experiment. An ICRH system is being set up for EAST in the institute of plasma physics, which can provide no less than 10MW RF heating power (frequency range is from 25MHz to 100MHz and pulse length is more than 1000s). This ICRH system comprises one ICRH unit whose ultimate output power is 2.5MW and five ICRH units, each of which can provide 1.5MW RF heating power. The 2.5MW ICRH system has been completed, and the other three 1.5MW ICRH systems are under way of construction.

Fig.1 is the schematic diagram of ICRH system. The working theory of ICRH system is that RF signal is amplified by RF amplifier and propagated to antenna through transmission line, and then RF power is fed in plasma. Liquid phase shifter is the equipment which can regulate the phase of RF wave. The 2.5MW ICRH system is introduced as an example in this paper.

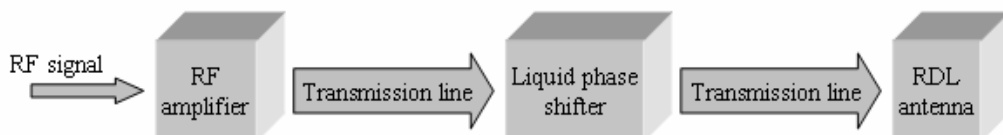


Fig.1 schematic diagram of ICRH system

2 RF amplifier

RF amplifier is the RF power source of 2.5MW ICRH system. Its technical indexes are:

- Maximum output power: 2.5MW.
- Maximum pulse duration: 1000s.
- Frequency range: 25MHz-100MHz.
- Output impedance: 50Ω .
- Bandwidth with 50Ω load: 2MHz (-3dB).

The schematic diagram of 2.5MW RF amplifier is shown in Fig.2. The RF power from the

signal generator is processed by the waveform generator (power level, duration time, rise time, fall time and other parameters which specify the waveform of the output RF power can be set). Then the RF power is amplified by the intermediate power amplifier (IPA), the drive power amplifier (DPA) and the final power amplifier (FPA) in turn and fed into plasma through the antenna. The output RF power of IPA is 6kW. DPA has 150kW output RF power and its tetrode tube is 4CW100000E. FPA has 2.5MW output RF power and its tetrode tube is 4CW2500KG. The anode power supply for the tetrode tube of the FPA is adopted the pulse step modulation (PSM) technology and has 3MVA maximum output power, 30kV output voltage and 100A output current. All important parameters in RF amplifier are taken into the protection circuit, such as the ratio of the reflected RF power to the incident RF power, voltages and currents of all power supplies, the flow rate and temperature of cooling water and the air quantity of forced airflow. When any parameter of them exceeds the threshold, the protection circuit will stop the output of the RF wave.

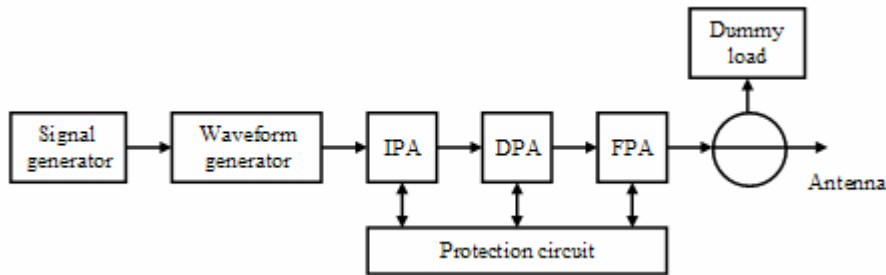


Fig.2 2.5MW RF amplifier

The input impedance matching circuit of FPA consists of an input tuning stub and an input matching capacitor. With variable capacitance and inductance, the input impedance can be matched from 25MHz to 100MHz frequency range. The double coaxial output cavity is adopted for the FPA output cavity in order to cover the wide frequency range, as shown in Fig.3. The output cavity is made of copper plates and its length is 3m. The cross section of the outer conductor is a square 0.9m long one side. The cross section of the intermediate conductor is a 12-regular polygon, the diameter of whose inscribed circle is 676mm. The cross section of the inner conductor is a circle whose diameter is 460mm. Two movable stubs are installed in the cavity. One between the outer and intermediate conductors is the matching stub and the other between the intermediate and inner conductors is the tuning stub. The anode of the tetrode tube is attached to the inner conductor through the blocking capacitor. The RF power is extracted via an external output coaxial transmission line. The inner conductor of the output coaxial transmission line is connected to the intermediate conductor of the FPA cavity. The outer conductor of the output coaxial transmission line is connected to the outer conductor of the FPA cavity. Force airflow is led inside the double cavity to remove ohm heat loss on the copper plates. The purified water is used to cool the tetrode tube and its flow rate is no less than $40\text{m}^3/\text{h}$ with $5\text{kg}/\text{cm}^2$ pressure ^[1]. Another important parameter is the ion pump current which indicates the vacuum pressure in the tetrode tube and is always monitored when the tetrode tube is in operation. Arcing will occur if the ion pump current is too high and the DC power supply will be shut off in $10\mu\text{s}$ to protect the tetrode tube.

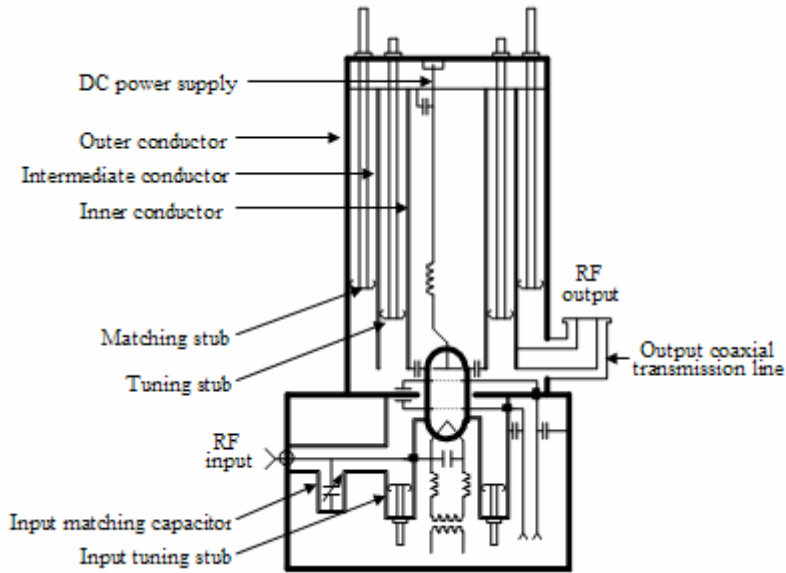


Fig.3 structure diagram of FPA

3 Liquid phase shifter

Liquid phase shifter is a section of transmission line and filled with silicon oil between its inner conductor and outer conductor, as shown in Fig.4. Because the dielectric constants of air and silicon oil are different, when RF wave propagates in the oil, its phases and wavelength will change^[2]. By changing the length of oil in the liquid phase shifter, the phase of RF wave can be regulated to make the RF power be fed in plasma more efficiently through the antenna. The maximum length and the diameters of the inner and outer conductor of the liquid phase shifter are 10m, 100mm and 300mm respectively. According to the dielectric constant of silicon oil (2.2), the characteristic impedance of liquid phase shifter is calculated to be 30.3Ω .



Fig.4 liquid phase shifter

4 RDL antenna

The RDL antenna has the merits of low voltage standing wave ratio, fast impedance matching and high power density. Fig.5 is the structure diagram of RDL antenna. In the RDL antenna scheme, a vacuum variable capacitor is connected to each terminal of the current strap, and RF power is fed via the feeder at the position which has the distance of $0.18l_a$ (l_a is the length of the current strap) to the centre of the current strap [3]. The current strap and these two capacitors form two RLC circuits. Variable capacitance and inductance is required to make the impedance of antenna and transmission line be matched over the frequency and load ranges. The length and width of the current strap are 540mm and 110mm respectively. The used vacuum capacitor is CVZV_150DW/90-AAB-JKNT. Its withstand voltage peak is 90kV and variable capacitance range is from 15pF to 150pF. The function of fluid drive is to regulate the distance between the antenna and the centre of plasma. There are two RDL antennas in each ICRH window of ESAT.

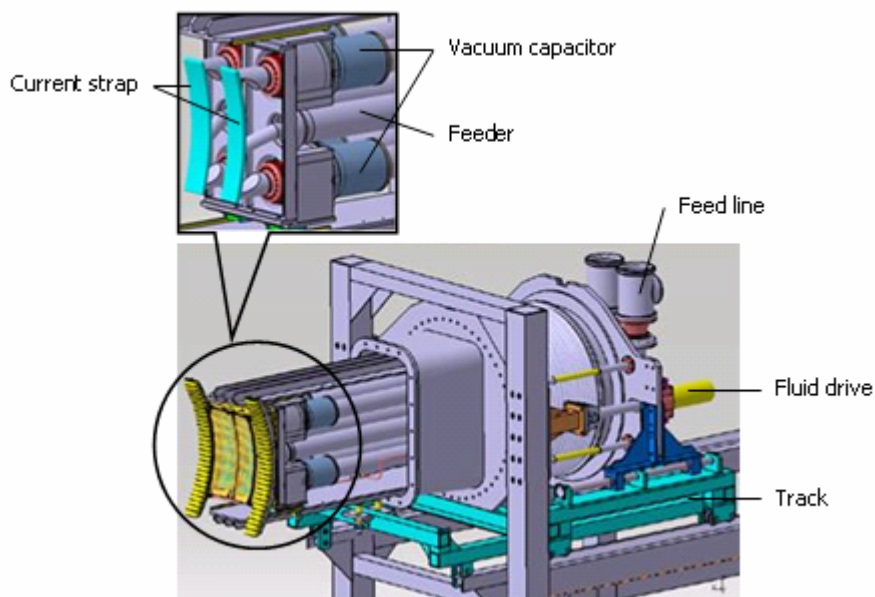


Fig.5 structure diagram of RDL antenna

5 Experimental data

In 2008 EAST tokomak experiment, the 2.5MW ICRH system has been employed for RF heating experiment. Fig.6 is the waveforms of No.7603 and No. 7606 EAST tokomak discharge. We can read that maximum of the injected RF power has reached to 200kW and the pulse length is 800ms.

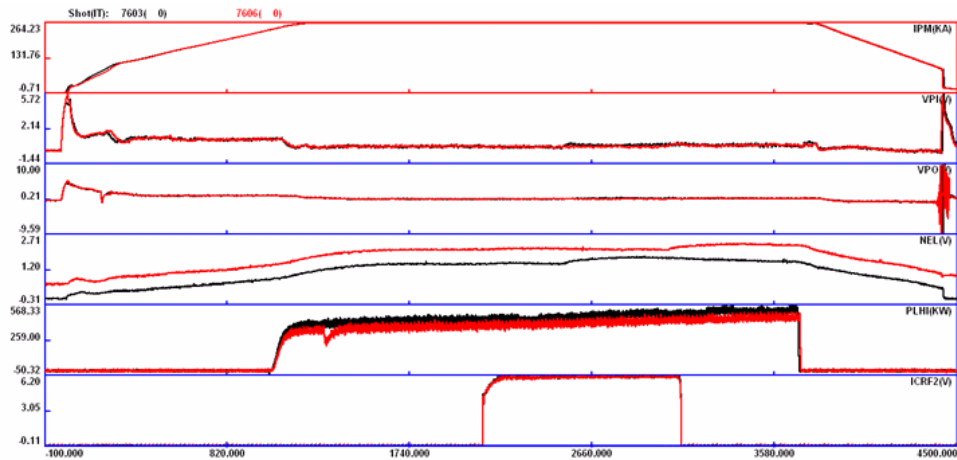


Fig.6 No.7603 and No.7606 EAST tokomak discharge

Acknowledgment

This work was partially supported by the JSPS-CAS Core-University program in the field of 'Plasma and Nuclear Fusion'.

Reference:

1. Tetsuo Seki, Ryuhei Kumazawa, Takashi Mutoh, et al. 2001, Fusion science and technology, 40: 253
2. Wang Peng, Zhao Yanping, Mao Yuzhou, et al. 2005, Atomic Energy Science and Technology, 39,:88(in Chinese)
3. QIN Chengming, ZHAO Yanping, Hiroyuki OKADA, et al. 2006 Plasma Sci Techno, 8:358

Agenda

JSPS-CAS Core University Program Seminar on
Production and Control of High Performance Plasmas with Advanced Plasma Heating and Diagnostic systems
麗江 (Lijiang), Nov.4~Nov.7, 2008

Nov.4, Tuesday, 2008

No	Time	Duration/min	Title	Chairman		Speaker	Affiliation
	9:00~9:10	10	Opening Welcome Speech	X.GAO	S1	WANG Kongjia	ASIPP
1	9:10~10:10	55	Basic elements in drift wave turbulence (Memorial talk)			TOI Kazuo	NIFS
	10:10~10:25	15	Group photo			WATARI Tetsuo	NIFS
	10:25~10:45	20	Coffee break				
2	10:45~11:10	20	RTEFIT/Isoflux plasma shape control on EAST			XIAO Bingjia	ASIPP
3	11:10~11:35	20	Recent Results of JT-60 Experiment			KOIDE Yoshihiko	JAEA
4	11:35~12:00	20	Recent Progress of the HL-2A tokamak	S.MORITA	S2	DUAN Xuru	SWIP
	12:00~14:00	120	Lunch				
5	14:00~14:25	20	Microwave torus experiment in the LATE device			MAEKAWA Takashi	Kyoto University
6	14:25~14:50	20	Research Activities and Plans of Electron Cyclotron Wave Startup and Alfvén Wave Current Drive at SUNIST	L.W.YAN	S3	TAN Yi	Tsinghua University
7	14:50~15:15	20	The Reconstruction of the TEXT-U tokamak in China			DING Yonghua	HUST
	15:15~16:00	45	Coffee break				
8	16:00~16:25	20	Contribution of Helical Devices to Alfvén Eigenmode Physics in Toroidal Plasmas	T.WATARI	S4	TOI Kazuo	NIFS
9	16:25~16:50	20	Progress on edge and core impurity transport study with the development of spectroscopic instruments in LHD			MORITA Shigeru	NIFS
10	16:50~17:15	20	Plasma sheath resistance measurement by reference probe in PECVD coating machine			WANG Qing	Northeastern University

Nov.5, Wednesday, 2008

	Time		Topic	Chairman		Speaker	Affiliation
11	9:00~9:25	20	Experimental Progress on the HT-7 superconductor tokamak	T.MIZUUCHI	S5	GAO Xiang	ASIPP
12	9:25~9:50	20	Plasma Transport Study on HL-2A			DING Xuantong	SWIP
13	9:50~10:10	15	Particles behavior in quasi-steady-state ac plasmas on HT-7 tokamak			JIE Yinxian	ASIPP
	10:10~10:50	40	Coffee break				
14	10:50~11:15	20	Investigation of experimental configuration of electron Bernstein wave heating on LHD	Y.ZHOU	S6	IGAMI Hiroe	NIFS
15	11:15~11:40	20	Study of high power ICRF antenna design in LHD			KASAHARA Hiroshi	NIFS
16	11:40~12:05	20	Energetics of resistive wall modes in flowing plasmas			HIROTA Makoto	JAEA
	12:05~14:00		Lunch				
17	14:00~14:25	20	Recent Progress of Neutral Beam Injector and Beam emission Diagnostic in LHD	T.MAEKAWA	S7	IKEDA Katsunori	NIFS
18	14:25~14:50	20	Density limit with different fuelling methods in HL-2A			YAN Longwen	SWIP
19	14:50~15:10	15	Modelling of L-and H-modes of EAST using ONETWO transport code			ZHOU Deng	ASIPP
20	15:10~15:30	15	Soft x-ray tomography on HT-7 tokamak			CHEN Kaiyun	ASIPP
	15:30~16:00	30	Coffee break				
21	16:00~16:25	20	Evaluation of the Optical Design of Laser Thomson Scattering Diagnostics for High Temperature EAST Tokamak and Low Temperature MAP-II Divertor Simulator	H.ZUSHI	S8	KADO Shinichiro	The University of Tokyo
22	16:25~16:50	20	Dust dynamics in HL-2A plasma			TOMITA Yukihiko	NIFS
23	16:50~17:15	20	Analysis on EAST operation space by using simple Core-SOL-Divertor			HIWATARI Ryoji	CRIEPI

Nov.6,Thursday,2008

	Time		Topic	Chairman		Speaker	Affiliation
24	9:00-9:25	20	Two dimensional density fluctuation measurement during non-inductive current ramp-up phase in the compact plasma wall interaction experimental device CPD	K.TOI	S9	ZUSHI Hideki	Kyushu Univ.
25	9:25-9:50	20	Recent Progress of the HL-2A Laser Interferometer			ZHOU Yan	SWIP
26	9:50-10:15	20	Development of Microwave Reflectometer for Density Profile and Fluctuation Measurements			TOKUZAWA Tokihiko	NIFS
	10:15-10:45	30	Coffee break				
27	10:45-11:10	20	Experimental progress on the EAST superconductor tokamak	G.ZHUANG	S10	HU Liqun	ASIPP
28	11:10-11:30	15	Divertor Probe diagnostics on EAST			WANG Jun	ASIPP
29	11:30-11:50	15	Electron temperature profiles obtained from soft x-ray PHA diagnostic on EAST			XU Ping	ASIPP
	12:00-14:00		Lunch				
30	14:00-14:25	20	Development of a heavy ion beam probe for measuring electrostatic potential profile and its fluctuation in LHD	K.J.WANG	S11	IDO Takeshi	NIFS
31	14:25-14:50	20	Recent progress on Heliotron J experiments for exploration of the helical-axis heliotron concept			MIZUUCHI Tohru	Kyoto Univ.
32	14:50-15:10	15	Ion Cyclotron Resonance Heating System in EAST			WANG Lei	ASIPP
	15:10-15:30	15	Short summary			GAO&MORITA	ASIPP/NIFS

Nov.7, Friday, 2008

	Time		Topic	Chairman			
	9:00-11:50		Plenary meeting on future J-C collaboration in fields of confinement, heating and diagnostics	X.GAO S.MORITA	S12		
	12:00-14:00	120	Lunch				
	14:00-16:00		Individual discussions in each category		S13		

List of participants

CHEN Kaiyun

Institute of Plasma Physics,
Chinese Academy of Sciences
P.O.Box 1126,Hefei,Anhui 230031,P.R.China
E-mail:kychen@ipp.ac.cn

HIWATARI Ryoji

Central Research Institute of
Electric Power Industry (CRIEPI)
2-11-1,Iwadokita,Komae-shi Tokyo,
201-8511Japan

DING Yonghua

Huazhong University of Science and
Technology
Wuhan,Hubei 430074,P.R.China
E-mail:yhding@mail.hust.edu.cn

HU Liqun

Institute of Plasma Physics,
Chinese Academy of Sciences
P.O.Box 1126,Hefei,Anhui 230031,P.R.China
E-mail:lqhu@ipp.ac.cn

DING Xuantong

Southwestern Institute of Physics
P.O.Box 432,Chendu,Sichuan,610041,
P.R.China
E-mail:dingxt@swip.ac.cn

HIROTA Makoto

Japan Atomic Energy Agency
801-1,Muko-yama,Naka-shi,Ibaraki,
311-0193,Japan
E-mail:hirota.makoto@jaea.go.jp

Dong Shaohua

Institute of Plasma Physics,
Chinese Academy of Sciences
P.O.Box 1126,Hefei,Anhui 230031,P.R.China

IDO Takeshi

National Institute for Fusion Science
322-6 Oroshi-cho,Toki-shi ,Gifu
509-5292,Japan
E-mail:ido@LHD.nifs.ac

DUAN Xuru

Southwestern Institute of Physics
P.O.Box 432,Chendu,Sichuan,610041,
P.R.China
E-mail:duanxr@swip.ac.cn

IGAMI Hiroe

National Institute for Fusion Science
322-6 Oroshi-cho,Toki-shi ,Gifu
509-5292,Japan
E-mail:igami.hiroe@LHD.nifs.ac.jp

GAO Xiang

Institute of Plasma Physics,
Chinese Academy of Sciences
P.O.Box 1126,Hefei,Anhui 230031,P.R.China
E-mail:xgao@ipp.ac.cn

IKEDA Katsunori

National Institute for Fusion Science
322-6 Oroshi-cho,Toki-shi ,Gifu
509-5292,Japan

E-mail:ikeda.katsunori@lhd.nifs.ac.jp

Kyoto University

Yoshida honmachi Sakyou-ku,

Kyoto 606-8501,Japan

E-mail:maekawa@energy.kyoto-u.ac.jp

JIE Yinxian

Institute of Plasma Physics,
Chinese Academy of Sciences
P.O.Box 1126,Hefei,Anhui 230031,P.R.China
E-mail:yx_jie@ipp.ac.cn

MIZUUCHI Tohru

Institute of Advanced Energy ,
Kyoto University
Gokasho,Uji ,Kyoto 611-0011,Japan
E-mail:mizuuchi@iae.kyoto-u.ac.jp

KADO Shinichiro

The University of Tokyo
E8-BLDG,7-3-1Hongo,Bunkyo-ku,
Tokyo 113-8656, Japan
E-mail:kado@n.t.u-tokyo.ac.jp

MORITA Shigeru

National Institute for Fusion Science
322-6 Oroshi-cho,Toki-shi,Gifu
509-5292,Japan
E-mail:morita.shigeru@lhd.nifs.ac.jp

KASAHARA Hiroshi

National Institute for Fusion Science
322-6 Oroshi-cho,Toki-shi,Gifu
509-5292,Japan
E-mail:kasahara@nifs.ac.jp

TAN Yi

Department of Engineering Physics,
Tsinghua University
Beijing100084,P.R.China
E-mail:zhegao@gmail.com

KOIDE Yoshihiko

Japan Atomic Energy Agency
801-1Muko-yama ,Naka-shi,Ibaraki,
311-0193,Japan
E-mail:koide.yoshihiko@jaea.go.jp

TOI Kazuo

National Institute for Fusion Science
322-6 Oroshi-cho,Toki-shi ,Gifu
509-5292,Japan
E-mail:toi.kazuo@LHD.nifs.ac.jp

LIU Jin

Yunnan University
No.2,North chihu road,Kunming,Yunnan
650091,P.R.China
E-mail:jinlj@ipp.ac.cn

TOKUZAWA Tokihiko

National Institute for Fusion Science
322-6 Oroshi-cho,Toki-shi ,Gifu
509-5292,Japan
E-mail:tokuzawa.tokihiko@lhd.nifs.ac.jp

MAEKAWA Takashi

Graduate School of Energy Science,

TOMITA Yukihiko

National Institute for Fusion Science
322-6 Oroshi-cho,Toki-shi,Gifu
509-5292,Japan
E-mail:tomita@nifs.ac.jp

WATARI Tetsuo

National Institute for Fusion Science
322-6 Oroshi-cho,Toki-shi ,Gifu
509-5292,Japan
E-mail:watari.tetsuo@toki-fs.jp

WANG Jun

Institute of Plasma Physics,
Chinese Academy of Sciences
P.O.Box 1126,Hefei,Anhui 230031,P.R.China
E-mail:jwang@ipp.ac.cn

XIAO Bingjia

Institute of Plasma Physics,
Chinese Academy of Sciences
P.O.Box 1126,Hefei,Anhui 230031,P.R.China
E-mail:bjxiao@ipp.ac.cn

WANG Kongjia

Institute of Plasma Physics,
Chinese Academy of Sciences
P.O.Box 1126,Hefei,Anhui 230031,P.R.China
E-mail:kjwang@ipp.ac.cn

XU Ping

Institute of Plasma Physics,
Chinese Academy of Sciences
P.O.Box 1126,Hefei,Anhui 230031,P.R.China
E-mail:pingxu@ipp.ac.cn

WANG Lei

Institute of Plasma Physics,
Chinese Academy of Sciences
P.O.Box 1126,Hefei,Anhui 230031,P.R.China
E-mail:wangl@ipp.ac.cn

YAN Longwen

Southwestern Institute of Physics
P.O.Box 432,Chendu,Sichuan,
610041,P.R.China
E-mail:lwyang@swip.ac.cn

WANG Qing

School of Mechanical Engineering &
Automation; Northeastern University
Shenyang 110004,P.R.China
E-mail:qingwang@mail.neu.edu.cn

ZHOU Deng

Institute of Plasma Physics,
Chinese Academy of Sciences
P.O.Box 1126,Hefei,Anhui 230031,P.R.China
E-mail:dzzhou@ipp.ac.cn

WANG Zhijiang

Huazhong University of
Science and Technology(HUST)
Wuhan,Hubei 430074,P.R.China
E-mail:wangzj0620@163.com

ZHOU Yan

Southwestern Institute of Physics
P.O.Box 432,Chendu,Sichuan,
610041,P.R.China
E-mail:zhouy@swip.ac.cn

ZHUANG Ge

Huazhong University of
Science and Technology(HUST)
Wuhan,Hubei 430074,P.R.China
E-mail:gezhuang@mail.hust.edu.cn

ZUSHI Hideki

Kyushu University
6-1 Kasuga-kouen,Kasuga,Fukuoka
816-8580,Japan
E-mail:zushi@triam.kyushu.ac.jp